



HAL
open science

Modélisation des écoulements d'eaux denses à travers des seuils topographiques dans les modèles réalistes de circulation océanique : une démonstration du potentiel que représente l'hybridation d'une coordonnée géopotentielle et d'une coordonnée suivant le terrain

Pedro Colombo

► **To cite this version:**

Pedro Colombo. Modélisation des écoulements d'eaux denses à travers des seuils topographiques dans les modèles réalistes de circulation océanique : une démonstration du potentiel que représente l'hybridation d'une coordonnée géopotentielle et d'une coordonnée suivant le terrain. Sciences de la Terre. Université Grenoble Alpes, 2018. Français. NNT : 2018GREAU017 . tel-01871732

HAL Id: tel-01871732

<https://theses.hal.science/tel-01871732>

Submitted on 11 Sep 2018

HAL is a multi-disciplinary open access archive for the deposit and dissemination of scientific research documents, whether they are published or not. The documents may come from teaching and research institutions in France or abroad, or from public or private research centers.

L'archive ouverte pluridisciplinaire **HAL**, est destinée au dépôt et à la diffusion de documents scientifiques de niveau recherche, publiés ou non, émanant des établissements d'enseignement et de recherche français ou étrangers, des laboratoires publics ou privés.

THÈSE

Pour obtenir le grade de

DOCTEUR DE L'UNIVERSITÉ DE GRENOBLE

Spécialité : **Océan, Atmosphère, Hydrologie (CEOAH)**

Arrêté ministériel : 7 août 2006

Présentée par

Pedro COLOMBO

Thèse dirigée par **Bernard BARNIER et Thierry PENDUFF**

préparée au sein du

Institut des Géosciences de l'Environnement

et de l'École Doctorale

Terre, Univers, Environnement

Modelling dense water flows through sills in large scale realistic ocean models: demonstrating the potential of a hybrid geopotential/terrain-following vertical coordinate

Soutenue le **28 juin 2018**,
devant le jury composé de :

M. Eric BLAYO

Professeur UGA, Laboratoire Jean Kuntzmann, Grenoble, Président

M. Arne BIASTOCH

Professeur, GEOMAR, Kiel, Germany, Rapporteur

M. Patrick MARSALEIX

Chargé de Recherche CNRS, Laboratoire d'Aérodynamique, Toulouse, Rapporteur

M. Jerome CHANUT

Docteur-Ingénieur de recherche, Mercator Ocean, Toulouse, Examineur

Mme. Julie DESHAYES

Chargée de recherche, Laboratoire d'Océanographie et du Climat, Paris, Examinatrice

M. Bruno ZAKARDJAN

Professeur, Institut Méditerranéen d'Océanologie, Toulon, Examineur

M. Bernard BARNIER

Directeur de Recherche, Institut de Géosciences de l'Environnement, Grenoble, Directeur de thèse

M. Thierry PENDUFF

Directeur de Recherche, Institut de Géosciences de l'Environnement, Grenoble, Co-Directeur de thèse



Contents

I	State of the art	11
1	The Denmark Strait Overflow in observations	13
1.1	Circulation scheme	13
1.2	Ship campaigns	14
1.2.1	Sill	14
1.2.2	Dohrn Bank section	16
1.2.3	Spill jet	17
1.2.4	TTO section	18
1.2.5	Angmagssalik section	18
1.2.6	Depth of the overflow	20
1.2.7	Microstructure measurements in the vein	20
1.3	Mooring arrays	21
1.3.1	Sill array	21
1.3.2	Dohrn Bank, TTO and Angmagssalik array	22
1.4	Satellite observations	25
1.5	Physical processes	26
2	Past modelling efforts	28
2.1	BBL parameterisation	28
2.2	Concerning vertical coordinates	30
2.2.1	Most used coordinate types	30
2.2.2	Some published results	31
3	Summary and discussion	34
II	Objectives and methodological approach	37
4	Objectives	39
5	Methodological approach	40
5.1	Model setup	40
5.2	Initial and boundary conditions	42
5.3	Diagnostic strategy	42
6	The reference simulation	47
6.1	Discussion	51
III	z-coordinate	53
7	Sensitivity tests in z-coordinate	55

7.1	BBL	56
7.2	Vertical resolution in 1/12°	57
7.3	Vertical mixing scheme in 1/12° 300L	58
7.4	Vertical resolution at 1/60°	59
7.5	Role of EVD	60
7.5.1	Vertical resolution in 1/12° - EVD=1	60
7.5.2	Vertical resolution at 1/60° - EVD=1	61
7.6	Lateral boundary condition - No slip	62
7.6.1	Vertical resolution in 1/12° - No slip	62
7.6.2	Vertical resolution at 1/60° - No slip	63
7.7	Momentum advection formulation - EEN vector	64
7.8	Analysis and understanding	66
7.9	A possible explanation for the behavior in the vertical resolution at 1/12°	68
7.10	Analysis of the 1/60° 300L simulation	72
7.11	Further comments of the 1/60° 300L simulation	75
7.12	Transient dynamics in A12L300	79
7.13	DSO in z-coordinates: What to retain	81
IV s-coordinates		82
8 From sigma to enveloping s-coordinates		84
8.1	Stretching	84
8.2	Pressure gradient errors	88
8.3	The enveloping bathymetry or VQS	89
8.3.1	Smoothing and saw-tooth issue	90
8.4	Estimation of PGE driven spurious currents	91
8.4.1	Stratification and setup	91
8.4.2	Sensitivity experiments for parameter selection	92
8.4.3	Masking effect	95
8.4.4	Stretching effect	98
8.4.5	Horizontal resolution	100
9 Realistic configuration results		101
9.1	Enveloping bathymetry	103
9.2	Stretching	104
9.3	Horizontal resolution	105
9.4	Griffies triads	106
9.5	Analysis and understanding	108
9.6	Further comments of most performing simulations	111
9.7	Summary and discussion	117
V Local s-coordinates		118
10 A first try		120
10.1	Implementation	120
10.2	Results	122
10.3	Summary and preliminary conclusions	124
10.4	Limitations	125

11 Local VQS Hybrid coordinate	126
11.1 Implementation	126
11.1.1 Connection improvement	126
11.1.2 Stretchings	126
11.1.3 Region definition	127
11.1.4 Overlapping between sigma regions	127
11.1.5 Inclusion of partial step	128
11.2 A bad connection case	129
VI Conclusion and perspectives	130
VII Appendix	135
12 Vertical levels distribution	136
13 Additional simulations	137
13.1 The 990L case	137
13.2 Adaptive EVD in 1/12° 300L	139
References	151

Abstract

Overflows play an important role distributing the heat and salt fluxes in the ocean, feeding deep boundary currents and most of the world ocean deep waters. Therefore, an unrealistic representation of overflows in global models may have impacts over many aspects of the simulated state of the ocean.

To achieve a realistic representation of overflows is still a challenge for ocean modelling. This work addresses this problem using the community ocean general circulation model NEMO with a regional configuration of the Denmark Strait Overflow (DSO) at eddy-resolving resolutions. This work first proposes a definition of the DSO in order to characterize its associated water masses and to find the main caveats in a control simulation that uses the most standard parameters of the commonly used global configurations of NEMO (e.g. Drakkar configurations).

Thanks to this definition we then study the impacts on the DSO of a large number of model parameters through a range of eddy-permitting to eddy-resolving resolutions (e.g. $1/12^\circ$ and $1/60^\circ$) in the classic z -coordinate system used in NEMO. Main findings were found increasing the horizontal and vertical resolution, but most model parameters have no significant impacts. In particular it was found that increasing vertical resolution without using a coherent horizontal resolution degrades the solution. The main reason is the EVD parameterisation that propagates the dense vein of fluid along a grid-slope, instead the topographic slope. Coherent and very high resolution both in the horizontal and in the vertical is needed in order to resolve Ekman bottom boundary layer dynamics and keep the EVD localized to the very bottom.

We also study the representation of the DSO with a hybrid terrain-following (s) and geopotential (z) coordinate system and obtained considerable improvements for a relatively small increase in computational cost. Finally, we propose a mixed s - z vertical coordinate that relies on a local implementation of s -coordinates within the z -coordinate model, limited to the area where DSO waters are produced. This local implementation is such that it minimizes the effects of pressure gradient errors linked to this type of coordinate, smoothly connects to the global z -coordinate, and does not add any significant computational cost. The improvement of the DSO is found to be drastic.

This work emphasizes the utility of adapting the vertical coordinate system to the main physical problem. A modeling challenge would be to have a vertical coordinate system that is locally adapted to the most critical ocean process.

Résumé

Dans le jargon de l’océanographie physique, un *overflow* est une masse d’eau dense, formée sur un plateau continental ou dans une mer marginale, qui rejoint l’océan ouvert en s’écoulant par-delà de fortes contraintes topographiques telles que d’étroits détroits, des seuils ou des talus continentaux particulièrement pentus. Ces processus d’overflow jouent un rôle important en distribuant les flux de chaleur et de sel dans l’océan, car ils alimentent les courants profonds et la plus grande partie des eaux profondes de l’océan global. Une représentation irréaliste de ces processus dans les modèles peut avoir un impact sur leur aptitude à simuler d’autres aspects majeurs de la circulation océanique globale.

Représenter de manière réaliste les overflows est encore un défi en modélisation numérique de l’océan. Cette thèse étudie ce problème en utilisant le modèle de la circulation générale océanique NEMO avec une configuration régionale de l’overflow du détroit du Danemark (Denmark Strait Overflow, DSO) avec des résolutions dites *eddy-permitting/resolving* (permettant la génération de turbulence de mésoéchelle). Dans ce travail je propose d’abord une définition du DSO pour pouvoir caractériser les masses d’eaux qui lui sont associées et pour mettre en évidence et quantifier les principaux défauts de représentation du DSO rencontrés dans une simulation de référence réalisée avec les paramètres standards couramment utilisés dans les configurations globales de NEMO (configurations Drakkar).

Grâce à cette définition, j’ai pu quantifier l’impact d’un grand nombre de paramètres du modèle sur la représentation du DSO avec des résolutions allant de l’eddy-permitting ($1/12^\circ$) à l’eddy-resolving ($1/60^\circ$). Cette étude, qui a nécessité un grand nombre de simulations de sensibilité, a été faite avec le système de coordonnées verticale classique utilisé dans NEMO, qui est la coordonnée géopotentielle z .

Les améliorations les plus importants ont été trouvées en augmentant la résolution verticale et horizontale de façon cohérente. Mes résultats ont cependant montrés que la plupart des paramètres du modèle ont un impact très faible sur la représentation finale du DSO. En particulier, nous avons trouvé qu’augmenter la résolution verticale sans utiliser une résolution horizontale cohérente détériore la solution. La principale raison est que la paramétrisation EVD, représentant la convection libre forcée par une instabilité statique de la colonne d’eau, propage la veine de fluide en direction de la pente de la grille, et non de la pente de la topographie, ce qui induit une trop forte dilution des propriétés de l’overflow. Une très haute résolution horizontale et verticale ($1/60^\circ$ et 300 niveaux) permet de résoudre la couche d’Ekman de fond et de maintenir l’EVD localisé au fond, limitant ainsi la dilution de la veine d’eau dense.

J’ai ensuite étudié la représentation du DSO dans un système de coordonnées hybride combinant une coordonnée suivant-le-terrain (s) avec la coordonnée géopotentielle (z). Les améliorations obtenues dans la représentation du DSO sont remarquables et pour une faible augmentation du coût de calcul. Finalement, nous proposons un système de coordonnées verticale mixte s - z qui consiste en une implémentation locale de la coordonnée s à l’intérieur de la grille du modèle en coordonnée z , limité à la région où le DSO se produit. Cette implémentation locale minimise les effets des erreurs du gradient de pression liés à ce type de coordonnée, fait une connexion lisse avec la coordonnée z , et n’introduit pas de coûts de calcul démesurés. L’amélioration de la représentation du DSO est encore très importante.

Ce travail souligne l’importance d’adapter le système de coordonnées verticale aux processus physiques les plus pertinents. Un défi de la modélisation serait d’avoir un système de coordonnées verticale qui est localement adapté aux processus océaniques dominants.

Para vos viejo, gracias por todo

Introduction

An oceanic overflow consists in a dense gravity current that is formed behind a topographic barrier or on a continental shelf, and by the effect of this density difference it is pushed to the interior of the ocean, overflowing the topographic constraint. The main important ones in magnitude are the ones associated with the Nordic Seas (Denmark Strait overflow and Iceland-Scotland overflow) driven mainly by cold water; the Mediterranean overflows which are driven mainly by salty water and the Antarctica continental shelf overflows which are driven mainly by cold water. This contribution of dense water into the open ocean is also counterbalanced by the intrusion of water to the different basins where the overflow water is formed. For example in the Denmark Strait overflow (DSO hereafter), very cold water comes from the Arctic and enters into the Atlantic through this strait; in exchange, warm and salty water escapes the Atlantic Ocean and enters into the Arctic Ocean. We see then that an overflow can play an important role distributing the heat and salt fluxes in the ocean. Moreover, the DSO joins with the Iceland-Scotland overflow to feed the Deep Western Boundary Current. This current at the same time, recirculates to the equatorial regions and becomes part of the thermohaline circulation. In fact the thermohaline circulation is driven in a significant part by the different overflows.

We see then that a correct representation of overflows by an ocean model is a key aspect in order to generate realistic boundary currents and realistic heat and salt fluxes with appreciable impacts all over the global ocean. However, the overflow representation has been a resisting flaw in most global ocean models and especially in z -coordinate models (z stands for geopotential) like the community ocean general circulation model NEMO (Madec, 2008¹). Previous studies tried to tackle this issue by the implementation of different parameterizations. Besides the high level of effort consecrated, overflows presently remain a challenge.

In this context we consider that there are some aspects that are missing in the way this problem is addressed. In first place we believe that more effort should be putted in realistic configurations, most studies having looked at this problem with idealized model configurations. In fact, we do not know the impacts that a large number of parameters have on the final representation of overflows among different resolutions. The general objective of this thesis is to improve the representation of overflows in realistic eddy-resolving applications of NEMO. More specifically, a first objective is to quantify the impacts of a large number of parameters through a range of eddy-resolving resolutions (e.g. $1/12^\circ$ and $1/60^\circ$) in the classic z -coordinate system used in NEMO. A second objective is to investigate the ways of improvements that the hybrid coordinate system σ - z is offering to the treatment of overflows (σ standing here for terrain-following). A third objective is to evaluate whether the present diagnostics used, correctly constrained the main properties of overflows according to the different definitions available. We therefore choose to work in a realistic configuration and we choose one overflow in particular to be able to make a large number of tests for a bearable computational cost. Because of its magnitude and the

¹The Nucleus for European Modelling of the Ocean (NEMO, Madec, 2008) is a state-of-the art modelling framework for oceanic research, operational oceanography, seasonal forecast and climate studies. NEMO includes several major components, namely NEMO-OPA for modelling the ocean dynamics and thermodynamics (blue ocean), LIM for the sea-ice dynamics and thermodynamics (white ocean), TOP for the on/offline oceanic tracers transport and PISCES for the biogeochemical processes (green ocean). NEMO also includes an adaptive mesh refinement software (AGRIF). <https://www.nemo-ocean.eu/>

relatively large amount of observations available, the overflow chosen is the DSO.

This report is divided in six parts

- In the first part, we explain the state of the art knowledge of the DSO and we set the basis for the comparison between model outputs and observations. We also make a summary of the different approaches that has been followed to model and study overflows and their success in the task.
- In the second part, we explain in detail the modelling challenge, we describe the original and realistic NEMO model configuration developed to simulate the DSO and the diagnostic strategy. The different diagnostics are applied to the reference simulation in order to show the problem characteristics.
- In the third part, we show the results obtained in z -coordinates. The total number of simulations is around 50 and among the different tests we study the impact on the model representation of the overflow of: vertical resolution (46, 75, 300 and 990 vertical levels), horizontal resolution ($1/12^\circ$ and $1/60^\circ$), lateral boundary condition (free slip and no-slip), and a few other parameters or numerical schemes.
- In the fourth part, we show the impact of the implementation of a terrain-followings vertical coordinate in the representation of the overflow. The series of tests are based on the use of Vanishing Quasi Sigma coordinates (Dukhovskoy et al., 2009) and both $1/12^\circ$ and $1/60^\circ$ horizontal resolutions are used.
- In the fifth part, we explain the development of a mixed type of coordinates where z and s -coordinates are used in the same domain, and demonstrate its ability to represent the overflow.
- In the sixth part we concluded the study with a summary of the main findings and we provide some short and medium term perspectives to this work.

Part I

State of the art

Chapter 1

The Denmark Strait Overflow in observations

An oceanic overflow is a dense water mass that flows over a relevant bathymetric feature. The dense water descent includes significant mixing, entraining ambient water and therefore significant changes in the properties of the vein of fluid. In particular the Denmark Strait overflow (DSO) is a current coming from the Arctic that passes through the sill located at the Denmark Strait (640m depth) and sinks into the North Atlantic (figure 1.1). Besides it accounts for almost 50% of the Nordic flows transports (Girton and Sandford, 2003), there are mainly two very important features characterizing this overflow. First it feeds the Deep Western Boundary Current (DWBC) of the North Atlantic, which is an important contributor of the Atlantic Meridional overturning circulation (AMOC). Second, it feeds the North Atlantic with deep waters (together with the Iceland-Scotland Overflow), determining the deep stratification of the basin. These two features make this very localized process a key player in the Ocean Global Circulation (OGC). We propose here a description divided in the sources that feeds the DSO, the transport observed through different mooring arrays situated in the Irminger Basin, and finally we focus on the properties of the vein obtained through research vessel campaigns.

1.1 Circulation scheme

Following the circulation scheme proposed by Appen et al., 2014 for fluxes of water of potential density greater than 27.6 kg/m^3 (figure 1.1), the DSO is formed with the contribution of the East Greenland Current (EGC) and the North Icelandic Jet (NIJ). The EGC bifurcates at the northern end of the Blossville Basin (not shown in the scheme) and its offshore part joins the NIJ, forming a unified branch of water that finally ends as the DSO. The other branch of the EGC keeps its way as a separated branch which bifurcates a second time, one part feeds the Kangerdlugssuaq Trough ("KG Trough" in the scheme), which later also feeds the Spill jet, and the other eventually joins the Irminger Current in direction to the Labrador Sea. The warm and salty Irminger current (IC) flows northward and bifurcates before arriving to the sill. One branch keeps its way to the north at the eastern side of the Denmark Strait as the North Icelandic Irminger Current (NIIC). This current is cooled by the atmosphere and vanishes in the Iceland Sea Gyre. It is believed that once this water mass is cooled, the dense water formed returns to feed the NIJ (Våge et al., 2013). The other branch of the IC keeps its way to the Labrador Sea interacting with DSO and with mesoscale eddies present in the Irminger Basin.

Finally, the DSO joins the Iceland Scotland Overflow (ISO) to form a unified Deep Western Boundary Current (DWBC). At the Cape Farewell Section there are three different currents flowing to the Labrador Sea. On the bottom the DWBC identified as the water denser than 27.8 kg/m^3 , in the middle the Spill Jet identified as the water between 27.6 and 27.8 kg/m^3 , and on the upper layer the EGIC (Brearley et al., 2012).

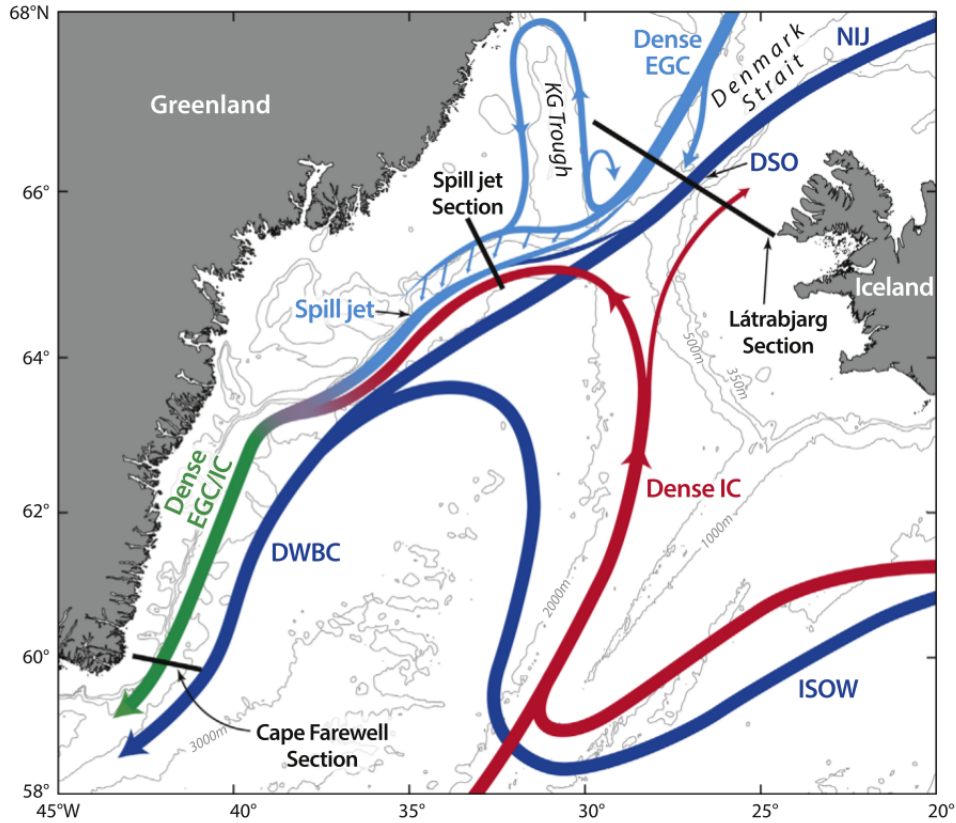


Figure 1.1: *Circulation scheme in the region of the Denmark Strait, from Appen et al., 2014*

Denmark Strait sill description

The flow of the DSO originates in a very narrow and shallow channel, in which the narrowest point is located at the sill. An orthogonal section of it can be observed in figure 1.4b. This portion of the channel along which the overflow passes has a horizontal amplitude of about 35km and a vertical amplitude of about 300m . At present eddy-resolving model resolutions ($\sim 1/12^\circ$), and at these latitudes, the model grid is about 5km , giving around 7 points to represent the vein in the horizontal. With such number of points we are not able to correctly resolve the bathymetry, and we are therefore far from resolving the mixing processes occurring in the vein. Moreover the changes in depth after the sill are rather abrupt.

1.2 Ship campaigns

As it will be seen, the information coming from localised long-term measurements (mooring arrays) is too sparse (in the vertical and in the horizontal) to show in detail the structure of the current. To this end we use the information given by hydrographic sections. Caution must be taken with this information as well, since the DSO presents a high variability, having big change of properties in a lapse time of a few days. A map of the region with the location of the main sections is shown in figure 1.12.

1.2.1 Sill

The sill section has received quite a lot of attention. Measurements of the overflow directly at this location are of importance since the overflow is still not modified by the entrainment of ambient water. It is therefore possible to study its properties and their relationship with climate

change events (Jochumsen et al., 2013). For ocean modelling the sill is the starting point for a correct representation of the overflow (source waters). Representative values of temperature, salinity and velocity are needed in order to obtain correct values of overflow product waters.

An idea of the high variability of the DSO can be obtained in the work of Mastropole et al., 2017, in which they studied the data coming from 111 ship campaigns at the Denmark Strait sill. These authors performed a diagram that we show in figure 1.2, in which we observe the different dates of these campaigns and a color was assigned according to whether or not the ship passed when a bolus of dense water was present (differentiating between a non-occupation, a short occupation or a bolus occupation). Only 41% of the campaigns performed measurements with the presence of a bolus of water.

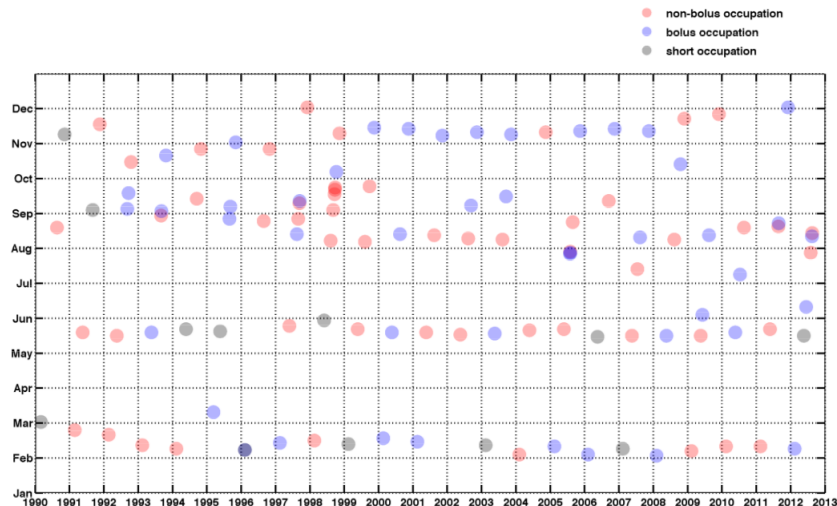


Figure 1.2: Planning of the 111 ship campaigns studied in Mastropole et al., 2017. A color was attributed whether there was a non-bolus occupation (light red), a bolus occupation (light blue) or a short occupation (gray)

Figure 1.3 shows the temperature profile when a bolus is present and when it is not. The difference is remarkable, and can be estimated of the order of $2^{\circ}C$. The mean temperature of all these sections can be found in figure 1.4a, where a very localized minimum mean bottom value of around $-0.5^{\circ}C$ is observed. A considerable region has a temperature of the order $0.5^{\circ}C$ and on top we found a large region with a temperature of around $1^{\circ}C$, which has probably already suffered mixing with surrounding waters.

Some efforts have been done in order to constraint the definition of the overflow with temperature thresholds (Macrandar et al., 2007, Dickson et al., 2008). We do not follow these approaches here. The reason is that while its usefulness can be argued at the sill, this approach rapidly becomes inadequate further downslope due to the intense mixing present along the path of the overflow.

Velocity, on the other hand, is a clear indicator of the presence of the DSO, with maximum values that can reach more than $1.5ms^{-1}$ heading southward. In figure 1.4b we can see that the 27.8 isopycnal considers a portion of the Irminger current in addition to constraining the DSO. The velocity related calculations, like the transport, should carefully choose the relevant properties, otherwise we will very easily consider water masses that are not of interest for the study and this could lead to misleading results.

One important thing to point out is that while a very high variability due to the boluses is present, reflecting the high changes in velocity, a pattern in temperature and density remains present (figure 1.3). Combining both aspects, could lead to an improved definition of the overflow.

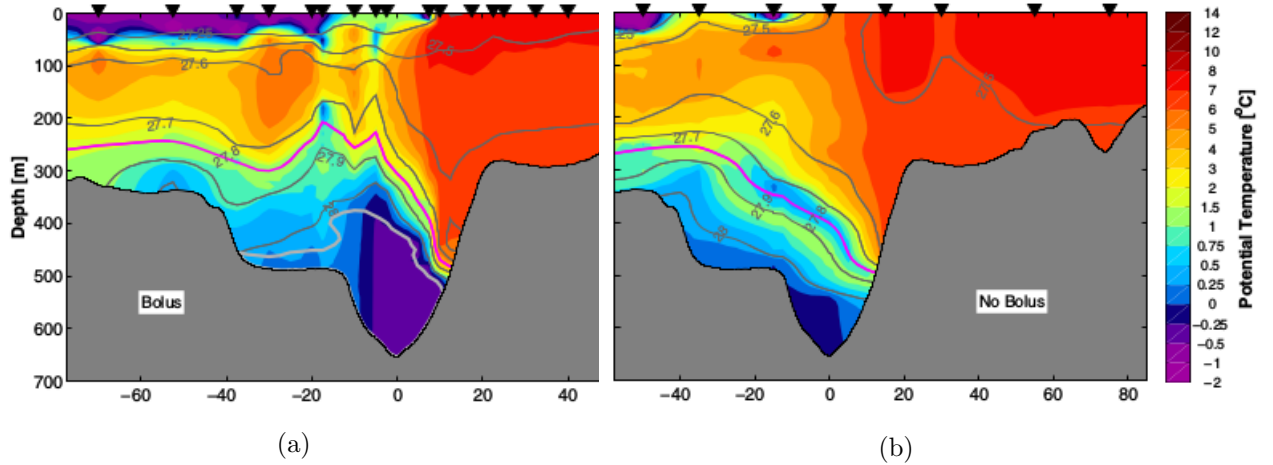


Figure 1.3: Potential temperature profile in colors and isolines of potential density (the magenta line corresponds to a density value of 27.8) showing a) presence and b) absence of a bolus of overflow water. From Mastropole et al., 2017

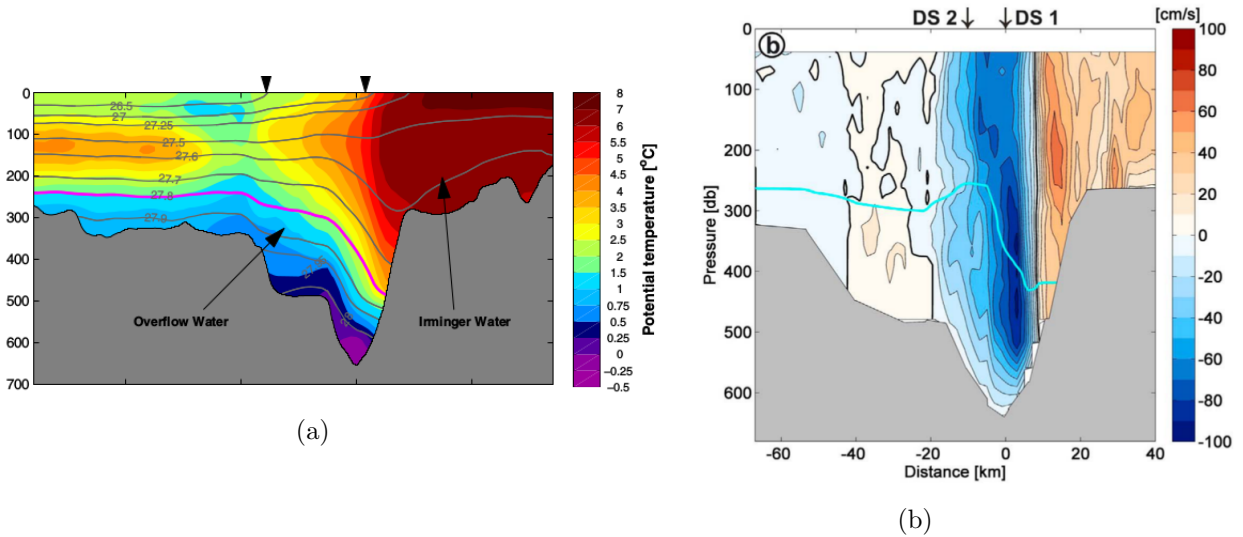


Figure 1.4: Sill of the Denmark Strait, hydrographic sections a) Potential temperature profile in colors and isolines of potential density (the magenta line corresponds to a density value of 27.8) showing the mean of all the available data between 1990 and 2012, from (Mastropole et al., 2017) b) Normal velocity to the section, in blue southward velocities and with a thick blue line the 27.8 density is contoured, from Jochumsen et al., 2013

1.2.2 Dohrn Bank section

The ASOF project (Arctic Sub-Arctic Ocean Flux, <http://asof.awi.de>) has performed repeated hydrographic sections along a number of sections in the Irminger basin (figure 1.5). The Dohrn Bank array section correspond in this case to the eastern portion of their section 1.

We show here the figures obtained from a Cruise performed in August 2004, which results can be found in Quadfasel, 2004. Profiles of temperature and density at the Dohrn Bank section can be found in figure 1.6. We observe there that even at such a short distance from the sill the DSO has already reach a depth of more than 2000m. The overflow is clearly defined by the 3°C isotherm and the 27.85 isopycnal.

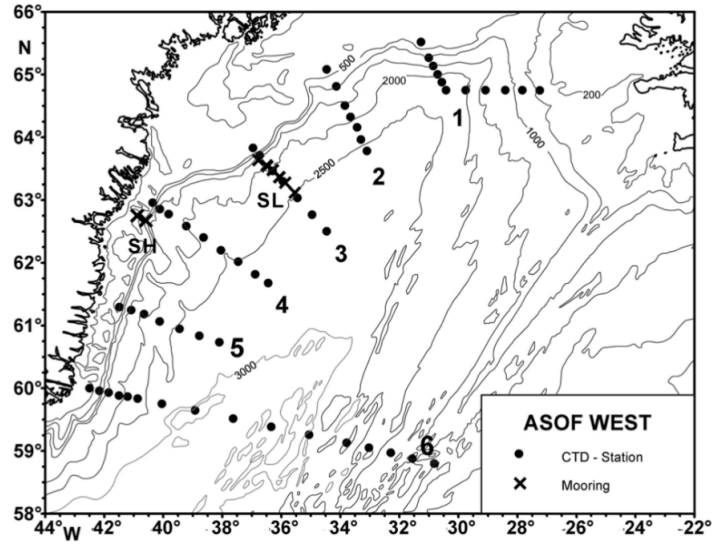


Figure 1.5: *Layout of the different sections in the Irminger basin of the ASOF project (Quadfasel, 2004)*

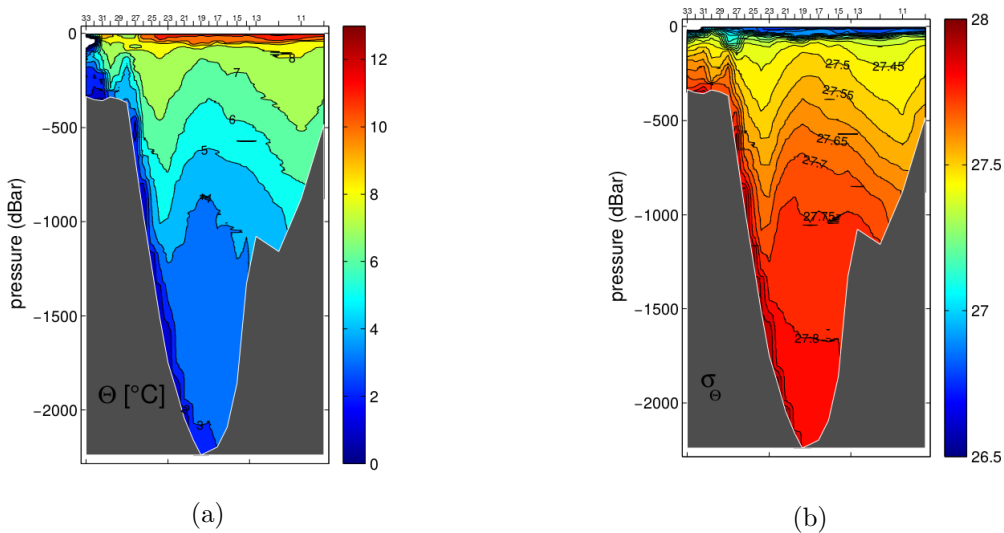


Figure 1.6: *Hydrographic sections number 1 in Quadfasel, 2004, which partially covers the Dohrn Bank array a) Potential temperature b) Potential density*

1.2.3 Spill jet

Another section of interest is the Spill jet section, which is between the Dohrn Bank and TTO sections, visible in figure 1.1. The spill jet first appeared in publications in Pickart et al., 2005. They defined it as *”an intense, narrow current banked against the upper continental slope [...] result of dense water cascading over the shelf edge and entraining ambient water”*. A scheme indicating the source and the overall mechanism of this spilling water mass can be observed in figure 1.1. In figure 1.7a we observe an example of the presence of this current. The spill jet is considered to be the current located on the shallowest part of the slope at $\sim 300m$ depth. The interest of this water mass comes from the belief that it adjust the final properties of the DSO.

The very high variability mentioned before remains present at this section, both for the spill jet and the DSO. In figure 1.7 we show the normal velocity for two different moments at the spill jet

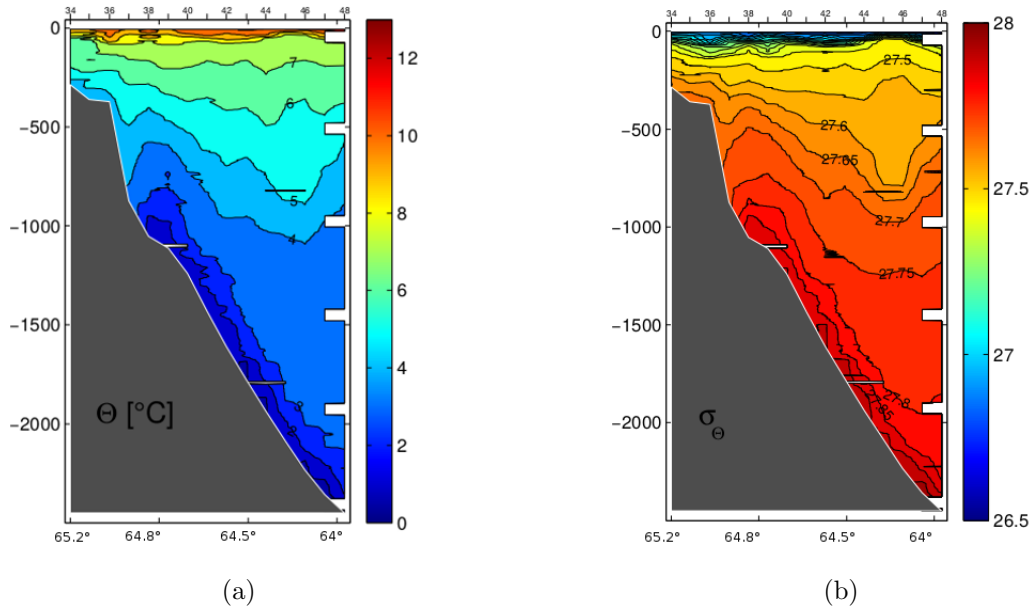


Figure 1.8: *Hydrographic sections obtained in Quadfasel, 2004 at the TTO section (the images have been modified to include latitude values) a) Potential temperature b) Potential density*

vein in direction to the interior of the basin.

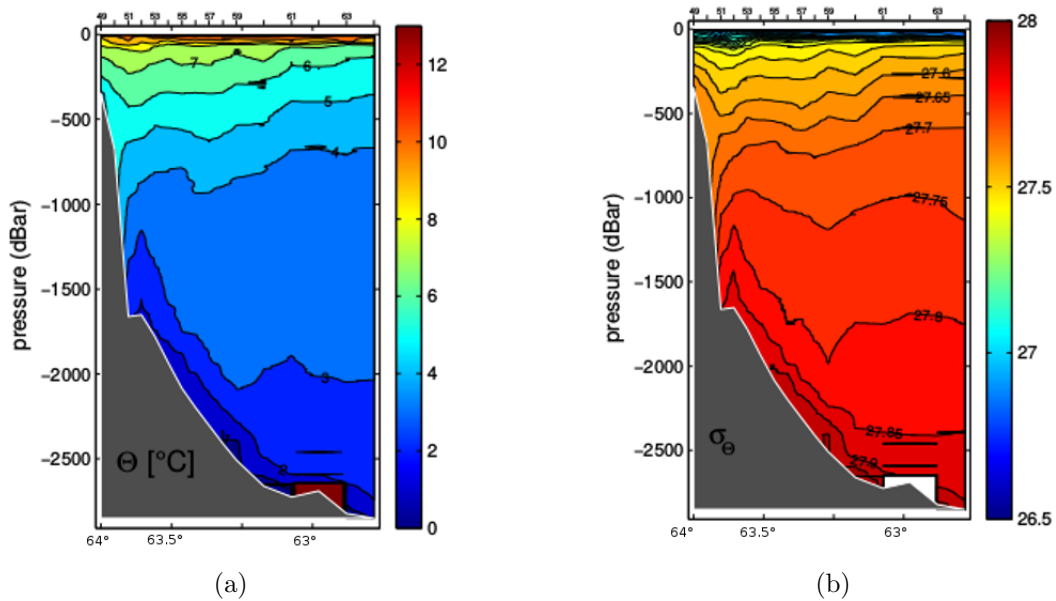


Figure 1.9: *Hydrographic sections obtained in Quadfasel, 2004 at the Angmagssalik section (the images have been modified to include latitude values) a) a) Potential temperature b) Potential density*

Besides the difficulty imposed by the high variability of the DSO to perform the comparison of model outputs with observations, we can use the different hydrographic sections to have an approximate idea of the structure of the current. The information coming from hydrographic sections will always be used for qualitative comparisons, leaving the quantitative comparisons almost exclusively to the data coming from long-term measurements as the ones obtained with mooring arrays.

1.2.6 Depth of the overflow

Of particular interest is the work done in Girton and Sandford, 2003. They studied the data of several cross-sections along the path of the overflow (figure 1.10a). Doing so, they were able to estimate different quantities during the descent process.

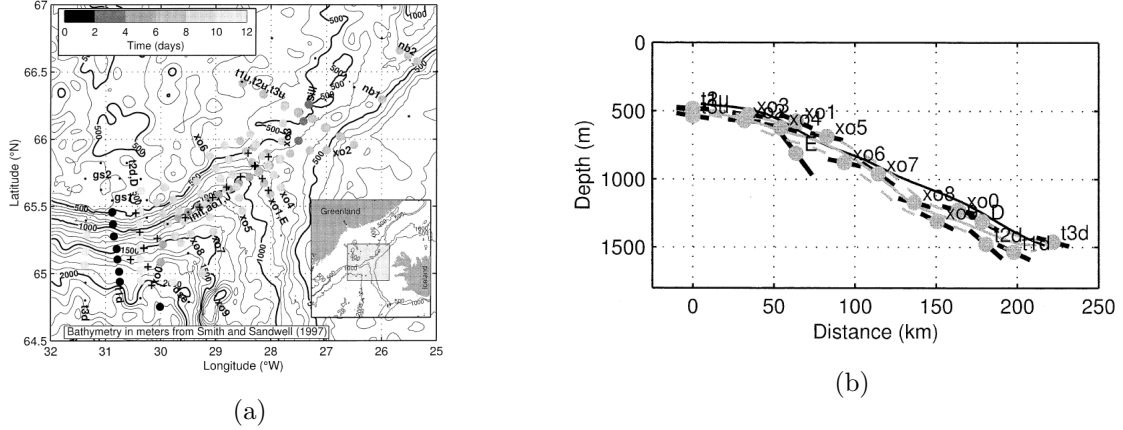


Figure 1.10: *a) Position of the different hydrographic sections in Girton and Sandford, 2003*
b) Depth of the DSO as a function of distance from the sill, from Girton and Sandford, 2003
(calculated using equations 1.1 and 1.2)

One interesting feature of this work is that they proposed a formulation to quantitatively study the depth of the overflow. For a given cross-section they defined the coordinates of the core of the overflow using X in the horizontal (the position of the center of mass anomaly)

$$X = \frac{\iint \rho' x dz dx}{\iint \rho' dz dx} \quad (1.1)$$

and H_b in the vertical (anomaly-weighted bottom depth)

$$\bar{H}_b = \frac{\iint \rho' H_b dz dx}{\iint \rho' dz dx} \quad (1.2)$$

where ρ' is the density anomaly, x is the horizontal distance within the section and H_b is the bottom depth of each station point. It is important to know that both X and H_b are independent of depth (z). Once these values were obtained, they limited geographically the extent of the overflow to a width where the 50% of the mass anomaly is contained. With this, they were able to draw the path and descent of the DSO as a function of the distance from the sill (figure 1.10b).

Besides the obvious limitation of considering a small amount of data, this study proposed a way to geographically locate the DSO without imposing very strict limits. This could be the basis for additional diagnostics, especially to perform a direct quantitative comparison with model outputs.

1.2.7 Microstructure measurements in the vein

Paka et al., 2013 used a microstructure profiler to study the vertical structure of the DSO at two stations located close to the spill jet section (at around 200km from the sill, both close to 30°W 65°N). An example of their results is shown on figure 1.11.

The signature of the overflow is characterized by a very clear bottom boundary layer that starts at $\sim 1250m$ and arrives to the bottom located at $\sim 1450m$, giving a layer thickness of $\sim 200m$. The temperature values varies from $4^\circ C$ above the vein to $0.25^\circ C$ at its bottom. The signature

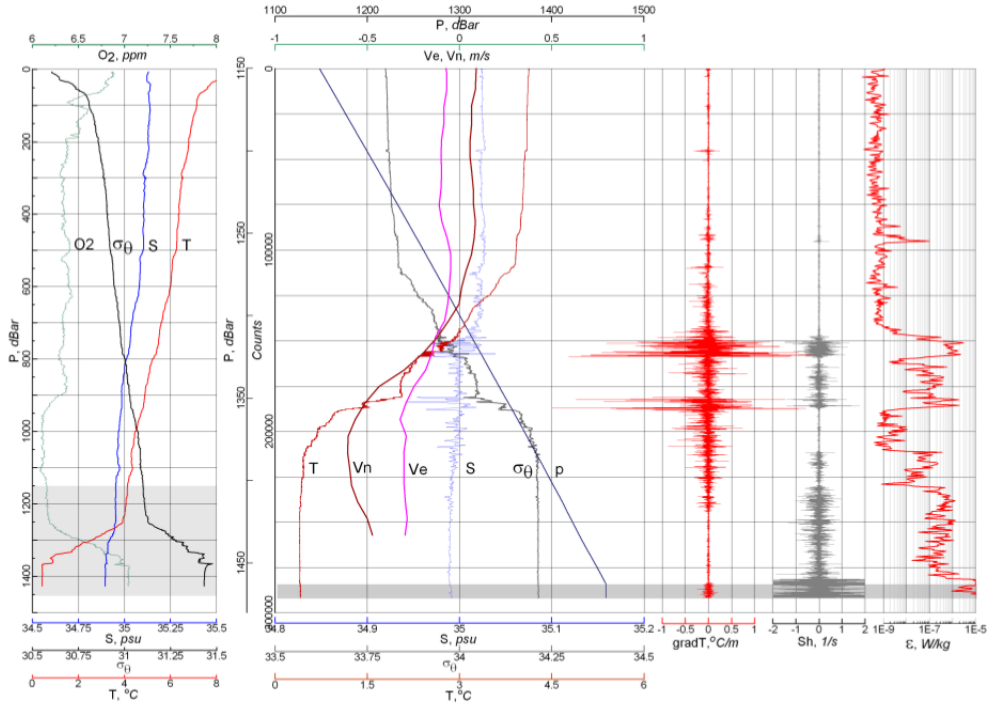


Figure 1.11: *Microstructure measurement of the DSO, from Paka et al., 2013*

on salinity is hardly noticeable and the measurements present a high level of noise at the very bottom. The normal velocity V_n have a value of 0.5ms^{-1} with respect to the values outside the layer, and the tangential velocity V_e of 0.2ms^{-1} . These velocity values are also in accordance with Jochumsen et al., 2017. This figure should serve as a basis for comparison, in case we show that NEMO v3.6 at a specific resolution is able to represent these processes.

1.3 Mooring arrays

Different mooring deployments have been performed in the Irminger basin (figure 1.12). The four arrays that have received most of the attention are (from north to south) the Sill array, the Dohrn Bank array, the TTO array and the Angmagssalik array. Two more arrays were studied in Ross, 1975, after and before the sill, but they are not taken into consideration since they were deployed only once.

1.3.1 Sill array

The DSO has been observed continuously at the sill since 1996 (Jochumsen et al., 2013). The data available comes from one to three moorings depending on the time of evaluation. Macrander et al., 2007 evaluated the data coming from 3 moorings (mooring locations shown in figure 1.13) from 1999 to 2003. The results of these measurements gave transport values of 3.66Sv for 1999 – 2001 to 3.07Sv in 2001/2002, showing a significant decrease (further comments about the methodology are done in the next section). They also measured a significant warming of 0.5° from 1999 to 2002, which was found to coincide with the transport decrease. For these measurements a significant interannual variability was found. Jochumsen et al., 2013 evaluated up to two moorings from 1996 to 2011 with a configuration as shown in figure 1.4b. The time series of the different deployments that make part of this study is shown in figure 1.14, where a blue color is assigned when data of the two moorings are available and magenta when only data from the DS1 mooring (see figure 1.4b) is available. This extended time series did not show

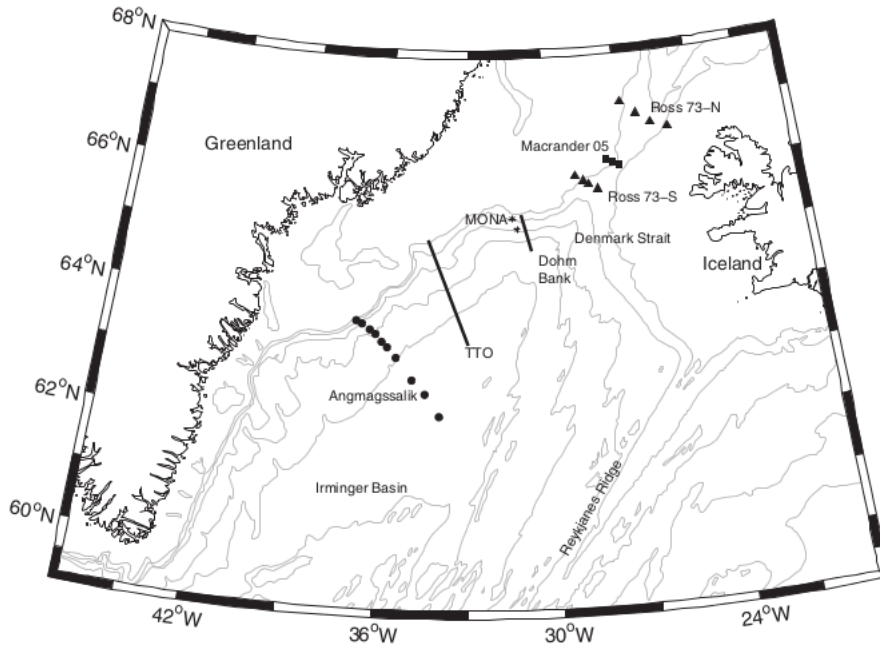


Figure 1.12: Main mooring arrays deployments to study the DSO, being the most important ones (from north to south) the sill array, the Dohrn Bank array, the TTO array and the Angmagssalik array. From Dickson et al., 2008.

that the decrease persisted, and a recovery was found in the 2007/2011 records. They showed a transport that can vary from $-1.4Sv$ to $8.7Sv$, direction inversion events being most likely linked with the fact that a part of the Atlantic current that flows to the north was included in the overflow definition (below isopycnal 27.8), as observed in figure 1.4b (a consideration in velocity values might be needed to reconsider a definition for the overflow). While the transport varies from day-to-day in the order of typically $0.5Sv$, extreme changes of up to $5.5Sv$ have been found. In addition the overflow did not present a pronounced seasonal modulation and the interannual variability was found to be of the order of $0.3Sv$. Finally they arrived to an estimate of the mean overflow transport which is supported by a large amount of data. The mean transport for all days (4337 days) is $3.4Sv$ with a standard deviation of $1.4Sv$ (figure 1.14a). In addition, the mean value for each deployment present similar values to this general mean of $3.4Sv$ (figure 1.14b).

These results seems to show that the sill has to be observed for time periods of the order of decades in order to evaluate specific trends. They also provide with a magnitude of the variability that the overflow transport presents.

More data at the sill were also studied by Voet and Quadfasel, 2010 and Dickson and Brown, 1994, but since the focus is set on the whole descent of the DSO by studying different mooring arrays, this will be commented in the next section.

1.3.2 Dohrn Bank, TTO and Angmagssalik array

Long-term comparisons can be performed with data coming from mooring arrays. This becomes of special interest if we consider that we have these long-term observations all along the path of the DSO. The main limitation of this data is that it is very sparse both in the horizontal and in the vertical. This situation is partially saved in the velocity measurement since the ADCPs are able to make velocity profiles over a few hundred meters. In the case of the temperature and salinity we generally have one or two values per mooring array, usually at the

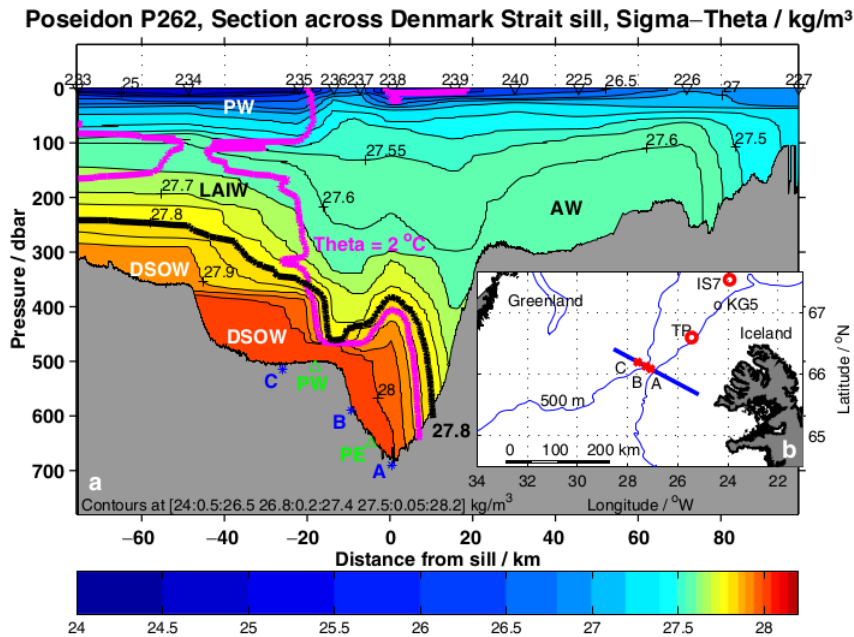


Figure 1.13: Section across the Denmark Strait sill with density in colours, from Macrander et al., 2007. The letters A, B and C indicates the mooring positions, the black thick line denotes the 27.8 isopycnal

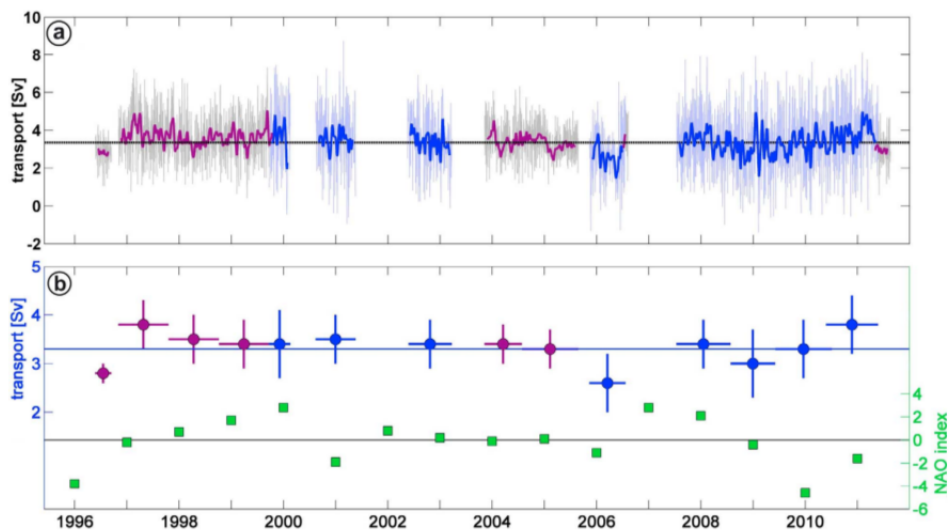


Figure 1.14: a) Transport for the mooring deployments at the sill from Jochumsen et al., 2013. The blue color is assigned when data of the two moorings are available and magenta when only data from the DS1 mooring is available. Light colors are used for the data and solid colors for the filtered version of the data using a hanning filter with a window of 20 days b) Mean transport for each deployment period (horizontal lines), with standard deviation (vertical lines) of the 20-day low pass filtered time series

bottom. For example Dickson and Brown, 1994 overlaid the isopycnal distribution obtained during deployment or recovery cruises onto the mean velocity distribution. Voet and Quadfasel, 2010 used hydrographic data to complement the high temporal resolution data coming from the moorings with snapshot of high spatial resolution. In Macrander et al., 2005 the measurements were simulated and optimized with a numerical model (Käse and Oschlies, 2000), and the same

method was used for Jochumsen et al., 2013. We see then that, in addition to the high variability of the overflow, the estimation processes can largely influence the transport estimate. In order to complement what was said before we add that each mooring is rotated to be aligned with the mean flow. Also, the coverage of each mooring array is less than 1 kilometer, a resolution hardly reached by our model simulations. Therefore, our model calculations will be as well an approximation, and only orders of magnitude should be considered. All in all, mooring arrays provide very valuable information at the bottom (temperature and salinity) and transport estimates. Dickson and Brown, 1994 estimated the transport through these 3 arrays considering a southward velocity ($v > 0$). In this case deployments from 1986 to 1990 were studied. For the Dohrn Bank array the transport was $5.2Sv$, for the TTO array $5.5Sv$ and the Angmagssalik array $10.7Sv$ (this last increase is believed to be caused by the merging with the Iceland-Scotland Overflow).

Bottom properties

Voet and Quadfasel, 2010, performed a similar study to the one of Dickson and Brown, 1994, with data obtained in the period 2001/2002 with four arrays, the Sill, Dohrn Bank (called A), TTO (called B) and Angmagssalik (called C) arrays. Transport estimates were not informed in this work but mean bottom temperature values were calculated, as shown in figure 1.15.

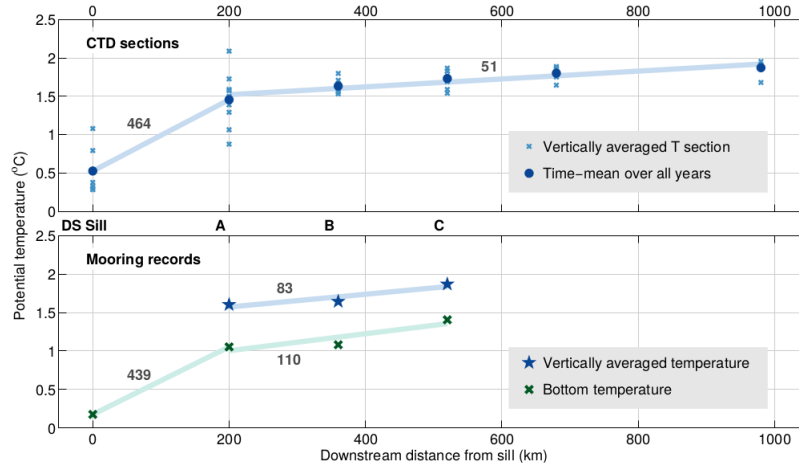


Figure 1.15: *Bottom Temperature values from Voet and Quadfasel, 2010. The upper panel shows the value obtained from hydrographic sections and the lower panel those obtained by mooring arrays*

Jochumsen et al., 2015 studied the data of 9 moorings on the period 2007/2012, the location of which are shown in 1.16a. The bottom temperature values (figure 1.16b) agree well with those published by Voet and Quadfasel, 2010. From the $\sim 0^{\circ}C$ at the sill (moorings D1 and D2), we go to a $\sim 1.1^{\circ}C$ at the spill jet section (moorings D5, D6 and D7), where most of the mixing occurs. The values in the Angmagssalik array present a large range, going from $2^{\circ}C$ for the shallowest point (F2New) to $1.27^{\circ}C$ for the deepest point (UK2).

Jochumsen et al., 2015 also presented mean properties at mooring locations in a form of TS diagram, shown in figure 1.17. Surprisingly, the values of salinity for all mooring arrays (from the sill to Angmagssalik array) are very similar, even smaller for the moorings at the Angmagssalik array. This could mean that the vertical mixing is not intense enough to mix the very bottom properties, or that the direction of mixing is not necessary vertical. This is in accordance with Rudels et al., 1999 who show through hydrographic observations that a capping of the overflow plume with low salinity water survived as the plume sank down the continental slope. The main difference between the different moorings comes from temperature. The mean temperature values are also present in figure 1.16b. Since this diagram summarized a large amount of data

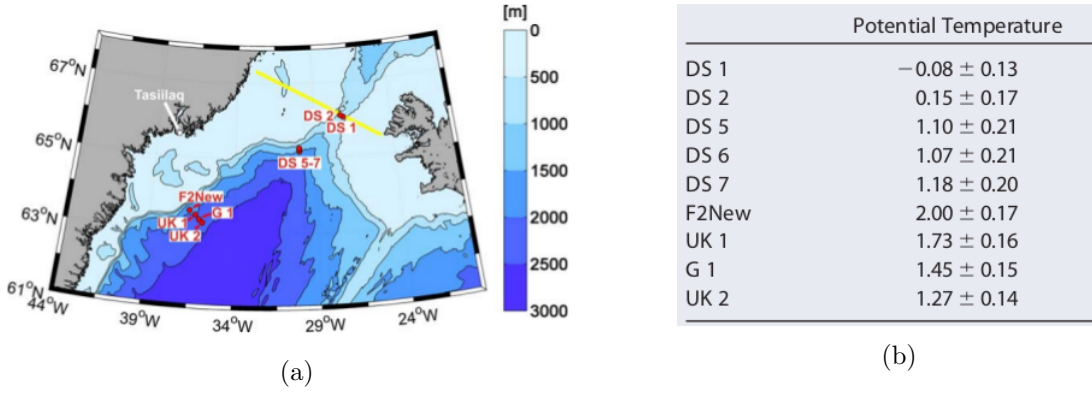


Figure 1.16: a) Mooring setup in Jochumsen et al., 2015 b) Mean values of the bottom temperature at the moorings

in long periods in time, it also appears as an interesting option for long-term comparison with model outputs.

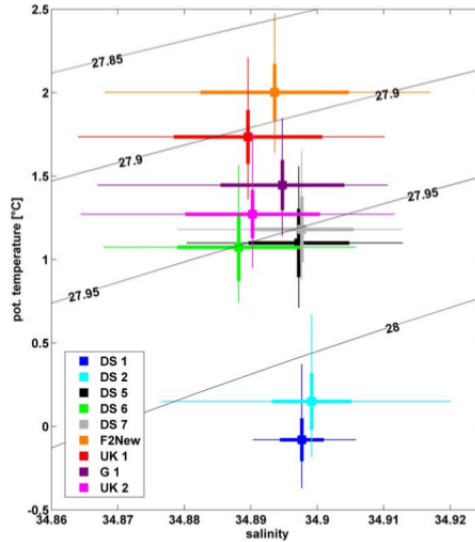


Figure 1.17: TS diagram for low-pass filtered mooring records data. The squares depict the average values, the thick horizontal and vertical lines the standard deviation of the mean, and the thin lines the maximum range of properties, from Jochumsen et al., 2017

1.4 Satellite observations

The study of overflows from SSH (sea surface height) coming from altimetry data have received some interest. According to Spall and Price, 1997: The DSO "shows remarkable mesoscale variability characterized by the continuous formation of mesoscale cyclones just south of the sill. These cyclones have a diameter of about 30km and clear signature at sea surface height". Hoyer and Quadfasel, 2001, presented evidence of temperature and velocity fluctuations associated with the eddies in overflows with an impact on the SSH. They found that the observed increase in SSH variability obtained from TOPEX/POSEIDON altimeter was in agreement with in-situ observations.

This idea was not developed further in the present study since the objective of the work was very different from this task. However, we find this approach very interesting. In case improvements

of the representation of the DSO is achieved, the model outputs can serve as a guide to study an inverse problem in which we could retrieve information of the DSO from the SSH.

1.5 Physical processes

We present here a synthetic description of the main physical processes that affect overflows, which are schematized in figure 1.18.

First dense waters pass through a channel or a sill (where hydraulic control may govern the transport and mixing (Girton et al., 2006)). In the case of the DSO, the channel is relatively wide in comparison with the Rossby radius and therefore the dense water is banked up in the western side of the channel (an effect of the Coriolis force). Then, the dense water descends the continental slope, accelerating because of its density anomaly. The associated vertical acceleration is a non-hydrostatic process (not represented in most OGCMs). The Coriolis force then steers the overflow waters along bathymetric features (Legg et al., 2009). It is important to point out that the gravity (and thus the non-hydrostatic processes) only plays a role on the first descent and then the DSO is rapidly affected by the Coriolis force. Once the DSO arrives at this point, it becomes a geostrophic current in which the equilibrium between the Coriolis force and the pressure gradient force can only be broken either in the bottom Ekman layer or by baroclinic instability (Cenedese et al., 2004). As we have shown in section 1.2.7, the microstructure measurements show very clearly the presence of this boundary layer, and it is believed that it plays a key role in the overflows descent.

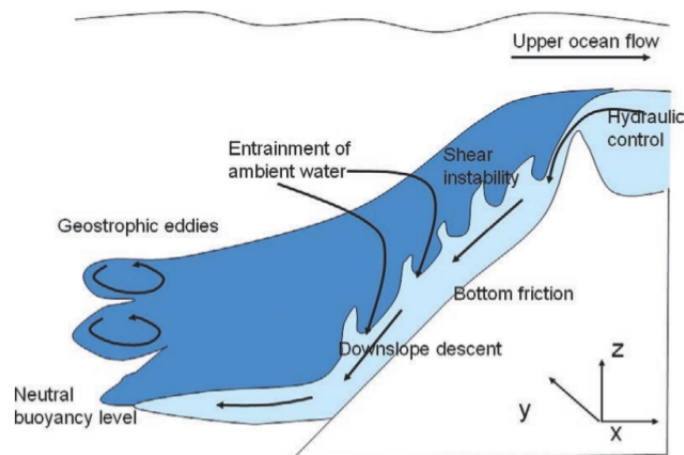


Figure 1.18: *Scheme of the main physical processes in overflows, from Legg et al., 2009*

During the descent, the velocity difference between overflow and the ambient water leads to shear, and therefore entrainment. This causes the dilution of the overflow and the increase in transport. In the case of the DSO, this shear instability was found to dominate the entrainment only within the first 100km from the Denmark strait (Paka et al., 2010). Observations from mooring arrays downstream of the Denmark Strait revealed the dominance of horizontal stirring by mesoscale eddies as the main driver for the entrainment of ambient water (Voet and Quadfasel, 2010, Jochumsen et al., 2015). This emphasizes the importance of the properties of the ambient waters on the final characteristics of the overflow. In a modeling context, it might be of significant importance to correctly represent the Irminger current to obtain a correct representation of the DSO waters. Finally, the overflow finds a neutral buoyancy level.

Scales of motion

The DSO transformations due to the intense mixing all along the path plays a key role in setting its final properties, but still they are the consequence of sub-grid scale motions and thus

are highly parameterized. Paka et al., 2013 elaborated a diagram of the Ozmidov scale versus the Thorpe scale with measurements in the interfacial layer of the DSO, which is reproduced in figure 1.19. The Thorpe scale is useful to extract a turbulent length scale of the mixing and the Ozmidov scale describes the size of the largest turbulent eddies that can exist in a stratified flow. We observe that the predominant mixing occurs in scales smaller than $3m$ and that the maximum value is of the order of $10m$. We see then that the vertical grid scale is of the order of the maximum turbulence scale only in very high vertical resolution simulations.

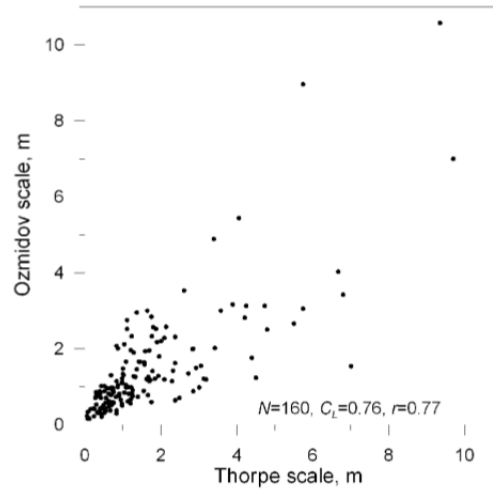


Figure 1.19: *Ozmidov scale versus Thorpe scale for the Denmark Strait Overflow. Measurements taken from a place next to the Dohrn Bank section ($30^{\circ}W, 65^{\circ}N$), from Paka et al., 2013*

Chapter 2

Past modelling efforts

Overflows are influenced by several different physical processes, and the resolution needed to represent them is very high for present ocean models. As it was explained in section 1.5 the vertical acceleration and the Ekman bottom boundary layer are main actors in the descent of the overflow and play a key role in the adjustment of the final properties of overflows. The problem of modelling this type of boundary layers is specially challenging in the context of the hydrostatic approximation in z-coordinates due to the step-like representation of the topography. With this representation, the "convective adjustment" algorithm plays a key role. A schematic of this process is available in figure 2.3a. The particle of dense fluid at the bottom has to be advected horizontally and then mixed on the vertical in order to reach the bottom of the next grid point. This process generates excessive mixing with surrounding waters, giving an unrealistic diluted overflow (Legg et al., 2006). To overcome this problem, overflow parameterisations (known as bottom boundary layer (BBL) parameterisations) and different coordinate type approaches have been proposed.

2.1 BBL parameterisation

Different types of these parameterisations have been proposed and the difference consists generally in different ways to connect bottom grid cells. NEMO includes a BBL parameterisation which is based on the one proposed by Beckmann and Doscher, 1997. The scheme is based on a connection of two consecutive bottom grid cells by an advective and a diffusive part, as it is schematized in figure 2.1. This connection is performed only if two conditions are met, the cell density of the upper grid cell has to be greater ($\rho_2 > \rho_1$) and the depth shallower ($h_2 < h_1$).

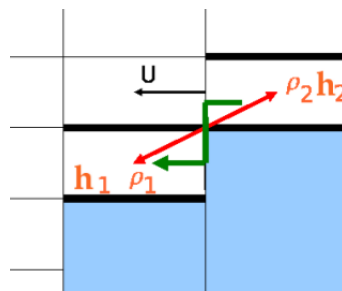


Figure 2.1: Schematic of the BBL scheme present in NEMO, from DeMiranda, 2003. The green line denotes the advective part of the scheme, and the red one the diffusive part

A series of sensitivity tests were performed by Hervieux, 2007, using the DOME configuration (Dynamics of Overflow Mixing and Entrainment), shown in figure 2.2.

The configuration is mainly represented by a prescribed slope (usually of a few degrees) in which a dense fluid with prescribed density and velocity is introduced through a flat channel

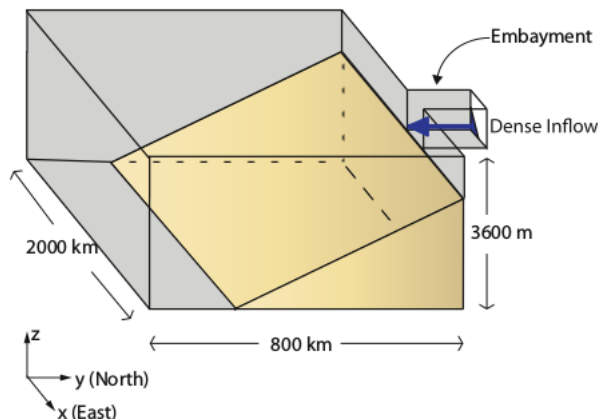


Figure 2.2: Schematic of the DOME configuration, from Reckinger et al., 2015

with prescribed dimensions (usually 600m depth). The vertical dimension is usually chosen to be equal to 3600m, and the lateral dimensions are of the order of 1000km. Since the configuration is idealized it permits to set the different parameters of the fluid with non-dimensional numbers and with different useful conditions for the problem in particular.

Among the numerous number of tests performed:

- Sensitivity tests to the diffusive and advective character of the BBL scheme: diffusive only, advective only and advective and diffusive.
- Sensitivity tests to the lateral boundary condition: free slip, no slip and no slip accurate
- Sensitivity tests to the bottom friction, testing values 32 times higher to the ones used in standard simulations
- Sensitivity tests to a modification of the topography

The goal of this work was to improve the current/topography interaction in NEMO with a target horizontal resolution of $1/4^\circ$. It was shown that in both idealized and realistic configurations, the implementation of the BBL parameterisation improves the solution but over-estimates overflow mixing downstream of the straits. Improvements were also found by increasing ageostrophic effects (like parietal friction, or momentum advection within the BBL). This work suggested that this BBL parameterisation reaches its limits beyond the eddy-permitting regime. All in all, the improvements were not significant enough in order to justify the overall impact of the changes included, especially the added cost of this parameterisation.

Snow et al., 2015, tested different BBL parameterisations with a 1° of horizontal resolution in a Atlantic configuration in MOM5 (Griffies, 2012). A schematic of 3 schemes tested in this study is shown in figure 2.3. In addition to these schemes they also tested a so called "Sigma Boundary Layer" scheme (which is based on Beckmann and Doscher, 1997, and Doscher and Beckmann, 2000) and the so called "Lagrangian point particles" (BLOBS scheme, based on Bates et al., 2012).

The conclusion of this work does not offer a strong message regarding the overall performance of these parameterisations. While in the North Atlantic they have found an increase in the transport of the AMOC in comparison with the reference run (where no BBL scheme is used), this increase was not found in the Antarctic. All the schemes gave a similar response, and the most performant one seemed to be the MIXD scheme.

In summary, besides the great effort put to develop these parameterisations, the overall result of the different approaches have not delivered a clean solution to obtain a good representation of overflows and deep/bottom water properties (Griffies et al., 2000, Legg et al., 2009).

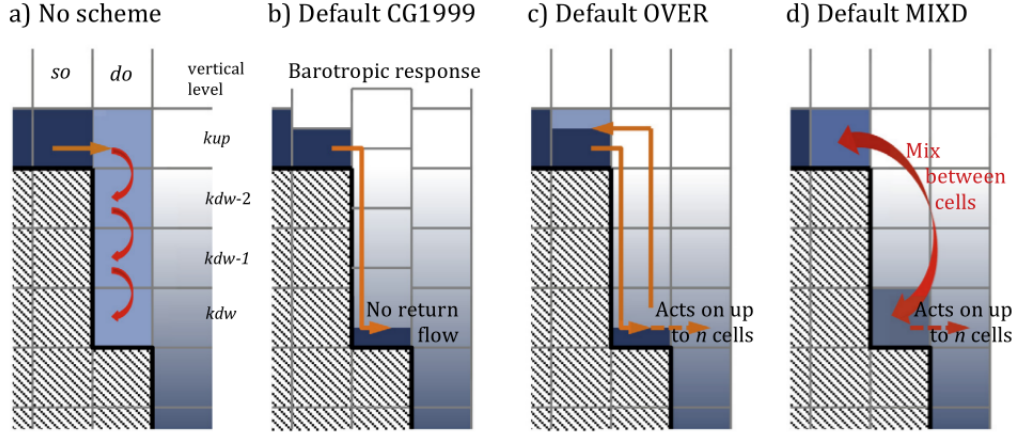


Figure 2.3: *Different BBL schemes implemented in Snow et al., 2015*

2.2 Concerning vertical coordinates

Besides the great effort dedicated to improve the representation of ocean processes, the type of the vertical coordinate implemented has a dramatic impact on the final solution (Griffies, 2003). Traditionally, the choice on the vertical coordinate (geopotential z -coordinate, isopycnal, terrain following) was a distinguishing factor between ocean models (Willebrand et al., 2001). Unfortunately, there is no clear single choice for realistic large scale ocean simulations. Each vertical coordinate has advantages and disadvantages (DYNAMO, 2001). In this scenario the use of hybrid or generalized vertical coordinates appears as an interesting framework which allows to tailor the choice of the vertical coordinate in order to adapt it to the representation of a particular flow regime.

2.2.1 Most used coordinate types

NEMO has traditionally been used in geopotential (z) coordinates in global simulations and in terrain-following coordinates in coastal simulations. It is not the intention of this work to make an extensive comparison of the most common vertical coordinate types. The focus will be settled on z and terrain following coordinates, since they are the options available in the present version of NEMO. However, we present below a short explanation of each type of coordinate (see figure 2.4 for reference).

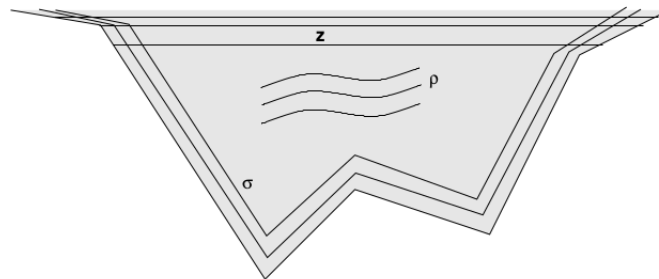


Figure 2.4: *Scheme of traditional coordinate types from Griffies, 2003*

z -coordinates

The vertical space is divided according a specific function onto levels of fixed depth. This function is chosen in order to vary the distance between consecutive levels, allowing to resolve

surface and upper ocean processes with a large number of levels, while keeping coarser levels in the abyssal ocean. This is a commonly used vertical coordinate system, at least for large scale ocean applications. The main advantage of this coordinate is its simplicity, its accuracy in the calculation of the pressure gradient and its good representation of surface processes. However, great care has to be taken when representing dynamics in the ocean interior (for example the thermocline) and next to the sea-bed because of a staircase representation of the bottom topography. A few variants of this coordinate type has been included to mitigate the poor representation of topography. One example of this is the use of partial cells where the thickness of the last level at the bottom is adjusted to the true ocean depth (Barnier et al., 2006). Some authors also pointed out the existence of spurious (i.e. induced by the numerical schemes) mixing associated with this type of coordinate (Legg et al., 2006, Ilıcak et al., 2011).

Terrain following coordinates

The vertical space is limited by the sea surface and the bathymetry. The concept resides on defining a dimensionless function varying usually between 0 to 1, with which we locate the vertical levels by multiplying this function by the local depth. In this way it is referred as σ coordinate when the levels are uniformly distributed ($\sigma = z/h$) or s-coordinates when a specific stretching function is used. The major advantage of this system is that it follows the topography and therefore naturally represents bottom boundary layers. The main drawback of this type of coordinate is the presence of errors in the calculation of the horizontal pressure gradient, that give place to spurious currents. For this reason they are most commonly used at very high resolution in shelf or coastal modelling (geographically restricted domains).

Isopycnal-coordinates

In this case the vertical space is divided by using iso-density targeted values. In this way, the first noticeable difference with the other two vertical coordinates is that its definition varies in time. Ocean's interior is believed to be dominated by isopycnal processes, and therefore this coordinate becomes a natural choice for this case. This type of coordinate is inappropriate to represent surface processes (when diapycnal processes dominate) and great care has to be taken in the formulation of the vertical mixing.

Arbitrary Lagrangian-Eulerian (ALE) formulation

The problem can gain in complexity if besides the consideration exposed above we set an adaptive behaviour of the grid in time; this is an Arbitrary Lagrangian-Eulerian (ALE) coordinate. When fully Eulerian, the vertical coordinate can be fixed to one of the vertical coordinate types described before; when it is Lagrangian at any degree the mesh moves with the fluid (Petersen et al., 2015). Again, one can choose the parameters taken into consideration to set the variation of the grid. A first step towards this directions has already been taken in NEMO v3.6, which includes a z-coordinate that adapts in time to variations in the SSH (z-star).

2.2.2 Some published results

We summarize here different published results linked with the grid construction of the problem. We emphasize as well different diagnostics used in realistic configurations. This summary is presented in a non-exhaustive way and focuses on recent studies.

Reckinger et al., 2015, performed a series of sensitivity tests in the DOME configuration in order to study the impact of the vertical grid, resolution and viscosity. It was found a strong dependence of the overall solution in z-coordinate to vertical resolution and vertical viscosity. The origin of the improvement of the solution was linked to Ekman layer dynamics. The horizontal resolution (tested in the range of $50km$ down to $2.5km$) was also found to affect the solution, but to a minor extent. Tests were also performed in sigma-coordinates with drastic improvements in the final results.

Ezer and Mellor, 2004, also compared z and sigma-coordinate results in the DOME configuration. They found that increasing horizontal and vertical resolution in z -coordinates gives a similar solution compared to the one obtained in coarser resolution in sigma-coordinates. These results are somewhat expected since the natural choice for a bottom flow is the use of a terrain following coordinate. However, these type of coordinates has been limited to idealized and regional simulations due to the strong presence of spurious currents associated with this type of coordinates (Griffies et al., 2000).

Using the DOME configuration Legg et al., 2006, performed z -coordinate simulations in horizontal resolutions ranging from $0.5km$ to $50km$ and isopycnal coordinate simulations with resolutions of $10km$ and $50km$. For the z -coordinate simulations the vertical resolution was adjusted according to the horizontal one, ranging from $30m$ to $144m$. The models used were the MITgcm model and HIM (Hallberg Isopycnal Model). In z -coordinates the overall behaviour of the plume descent showed to be highly dependent on the resolution. The vertical viscosity also appeared as a key parameter in controlling the plume descent. The results obtained using isopycnal coordinates showed to resemble the ones obtained at much higher resolution in z -coordinates. They also performed a comparison with the sigma-coordinates results obtained by (Ezer and Mellor, 2004), where they found that *"The sigma-coordinate calculation is qualitatively similar to the isopycnal coordinate calculation at the same resolution. Like the isopycnal coordinate simulations, sigma-coordinate simulations show less resolution dependence than z -coordinate simulations."*

All DOME experiments use mainly a passive tracer concentration for diagnostics. In this configuration the comparison is straightforward since the source as the processes simulated are completely linked to the vein of fluid. Regarding experiments in realistic configurations, different model setups have been used, as well as different diagnostics.

Shapiro et al., 2013 used different grids (different combinations of z and terrain following grids) to study a realistic configuration of the Black Sea (the circulation in this region is highly affected by shelf processes and overflowing water is also present). They found that the z -coordinate performed well to represent surface phenomena (like surface temperature), but presented difficulties in simulating overflowing water, where the terrain following coordinates presented very realistic results. In the case of the realistic simulation only surface temperature were used as diagnostics.

Riemenschneider and Legg, 2007, studied the Faroe Bank Channel overflow using an hydrostatic z -level version of MITgcm, with horizontal resolutions varying from $2.5km$ to $50km$ and vertical resolutions going from $25m$ to $100m$. It was found that at resolutions coarser than $2km$ the plume became too thick due to large entrainment. The comparison with observation had mainly two approaches. On one hand Riemenschneider and Legg, 2007, performed qualitative comparisons with a series of successive density profiles (from a specific ship campaign) along the path of the overflow. On the other hand they compared observed values of bottom density, layer thickness and core thicknesses. The main issue with this approach is that the comparison remains limited, since mainly the density was compared.

Koszalka et al., 2013, studied the DSO using a non-hydrostatic version of the MITgcm in z -coordinates with $2km$ of horizontal resolution and 210 vertical levels. The comparison with observations in this case was done mainly with two approaches. First they used the integrated transport below the 27.8 isopycnal at the location of the three main mooring arrays (deployment explained in Dickson et al., 2008). Many other studies have also considered transport as a diagnostic (Danabasoglu et al., 2010, Legg et al., 2009, Hervieux, 2007). The problem with the transport comparison is that the straightforward comparison with observations might be misleading, since the calculation is performed with different amount of available data. Second, Koszalka et al., 2013, used lagrangian particles to identify the overflow in the Irminger basin and with this information they compared different quantities with hydrographic information. The approach has shown to be very useful in order to identify the source of the different waters acting in the overflowing water transformation. The only issue is that this study is not directly comparable with observations, especially if we consider that the DSO has different sources in

addition to the sill.

This study is in the context of the DRAKKAR project¹, in which global ocean numerical simulations based on the NEMO platform over long periods (five decades or more) are performed. As seen, the sensitivity tests presented in previous works were based on the idealized DOME configuration and some of them performed in other models. Regarding realistic configuration, very few studies focus on the large scale implementation. The different approaches followed in this work should always keep in mind their implementation in large realistic configurations at nowadays resolution ($1/12^\circ$) and in reasonable agreement with the simulations cost.

¹<https://www.drakkar-ocean.eu/>

Chapter 3

Summary and discussion

The DSO was quantitatively first defined in Dickson and Brown, 1994, with a density criteria $\sigma_\theta \geq 27.8$, considering that this value covers the range of water masses that forms the North Atlantic Deep Waters (NADW). As seen before, the DSO is a highly variable vein of fluid and therefore a high level of coverage in time and space is needed in order to well capture its particularities. Unhopefully, only few measurements of temperature and salinity are available for each mooring. This is not the case for velocities, in which current profilers reaching up to 700m in vertical distance are available nowadays. For the Dohrn Bank, TTO and Angmagssalik arrays, Dickson and Brown, 1994, overlaid isopycnal distribution obtained during deployment or recovery cruises onto the mean distribution in order to identify the DSO. In addition, they used a velocity superior to zero as an additional criteria in order to guarantee that the water mass considered had a southward direction. This velocity criteria seems reasonable, since the arrays include a large part of the Irminger basin in which deep flows might have northward direction, and would therefore be wrongly considered part of the DSO.

The task of defining the DSO from hydrographic measurements is not easier. Macrander et al., 2007, proposed a temperature threshold to identify the overflow at the sill. But this becomes more difficult for the rest of the arrays, where the DSO is affected by the nature of different currents. Brearley et al., 2012, used specific geographical and density criterias to fit the vein of fluid in their hydrographic sections. The criteria for each hydrographic section changed in order to fit the strongest currents. This might be useful for some hydrographic sections but not for long-term comparisons. A very interesting approach was followed by Girton and Sandford, 2003, in order to locate the overflow. Thanks to the use of integrated quantities they were able to use minimal geographical constraint. This approach allows the definition of a main path of the DSO, which can be used to investigate the different transformations in the descent of the overflow. Unhopefully, the amount of information was quite limited, since their study was also coming from research cruises.

The hydrographic information has been very useful to illustrate the highly variable nature of the DSO and has given a more comprehensive understanding of its nature. However, as the information on the DSO properties vary at very short time scales (few days), the use of hydrographic information is reserved for qualitative comparison purposes only. The information about bottom temperature given in figure 1.15 (Voet and Quadfasel, 2010) seems to be very useful in order to capture the effect of the feeding of cold water to the bottom of the Irminger basin. The information provided makes possible a direct comparison with model outputs.

The lack of a unique definition among all the authors makes more difficult the task of direct quantitative comparison in transport values, especially if we consider that the model might not well represent the location of the 27.8 isopycnal. If this is the case the whole comparison loses reliability. On the modelling side Koszalka et al., 2013, pointed out the problematic characteristic of the density definition, by affirming that the temperature and salinity transformation downstream of the Denmark Strait are not yet well quantified. To tackle this issue they proposed

a complementary description of the overflow by using Lagrangian particles in an offline integration. While this method could be useful to answer some questions, its link with observations is not direct.

We defined three main directions of work based on the main aspects observed in the state of the art:

- **A definition of the overflow:** We aim here for the necessity of a more extensive definition, specifically for model output comparison, in which the unrealistic location of the 27.8 isopycnal could lead to misleading conclusions. We have observed that different authors performed different adaptations of the DSO definition. The definition considered in this work should allow the direct comparison with observations and provide the means for a better understanding on the processes during the DSO descent. Furthermore, we emphasize the necessity of a set of diagnostics that fully characterizes the DSO. The information coming from observations is very sparse in time and space and therefore qualitative comparisons are needed. We consider then that a qualitative approach with hydrographic information is needed in order to evaluate if the distribution of the DSO properties is acceptable. Then, a set of quantitative diagnostics is also needed to compare quantities in longer time scales.
- **Sensitivity to horizontal and vertical resolution:** From the modeling point of view we found very interesting the results that other authors obtained by varying the horizontal and vertical resolution. Unfortunately these studies were done in an idealized configuration and the impact is not fully rationalized and vastly established in realistic configurations. This is particularly true in NEMO, where very few studies were published on realistic configurations. In this way, we know that the interactions with other circulation features (for example the Irminger current or the properties of the ambient waters entrained in the descent) could also be sensitive to model resolution and impact the final overflow representation. For this reason, we choose an approach based on a realistic regional configuration.
- **Vertical coordinate:** We would like also to point out the large number of possibilities that have been considered to discretize the vertical domain in ocean models past works with remarkable differences in the overflow representation. A modeling challenge would be to have a vertical coordinate system that is locally adapted to the most critical ocean processes. The terrain following coordinates appear as a natural choice for overflows and the possibility of adapting them to a main z-coordinate would provide the possibility of having the advantages of both vertical coordinates in the same configuration. The degree of freedom regarding the distribution of the grid in the vertical space is very high and this scenario is an opportunity to explore in challenging problems as overflows.

Part II

Objectives and methodological approach

Chapter 4

Objectives

Continuing with the three main directions of work exposed in the precedent chapter, in this section we adapt these directions of work to our particular context.

The past works have shown that using a sufficiently high horizontal and vertical resolution in z-coordinates might offer a considerable improvement in the overflows representation. However, these studies have mainly focused in idealized configurations. In addition, the implementation of a very high horizontal and/or vertical resolution in a global configuration have associated very high computational costs. The possibility of local horizontal refinement that AGRIF offers, opens the possibility of applying a local treatment to overflows.

A **first objective** is to develop a set of diagnostics that allow us to study and to understand what might be causing the misrepresentation problem of the DSO in z-coordinates. A part of this development should take into account the definition of the DSO problematic and the comparison with observations and the need to assess improvements or degradation in the model representation of the overflow regarding parameterization or resolution changes.

A **second objective** of this work is to study the DSO representation at present horizontal resolution, $1/12^\circ$, and the maximum horizontal resolution that is possible to reach with AGRIF in this case ($1/60^\circ$, 5 being the maximum multiplicative factor that AGRIF allows in a single zoom). In case the horizontal resolution increase is not sufficient to correctly represent the DSO, we plan to use different number of vertical levels (46, 75 and 300 vertical levels).

The vertical coordinate option present in NEMO has been recently enlarged, and now we have the possibility of using z and s coordinates. However, the use of s-coordinates have been usually limited to coastal and regional configurations, while the final target of this work is a global configuration. A **third objective** of the work is therefore dedicated to study the viability and convenience of the use of s-coordinates to locally treat the overflows problem using a realistic configuration at $1/12^\circ$.

Chapter 5

Methodological approach

The approach of this work is focused on the improvement of overflows in a realistic context. We therefore present here the realistic regional configuration of the region of the Denmark Strait (DENST12) used for this study as well as the main numerical setup (some changes are performed afterwards in the different sensitivity tests).

Since there are many different ways between the different authors regarding the diagnostics to be used in the description of overflows (especially to compare with observations), a specific set of diagnostics is developed. This development is done in a generic way, in order to be able to apply the same method for all the simulations present in this work. We then offer in this part a diagnostic strategy explanation and a justification for the different choices.

Finally, in order to illustrate the problematic, explain the motivation and illustrate the different diagnostics that will be used, a detailed description of the reference simulation (1/12° 46 levels) is performed.

5.1 Model setup

In this work we employ the version 3.6 of NEMO (Madec, 2008) which is the one that will be implemented in most CMIP6 simulations. NEMO (Nucleus for European Modelling of the Ocean) is a state of the art modelling framework for oceanic research, ocean forecasting and climate studies. NEMO includes several major components, namely NEMO-OPA for modelling the ocean dynamics and thermodynamics (Blue Ocean), LIM for the sea-ice dynamics and thermodynamics (White Ocean), TOP for the on/offline oceanic tracers transport and PISCES for the biogeochemical processes (Green Ocean). NEMO also includes an adaptive mesh refinement software (AGRIF). The Blue Ocean component is the one of interest here. It resolves in a realistic context (realistic bathymetry and coastlines, observation based initial conditions for the ocean stratification and observed atmospheric surface boundary conditions) the so called Primitive Equations that describes, under some approximations, the evolution in time of the variables describing the physical state of the ocean (temperature and salinity, velocity fields, sea surface elevation, physical fluxes at the air-sea interface). Approximations made to derive the Primitive Equations from the general Navier-Stokes equations as well as the numerical methods used to discretize and solve the equations are described in detail in the reference manual (Madec, 2008) and are not presented here. Important to this work is to mention that the Primitive Equations make the hypothesis that the ocean is incompressible and the pressure is hydrostatic. Therefore, the equations do not include a vertical acceleration, the vertical velocity being diagnosed from the non-divergence of the tri-dimensional flow. Consequently, the dynamical processes that are in nature driven by a large vertical acceleration of the fluid, such as the deep convection or the gravity currents are parameterized in this model. Note that this is not specific to NEMO, as most actual Ocean General Circulation Models rely on the same hypothesis. NEMO also proposes a variety of numerical schemes that one have to choose according to applications. In

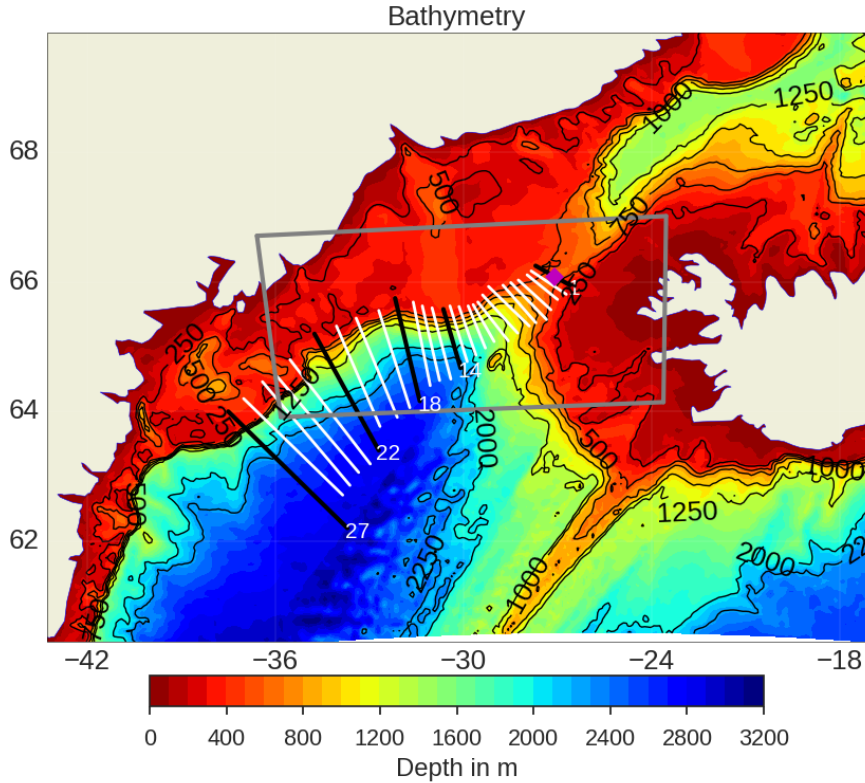


Figure 5.1: *a) Model domain. In color the ocean depth. The 250, 500m, 1000m, 1500m and 2000m isobaths are contoured. The gray box indicates the region where the grid refinement (to arrive to $1/60^\circ$) is applied in some simulations. The point in magenta denotes the reference point chosen for the sill. The white lines denotes the section used for the different calculations in this work (in black the most relevant ones)*

this study, different schemes for momentum advection are considered.

Also of interest for our study is the AGRIF mesh refinement software that gives the possibility to refine the horizontal grid (up to a factor of 5) over a local domain within a given model configuration. This facility will be used to obtain a very high resolution in the Denmark Strait and its vicinity.

The configuration developed for this study is shown in figure 5.1. Open boundaries are located at the northern, southern and eastern limits of the domain. The data used at the boundaries and for initial condition is provided by a global $1/12^\circ$, 46 levels, z-partial step simulation (more information in section 5.2). All simulations are started from rest and the integration is performed over 5 years. The model includes the possibility of choosing among three different vertical coordinates z-partial step, z-full step and hybrid s-coordinates (it is possible to hybrid s and z coordinates). The momentum advection scheme is the UBS scheme, an upstream-biased third order scheme. It includes a viscosity term which is a biharmonic operator with an eddy coefficient which is proportional to the velocity. No additional viscosity is therefore applied on momentum (unless specified). A test with the vector invariant form of the momentum advection scheme (the EEN scheme) is also performed. The diffusivity on tracers uses the TVD scheme with the Laplacian diffusive operator rotated along isopycnals.

The vertical physics uses the TKE mixing scheme (Gaspar et al., 1990). Because the model uses a hydrostatic pressure, the case of unstable stratification is treated with an enhanced vertical diffusivity (EVD) of $10 \text{ m}^2 \text{ s}^{-1}$ applied on tracers only or on tracers and momentum to represent the mixing induced by the sinking of the dense water. We use here the filtered free surface scheme

with a linear free surface. Sea-ice is modeled with LIM2. Finally, a horizontal refinement of the grid is performed thanks to AGRIF (Debreu et al., 2005). The refinement region (using a factor of 5 to reach a resolution of $1/60^\circ$) is outlined by the gray contoured box in figure 5.1.

5.2 Initial and boundary conditions

The data used to initialize the simulation and to drive the flow at the open boundaries is obtained from a global $1/12^\circ$ 46L z-partial step simulation. This global simulation was initialized with temperature and salinity values from a climatology (Levitus 98) and started from rest. The atmospheric forcing used was a daily mean climatology of the DFS 4.4 forcing (Brodeau et al., 2009). The data of each day is the climatological mean of that day calculated over the period 1958 to 2004 (Penduff et al., 2011). By doing this, any interannual variation can be only attributed to the ocean model (Serazin et al., 2015, Gregorio et al., 2015). This global simulation was performed for almost 9 decades and the data used for the DENST12 configuration comes from the year 72 until the year 76 (5 years in total). We have chosen this years in particular because the transport at the Denmark Strait sill was close to observed values ($\sim 3Sv$) and because several decades has passed from the initialization of the run. In this scenario, the bottom stratification is expected to be particularly affected by the unrealistic results that z-coordinate offers (more details in chapter 6), and any improvement achieved in the representation of the DSO should be rapidly identified.

To illustrate the unrealistic character of the abyssal waters of the initial condition, we show the bottom temperature of the Irminger basin in figure 5.2a. We see there that the basin does not present a clear signature of the DSO, with relatively warm bottom waters (especially between $1000m$ and $1500m$ right after the sill). This unrealistic character is also visible in the section of temperature (figure 5.2b), where the $3^\circ C$ contour is not even present (observed at $2000m$ in the observations in figure 1.9); in the density, where the 27.8 isopycnal is at $1000m$ (observed at $\sim 1800m$ in figure 1.9); and the salinity (figure 5.2c), where relatively high salinity values are observed at mid-depth close to where the overflow should be located (below 27.8 isopycnal and below $1000m$). These aspects will be revisited in detail in the analysis of the reference simulation (chapter 6), but it is important to retain that a warm bias between 1° and 2° in the temperature is already present and expected to persist in the overall solution.

One disadvantage of this setup is that when an improvement in the representation of the DSO is obtained, this configuration is not appropriate to evaluate long term changes in the basin properties. The small characteristic of the model domain imposes that the boundary conditions highly influence the overall solution. This is one additional reason why we expect the bias between 1° and 2° to remain present in the overall solution.

5.3 Diagnostic strategy

In addition to the problematic exposed just above, there are many different ways used in the literature to adequately characterize the overflow. As explained in section 3, the high variability of the overflow combined with the different model biases in temperature and salinity properties makes the use of a density value as the only parameter to define the DSO problematic. From this starting point we asked ourselves in which way we could improve this definition in order to be able to measure improvements in our different model simulations. For this end we explain our diagnostic strategy which covers different characteristics of the DSO.

Position of the overflow

Dickson and Brown, 1994, used the density criteria $\sigma_\theta \geq 27.8$ to characterize the DSO considering that this value covers the range of water masses that forms the North Atlantic Deep Waters (NADW). In addition, for the Dohrn Bank, TTO and Angmassalik arrays Dickson and Brown,

In this context we understand that a main characteristic that is not being taken into account for a vein of fluid that is characterized by a large transport is its velocity. Truth is that finding a correct threshold for the southward velocity that works both for observations and model outputs is not an easy task. Of course this value has to be greater than zero. We might go a bit further and think that we probably should avoid including small velocities related to eddy processes in the Irminger Basin. Fan et al., 2013, observed mean peak azimuthal speeds for the anticyclones present in the Irminger basin of $0.1ms^{-1}$.

From this point of view any discussion considering a lower threshold value for the overflow should start from at least $v \geq 0.1ms^{-1}$. We propose here a value of $v \geq 0.2ms^{-1}$ because we obtained very robust results. However intermediate values between $0.1ms^{-1}$ and $0.2ms^{-1}$ can be tested. We then propose a definition similar to the one given by Girton and Sandford, 2003 for horizontal and vertical positions of the DSO, doing so we define our understanding of the vein and its center.

$$X_{DSO} = \frac{\iint vxdzdx}{\iint vdzdx}; (\sigma_0 \geq 27.8, v \geq 0.2ms^{-1}) \quad (5.1)$$

$$Z_{DSO} = \frac{\iint vxdzdx}{\iint vdzdx}; (\sigma_0 \geq 27.8, v \geq 0.2ms^{-1}) \quad (5.2)$$

Compared to the definition used in Girton and Sandford, 2003, we use the local depth of the grid point as a weight instead of the local value of the total depth. As said before, the velocity was also added as a parameter to weight the position of each point. The value of X_{DSO} and Z_{DSO} give the horizontal and vertical position of the core of the vein for each section in particular. Since we have the definition of each section we can locate X_{DSO} in latitude and longitude and make plots as the ones observed in figure 5.3a.

The idea is that for a given section we weight each point that is at or below the 27.8 isopycnal by its velocity value (considering velocities only higher than a threshold value of the velocity, in this case $v \geq 0.2ms^{-1}$). In figure 5.3a we can observe the different sections chosen, starting at the sill and ending at the Angmassalik array.

Figure 5.3d shows a daily mean of section 18 with the position of the center of the vein calculated with equations 5.1 and 5.2 for different velocity thresholds. As observed, the position for $v \geq 0ms^{-1}$ and $v \geq 0.1ms^{-1}$ is not strictly related with the vein of fluid. This can be explained by observing the density contours for both thresholds. Velocities such that $0ms^{-1} \leq v \leq 0.1ms^{-1}$ occupy a large portion of the interior of the basin and can be easily related with the eddy field rather than with the overflow itself. Velocities between $0.1ms^{-1} \leq v \leq 0.2ms^{-1}$ are a better approximation to the vein, but still we can observe some eddy structures with densities greater than 27.8 and with these velocities values. While setting a threshold $v \leq 0.2ms^{-1}$ seems to capture well the velocity field of the vein. This story repeats itself along almost all daily snapshots of velocity. Moreover, in figure 5.3c we observe in colors the path depicted by all the points of the sections for the three velocity thresholds. We see there clearly how the eddy structures affects the calculation for the center of the vein for the $v \geq 0ms^{-1}$ and $v \geq 0.1ms^{-1}$ cases. Using 27.85 as a threshold for the density (figure 5.3b) does not offer a path related with the overflow for any of the velocities threshold. The reason for this is that the position of the 27.85 isopycnal in the simulation is unrealistic and is located only at the very bottom of the basin (not related with the overflow).

Transport estimates

For consistency with the previous rationale, transport calculations consider only points that are considered part of the vein, such that $\sigma_0 > 27.8$ and $v \geq 0.2ms^{-1}$. Not doing that would include values in the transport calculation associated with other physical phenomena, like eddies present in the Irminger basin or other currents that are not strictly part of the overflow. This will be shown in the next section in detail.

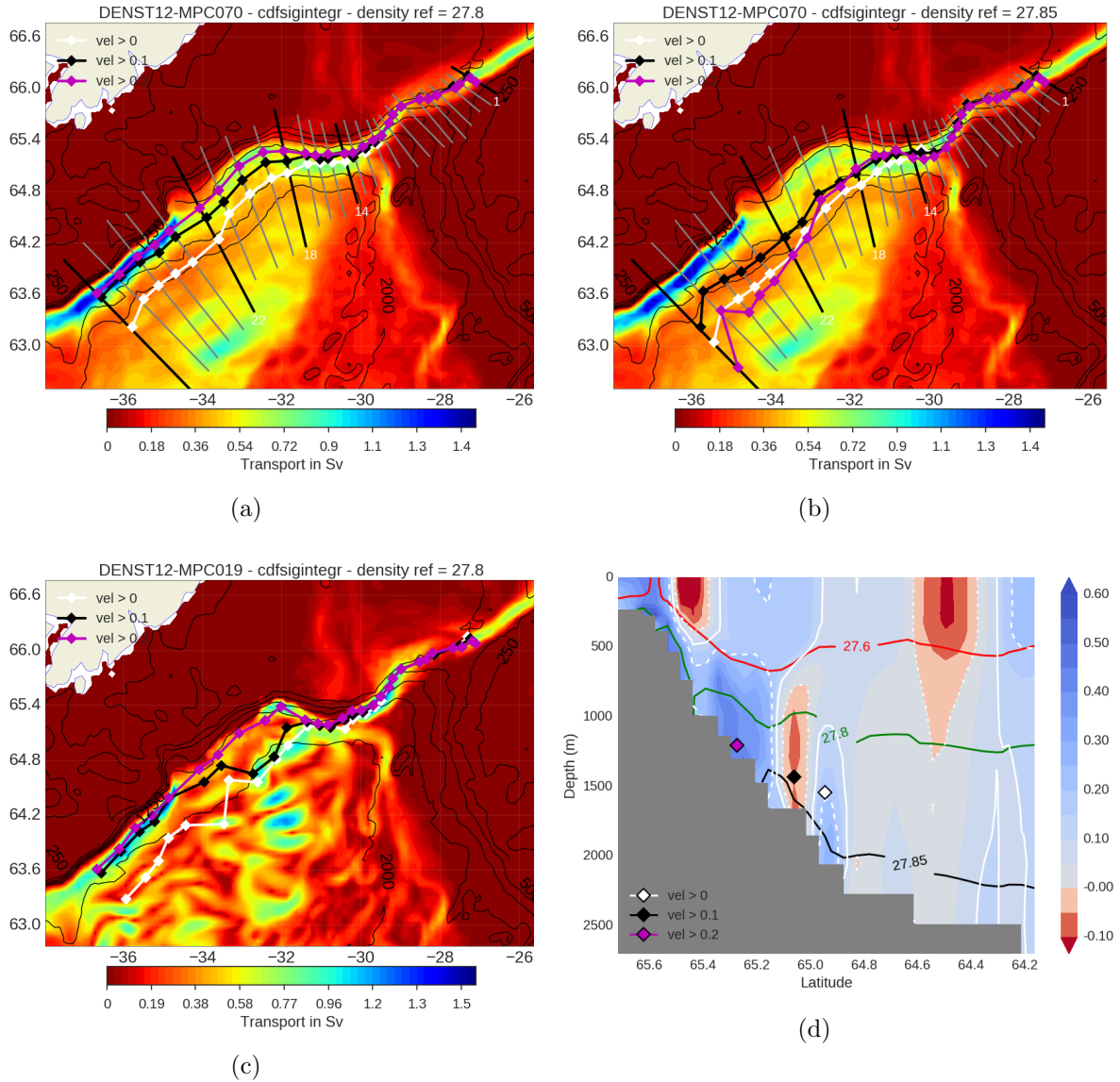


Figure 5.3: Path of the overflow calculated using different velocity thresholds and different density thresholds. Color indicates the volume transport below 27.80 isopycnal. The magenta lines correspond to a threshold value of 0.2 ms^{-1} , black lines 0.1 ms^{-1} and white lines 0 ms^{-1} a) Using a density threshold of 27.80: annual mean values b) Using a density threshold of 27.85: annual mean values c) Density threshold 27.80: daily snapshot (10/June of year five). Observe the impact of the eddies in the path of the overflow for the velocity thresholds 0 ms^{-1} and 0.1 ms^{-1} d) Normal velocity to section 18 with density contours, daily snapshot (7/January of year five). $1/60^\circ$ horizontal resolution and 300 vertical levels (child grid). Points calculated with different velocity thresholds according to 5.2 and 5.1. Point-dashed white lines denotes 0 ms^{-1} velocity contour, 0.1 ms^{-1} velocity contour in solid white lines and 0.2 ms^{-1} velocity contour in dashed white lines.

Bottom temperature

An interesting reference for the model overall performance in representing the DSO is the bottom temperature. First, because the temperature is a better marker of overflow waters than density. If we use the bottom density to observe how the overflow feeds bottom waters the gain in density by cold water will be partially compensated by a reduction in density by fresh water. Second, because microstructure measurements of the vein (Paka et al., 2013) show a more clear

signature of the overflow in the case of the temperature in comparison with the salinity. And third, there are long-term observations of bottom temperature at four mooring arrays (Voet and Quadfasel, 2010) that can be used for validation.

Qualitative comparison

We found necessary as well a qualitative comparison with hydrographic information, since they contain higher spatial resolution than mooring arrays. We can therefore have an idea of the distribution of the velocity, temperature and salinity and specially the distribution of the 27.8 isopycnal.

Chapter 6

The reference simulation

We present here a detailed description of the DSO in our reference simulation, a $1/12^\circ$ 46 vertical levels z-partial step simulation. By doing this, we explain with more details the motivation of our problem and we set the basis for the comparison with the rest of the simulations, according to our diagnostic strategy.

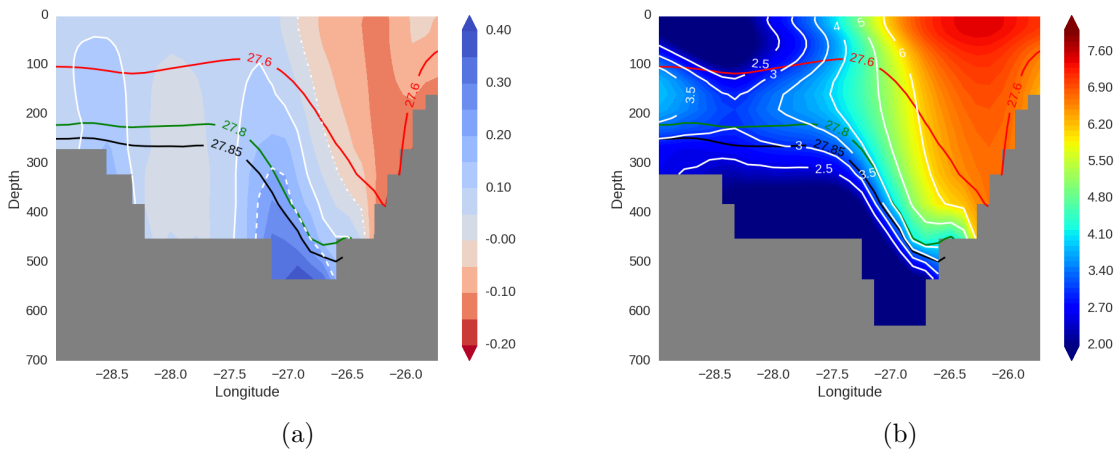


Figure 6.1: *Reference simulation, annual mean of year 5 at the Sill a) Normal velocity in colors with specific velocity values in contours (point-dashed white lines denotes $0ms^{-1}$ velocity contour, $0.1ms^{-1}$ velocity contour in solid white lines and $0.2ms^{-1}$ velocity contour in dashed white lines) b) Temperature in colors and specific temperature values in white contours. Density values in contours (27.6 in red, 27.8 in green and 27.85 in black)*

This work focus on the description of the descent of the DSO and its transformation in the Irminger basin. However, one would want to make sure that the source of the overflow, at the sill, is as close to the observations as possible. The analysis done in Behrens et al., 2017 already showed that NEMO in a $1/20^\circ$ 46 levels simulation was able to simulate the local conditions in the Denmark Strait and north of Iceland with high realism. We therefore show here a short analysis of the different properties of the overflow at the sill.

In figure 6.1 we observe the normal velocity and the temperature at the sill. The current present a clear stratification with isopycnal lines well identified with the temperature contours. At the right part we observe the Irminger current with northward direction, presenting drastic differences in its properties regarding the DSO.

In figure 6.2 we observe the transport at the sill below the 27.8 isopycnal. In this case a threshold of $0ms^{-1}$ was chosen in order to consider all southward velocities. A mean value $\sim 3Sv$ is obtained with a standard deviation of $\sim 0.6Sv$. The mean is close to the values published in Macrande et al., 2005: 3.68 and $3.66Sv$ for 1999– 2001, $3.16Sv$ in 2001/2002,

3.07Sv in 2002/2003, and agrees as well with the values published in the 1996–2011 study of Jochumsen et al., 2013. The standard deviation is clearly smaller when compared to the 1.6Sv of Macrandar et al., 2005.

We can also observe in the smoothed version of the time series a clear annual cycle which might be related with the climatological nature of the forcing. One important aspect is that the feeding of overflows waters, even from the very beginning, is continuous and steady during the whole simulation. The overflow transport remains close to the mean at the very beginning of the time series.

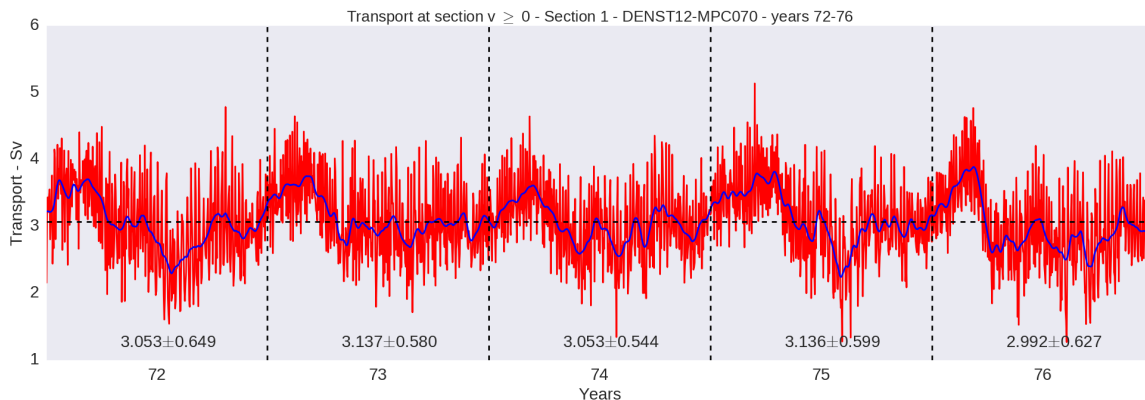


Figure 6.2: *Time evolution of the volume transport of southward ($v > 0\text{ms}^{-1}$) waters denser than 27.80 in the reference simulation. In red daily values and in blue the smoothed time series (20 day hanning window)*

We continue in this case with the qualitative comparison of temperature and density fields in specific sections along the path of the overflow. We can notice in figures 6.3a to 6.3c that the 27.8 isopycnal hardly varies its depth ($\sim 1000\text{m}$), which denotes the limited impact of the DSO in the overall distribution of this isopycnal. Instead the 27.85 isopycnal shows a more clear signature of the overflow for these 3 figures. In this way the density contour 3.5°C seem to show a signature of the DSO, but still it is very weak.

One might focus in figure 6.3c which shows a portion of the Angmassalik array and compare it with the observation shown in figure 1.9. For the observations the 27.8 isopycnal reach down to 2000m while here it remains around 1000m and the signature on temperature is evident. Due to the initial and boundary conditions (obtained from a 72 year-long z-coordinate run, see 5.2 for details) a biased was expected from the observations, but in fact what we observe here is that the overflow properties and structure are unrealistic in the reference simulation (not deep enough, waters too warm and salty).

We also observe a very well stratified interior of the basin, which might influence the final results, as the overflow will entrain these ambient waters as it sinks. There are mainly two sources that can increase the bottom density associated with the DSO waters (DSOW), one is the cold and relatively fresh water coming from the Arctic and the other is the warm but salty water entrained from the Irminger current. We note here a second condition for a proper representation of the DSOW: it is important to have a correct representation of the Irminger current. This is in accordance with a number of papers that have already explain the impact of ambient waters in the final representation of the overflow, see for example Legg et al., 2006. In fact the vein does not seems to find good reasons to sink, and instead a large diffusivity is observed. This can be easily seen if we consider that the overflow departs at a maximum depth $\sim 500\text{m}$ at the sill, and stays at intermediate depths all along its trajectory.

The bottom temperature in figure 6.3d shows no significant signal of cold water coming from the sill. The same plot for the salinity (not shown) indicates increased values of salinity in the location of the overflow when compared with the rest of the bottom of the basin, confirming

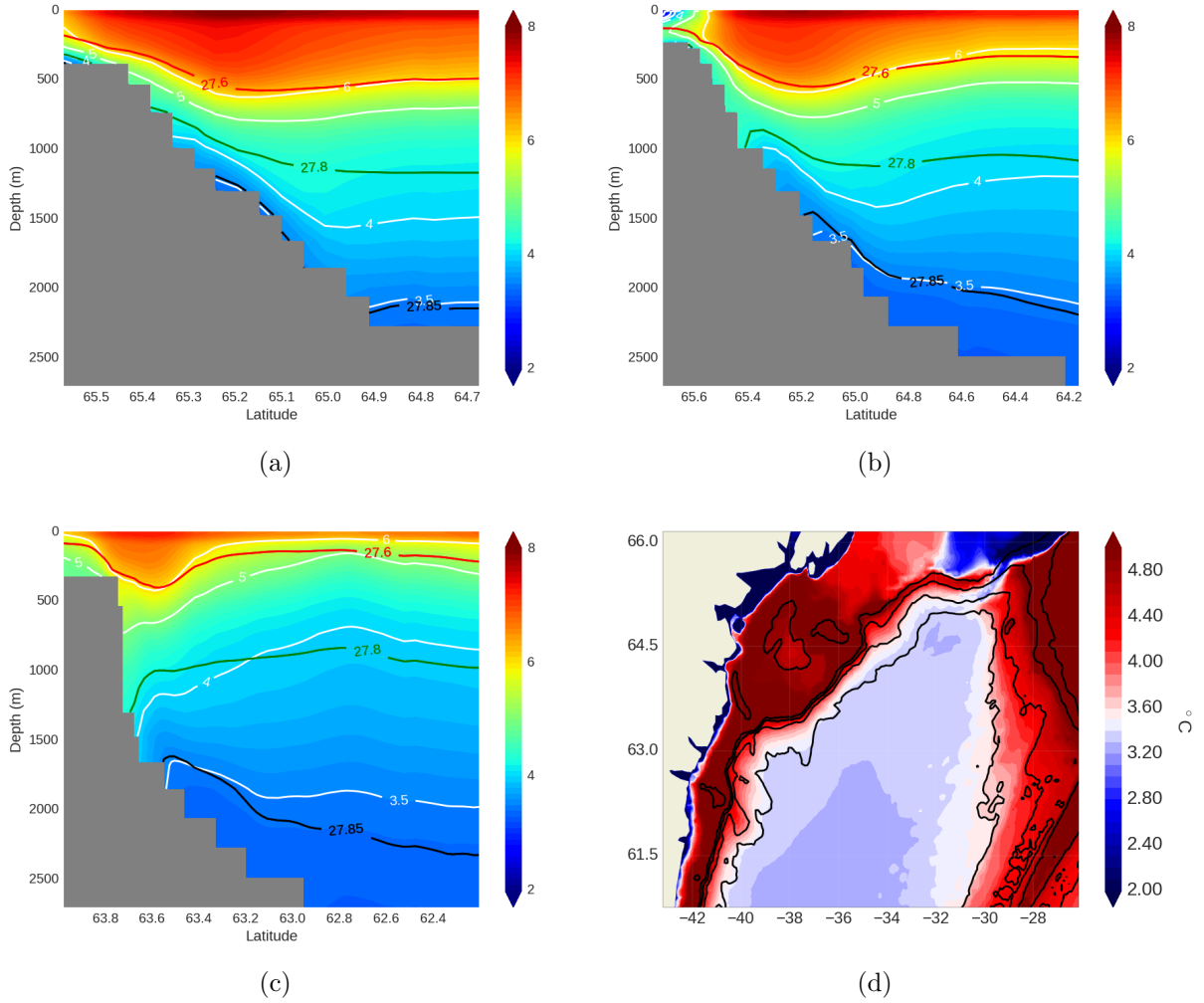


Figure 6.3: *Reference simulation, annual mean temperature of year 5 with temperature and density contours (except in d) a) Section 14 (Dohrn Bank array) b) Section 18 (spill jet section) c) Section 27 (Angmassalik array) d) Bottom*

the predominant impact of the Irminger current in the final solution. Such plot of the bottom temperature summarizes rather well what we also learned in the analysis of the cross sections (figures 6.3a to 6.3c). In addition, a good representation of the overflows should have a direct impact on the bottom temperature as figure 1.15 shows. A less illustrative but more straightforward way to evaluate the impact of the overflow on the bottom temperature is to compare the mean values at the location of the mooring arrays. This is done in figure 6.4a, and we also take advantage from this to compare the values with observations using the published results of Voet and Quadfasel, 2010 (original figure 1.15). The difference is evident, our simulation produces unrealistic results between the sill and the Dohrn Bank array (200km downstream), where simultaneously most of the sinking of the overflow and the mixing with the Irminger current occurs (Girton and Sandford, 2003).

In figure 6.4b we show the results of the transport calculation for different velocity thresholds and the observations (from (Dickson and Brown, 1994)) that serve as a reference. The impact of the different thresholds is clear, and a transport of around 3 times higher is obtained with a threshold $0ms^{-1}$ in contrast with $0.2ms^{-1}$. Transport values show reasonable agreement with observations at the sill, at TTO and at Angmassalik arrays when taking velocity thresholds of $0.1ms^{-1}$ and $0.2ms^{-1}$. The increase in transport in observations at Angmassalik array is

believed to be due to the presence of the Faroe Bank Channel Overflow (FBCO). Since the FBCO is not well represented in our simulation either we do not expect this contribution to be correctly accounted for.

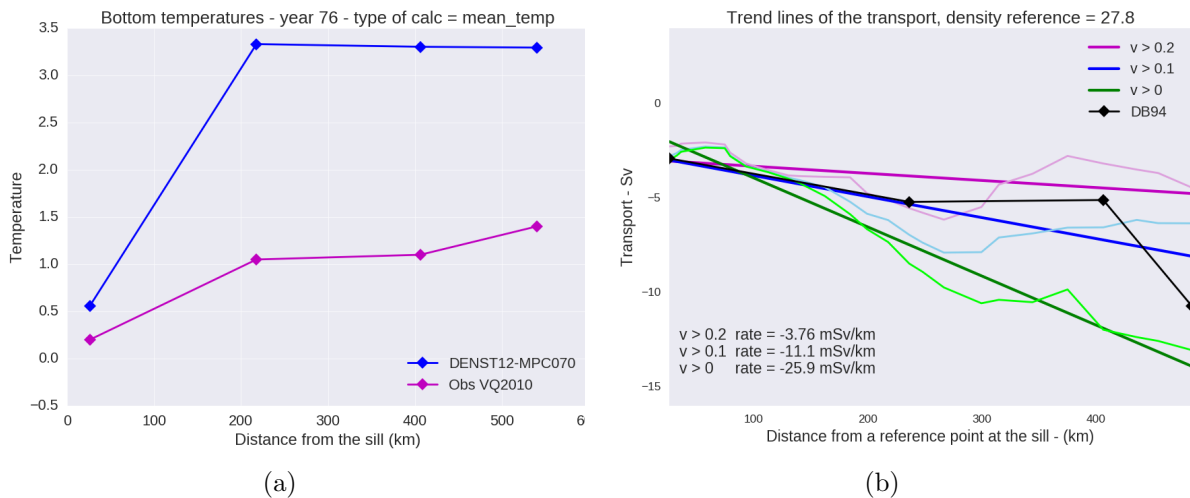


Figure 6.4: *Reference simulation, annual mean of year 5* a) *Minimum mean temperature value for each array. Observations from (Voet and Quadfasel, 2010) (Obs VQ2010)* b) *Transport along the path of the overflow for different velocity thresholds (light thin lines) and their associated tendency lines (dark large lines). Observations from (Dickson and Brown, 1994) (DB94). For both figures, the first point corresponds to array 1 (the sill), the second point to array 14 (the Dohrn Bank array), the third point to array 22 (the TTO array) and the fourth to array 27 (the Angmassalik array)*

One last diagnostic is here offered that will serve as a general explanation for the overflow problem in z-coordinates. Different properties can be plotted along the path of the DSO. In figure 6.5 we show the along path temperature with the density contours. After the first 100km the cold water coming from the sill shows an abrupt change. The 27.85 isopycnal presents the same behaviour. At the same location and at the top we found the Irminger current (with the very warm signature that characterizes its water mass). At 200km from the sill, the very cold water coming from the sill is completely diluted and the 27.8 isopycnal shows not apparent link with this water mass.

Another quantity of interest is the vertical diffusivity along the path of the overflow, shown in figure 6.6. All along the path at the bottom and in the mixed layer we observe values of the order of 1 to $10m^2s^{-1}$, indicating a frequent occurrence of the EVD (static instability correction). In the mid-depths the vertical diffusivity is of the order of $10^{-5}m^2s^{-1}$ (the background value). This indicates that the vertical mixing dominates our problem. We link the vertical mixing present in the mixed layer with winter deep convection, which seems to sometimes reach the overflow depth at around 100km from the sill. Within the DSO the vertical mixing is associated with the convective adjustment. Further details will be given later for this diagnostic and its usefulness to compare between different simulations will be demonstrated.

The analysis of the DSO in the reference experiment, whose settings are very similar to those used in usual ORCA12 global simulations, demonstrates that the DSO is not adequately represented. The main flaws are the depth reached by this current and its temperature and salinity properties due to overmixing with ambient waters. In the following sections we will study the sensitivity of the DSO characteristics that we have just described to various model parameters and resolutions in order to identify ways of improvement.

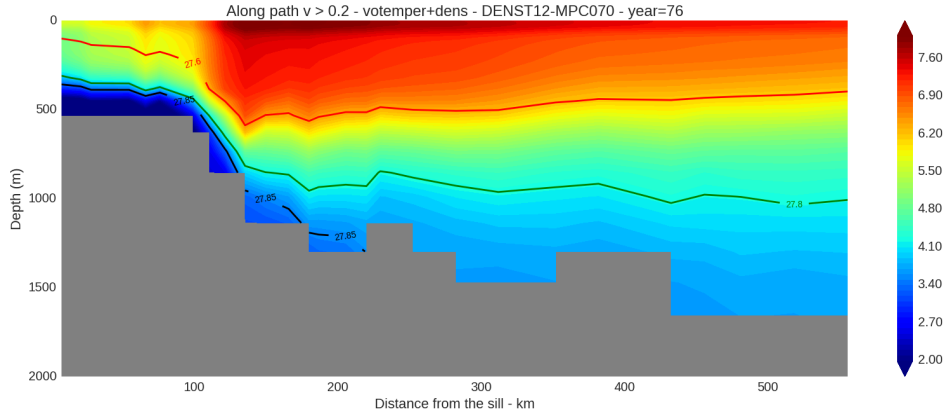


Figure 6.5: *Temperature annual mean of year 5 along the path of the overflow (magenta line in figure 5.3a). Density values in contours (27.6 in red, 27.8 in green and 27.85 in black). Reference simulation.*

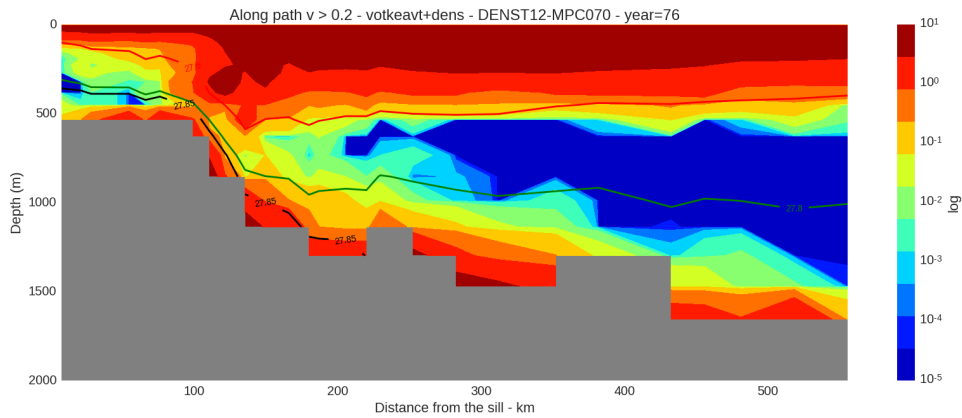


Figure 6.6: *Vertical diffusivity coefficient annual mean of year 5 along the path of the overflow (magenta line in figure 5.3a). Density values in contours (27.6 in red, 27.8 in green and 27.85 in black). Reference simulation.*

6.1 Discussion

We addressed here the concept of the DSO as a very dense, cold and fast bottom vein of fluid. To this end we proposed a complementary definition to the usual density-only definition. With this and the help of observed published results we first evaluated a standard NEMO 1/12° 46 vertical levels simulation in order to explain our motivation and to set a benchmark for future improvements.

We have shown in this part of the work that it would be useful to complement the classic definition of the overflow ($\rho \geq 27.8$) with a velocity threshold ($v \geq 0.2$). With this definition we were able to isolate the study of the overflowing process from the rest of the processes occurring in the Irminger basin. This definition also allowed us to develop new diagnostics that led to a better understanding of what might be causing the unrealistic representation of the DSO by NEMO. In this way, the set of diagnostic presented here seemed to correctly achieve the purpose of an overall DSO description. We would also like to highlight the complementary nature of the qualitative and quantitative diagnostics used here.

Now that the problematic is posed and the method to study is defined, the next step of this work is the study of the DSO with a set of sensitivity tests in z-coordinates.

Part III
z-coordinate

Chapter 7

Sensitivity tests in z-coordinate

We present here a series of experiments that have been performed with different settings in order to better understand the impact of the different model aspects on the final representation of the DSO at $1/12^\circ$. We started by studying the effect of the BBL parameterization (BBL hereafter) present in NEMO. Since BBL is shown to worsen the representation of the overflow it was decided not to use it in the following experiments. Second we study the impact of the vertical resolution. In order to better understand the vertical resolution impact a third series of tests was conducted with different approaches regarding the vertical mixing. In fourth place we studied the effect of vertical resolution with a local horizontal refinement to reach $1/60^\circ$. In fifth place we decided to apply the EVD in tracers and momentum (EVD=1, previous tests being with EVD on tracers only, EVD=0) with different vertical resolutions, with and without the horizontal refinement. One final series of experiments changing from free slip to no slip condition was performed with different vertical resolutions, with and without the horizontal refinement.

Since most of the work presented here is resolution related, we therefore establish an abbreviation of the simulations names according to horizontal and vertical resolution. This is shown in table 7.1.

Table 7.1: *Reference names of the configurations*

Levels/Resolution	$1/12^\circ$	Agrif zoom $1/60^\circ$
46	E12L46	A12L46
75	E12L75	A12L75
300	E12L300	A12L300

Any additional characteristic of the simulation will be added to this abbreviation. We will first describe the results obtained and we provide analysis and understanding of the results at the end of the chapter.

One previous consideration

The problem of cascading waters has been a resisting flaw in z-coordinates. As it was explained in section 2.1 the BBL strategy used in the work of Hervieux, 2007 has not shown significant improvements. The work of Snow et al., 2015 (detailed explanation in section 2) used a number of different BBL parameterizations at a horizontal resolution of 1° in MOM5 (Griffies, 2012). This study did not present either significant improvements. So far, BBL parametrizations have shown inefficiency to tackle the overflow problem. However, it is expected that at some point the increase in horizontal and vertical resolution will allow z-coordinates to well represent cascading waters. In this way, up to date there is no work that studies the impact of the different model parameters in the final representation of the overflow in NEMO in a realistic configuration.

7.1 BBL

We compare here simulations at $1/12^\circ$ 46L in partial step (PS) and full step (FS), with and without the BBL parameterization at work. These simulations were performed with NEMO v3.5beta since they were done at the beginning of the PhD (while the rest of the simulations of this study were done in NEMO v3.6). The EEN vector formulation is used for momentum advection.

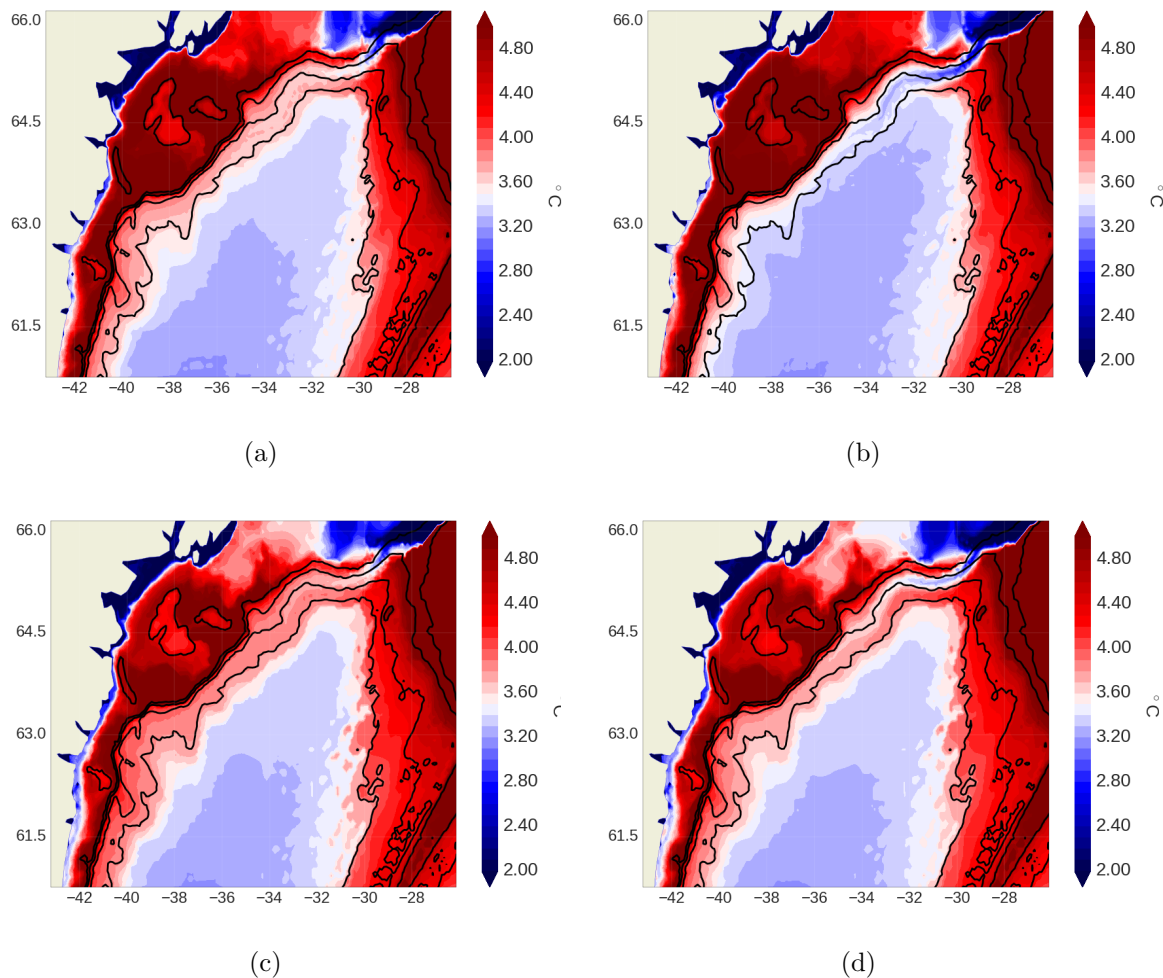


Figure 7.1: *E12L46*, annual mean of the bottom temperature of year 5, in simulations with a) PS with BBL b) PS without BBL c) FS with BBL d) FS without BBL. Isobaths 500m, 1000m, 1500m and 2000m are contoured

We show the bottom temperature of these 4 simulations in figure 7.1. The PS without the BBL is clearly the setting that performs best (figure 7.1b) as it shows the coldest bottom temperature between the 1500m and 2000m isobaths. The PS always performs better than FS, the worst case being the FS with BBL. However the best solution (figure 7.1b) is still far from what could be accepted as a fair representation of the overflow. We observe bottom temperatures of the order of 3.2°C around the overflowing region.

A word on 75 and 300 levels

These BBL tests were also conducted with 75L and 300L, completing a set of 12 simulations. The above conclusion remains no matter which of these 3 vertical resolutions are used and results are not shown to avoid redundancy. Only one comment is done in this way: at 300L the impact of PS against FS seems to have very small effect on the final solution.

7.2 Vertical resolution in $1/12^\circ$

We compare here simulations at $1/12^\circ$ with different vertical resolutions (46L, 75L and 300L). All simulations uses PS and no BBL because this setting has shown to perform best in the previous section. In this first approach EVD is applied on tracers only (EVD=0).

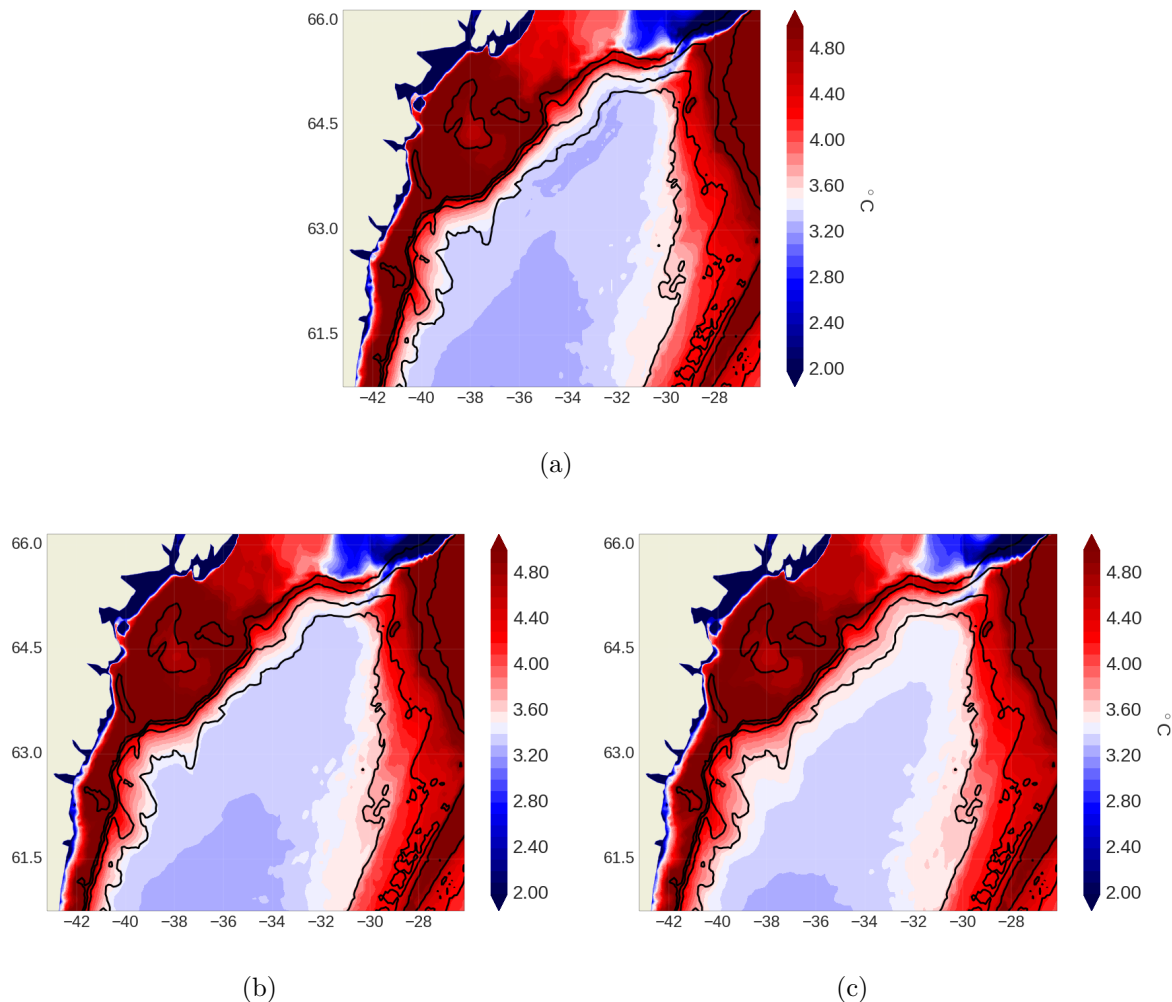


Figure 7.2: *Annual mean of the bottom temperature of year 5 at $1/12^\circ$ with EVD applied on tracers only a) E12L46 b) E12L75 c) E12L300. Isobaths 500m, 1000m, 1500m and 2000m are contoured*

We show the bottom temperature of these 3 simulations in figure 7.2. The vertical resolution that performs the best is the one obtained with 46L (figure 7.2a). The bottom temperature is better preserved and the temperature along isobaths 1500m and 2000m is colder. The rest of the diagnostics support this conclusion and are not shown to avoid redundancy.

Time step

One of the hypotheses regarding the worsening in the representation of the overflow with increasing vertical resolution was done regarding the time step. The time discretization scheme used by NEMO v3.6 is a leap frog scheme followed by an Asselin filter, which presents truncation errors of first order. As we increase the vertical resolution the magnitude of the truncation error produced in space becomes smaller, and it might be possible to consider that the truncation error in time dominates in the solution. One test using a $\Delta t = 50s$ instead of $\Delta t = 300s$ was performed in $1/12^\circ$ 300L. No remarkable changes were found with the time step reduction.

7.3 Vertical mixing scheme in 1/12° 300L

Another hypothesis regarding the degradation of the representation of the overflow as the vertical resolution increases was done regarding the vertical mixing scheme used (TKE). We compare here the result of four simulations: TKE scheme with no EVD, no closure scheme but a constant background diffusivity of $1.2 \times 10^{-5} \text{m}^2 \text{s}^{-1}$ associated to EVD, and GLS scheme with EVD and GLS scheme with no EVD. When used, the EVD is applied on tracers only. Both the TKE and GLS schemes include a term in their equations which depends on the value of the Brunt Vaisällä frequency (N^2). In a presence of a density inversion this term becomes positive and increases the vertical diffusivity value (making the use of EVD not mandatory).

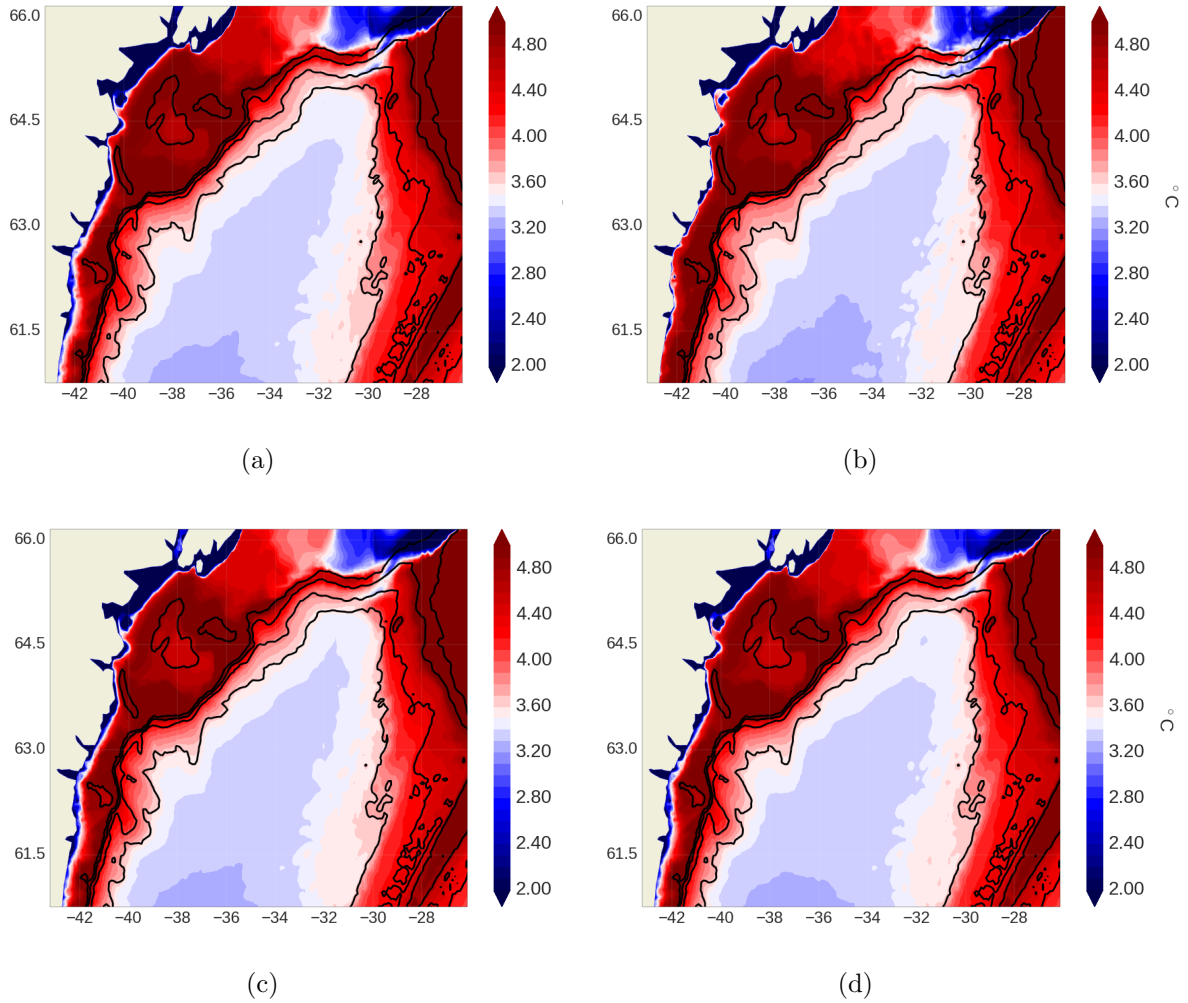


Figure 7.3: *E12L300* annual mean of the bottom temperature of year 5, using a) TKE scheme with no EVD b) Constant background diffusivity of $1.2 \times 10^{-5} \text{m}^2 \text{s}^{-1}$ and EVD c) GLS scheme with EVD d) GLS scheme with no EVD. Isobaths 500m, 1000m, 1500m and 2000m are contoured

We show the bottom temperature of these 4 simulations in figure 7.3. All these simulations give a very similar result, even the one with constant background diffusivity. Detail explanation and analysis will be given afterwards, but the representation of the overflow seems not to be linked to the vertical mixing scheme at 1/12° 300L.

7.4 Vertical resolution at $1/60^\circ$

We compare here simulations at $1/12^\circ$ with a local refinement to reach $1/60^\circ$ with different vertical resolutions (46L, 75L and 300L). The vertical mixing scheme is still the TKE scheme with EVD applied only on tracers.

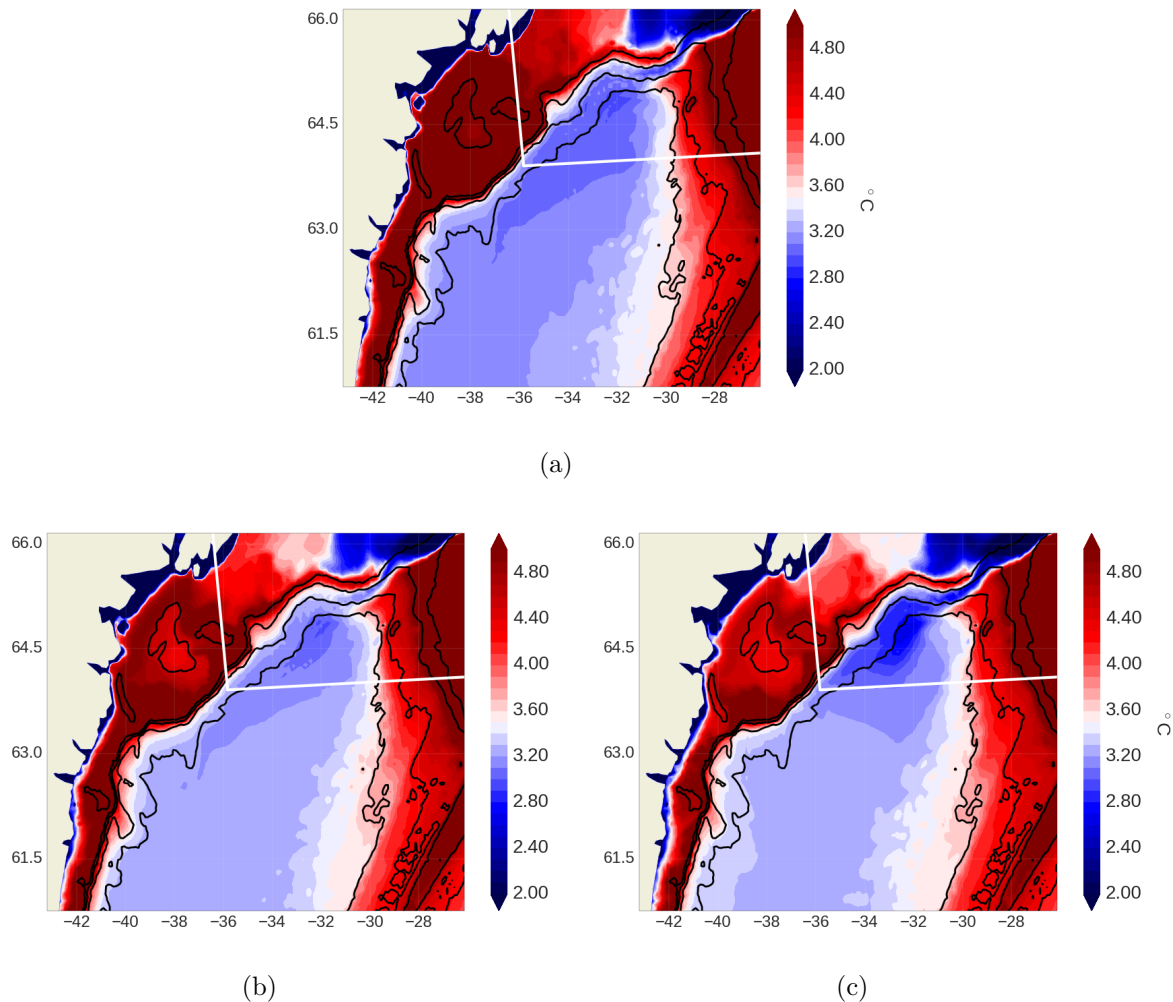


Figure 7.4: Annual mean of the bottom temperature of year 5 at $1/12^\circ$ with EVD applied on tracers only a) A12L46 b) A12L75 c) A12L300. Isobaths 500m, 1000m, 1500m and 2000m are contoured. In white lines the region where the local refinement is applied

We show the bottom temperature of these 3 simulations in figure 7.4. The vertical resolution that performs the best at $1/60^\circ$ is the one obtained with 300L (figure 7.4c). The bottom temperature went from a value of $\sim 3.6^\circ\text{C}$ in the region of the overflow at $1/12^\circ$ (figure 7.2c) to a value of $\sim 2.6^\circ\text{C}$, showing a remarkable cooling of $\sim 1^\circ\text{C}$. However this improvement seems to be limited to the area where the local horizontal refinement is applied, and this will be subject of further analysis. The propagation outside the refinement region seems to be clearly better for the 46L case (figure 7.4a) than for the 300L case. The worsening on the representation of the overflows with increasing vertical resolution seems to happen at $1/60^\circ$ as well, but only limited to the case of 75L (figure 7.4b).

A complete description of the A12L300 simulation is performed afterwards.

7.5 Role of EVD

7.5.1 Vertical resolution in $1/12^\circ$ - EVD=1

We compare here simulations at $1/12^\circ$ with different vertical resolutions (46L, 75L and 300L). In this case EVD is applied on tracers and momentum (EVD=1).

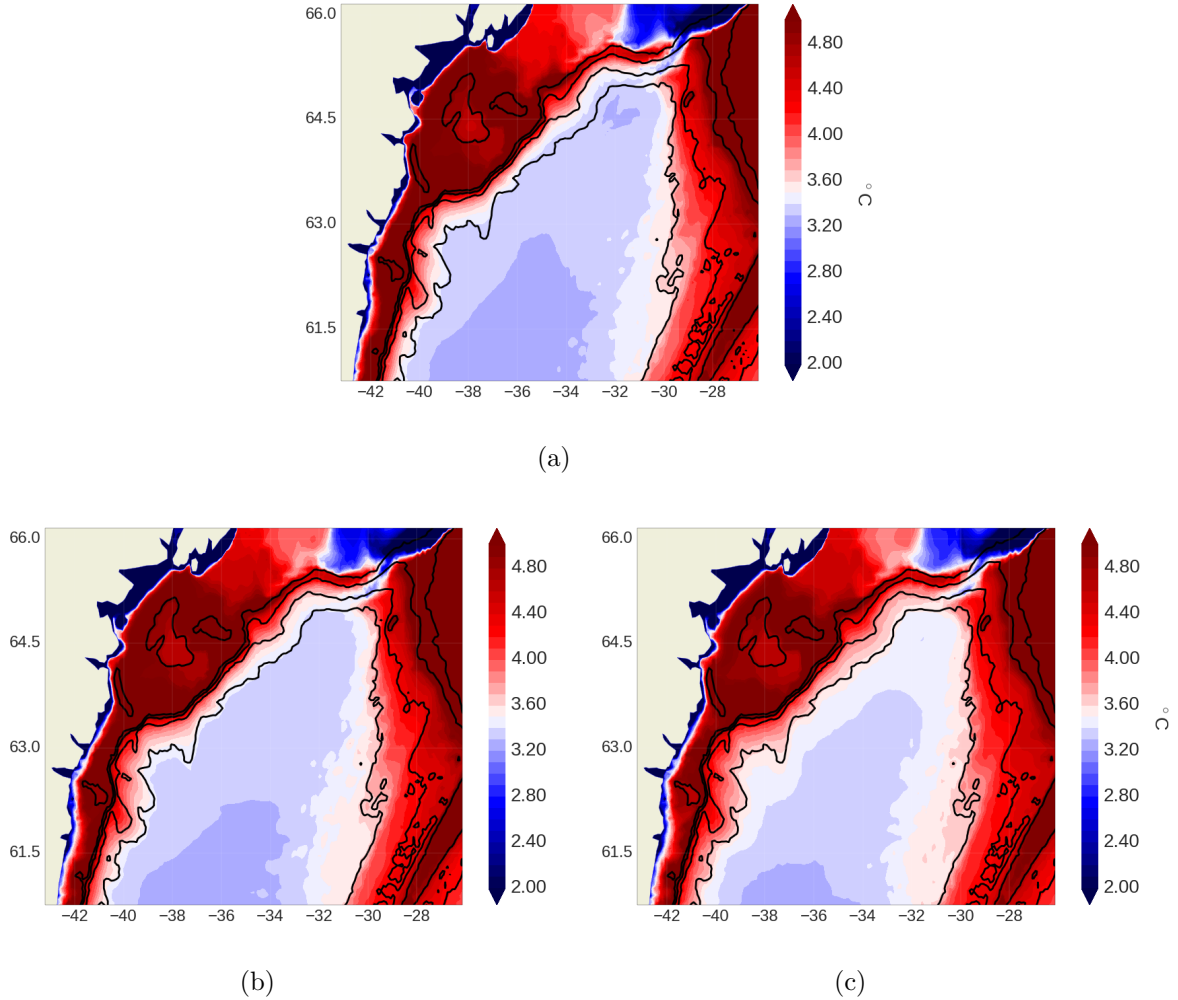


Figure 7.5: Annual mean of the bottom temperature of year 5 at $1/12^\circ$ with EVD applied on tracers and momentum (EVD=1) a) E12L46 b) E12L75 c) E12L300. Isobaths 500m, 1000m, 1500m and 2000m are contoured

We show the bottom temperature of these 3 simulations in figure 7.5. EVD on both tracers and momentum does not change the conclusions obtained before with EVD on tracers only regarding vertical resolution at $1/12^\circ$ (figure 7.2) and does not bring any significant changes. Again the 46L performs best.

7.5.2 Vertical resolution at $1/60^\circ$ - EVD=1

We compare here simulations at $1/12^\circ$ with a local refinement to reach $1/60^\circ$ with different vertical resolutions (46L, 75L and 300L). In this case EVD is applied on tracers and momentum (EVD=1).

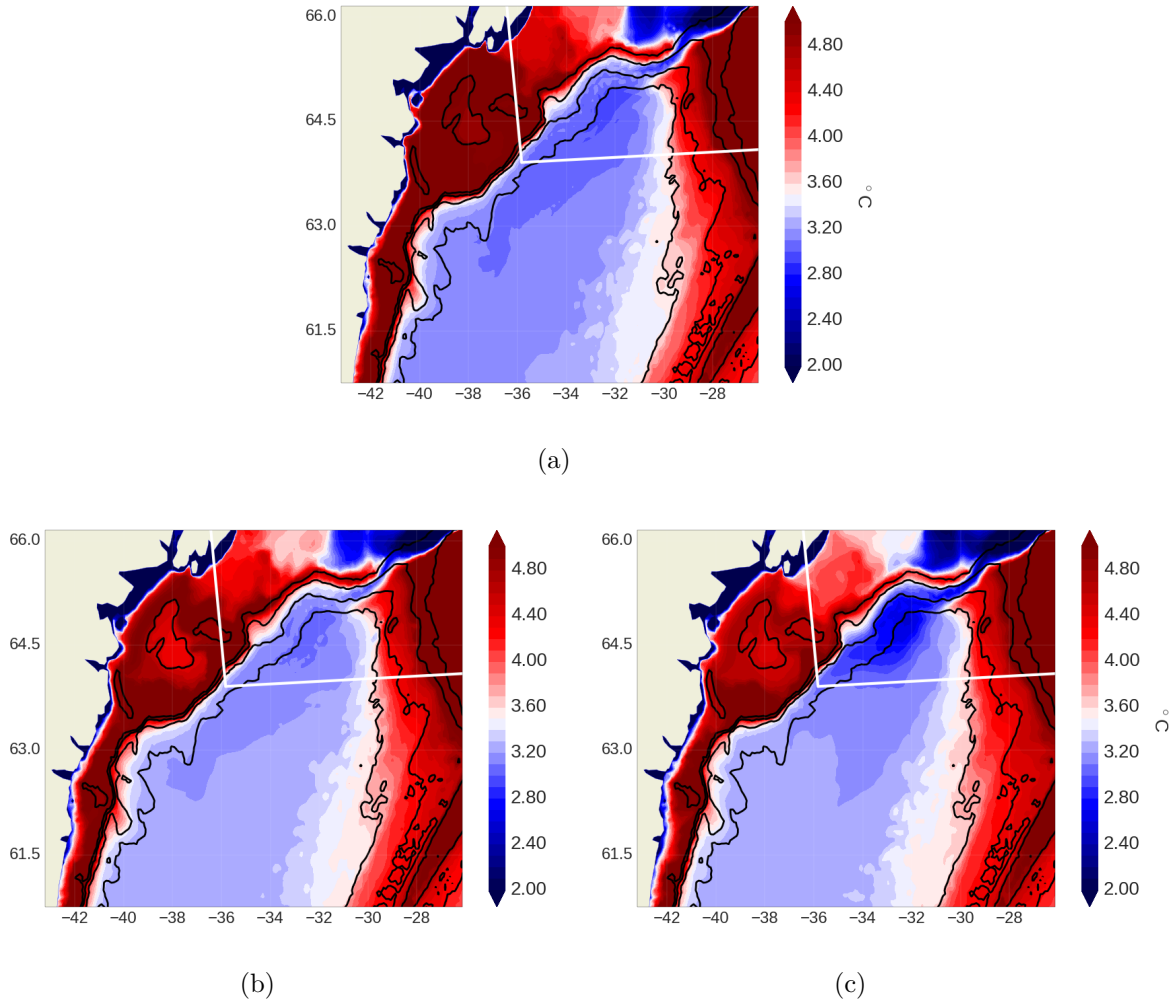


Figure 7.6: Annual mean of the bottom temperature of year 5 at $1/12^\circ$ with EVD applied on tracers and momentum (EVD=1) a) A12L46 b) A12L75 c) A12L300. Isobaths 500m, 1000m, 1500m and 2000m are contoured. In white lines the region where the local refinement is applied

We show the bottom temperature of these 3 simulations in figure 7.6. EVD does not change the conclusions done before regarding vertical resolution at $1/12^\circ$ with local refinement ($1/60^\circ$, figure 7.4) and does not bring any significant changes. However, we do not find any significant arguments to keep dividing the implementation of the EVD scheme and in the following simulations EVD will be applied on tracers and momentum (EVD=1).

7.6 Lateral boundary condition - No slip

While the default setting uses a free slip lateral condition, we test here a no slip lateral boundary condition. A series of global simulations at $1/4^\circ$ has shown that the global circulation is better represented with a free slip lateral boundary condition (Penduff et al., 2007). However, Hervieux, 2007 showed in the DOME configuration that the no slip boundary condition provides better representation of overflowing water. If this would be true in this realistic case, we could provide a local implementation of the no slip lateral boundary condition.

7.6.1 Vertical resolution in $1/12^\circ$ - No slip

We compare here simulations at $1/12^\circ$ with different vertical resolutions (46L, 75L and 300L). EVD is applied on tracers and momentum (EVD=1). No slip lateral boundary condition is implemented instead of a free slip lateral boundary condition.

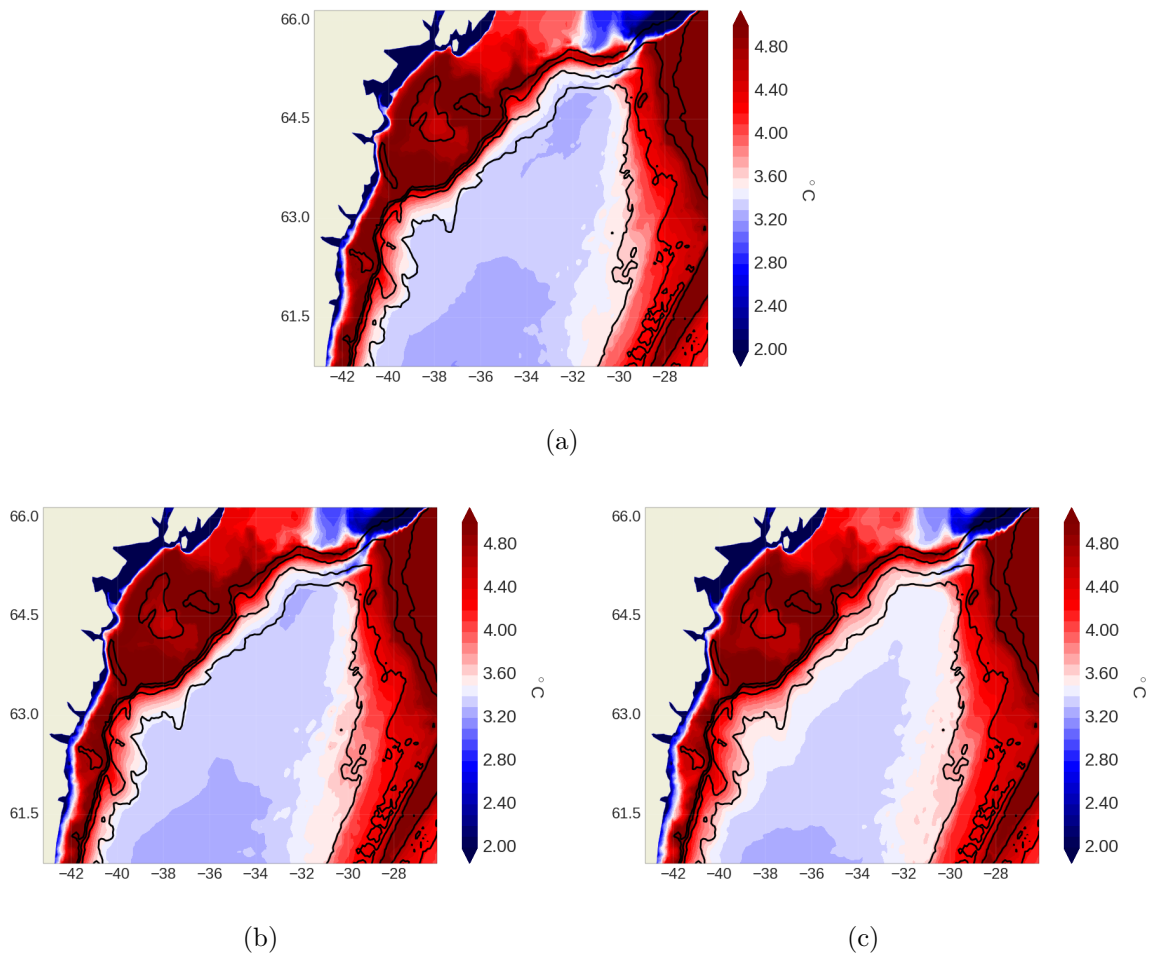


Figure 7.7: Annual mean of the bottom temperature of year 5 at $1/12^\circ$ with no slip lateral boundary condition a) E12L46 b) E12L75 c) E12L300. Isobaths 500m, 1000m, 1500m and 2000m are contoured

We show the bottom temperature of these 3 simulations in figure 7.7. The no slip lateral boundary condition does not change the conclusions done before regarding vertical resolution at $1/12^\circ$ (figure 7.2) and does not bring any significant changes.

7.6.2 Vertical resolution at $1/60^\circ$ - No slip

We compare here simulations at $1/12^\circ$ with a local refinement to reach $1/60^\circ$ with different vertical resolutions (46L, 75L and 300L). EVD is applied on tracers and momentum (EVD=1). No slip lateral boundary condition is implemented instead of a free slip lateral boundary condition.

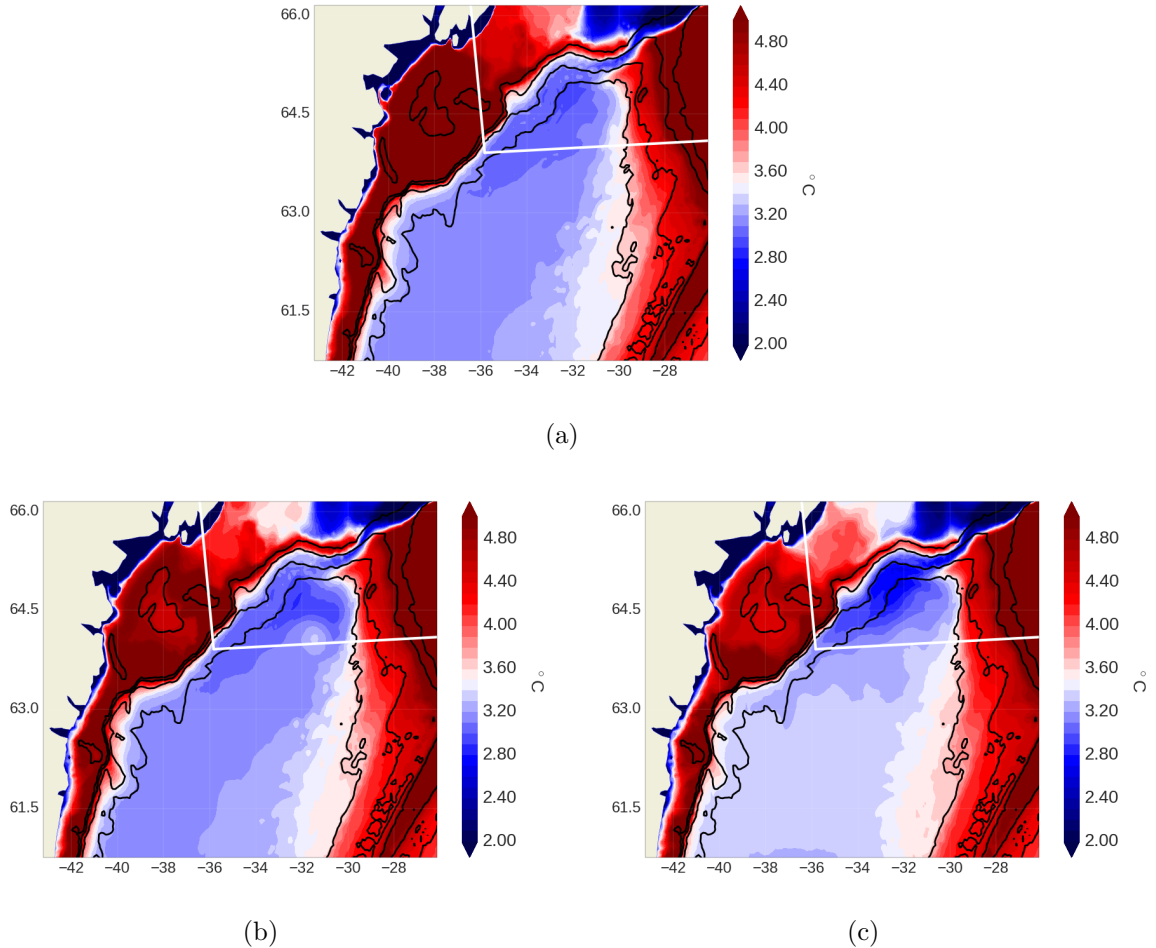


Figure 7.8: *Annual mean of the bottom temperature of year 5 at $1/12^\circ$ with no slip lateral boundary condition a) A12L46 b) A12L75 c) A12L300. Isobaths 500m, 1000m, 1500m and 2000m are contoured. In white lines the region where the local refinement is applied*

We show the bottom temperature of these 3 simulations in figure 7.8. EVD no-slip lateral condition does not change the conclusions obtained before regarding vertical resolution at $1/12^\circ$ with local refinement ($1/60^\circ$, figure 7.6) and does not bring any significant changes. We therefore conserve the use of a free slip lateral boundary condition, since the no slip one deteriorates the global ocean circulation as explained before.

7.7 Momentum advection formulation - EEN vector

We compare here simulations using the EEN vector formulation for the advection of momentum instead of the UBS scheme. The $1/12^\circ$ 46L NEMO v3.6 simulation with the EEN scheme is shown on figure 7.9a. It is interesting to note that it is not different from the solution produced with NEMO v3.5 with the EEN scheme (7.1b), demonstrating that the change of version of the code does not affect the overall performance in the overflow representation. Two other simulations are shown at 300L with the horizontal refinement, one using free-slip (figure 7.9b) and the other using no-slip (figure 7.9c) for the lateral boundary condition.

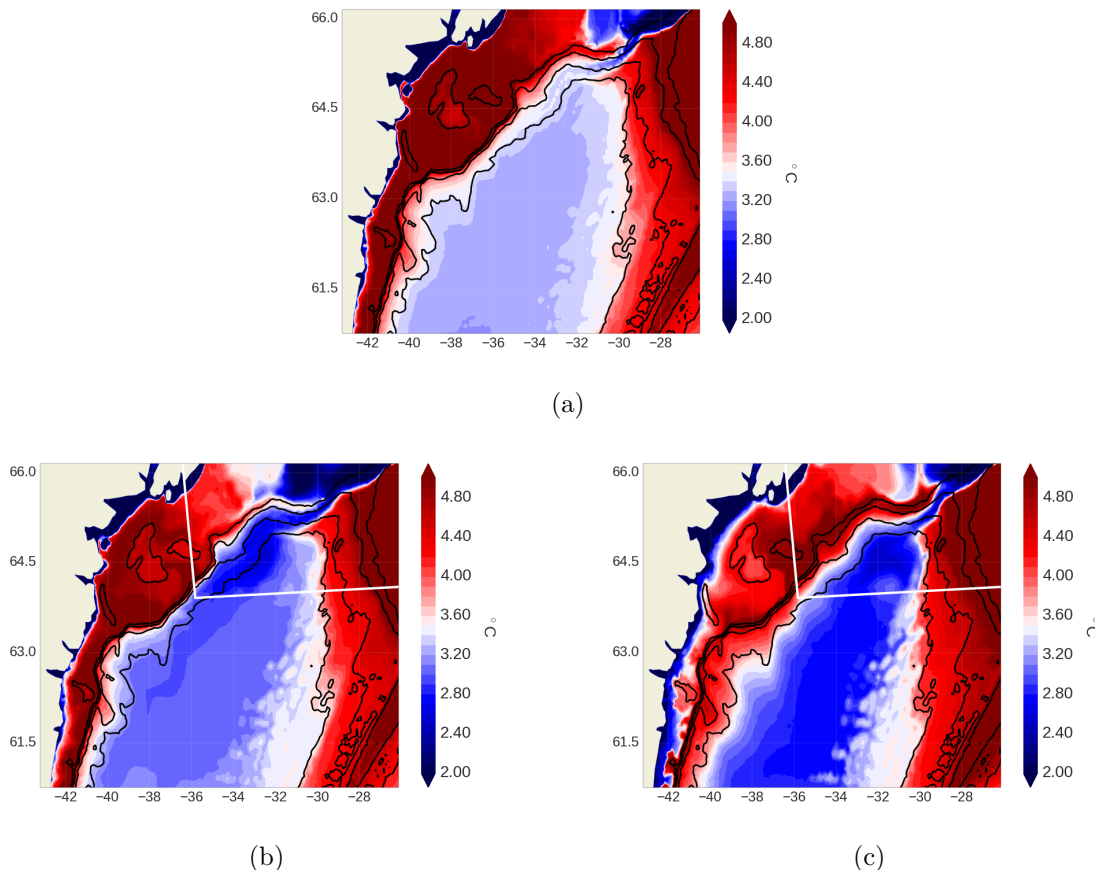


Figure 7.9: Annual mean of the bottom temperature of year 5 at $1/12^\circ$ using the EEN vector formulation for the momentum advection ($EVD=1$) a) E12L46 free-slip b) A12L300 free-slip c) A12L300 no-slip. Isobaths 500m, 1000m, 1500m and 2000m are contoured. In white lines the region where the local refinement is applied

Both figures 7.9b and 7.9c are very similar, confirming the previous results that the lateral boundary condition does not have a strong effect on the overall representation.

Since the no-slip lateral boundary condition was shown to be inadequate for global modelling (Penduff et al., 2007), care must be taken when using this option and only a local approach should be followed. No further reference to the no-slip lateral boundary condition is done and only the free-slip condition is considered.

When comparing with figure 7.6c (UBS scheme) the improvement on the propagation outside the AGRIF zoom is quite noticeable. In this case the cold water spreads over further from the zoom to the rest of the Irminger basin. The bottom temperature seems to be somewhat colder inside the AGRIF zoom than with the UBS scheme. After evaluation of the whole set of diagnostics, not significant differences are found inside the AGRIF zoom with the simulation

using the UBS scheme. This is commented in the following section.

7.8 Analysis and understanding

The previous and succinct analysis of the simulations seem to indicate that the main parameters affecting the overall representation of the overflow are the horizontal and vertical resolution, with no significant impact for the rest of the parameters tested.

The no-slip lateral boundary condition did not bring any significant deepening of the vein at any resolution in contrast with what was expected (Hervieux, 2007). At $1/12^\circ$ 300L it was notorious how the representation of the overflow was almost not affected by the changes in the vertical mixing scheme, to the limit that the use of a background vertical diffusivity with EVD was equivalent to the use of other schemes. This might be indicating that the convective adjustment dominates in the plume formation.

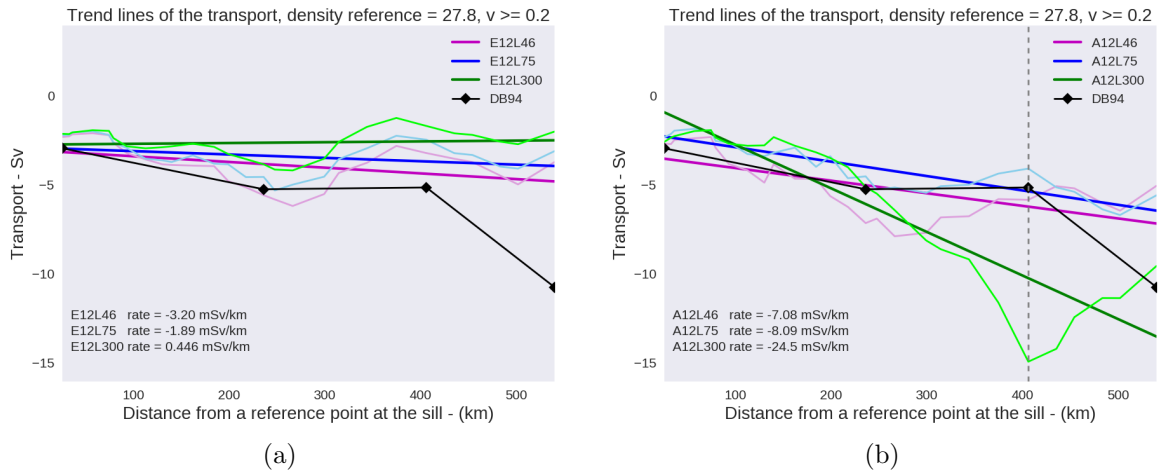


Figure 7.10: *Transport calculated along the 27 sections shown in 5.3 and its correspondent tendency lines for a) $1/12^\circ$ simulations b) $1/12^\circ$ + agrif simulations. In pointy black line the transport values presented in Dickson and Brown, 1994 for the sill, the Dohrn Bank, TTO and Angmassalik arrays.*

The increase of the vertical resolution at $1/12^\circ$ was to the detriment of the representation of the overflow. In figure 7.10a we show the transport of the vein (27.8 and $v \geq 0.2 \text{ m s}^{-1}$) for the three vertical resolutions used at $1/12^\circ$ (EVD=1). The pattern of these 3 curves seems to be the same and with increasing vertical resolution we observe a decrease in the tendency lines (which slope is the rate indicated in the figure). This situation seems to repeat itself, at least until a certain extent, at $1/60^\circ$ with 46L and 75L (figure 7.10b). A complete different behavior of the transport is observed for the A12L300 case ($1/60^\circ$, 300 levels). The first 200 km show an agreement with the rest of the simulations at $1/60^\circ$, but from this point until down to 400 km from the sill (the gray vertical line in figure 7.10b), the transport increase is drastic. In section 1.5 it was mentioned that the physical mechanism of entrainment might be different for this second part of the descent of the DSO according to observations.

Regarding the gray vertical line in figure 7.10b, it corresponds to section 22 (TTO array), which is the first section an important portion of which remains outside the AGRIF zoom (see figure 5.1). The following sections downstream are more affected by the change of resolution (from $1/60^\circ$ back to $1/12^\circ$) and this clearly impacts the transport values. Quantitatively speaking all transport values are in reasonable agreement with observations with exception of the E12L300 ($1/12^\circ$, 300 levels) case which shows a rather small amount of transport and A12L300 which presents a drastic increase of transport after 200 km from the sill.

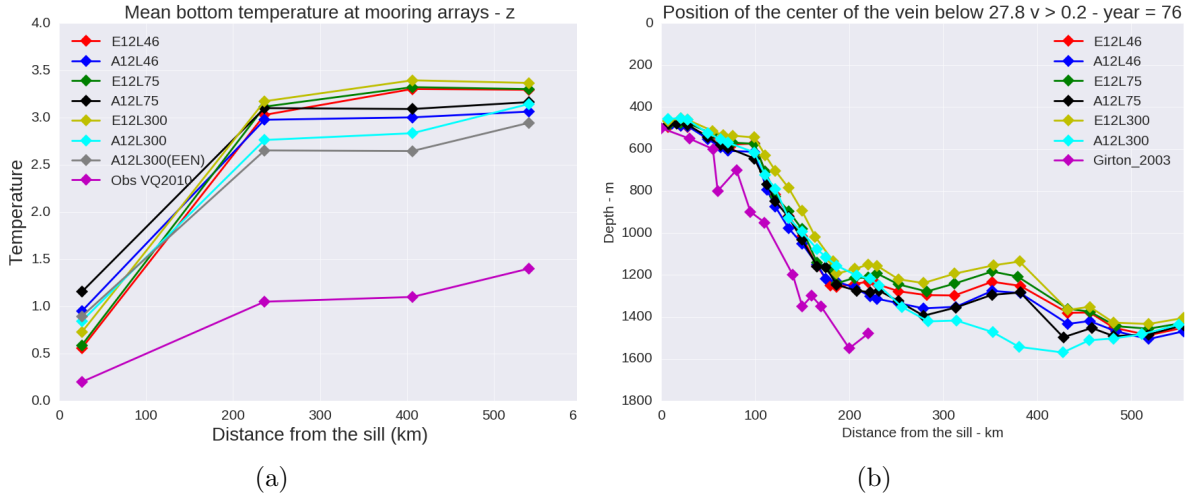


Figure 7.11: *a) Minimum mean bottom temperature of the 5th year of calculation of the grid points conforming arrays 1, 15, 22 and 27 (figure 5.3). In pointy magenta line the transport values presented in Voet and Quadfasel, 2010 for the sill, the Dohrn Bank, TTO and Angmassalik arrays. b) Vertical position of the center of the vein. In pointy magenta line the values found by Girton and Sandford, 2003.*

Another quantitative long-term comparison can be done with the bottom temperature at mooring arrays (figure 7.11a), supporting what was said for the domain bottom temperature. At $1/12^\circ$ the temperature at the four mooring arrays increases with increasing vertical resolution. This is the case as well with $1/60^\circ$ 46L and 75L. Again the A12L300 simulation shows a different behavior, with $\sim 0.5^\circ C$ colder at the Dohrn Bank array, $\sim 1^\circ C$ at TTO array, and similar values at Angmassalik array. This latter behavior is also explained by the fact that the Angmassalik array is outside the AGRIF zoom. At the sill we observe an increase of temperature of $\sim 0.5^\circ C$. Either way, these values are still far from observations.

Regarding the geographical evolution of the vein, we show in figure 7.11b the vertical position of the center of the vein along the 27 sections. Again, $1/12^\circ$ simulations (46L, 75L and 300L) and $1/60^\circ$ with 46L and 75L show similar behaviours, with shallower results as the vertical resolution increases. The A12L300 shows a comparable behaviour, except between $300km$ and $400km$ from the sill, where deeper values are observed. For reference only, we included the observations from Girton and Sandford, 2003. In this work they take the bathymetric value instead of the vertical weighted one, with the resulting differences found.

Finally, we would like to comment the A12L300 using the EEN vector formulation for the momentum advection. The diagnostics related with the bottom temperature (figures 7.9b and 7.11a) indicates that this solution offers a colder bottom temperature, of the order of $0.2^\circ C$. However, evaluation of cross-sections show very limited differences on the overflow characteristics. The principal gain of this solution comes most likely of an apparent better connection between mother and child grid solutions than in the case when the UBS scheme is used, which point out toward an issue in the implementation of AGRIF (that will have to be investigated).

7.9 A possible explanation for the behavior in the vertical resolution at $1/12^\circ$

Here we try to understand why at $1/12^\circ$ increasing the number of levels (from 46 to 75 and 300 levels) degrades the overall DSO solution.

A hint for what might be causing this degradation can be found by observing the vertical diffusivity along the path of the overflow. The case of the $1/12^\circ$ 46L run is shown in figure 7.13. In order to have an idea of the dimension of the numbers present in the plot, we have to consider that they are an annual mean value, so if we observe a value of $10m^2s^{-1}$ it means that the EVD has been applied at that grid point each time step all along the year in consideration. When a value of $2.5m^2s^{-1}$ (or $1.0m^2s^{-1}$) is present this could mean that the EVD was applied 25% (or 10%) of the time and the rest of the time the background diffusivity was present. This is the case for part of the mixed layer and the very bottom of the overflow. In the Irminger basin, in the intermediate region between the mixed layer and the overflow, we found values of the order of $10^{-5}m^2s^{-1}/10^{-4}m^2s^{-1}$. It is important to note that the minimum value of the vertical diffusivity set for the simulation is $10^{-5}m^2s^{-1}$ (background value). Preponderant values found in figure 7.13 are between $1m^2s^{-1}$ to $10m^2s^{-1}$ and $10^{-5}m^2s^{-1}$, especially in the $1/12^\circ$ 300L case (figure 7.13c). This might mean that the detail of the vertical mixing scheme has a low impact on the final solution of the overflow, and that the predominant driving of the overflow in this case is the EVD convective adjustment (a non-physical behavior of the model due to the step-like representation of the topography). This statement is in agreement with the results presented in section 7.4 (sensitivity of the solution at $1/12^\circ$ 300L to the vertical mixing scheme). Coming back to figure 7.13a we observe that at around $120km$ from the sill there is intense vertical mixing at intermediate depths which even connects the mixed layer with the overflow (corroborated with cross sections at this location). This intense mixing is increased towards the bottom and persists along the path of the overflow.

In the $1/12^\circ$ 300L case, figure 7.13c, the vertical diffusivity is augmented all along the overflow path when compared with the $1/12^\circ$ 46L case (figure 7.13a). One clear consequence is that the 27.85 isopycnal disappears rapidly after the descent. The vertical mixing is so strong that even at $200km$ and $300km$ from the sill, the mixing in the overflow connects with that of the mixed layer.

One possible explanation to this can be found in Winton et al., 1998. In this work it is explained that the horizontal resolution must be adjusted to the slope in order to reduce the size of the vertical grid over which the vertical mixing is done for every movement downslope. In other words, the horizontal and vertical resolution should be chosen such that the observed topographic slope α is properly resolved,

$$\Delta z = \Delta x \tan(\alpha) \quad (7.1)$$

We extend a bit this statement in order to explain the excessive vertical mixing observed. Let us consider a simple 2D space of an unspecified length, discretized in a square shape grid in which each element has a size $\Delta x = 1m$ by $\Delta z = 1m$. In this domain we put a bottom-slope set by an angle of 45° , which will be represented by a staircase of one grid point length. In this case the grid-slope, $\Delta z/\Delta x$, and the bottom slope are equal. Once we filled this domain with a static constant temperature and salinity fluid, we set a colder (denser) parcel of fluid at the very top and advect it horizontally with a velocity $U = \Delta x/\Delta t$. By the conservation of mass we can obtain the vertical velocity

$$W = U \frac{\Delta z}{\Delta x} = \frac{\Delta x}{\Delta t} \frac{\Delta z}{\Delta x} = \frac{\Delta z}{\Delta t} \quad (7.2)$$

This is, the parcel would have a vertical velocity that would displace it one grid point in the vertical for each time step. In fact, this equation also imposes that the Courant number in the

vertical cannot be greater than the one on the horizontal, so the maximum displacement possible is one grid point for each time step. A schematic of this is shown in figure 7.12a.

Now let's double the vertical resolution but keep the horizontal resolution unchanged. This means that the grid-slope is reduced by a factor of two but the bottom slope has not changed. Now this dense parcel will be represented by two grid points of $1m$ wide by $0.5m$ thick, as shown in figure 7.12b. We then advect these particles in the horizontal as we did before (same time-step), and now they would move again one grid point in the vertical, except that in this case they will end up one grid point away from the bottom. If we continue with this exercise after a few time steps this parcel will end up completely separated from the bottom, in contrast with the first case. In other words, the convective adjustment makes the flow to follow the grid-slope rather than the topographic slope (as illustrated in figure 7.12).

In fact, in a hydrostatic model like NEMO what would happen is a little bit more complex but follows the same rationale. After the horizontal advection, a density inversion would take place, in which the model will correct this instability by applying a large value of vertical diffusivity (EVD). We might trace a parallelism of this situation with our overflow problem. Increasing the resolution would generate the overflow to detach from topography and generate density inversions far from expected locations. This would generate large amount of vertical mixing in direction to the interior of the basin as we increase the vertical resolution and give as a result a more diluted vein, which is in fact what we observe in figure 7.13c.

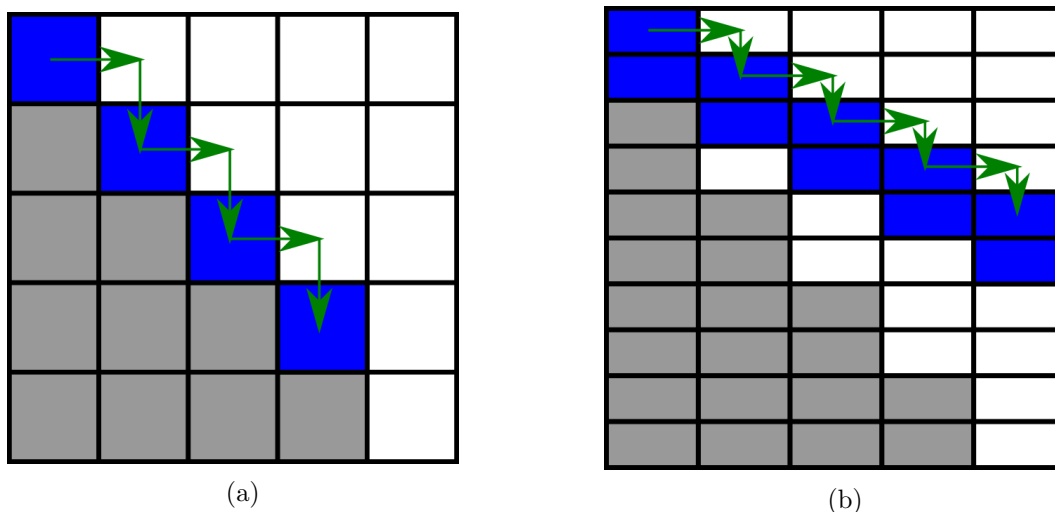


Figure 7.12: Scheme representing the successive operations for a particle at the top of a seamount in z -coordinates which is advected in the horizontal and the vertical a) For a vertical resolution equal to the horizontal one b) For an increased vertical resolution of two times

On the contrary, increasing the horizontal resolution only might lead to a diminution of the vertical mixing. This is what we observe in the mother grid solution both for $1/60^\circ$ 46L case (figure 7.13b) and $1/60^\circ$ 300L case (figure 7.13d). In those two cases is also remarkable how the 27.85 isopycnal is present in the Irminger basin, in contrast with the $1/12^\circ$ cases.

A specific issue arises in $1/60^\circ$ 300L case (figure 7.13d). At about $500km$ from the sill, where the AGRIF nest arrives to an end, high values of vertical diffusivity are generated for a reason that we did not identified. This is intriguing since this effect is not observed in the $1/60^\circ$ 46L case in figure 7.13b.

It is also noticeable in the four cases present in figure 7.13 that the rises in the iso-density lines appears to be linked to high values of vertical diffusivity, for example around $200km$ from the sill. This should not be a surprise if we consider that these isopycnals are highly related with the overflow and therefore with the EVD, whose functioning is density related. These results are in accordance to what is explained in Laanaia et al., 2010. In this work they state

that the convective adjustment destroys the gravity current dynamics, blocking the downslope movement. We therefore think that it is important to control the EVD occurrence in overflow problems. Coming back to our example of figure 7.12a, we observe that the whole dynamics is not related to resolution itself. In fact we did not consider the relationship $\Delta z/\Delta x$ in our explanation. The important aspect is that for a given step in the x direction there is a step in the z direction, in other words the importance here is the relationship between grid point numbers

$$N_z = N_x \tag{7.3}$$

where N_z and N_x are the number of grid points in z and x, respectively. By respecting equation 7.3 we guarantee that convective adjustment will happen close to the bottom topography for any slope and that EVD will not irrupt to modify the interior of the basin as in figure 7.12b. Equation 7.3 is nothing more than replacing the vertical and horizontal lengths in equation 7.2 ($\tan(\alpha) = \frac{L_z}{L_x}$).

Having said all this, the vertical resolution approach has shown to be useful in the improvement of the representation of the overflow in other problems and we do not argue with this. In Reckinger et al., 2015, they test the representation of the overflow with different vertical resolution among other tests. In their results they show an improvement on the overall representation of the overflow when the vertical resolution increases in the DOME configuration. They explained their improvement by saying that the finer vertical resolution puts the Ekman layer physics to work.

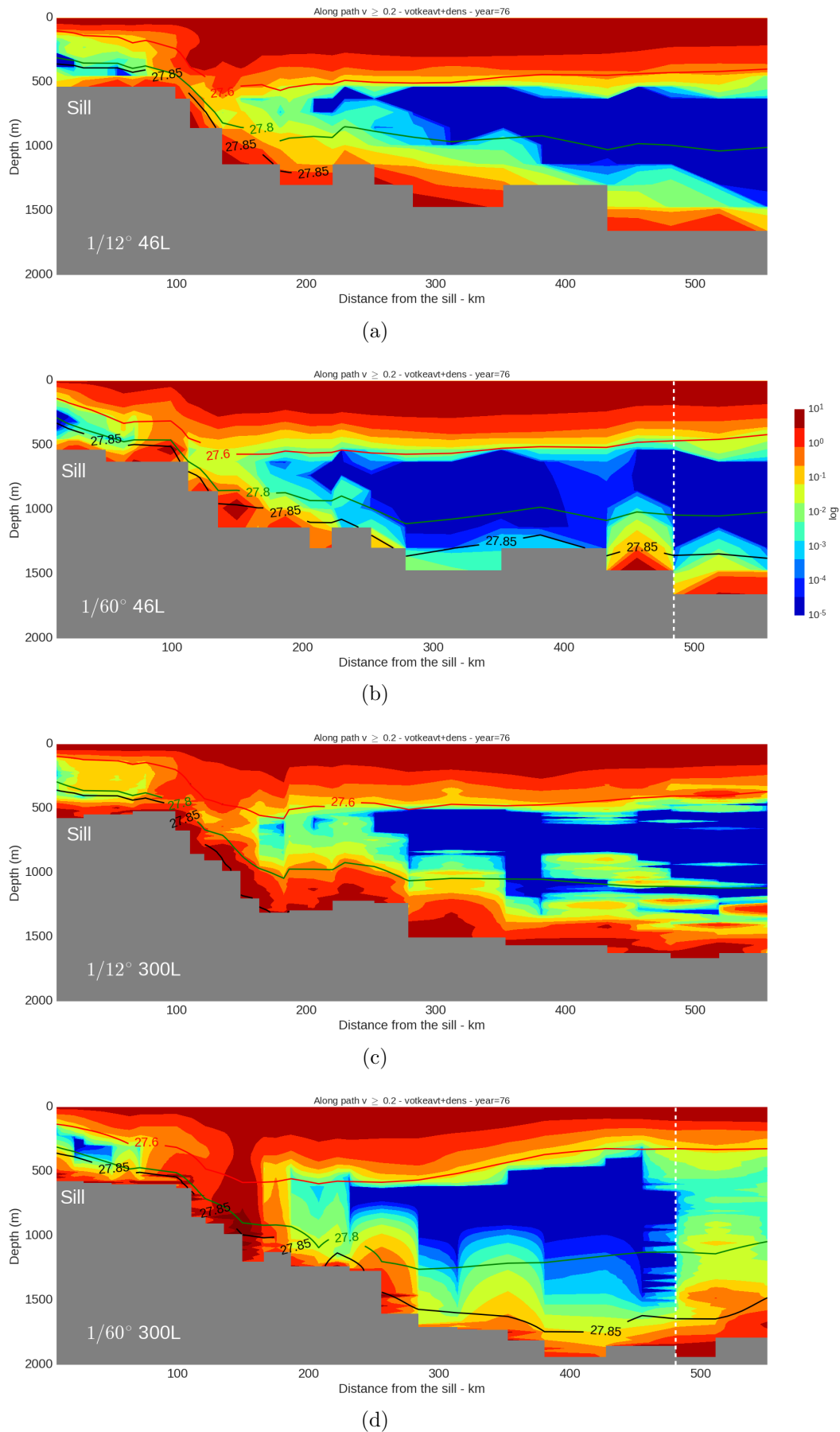


Figure 7.13: Annual mean of year 5 of the vertical diffusivity along the path of the vein calculated for each simulation a) E12L46 b) A12L46 c) E12L300 d) A12L300. The values of the depth of the vein can be found in figure 7.11b. For figures b and d the vertical white lines denotes the end of the AGRIF zoom.

7.10 Analysis of the $1/60^\circ$ 300L simulation

We extend the analysis of the A12L300 simulation, continuing with what was started in section 7.8. In particular, we explore why the simulation A12L300 presents a very different solution from the other simulations.

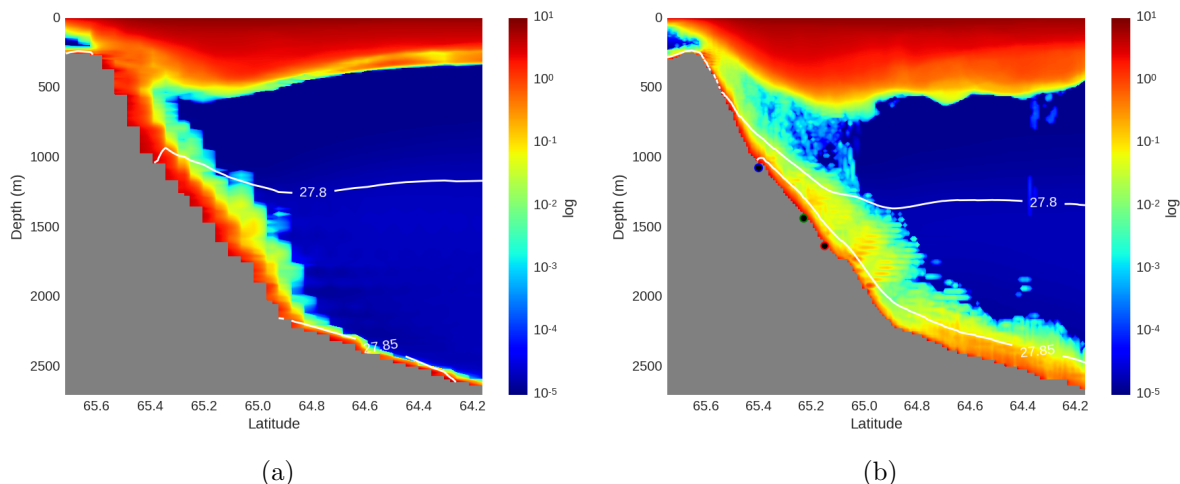


Figure 7.14: Annual mean of year 5 of the vertical diffusivity at section 18 a) E12L300 b) A12L300. In white contours isopycnals 27.80 and 27.85. The three points in colors are the locations where the vertical profiles are plotted in figures 7.16 and 7.15

In figure 7.14 we show the annual mean of the vertical diffusivity for the section 18 in the case without and with horizontal grid refinement. In the case of E12L300 (figure 7.14a) we observe that the vertical diffusivity is very intense in a rather thick layer all along the slope (between 500m and 2200m) and, according to the rationale of section 7.9, the reason is the convective adjustment (EVD) governing the near bottom physics. Below 2200m, the intense (i.e. EVD driven) mixing is limited to a very thin bottom layer, suggesting the absence of a sheared flow that would drive diffusivities values greater than the background one.

In the case of A12L300 (figure 7.14b) this convective adjustment is mainly constrained to the very bottom, the EVD driven mixing being confined below the 27.85 isopycnal. In addition, vertical diffusivity values of $\sim 10^{-1}m^2s^{-1}$ or lower are found above this thin bottom layer. If driven by the density inversions leading to EVD mixing, such values indicate a rare occurrence of such events (1% of the time or less). It is more likely that these values are driven by the vertical shear of the overflow vein (entrainment): in the presence of a persistent and sheared bottom current, the TKE scheme would produce such values. In fact this is what we would expect according to the physical processes explained in section 1.5, the shear governing the entrainment in the overflow plume. In this way, the resolution plays a key role since it allows the convective adjustment to occur in a limited portion of the vein without interfering with the rest of the physics in the vein.

This hypothesis is investigated via the analysis of the vertical profiles of different properties among the different simulations. As an example, we show in figure 7.15 the vertical profile of the downslope velocity at section 18 for 3 different points (indicated in figure 7.14b) for four different simulations. The A12L300 simulation is the only one that presents at all depths a well-marked intensified and vertically sheared current confined near the bottom. This feature is observed all along the integration and its origin can be linked with the Ekman bottom boundary layer, the resolution of which contributes to the generation of the shear. This bottom signature has already been described in observations (see section 1.2.7) and constrains the different properties of the overflow. In the other $1/60^\circ$ cases with lower vertical resolution (A12L46 and A12L75),

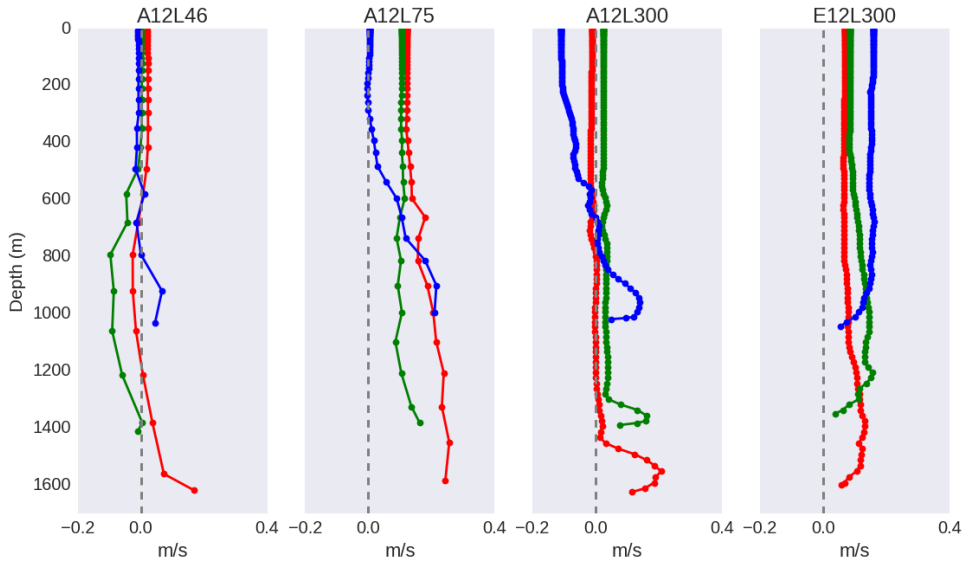


Figure 7.15: Vertical profiles of downslope velocity for 12/March of year 5 at section 18 at the locations indicated in figure 7.14b a) A12L46 b) A12L75 c) A12L300 d) E12L300

the low vertical resolution does not allow to resolve the Ekman driven vertical shear and the whole dynamics of the current is dominated by the EVD mixing, being the flow maximum at the bottom level which is quite unrealistic. In the case E12L300 ($1/12^\circ$ 300L), because of the large thickness of the EVD driven layer, the vein of fluid is spread over a greater depth and the vertical shear of the flow is weak.

To investigate with more detail the plume of the overflow in the A12L300 simulation, we show in figure 7.16 instantaneous vertical profiles of salinity, temperature, downslope and alongslope velocities at the points indicated in figure 7.18a (in this case it is section 14, upstream of section 18). All these properties show the signature of this bottom boundary layer.

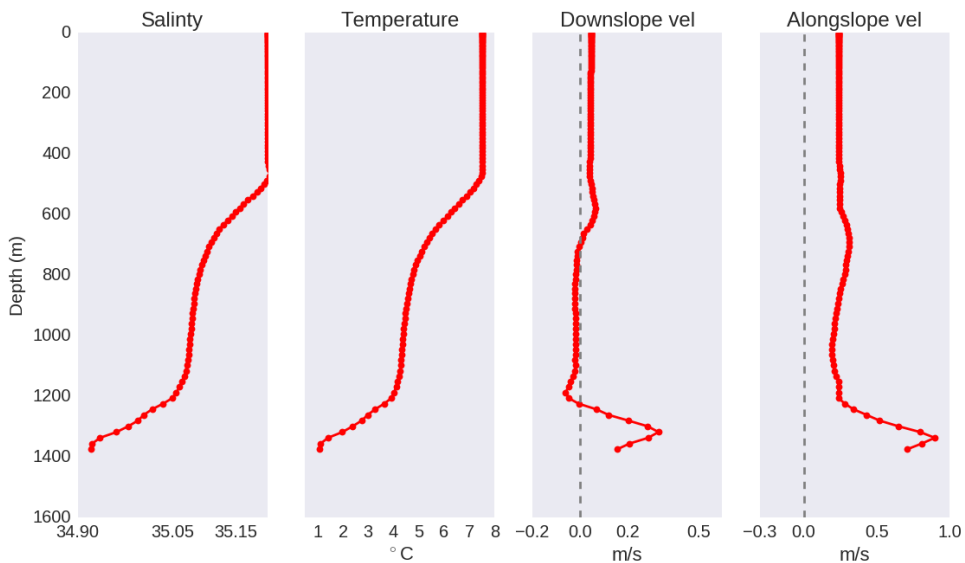


Figure 7.16: Vertical profiles of different quantities for A12L300 for 02/January hour 3 of year 5 at section 14 for the location indicated with a red dot in figure 7.18a a) Temperature b) Salinity no c) Cross-slope velocity d) Along-slope velocity

This agrees with what is exposed in Laanaia et al., 2010, it is not the increase of vertical viscosity that enables the downslope movement, but the resolution of the Ekman layer dynamics. Observations of the DSO plume from microstructure measurements (Paka et al., 2013) show a freshening across the front of the plume of the order of 0.05 to 0.10 (coherent with the properties of Arctic waters), while figure 7.16a shows a freshening of ~ 0.15 in the model. For the temperature the observations show a cooling of $3.5^{\circ}C$ in the plume layer, while in figure 7.16b we obtained a cooling of $3^{\circ}C$. Downslope and alongslope velocities show an acceleration of the flow in the plume of $0.2ms^{-1}$ and $0.6ms^{-1}$ respectively in observations, while in figures 7.16c and 7.16d we obtained $\sim 0.3ms^{-1}$ and $\sim 0.7ms^{-1}$. These values are in reasonable agreement. The location of the red curve is $30.4^{\circ}W$ $65.2^{\circ}N$ of figure 7.16, coherent with the measurement point used in Paka et al., 2013.

7.11 Further comments of the $1/60^\circ$ 300L simulation

We complete here the description of the $1/60^\circ$ 300L simulation. This is done first to compare this simulation with observations and second to evaluate the improvements regarding the reference simulation.

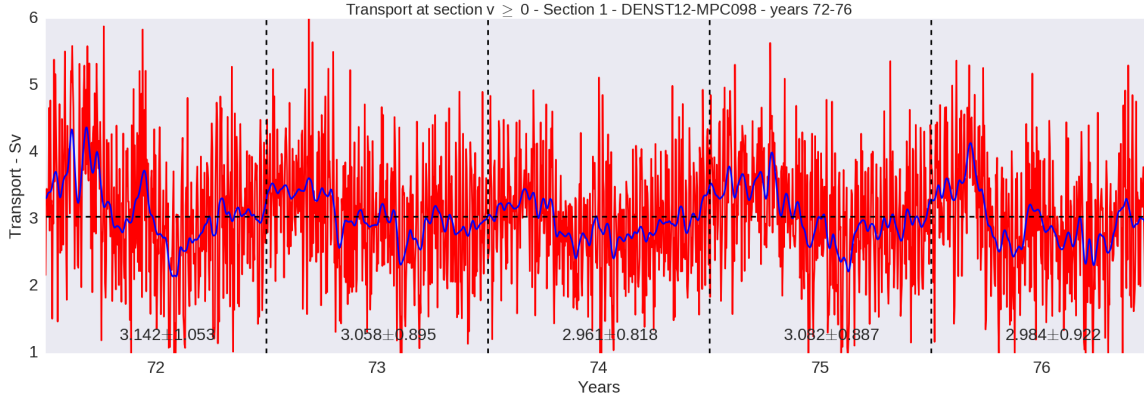


Figure 7.17: *Time evolution of the volume transport of southward ($v > 0\text{ms}^{-1}$) waters denser than 27.80 in A12L300. In red daily values and in blue the smoothed time series (20 day hanning window)*

Proceeding in the same way as in the reference simulation we start by describing the transport time series at the sill (figure 7.17). In this case the transport is still $\sim 3Sv$, but a higher standard deviation of $0.9Sv$ (instead of the $0.6Sv$ of the reference simulation) is obtained. More pronounced transport peaks can also be observed in the time series, which can reach a difference of up to $\sim 3Sv$ when compared to the mean. With the smoothed version of the time series, we can observe an annual cycle also present in the reference simulation. In this case the feeding of overflow waters is also continuous and steady along the whole simulation.

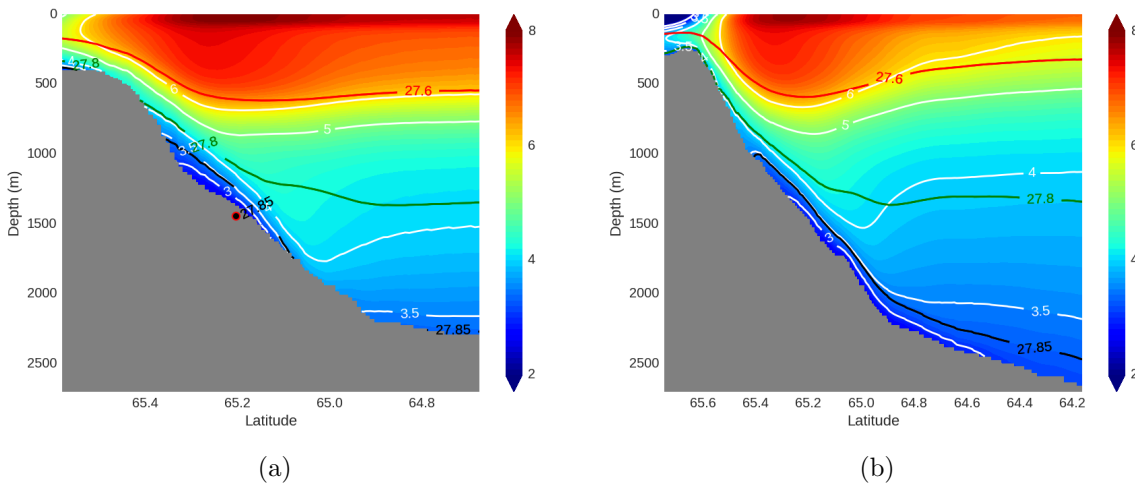


Figure 7.18: *A12L300 simulation, annual mean temperature of year 5 with temperature and density contours a) Section 14 (Dohrn Bank array). The red dot indicates the location of the profile shown in figure 7.16 b) Section 18 (spill jet section)*

In figures 7.18 and 7.19 we present different sections for qualitative comparison ends. Figure 7.18a shows a very clear presence of a vein well confined along the slope at depths from 500m down to $\sim 1600\text{m}$ and temperatures below 3.5°C , at least 0.5°C colder when compared to

the reference simulation (figure 6.3a). This is still far from observations (figure 1.6), where temperatures of 2°C are found down to 2000m . In the case of figure 7.18b, the plume reaches the depth of 2500m , while in the reference run (figure 6.3b) the signature of the plume is hardly noticeable. We included in this case the section 22 (figure 7.19a) in order to compare it with observations (figure 1.8). In this case our results present remarkable similarity for the isopycnal 27.85 , and some similarities for the temperature contour 3°C (still $\sim 1^{\circ}\text{C}$ too warm). Isopycnal 27.8 is still unrealistic, which most likely is related with basin interior properties. The end of the AGRIF zoom clearly impacts on section 27 (figure 7.19b), where many of the improvements obtained in the interior of the AGRIF zoom are no longer visible. This fact could also be affecting section 22, and a larger AGRIF zoom could make our results more comparable with observations. From this point of view it is important to remark that the $\sim 1^{\circ}\text{C}$ warm bias observed could be caused by the unrealistic initial and boundary conditions (which already exhibit a warm bias).

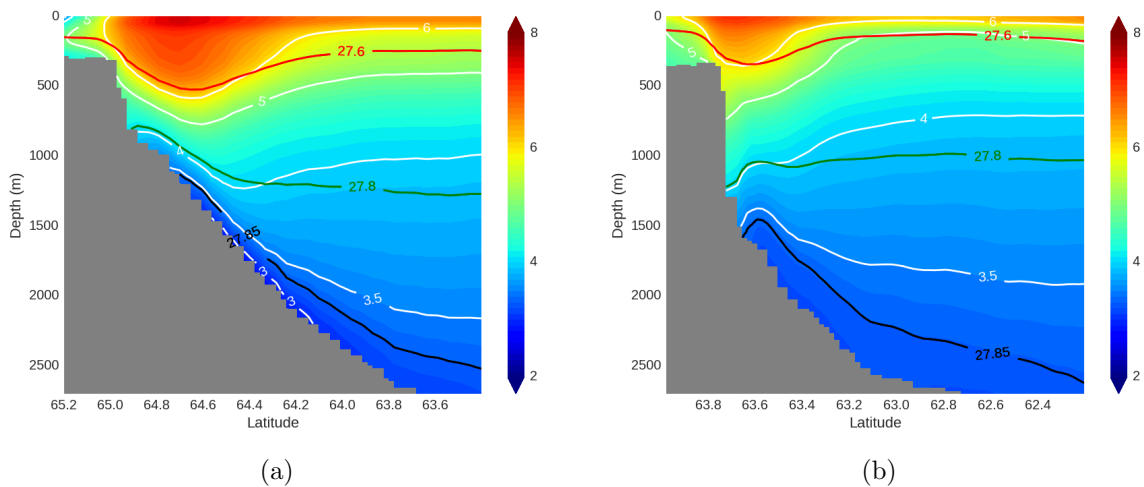


Figure 7.19: *A12L300 simulation, annual mean temperature of year 5 with temperature and density contours a) Section 22 (TTO array) b) Section 27 (Angmassalik array)*

The along path temperature in A12L300 (figure 7.20) shows a dramatic improvement when compared to the reference run (figure 6.5). The cold water coming from the sill propagates down to 2000m as well as the 27.85 isopycnal that can be clearly followed 500km downstream.

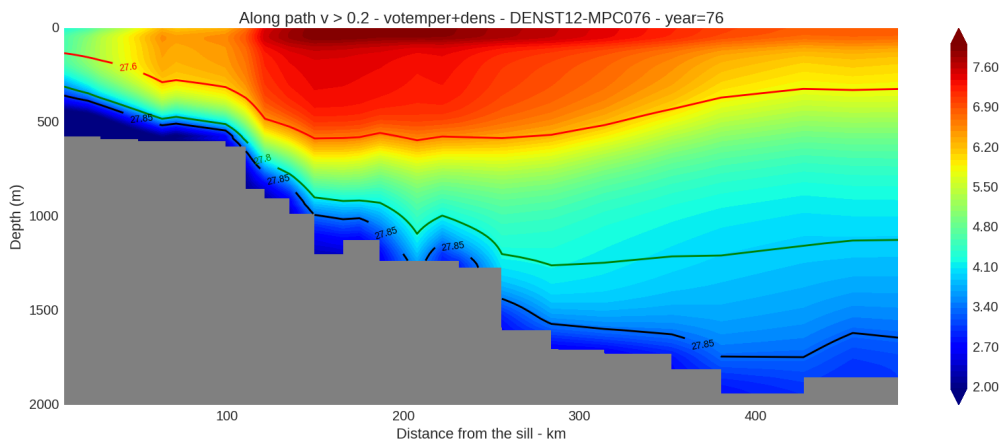


Figure 7.20: *Temperature annual mean of year 5 along the path of the overflow (magenta line in figure 5.3a). Density values in contours (27.6 in red, 27.8 in green and 27.85 in black). Reference simulation.*

Finally, we complement the previous diagnostic of bottom temperature shown on figure 7.11a, with the TS diagram of figure 7.21 (with the respective locations of the points on the map). When compared with observations (figure 1.17) model outputs show an increase in salinity of the order of 0.1 when going from the sill (34.92, DS1 and DS2) to the Angmagssalik array (35, F2New, UK1, UK2, G1), while observations keeps an approximately constant value of 34.89. Regarding the evolution of temperature the comment is the same than for figure 7.11a. There is a drastic warming from the sill to the Dohrn Bank array (DS5, DS6 and DS7), largely due to mixing with the lower part of the Irminger current, already too warm in the model, but a limited evolution when compared with the minimum temperature at the Angmagssalik array. All in all the difference with observations is of the order of $\sim 1^\circ C$ (attributed for a part to initial and boundary conditions). The distribution of temperatures at the Angmagssalik array presents low amplitude $\sim 0.3^\circ C$, while in the observations the difference from the coldest to the warmest point is $\sim 0.7^\circ C$. It is also interesting to see that the amplitude between maximum and minimum values (thin lines) at the Angmassalik array are considerably smaller than for the points in the Dohrn Bank array.

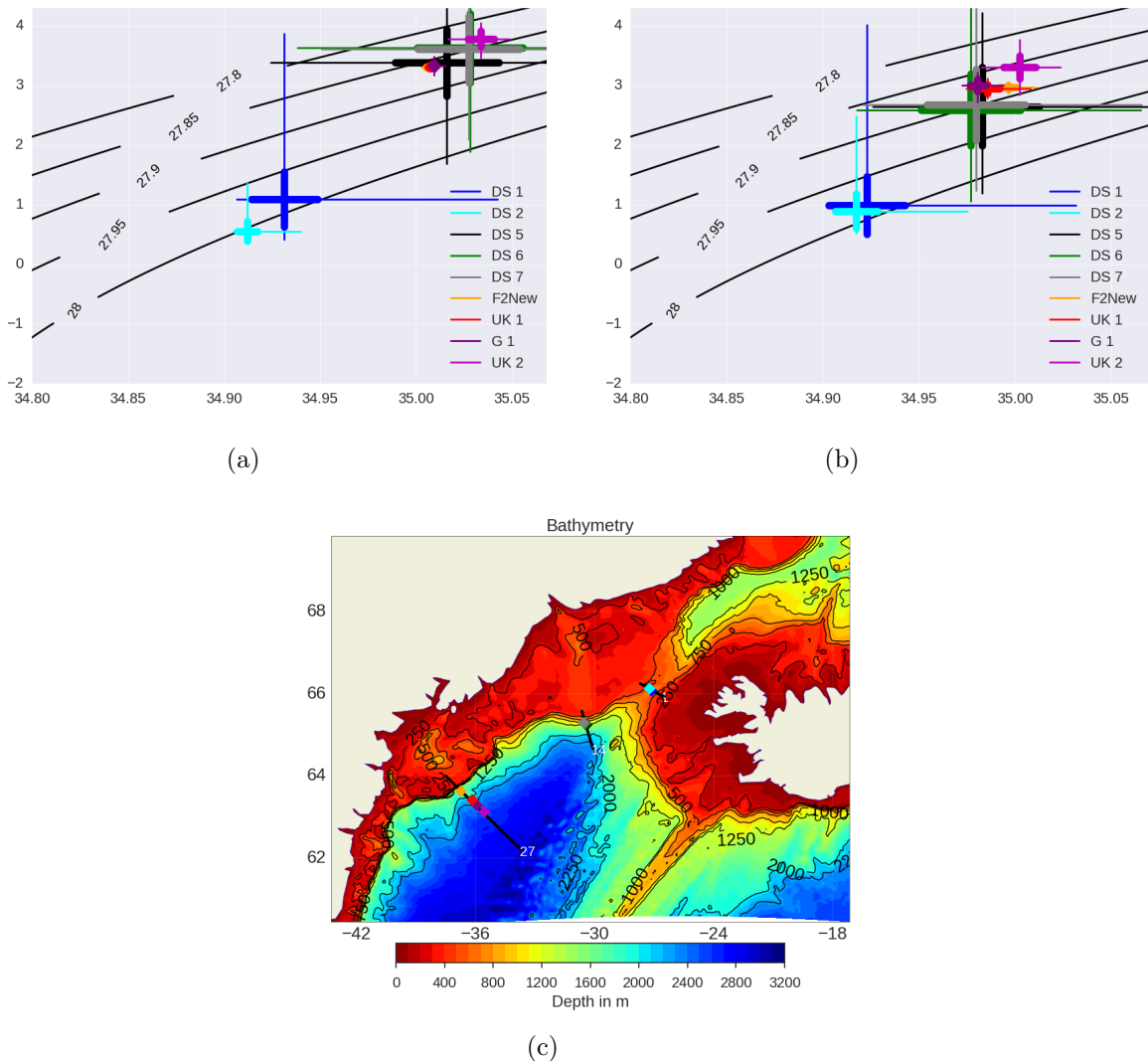


Figure 7.21: Annual mean TS diagram of year 5 of a) E12L300 (reference simulation) b) A12L300. Comparable with figure 1.17 from Jochumsen et al., 2015 c) Configuration domain with the location of the points. The thick horizontal and vertical lines are the mean values plus/minus one standard deviation, and the thin lines are the maximum range of properties.

A complementary diagnostic to these two TS diagrams is presented in figure 7.22. In this figure we show the difference of the TS diagrams between A12L300 and E12L46 annual mean of year 5 at section 27 (Angmagssalik array). The properties of waters have shifted towards colder and fresher values (the blue spot to the lower left respect the red spot). Denser waters were created (increase of the volume of waters of density greater than 27.85 - green curve), mainly because of cooling (not due to salinity change).

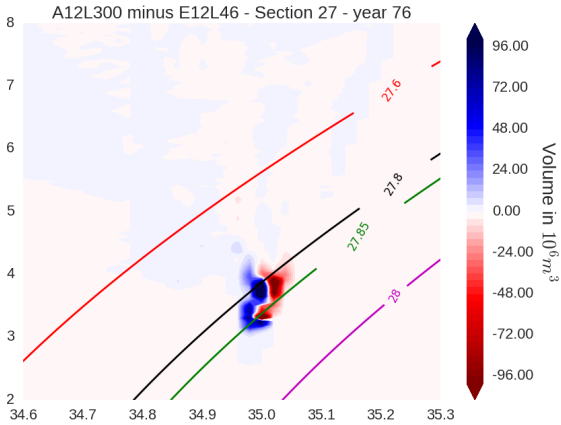


Figure 7.22: *Difference of the TS diagrams between A12L300 and E12L46 annual mean of year 5 at section 27 (Angmagssalik array). Density values in contours.*

7.12 Transient dynamics in A12L300

As seen in the time series of figure 7.17 and as explained in chapter 1, the DSO overflow presents a high variability (pulses of water with a time scale of few days). For this reason, the approach followed by different authors and in this work in particular is to characterize the DSO with mean quantities. However, the small scale dynamics are a key aspect to understand the overflowing process and are the important contributors to the final properties of the DSO. As explained in section 1.5, the mixing processes are still sub-grid motions, but the A12L300 has shown to reproduce processes that are not present in the simulations of coarser horizontal and vertical resolution. For example, this is the case for the bottom boundary layer observed in figure 7.16. We did not have the time to fully evaluate these processes, but we present here a short description of two additional aspects that we found interesting about the overflowing process.

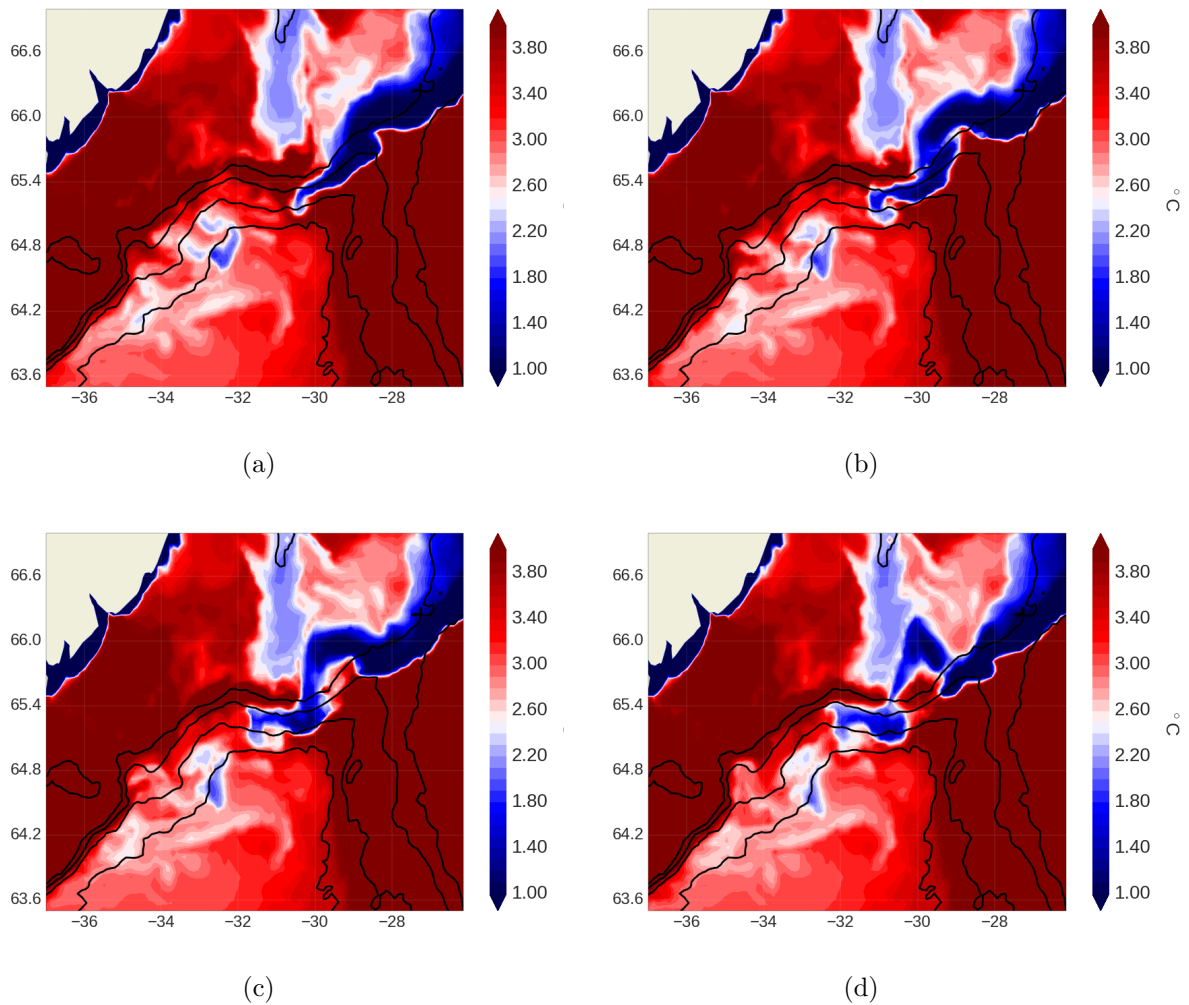


Figure 7.23: *A12L300 simulation, hourly snapshots of bottom temperature a) 23/April year 3 - 9h b) 15h after c) 26h after d) 39h after. The 500m, 1000m, 1500m and 2000m isobaths are contoured.*

First, the cold bottom temperature observed in figure 7.6c is in fact the time-average of pulses of cold dense water coming from the sill. To illustrate this we show in figure 7.23 hourly outputs of the bottom temperature in the third year of simulation. The whole sequence last only ~ 40 hours. First in figure 7.23a the DSO has already started its descent crossing isobaths until

$\sim 1000m$ mainly constrained by topographic features. Then in figure 7.23b (15h later) the DSO is constrained by geostrophy, turning to the right and tends to flow along isobaths. A separation into two boluses begins to appear, one in the DSO itself and a second bolus towards the Kangerdlugssuaq Trough ("KG trough" in figure 1.1). In figure 7.23c both boluses start to detach from each other and the DSO reaches the 1500m isobath, the effect of gestrophy becomes evident, stirring the DSO bolus to the bathymetry. In the end, in figure 7.23d, both boluses are almost completely separated, except for a thin residual filament. The DSO has almost reached the 2000m isobath and it will continue its way to the Angmassalik array. The formation of the boluses happened in only 30 hours, showing the high frequency variability of the overflow and illustrating the difficulty of diagnosing its properties. The model allows to establish mean properties with a good accuracy, but this is not the case for most observations, and this makes the model validation a difficult task.

Second, the role of lateral mixing processes (i.e. advection by the mesoscale eddies and boluses) might become important for the A12L300 simulation. We showed in section 7.10, that there was a decrease in the vertical diffusivity thanks to the fact that the convective adjustment happens in a limited portion of the vein. However, a clear increase of the transport was observed in figure 7.10b. Some works (see Jochumsen et al., 2015 for example) explain that the main entrainment process might not be the vertical mixing as some authors suggested (Legg et al., 2006). Instead they consider that the lateral mixing plays a major role in the entrainment (as mentioned in section 1.3.2). Looking the relative vorticity (figure 7.24), we found considerable higher values for the case of A12L300 (figure 7.24b) than in the case of E12L46 (figure 7.24a). Another interesting aspect present in the A12L300 case is the presence of very small spatial scale features all along the overflow path. These vorticity patterns are indicators of a greater lateral mixing. More analysis is needed from this point of view, especially if the lateral entrainment becomes dominant with increasing resolution and the resulting overflow transport becomes considerably higher than in observations. This is one of the perspectives of this study.

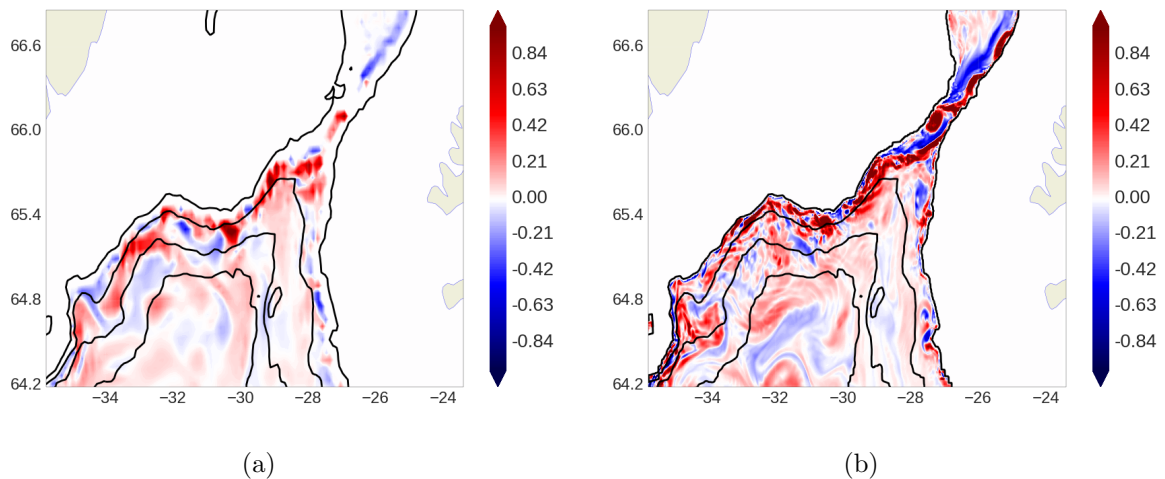


Figure 7.24: Hourly snapshot of the relative vorticity at 540m a) E12L300 b) A12L300

7.13 DSO in z-coordinates: What to retain

We evaluated in this Part III the sensitivity of the representation of the Denmark Strait overflow in the regional z-coordinate configuration of NEMO to the grid resolution and to numerical parameters. Contrary to expectations, in the given numerical set-up, the increase of the vertical resolution (from 46 to 75 then to 300 levels) did not bring any improvement at $1/12^\circ$ for the horizontal resolution. We found a greater dilution of the overflow as the number of vertical level was increased, the vein of current becoming warmer, saltier and shallower, the worse solution being the one with 300 vertical levels. Thanks to the point-wise definition of the center of the vein of current we were able to diagnose the vertical diffusivity along the path of the overflow. Our results show that, as expected in a z-coordinate hydrostatic model like NEMO, the sinking of the dense overflow waters is driven by the enhanced vertical diffusion scheme (EVD) that parametrizes the vertical mixing in case of a static instability in the water column. But our analysis showed that the EVD scheme is propagating the dense water preferentially along the grid slope and not necessarily along the topographic slope. Since the grid-slope reduces as the number of vertical levels increases, the overflow is more diluted when a large number of levels is used. The EVD parameterization may be adequate for bottom flows only when the vertical resolution is coarse.

We then tested the effect of increasing the horizontal resolution by a factor of 5, reaching $1/60^\circ$ (in the area where the local horizontal grid refinement was implemented using AGRIF). The $1/60^\circ$ resolution generally provides a significant improvement of the overflow (compared to the $1/12^\circ$), especially in the fine grid region, but a similar degradation was found when increasing the number of levels from 46 to 75. Finally, we observed that when increasing to 300 levels at $1/60^\circ$, the whole overflow representation changes, leading to drastic improvements. At such horizontal and vertical resolution the EVD convective adjustment associated with the step-like representation of the topography remains limited to a relatively thin bottom layer representing a minor portion of the vein. The major additional player that contributes to the sinking of the overflow is the resolved vertical shear that results from the resolution of the dynamics of the Ekman boundary layer. This allows a proper calculation of the entrainment by the TKE scheme and an improvement of the properties of the overflow waters. The computational cost associated with such a high resolution is still prohibitive for most of the applications in z-coordinates. In addition, our simulations pointed out several parametrization issues regarding the behaviour of the AGRIF refinement with such a large number of vertical levels (300).

One additional interesting conclusion of this work is that for most of the cases tested the EVD convective adjustment was the main parameter that controls the physics of the overflow, becoming the dominant player of the vertical mixing scheme. Indeed, the importance of many other tuning or numerical parameters were tested (advection scheme, lateral friction, BBL parameterization, etc.) but none had a significant impact on the overflow representation.

All in all, the best results are achieved with the implementation of AGRIF reaching $1/60^\circ$ with 300 vertical levels. With this dramatic increase in horizontal and vertical resolution, the highest to our knowledge in this type of study, we were able to at least partly resolve the bottom boundary layer dynamics, reaching results comparable with those in observations. Some discrepancies remained between the model and the observations, being possibly attributed to the bias in the initial conditions (the ambient waters being too warm and salty at the beginning of the simulations).

For a given vertical number of levels the cost of the implementation of AGRIF in this regional configuration case was around 70 times the original cost. Even if this implementation was effective and considering that smaller proportional costs are expected in configurations of larger domains, this appears as a very costly option. We therefore concluded that a more suitable solution should be searched. In the Part IV of this work we investigate the representation of the DSO in the terrain following s-coordinate context.

Part IV
s-coordinates

Chapter 8

From sigma to enveloping s-coordinates

This terrain following coordinate was briefly presented in section 2.2. Since its first presentation for meteorological modeling by Phillips, 1957, this type of coordinate has greatly evolved. As mentioned, it evolved from the uniformly distributed σ -coordinate ($\sigma = z/h$) to the function dependent distributed s-coordinate. Another degree of complexity was included by forcing the coordinate to follow an enveloping (smoothed) version of the original topography instead of the real one. In this case Dukhovskoy et al., 2009 adopted the name of Vanishing Quasi-Sigma coordinates (VQS). In this chapter we describe the particularities and the pressure gradient errors associated with this type of coordinate.

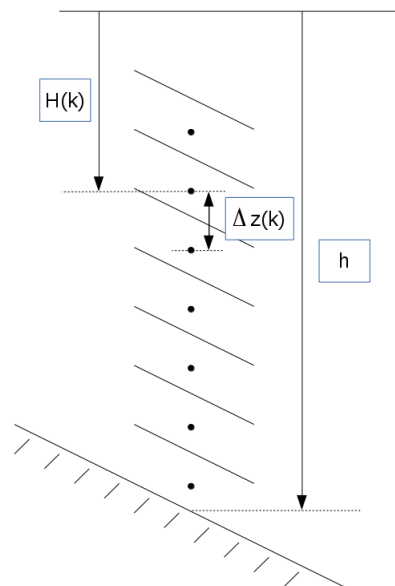


Figure 8.1: Scheme of the terrain following coordinate for a given depth (h). The depth of a given vertical point is $H(k)$ and the cell thickness associated to this point is $\Delta z(k)$. The superior line represents the surface.

8.1 Stretching

In order to minimize the coordinate slope to avoid computational errors and/or tailor the coordinate for a specific application, we can set the distribution of the vertical levels according

to a specific function. Different stretching functions have been developed for this end. For example, NEMO v3.6 includes three different standard options. In general, a stretching is defined by a stretching function $C(k)$ (when expressed as function of the model levels) or $C(s)$ (when expressed as function of $s(k)$) which varies between 0 and 1 and a depth distribution function $H(k)$ or $H(s)$ which is the results of multiplying this stretching function by the local depth. $s(k)$ is the homogeneous sigma distribution in this case and adopt the following form

$$s(k) = -\frac{k}{N} \quad (8.1)$$

where k is a given level and N is the total number of levels. Finally the cell thickness Δz is given by the difference of the depth distribution

$$\Delta z = H(k+1) - H(k) \quad (8.2)$$

All these characteristics are schematized in figure 8.1. In this way we can think the process of building a specific terrain following vertical grid as a succession of steps:

- Choose a number of vertical levels (N)
- Define the main varying parameter, $s(k)$ or k
- Define the stretching function that defines the dimensionless distance between two consecutive s levels: $C(s)$ or $C(k)$
- Set the depth distribution and the cell thickness as $H(k) = C(s(k))h$ (with h the local depth) and $\Delta z = H(k+1) - H(k)$

Hiperbolic tangent stretching

The scheme proposed by Madec et al., 1996 is the default option in NEMO v3.6 and uses an hiperbolic tangent function for the stretching

$$C(s) = \frac{\tanh(\theta(s+b)) - \tanh(\theta b)}{2 \sinh(\theta b)} \quad (8.3)$$

where θ and b are parameters to control the stretching. Then, the depth distribution is expressed as

$$H(s) = C(s)(h_{env} - h_{min}) + h_{min}s(k) \quad (8.4)$$

where h_{min} is the depth at which the s -coordinate stretching starts and allows a z -coordinate to be placed on top of the stretched coordinate, h_{env} receives the name of enveloping bathymetry (and for the moment equals the real model bathymetry), and H is the depth (negative down from the sea surface) for a given s .

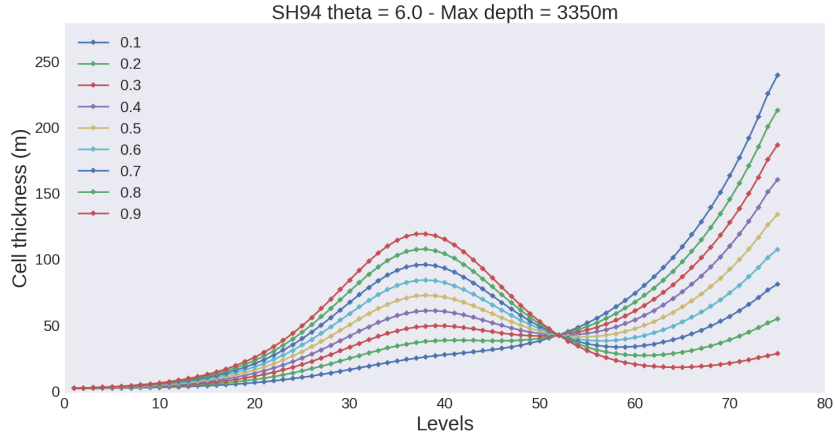
SH94 stretching

The classic SH94 stretching Song and Haidvogel, 1994

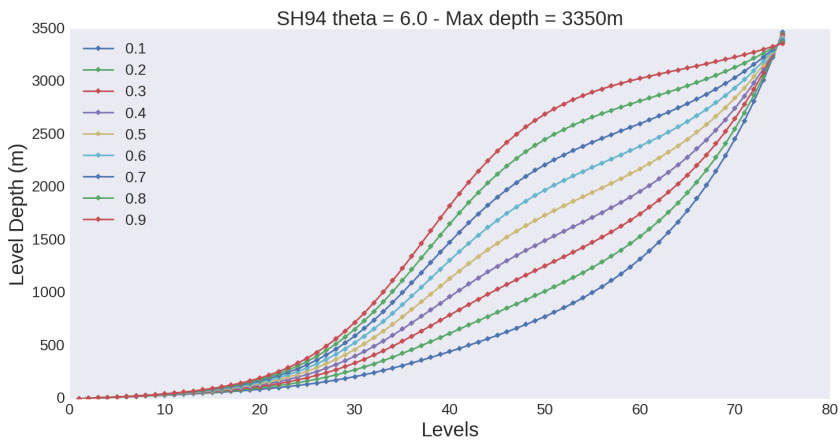
$$C(s) = (1-b) \frac{\sinh(\theta s)}{\sinh(\theta)} + b \frac{\tanh[\theta(s+1/2)] - \tanh(\theta/2)}{2 \tanh(\theta/2)} \quad (8.5)$$

where θ and b are the surface and bottom control parameters such that $0 \leq \theta \leq 20$, and $0 \leq b \leq 1$. b allows surface and/or bottom increase of the vertical resolution. Then, the distribution of s levels with depth is expressed as

$$H(s) = C(s)(h - h_{cr}) + h_{cr}s \quad (8.6)$$



(a)



(b)

Figure 8.2: *SH94 Stretching as a function of 75 vertical levels and 3350m maximum depth (approximate maximum depth in the DENST12 configuration), $\theta = 6.0$ and different values of b (ranging from 0.1 to 0.9) a) Cell thickness b) Level depth*

where h_{cr} is the depth at which the coordinate transitions from pure σ to the stretched coordinate. This is particularly useful for very shallow areas where the stretching can cause very small cell thicknesses.

The use of this general stretching function is limited by two constraints. First the surface resolution (governed by θ), and the bottom resolution (governed by b). A surface resolution of the order of 1 to 3 meters is needed at the surface, and therefore the value of theta can not be significantly changed. After several tests in the values of θ we arrived to the conclusion that not many values can be set for this parameter if a cell thickness of 1m is expected at the first level. In addition, the standard value use in (Song and Haidvogel, 1994) is $\theta = 6$, and therefore is the one used for our problem. In figure 8.2a we observe the distribution of the cell thickness as a function of the vertical levels for $\theta = 6$ and different values of b ranging from 0.1 to 0.9 for a depth of 3350m (maximum depth of our configuration). As observed, for low b values we obtain a regular increase of the level thickness with depth (figure 8.2a). When b increases, resolution decreases at mid depth and increases at the bottom. We also see the smooth character of this stretching in the depth distribution shown in figure 8.2b. A correct representation of overflows demands the best resolution possible at the bottom, which according to figure 8.2a is obtained with $b = 0.7$ or grater (values smaller than 0.7 locates the coarsest cell thickness at the bottom). A second constraint of this stretching is that the vertical resolution is higher between middle

depths and the bottom (around level 60) for values of b between 0.7 and 0.95, which is not needed in our problem. One would prefer to have higher resolution right at the bottom, but values of b greater than 0.95 generates big slopes in the grid. We therefore observe that this generic function ends up with very limited options for our particular case. This stretching does not appear as the ideal stretching for the modeling of overflows, and a specific stretching should be investigated.

SF12 stretching

Siddorn and Furner, 2013 proposed an stretching function and claimed to obtain fewer spurious currents related to pressure gradient errors. Its implementation is less straight-forward than SH94. We have found values of their coefficients to provide negative values of cell thicknesses. We were not able to corroborate any advantage regarding the diagnostic of pressure gradient errors in comparison with SH94. Therefore, we did not use this stretching for our realistic test cases and we do not provide here an extensive description of this stretching. As in Song and Haidvogel, 1994, this stretching also considers a critical depth H_{cr} for shallow waters' stretching.

JC17 stretching

We describe here the stretching proposed by Jérôme Chanût (personal communication, JC17 from now on), who very kindly provided his script. This stretching is essentially an hyperbolic tangent distribution given by,

$$C_b(k) = \frac{\tanh(\gamma_b C_s(k))}{\tanh(\gamma_b)}; \gamma_b = 1.4 \quad (8.7)$$

where C_s is function considering the depths of a reference z-coordinate,

$$C_s(k) = -\frac{h_z(k)}{h_{zMax}} \quad (8.8)$$

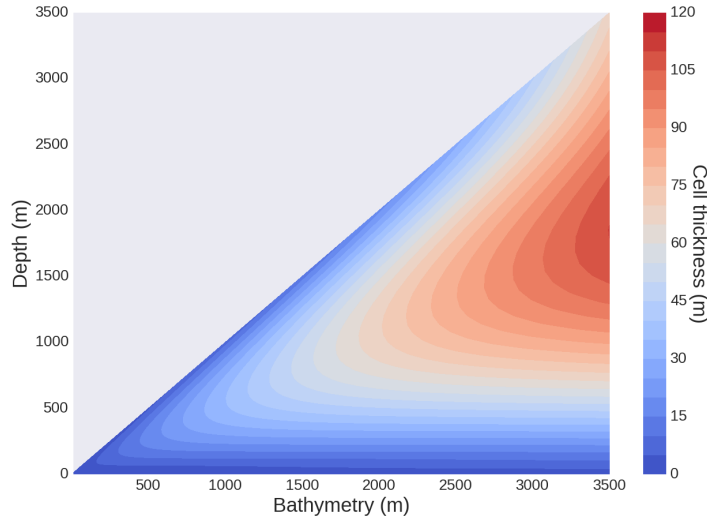


Figure 8.3: *Cell thickness as a function of levels with 75 vertical levels and 3350m maximum depth (approximate maximum depth in the DENST12 configuration) JC17 stretching*

Then a smooth way to transition from the stretched coordinate to a sigma-coordinate in shallow regions (depths smaller than h_c) is included

$$C'(k) = -\frac{h_{cr}C_b(k) - h_{env}s(k)}{h_{cr} + h_{env}}; h_{cr} = 50m \quad (8.9)$$

Before calculating the final stretching function we define a weight function (that varies between 0 and 1),

$$f\left(\frac{h_{env}}{h_{zMax}}\right) = \frac{1}{2}\left(1 - \cos\left(\frac{h_{env}}{h_{zMax}}\alpha\pi\right)\right); \alpha = 2 \quad (8.10)$$

Then, the final stretching function is a weighted function of the z-reference distribution C_s and the preliminary stretching function C'

$$C(k) = f\left(\frac{h_{env}}{h_{zMax}}\right)C_s(k) + \left(1 - f\left(\frac{h_{env}}{h_{zMax}}\right)\right)C'(k) \quad (8.11)$$

where h_{env} is the enveloping bathymetry and h_{zMax} is the maximum model domain depth. The depth distribution of levels associated is

$$H(k) = -C(k)h_{env} \quad (8.12)$$

Is important to note that C_s is defined with depths that comes from a referenced z-coordinate. When h_{env} approaches to h_{zMax} the distribution of the sigma levels tends to distribute in the same way as the reference z-coordinate level. This can be specially useful for an hybrid terrain coordinate including terrain-following and z coordinates.

The general shape of this stretching is shown in figure 8.3. We observe that in the whole range of depths this stretching privileges thin s cells at the surface and the bottom and leaves the mid-depth less resolved, which is a good strategy to simulate overflows. We will see later how the pressure gradient errors reacts to this stretching.

Further remarks

Finally, we would like to mention that other hybrid vertical coordinates has also been developed. We cite for example Shapiro et al., 2013 in which an enveloping s-coordinate above a z-coordinate was implemented.

8.2 Pressure gradient errors

The horizontal pressure force in generalized terrain following coordinates consists of two terms,

$$\nabla_z p = \nabla_\sigma p + \rho g \nabla_\sigma z \quad (8.13)$$

Where $\nabla_z p$ is the horizontal pressure gradient (along geopotential surfaces), $\nabla_\sigma p$ is the pressure gradient along constant σ surfaces, ρ is the density, g the gravity and $\nabla_\sigma z$ is the slope of the σ surface relative to z-surfaces. In other words, the pressure gradient that we want to calculate consists in the traditional pressure gradient calculation performed in z-coordinates minus a correction term. This correction term can be as large as the main term, and both are much greater than the difference, such that small errors in the calculation of any of these terms may result in errors of the final pressure gradient. We can observe a large number of parameters affecting the calculation of $\nabla_z p$: the way $\nabla_\sigma p$ is calculated; the slope ($\nabla_\sigma z$), which can get very large, specially near continental shelves; the stretching, which defines the relative slopes of coordinate points (and might lead to greater slopes than the bathymetric ones); the stratification and its calculation manner (equation of state); the finite difference scheme used in this calculation (two options in NEMO v3.6: the usual leap-frog scheme and a semi-implicit scheme); and of course the resolution plays its role as in every truncated calculation.

While the source of this error is clear for all authors, the estimation is a different story. Different parameters have been suggested to estimate the magnitude of pressure gradient errors (PGE) in sigma models.

Coefficients

Among all these sources of possible errors, those related to the grid slope and bathymetry slope can be minimized by acting on the stretching and on the smoothing of the enveloping topography. To provide a guideline regarding this problematic, a variety of dimensionless coefficients have been proposed. From empirical studies these coefficients provide threshold values beyond which PGE could have a significant impact on the solution. The grid geometry should therefore be such that the value of these coefficients do not go beyond those limits.

Haney, 1991 presented the PGE problem as a violation to the “hydrostatic consistency” (R) (henceforth Haney coefficient)

$$R = \frac{\sigma \partial_x H}{H \partial \sigma}; |R| < 1 \quad (8.14)$$

where σ is the sigma coordinate of a numeric cell, H its depth below sea surface, $\partial_x H$ the horizontal change in depth of adjacent grid cells, and $\partial \sigma$ the vertical grid size in sigma coordinates (in pure sigma coordinates the vertical space is evenly distributed). Mellor et al., 1994 and Mellor et al., 1998 questioned the utility of the hydrostatic consistency and proposed an analytical formulation of the PGE. In Mellor et al., 1998 they also differentiate Sigma Errors of the First and Second Kinds (SEFK and SESK, respectively). Beckmann and Haidvogel, 1993 evaluated the local truncation error and found it to be function of a so called “slope parameter” (among other parameters already mentioned)

$$rx_0 = \frac{|\Delta h|}{|2\bar{h}|} = \frac{|h_i - h_{i-1}|}{|h_i + h_{i-1}|} \quad (8.15)$$

Where h_i is the depth of each grid point (the actual definition present in Beckmann and Haidvogel, 1993 does not consider absolute values). The Haney coefficient can be written as follows Sikirić et al., 2009

$$rx_1 = \frac{|h_{i,k} - h_{i+1,k} + h_{i,k-1} - h_{i+1,k-1}|}{|h_{i,k} + h_{i+1,k} - h_{i,k-1} - h_{i+1,k-1}|} \quad (8.16)$$

If the vertical discretisation is uniform $z(i, k) = h(i)s(k)$ then rx_1 can be expressed as a function of the slope parameter

$$rx_1 = rx_0 \frac{s(k-1) + s(k)}{s(k-1) - s(k)} \quad (8.17)$$

giving in this case a dependence of rx_1 to the slope parameter and the stretching. Both rx_0 and rx_1 can be extended to the tridimensional grid. The approach followed in this work is based on the VQS mentioned before. The conclusions derived in the bibliography from these metrics parameters are not directly applicable to the VQS grid since the rationale to arrive to their expressions is different (Dukhovskoy et al., 2009). However, the slope parameter and the Haney coefficient will be considered as guides in order to set the enveloping bathymetry, evaluate the resulting grid and give an interpretation to the results of a series of idealized tests (performed in the realistic configuration). Just as a reference, in Sikirić et al., 2009 they recommend values of $rx_1 < 3$, and indicates that most of the ROMS simulations are done with $rx_0 < 0.2$ and $rx_1 < 6$. As we will see this values are hard to obtain without smoothing the bathymetry.

8.3 The enveloping bathymetry or VQS

One possible strategy to reduce the PGE is to switch from s-coordinates to z-coordinates in places where the value of this errors can be large. The concept introduced by Dukhovskoy et al., 2009 consists in masking sigma levels when a specific metric (for example the topographic slope, or the Haney coefficient) exceeds a specific value. In those specific places the s-coordinate becomes a z-coordinate, hence the name of Vanishing Quasi Sigma (VQS). The VQS therefore allows the use of a pure s-coordinate in all places where the condition is met, and where the PGE are likely to be large a z-coordinate is set in place. By doing so, there is no need of smoothing the topography and therefore the realistic bathymetric features are conserved.

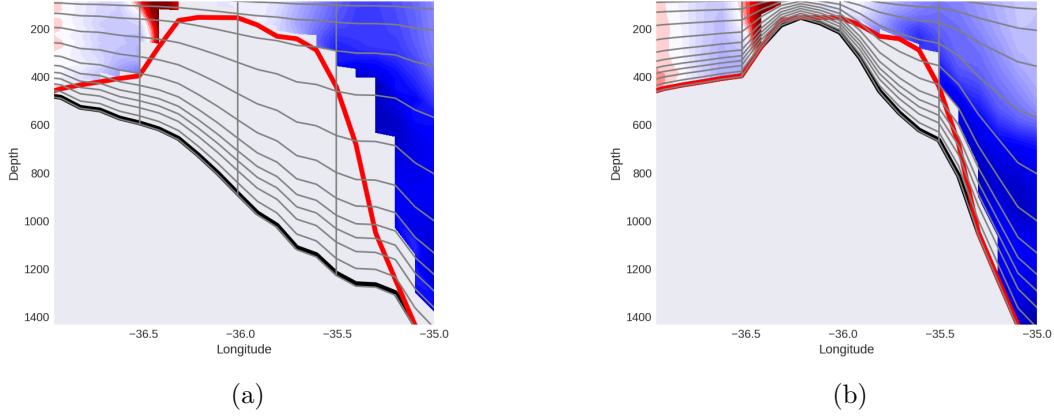


Figure 8.4: *Detail of the resulting masking in an example section. In colors the normal velocity. The red thick line represents the real bathymetry and the black thick line represents the enveloping bathymetry. In order to improve the visibility of the plot not all the vertical and horizontal grid points are plotted a) $rx_{0M} = 0.05$ case b) $rx_{0M} = 0.2$ case*

In practice, the construction of the grid is done with two bathymetries. First, a bathymetry called "enveloping bathymetry" is defined as a smooth version of the original bathymetry. Once the enveloping bathymetry is generated, a mask is set in all places where the condition defined by a specific metric was not met, this is, between the real bathymetry and the enveloping one. To illustrate this we show in figure 8.4 two examples of the grid. NEMO v3.6 uses the slope parameter as the metric to set the enveloping bathymetry, and in one case (figure 8.4a) we set a threshold value of $rx_0 \leq 0.05$. In other words the maximum value of rx_0 in the resulting grid is 0.05 ($rx_{0M} = 0.05$). For clarity only a few lines of the grid are shown, but we can see how the grid follows the smoothed version of the real bathymetry (the enveloping one) and how the grid intersects the real bathymetry. The masking happens to be very sensitive to this value. To contrast this, we show in figure 8.4b the same section, but in this case the enveloping bathymetry was built complying with a slope parameter close to the maximum acceptable value $rx_{0M} = 0.2$.

One problem of smoothing with respect to the maximum of rx_0 (rx_{0M}) is that the PGE error is concentrated at the points where these factors are maximal. There can be many such points and the total effect of the PGE can be significant despite of rx_0 being low. A possibility to be explored is the minimization of the sum of rx_0 or the total PGE for a given analytical T/S profile. Unfortunately, such minimization problems are non-linear and there is no general method for solving them exactly and efficiently. Consequently, we have to settle for approximate solutions Sikirić et al., 2009.

8.3.1 Smoothing and saw-tooth issue

The smoothing process present in NEMO v3.6 is quite basic. The enveloping bathymetry is set by an iterative process. First it is checked if the condition of rx_0 is met at a given point of the enveloping bathymetry. If this is the case the enveloping bathymetry equals the real one. In the case this requirement is not met, the enveloping bathymetry is calculated as

$$h_{env} = \frac{1 - rx_{0max}}{1 + rx_{0max}} h_{bathy} \quad (8.18)$$

in the possible four directions around a given point. Once these four calculations are done, the value of the enveloping bathymetry is set as the deepest point between these four and the initial value of the enveloping bathymetry for the point in question. Doing so, we guarantee that the enveloping bathymetry will be always deeper or at the same depth than the real bathymetry.

The new value in the enveloping bathymetry for a given point influences what was calculated for the previous surrounding point points. Then, the iterative process run again until the condition is met at every point. Once this process is finished the stretching is applied and the masking is set by comparing the depth of the grid points to the real bathymetry. In those points where the enveloping bathymetry equals the real one (not modified by the smoothing), no mask is applied.

One issue with this type of masking is that the masking is applied using the s-coordinate levels. This gives in some regions a "saw-tooth" like masking which is not necessary equivalent to a z-coordinate. Further development of the smoothing and the grid construction is needed to avoid this type of problems.

8.4 Estimation of PGE driven spurious currents

Given the considerations above, we now try to estimate the order of magnitude of the PGE. The normal procedure for this case is to set a neutral stratification with no additional source of movement than the Coriolis force that balance the effect of the pressure gradient and observe the spurious currents generated as the time pass by (Barnier et al., 2006, Shapiro et al., 2013, Siddorn and Furner, 2013). There are two main limitations associated with this test. First, the stratification which directly influences the PGE is not particularly relevant to the overflow problem adressed in this work. As seen, a strong stratification is found near the slopes. Second, once a perturbation is generated the evolution of the currents is not purely associated with the PGE. However, the intention here is only to have an idea of the order of magnitude and the spatial pattern of the spurious currents and how the different parameters chosen affect the PGE magnitude.

8.4.1 Stratification and setup

The stratification was chosen following Siddorn and Furner, 2013 and can be observed in figure 8.5. The temperature profile is given by

$$T_z = 5(1 - \tanh(\frac{z - 120}{20})) + 10(\frac{5500 - z}{5500}) \quad (8.19)$$

and the salinity is chosen to be uniform and constant (35). This gives a mixed layer of around 120m and similar Burger numbers to the seamount test case of Beckmann and Haidvogel, 1993.

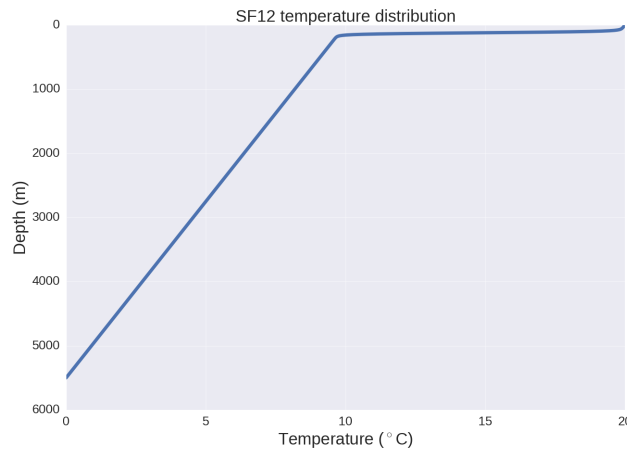


Figure 8.5: *Stratification used for the PGE test case, from Siddorn and Furner, 2013*

Regarding the numerical setup used for these tests, it is the normal DENST12 setup for our experiments with the following particularities. 75 vertical levels in $1/12^\circ$. No external forcing is

applied; the boundaries are set to be equal to the initial conditions (volume conservation is false in order to not affect the final solution); the advection scheme chosen for momentum is the UBS scheme (this scheme is coded with an horizontal bilaplacian explicit viscosity included); tracers are advected with the TVD scheme; sea-ice and run-offs are not included; the bottom friction is non-linear and the same value is kept for $C_D = 1 \times 10^{-3}$. No explicit horizontal or vertical diffusion is applied (the TKE vertical mixing scheme is not used). In the vertical the viscosity is chosen to be constant and different values are tested. Any velocities present in the simulation will therefore be linked with the PGE. In all the cases the EVD was activated because the codes explicitly needs to solve vertical instabilities in the absence of a specific scheme. In this case the EVD value was set equal to the background one (for each case in particular).

8.4.2 Sensitivity experiments for parameter selection

We first performed a series of sensitivity tests regarding the vertical physics in order to study the compatibility of our standard setup with this experiment. For this case we have chosen $rx_{0M} = 0.05$. Since we expect motions of small amplitude we want to know which order of magnitude of the background vertical viscosity will efficiently damp these motions. Different values are therefore tested: $0m^2s^{-1}$, $1.2 \times 10e - 4m^2s^{-1}$ (molecular), $1.2 \times 10e - 3m^2s^{-1}$, $1.2 \times 10e - 4m^2s^{-1}$ with $EVD = 10m^2s^{-1}$. We have also run the same experiment with the vector formulation of the momentum advection in order to see if our results resemble to the one present in Siddorn and Furner, 2013.

In order to diagnose the overall response we proceed as in (Siddorn and Furner, 2013) and we show the maximum and the mean velocity for the whole domain.

Initial response (first 120 hours)

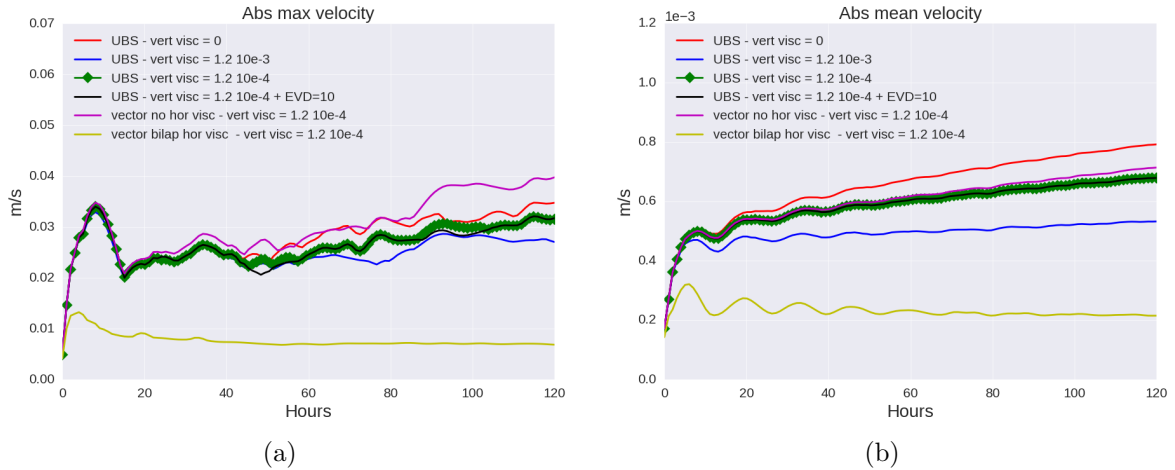


Figure 8.6: *Initial response of the series of sensitivity tests using the DENST12 configuration and $rx_{0M} = 0.05$. Hourly mean values of the first 5 days a) Maximum of the absolute zonal velocity in the domain b) Mean of the absolute zonal velocity in the domain*

In figure 8.6 we observe the maximal and the mean value of the currents present in the domain for the first 120 hours. All the runs with UBS and one for the vector formulation were done without explicit viscosity. In figure 8.6a we observe that all the cases present a response for the first 20h that consists in a increase in the value of the currents until a value of around $3.5cm/s$ followed by a rapid decrease to $2cm/s$. Later, they all present comparable behaviors with some differences that grows as time goes by. Besides this difference they all seem to conserve the same order of magnitude in this first period of 120 hours. The only simulation that presented a difference is the one with explicit horizontal diffusivity, in which the initial motions are damped

and reach a final value of less than 1cm/s . In this case the horizontal diffusivity does not depend on the motion (as it is the case for the UBS scheme), damping small amplitude motions. Considering that the biharmonic diffusive operator efficiently damps the small scale and leaves the large scales relatively untouched (Griffies et al., 2000), this results might indicate that these PGE driven currents are of very small scale.

By observing the mean response in figure 8.6b we can see the oscillations likely coming from the first perturbation and we corroborate what was said for the maximal spurious currents, since we guarantee the consideration of a large number of points for this plot.

Long-term response (75 days)

In the long-term response (figure 8.7a) the maximum velocities acquire similar values regarding the vertical diffusivity (UBS simulations). In this way the case with $EVD = 10\text{m}^2\text{s}^{-1}$ offers a similar response to the cases without EVD. One remarkable aspect of the long term response is that the viscosity present in the UBS scheme (which should be very small due to its velocity dependence) present intermediate behaviors between the vector momentum advection formulation with and without viscosity. Still the response in the UBS simulation seems not to offer a completely damped response for this period of 75 days. The role of the horizontal viscosity seems to be predominant for this type of tests when compared with the vertical viscosity.

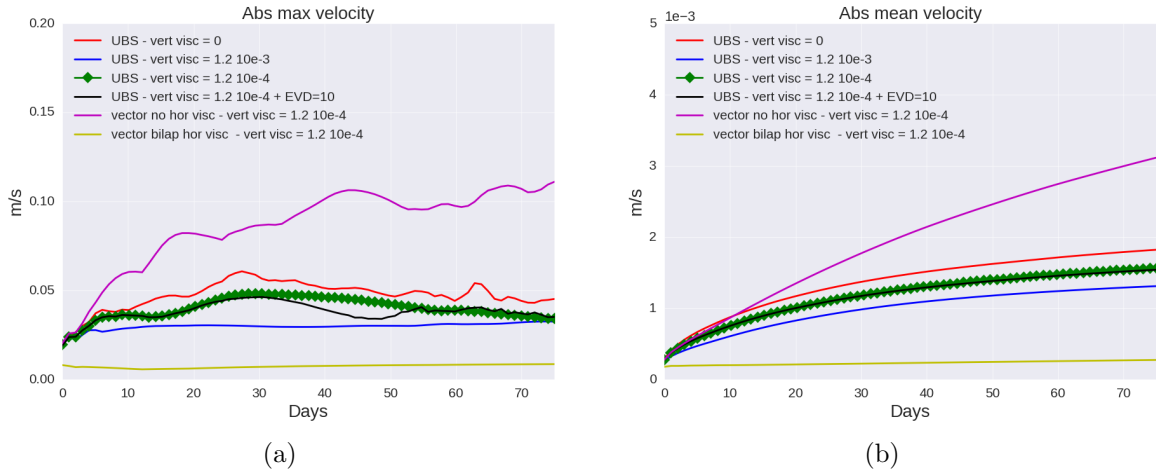


Figure 8.7: Long-term response of the series of sensitivity tests using the DENST12 configuration and $r_{x_{0M}} = 0.05$. Daily mean values a) Absolute maximum zonal velocity in the domain b) Absolute mean zonal velocity in the domain

From the mean response point of view observed in figure 8.7b, all simulations present a coherent response and 75 days seems to be an appropriate amount of time for these tests.

Discussion

The test has shown to be robust for the initial response since it shows low dependence on the vertical viscosity value, either on the momentum advection formulation. It also presents a similar shape for the very initial response when changing the horizontal viscosity. The horizontal viscosity added seems to damp the initial motions effectively but a residual response is observed in the long term. This is probably due to the balance between the geostrophic adjustment of the density field and the spurious velocities (since they persist over an inertial period). In this way it is not clear to us which is the most appropriate value to be considered for the spurious currents, the maximal in the very initial response or the final dumped value. Either the way they are not very different from the order of magnitude point of view. We therefore associate the value of 1cm/s to 4cm/s to the order of the magnitude of the maximum amplitude for the spurious currents present for the case of $r_{x_{0max}} = 0.05$. We also retain that only a very limited

amount of points will get such error (considering the difference in scale between maximum and mean response), and that in average on the basin, spurious currents are $5 \times 10^{-2} \text{ cm/s}$. For the following tests we choose a value of vertical viscosity of $1.2 \times 10^{-4} \text{ m}^2 \text{ s}^{-1}$, since it is a very small value (no further perturbations included) and the final response seems to not depend highly on it at this order of value. The following tests will use the UBS scheme since it is the scheme present in the realistic setups with no horizontal viscosity for the same reason. In order to avoid redundancy only long-term tests will be performed for the following cases.

8.4.3 Masking effect

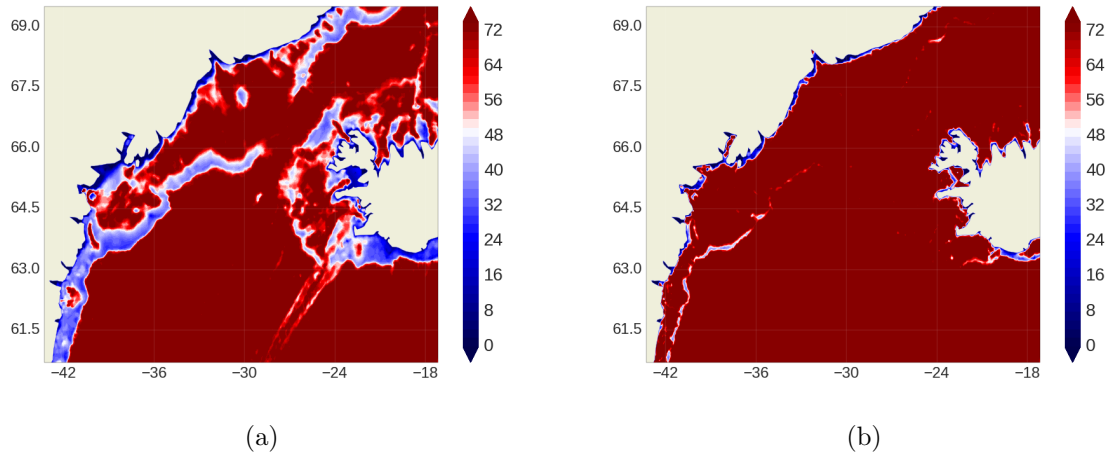


Figure 8.8: Available levels for calculation (*mbathy*) for our 75 vertical level tests a) $rx_{0M} = 0.05$ case b) $rx_{0M} = 0.2$ case

We compare here the results obtained using two different values of rx_0 to set the enveloping bathymetry. The SH94 stretching is used with the UBS momentum advection scheme and a vertical viscosity of $1.2 \times 10^{-4} m^2 s^{-1}$. After a set of tests we identified first a lower bound value for the maximum value of $rx_0 = 0.05$. Below this value the masking starts to be massive, having z-coordinates everywhere and losing the benefits of the s-coordinates. The number of available levels for calculation is shown in figure 8.8. Where 74 levels are available we have a pure s-coordinate (the last level is always masked), everywhere else we have conjunction of z and s-coordinates (s-levels are masked). The upper bound for the maximum value of rx_0 was fixed at $rx_0 = 0.2$. For this value (figure 8.8b) the masking is hardly noticeable (very limited in space), then the s-coordinate is over most of the domain, but the spurious currents generated by the PGE begin to be large.

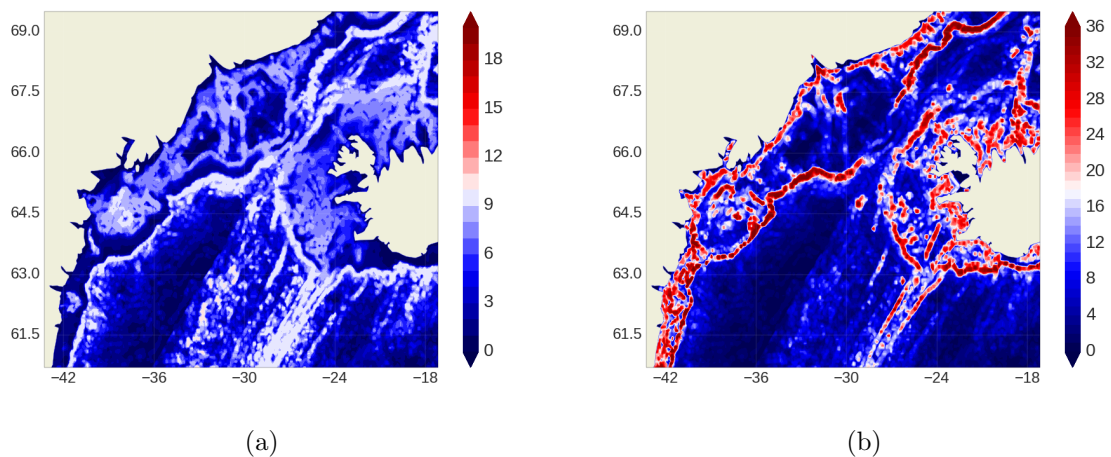


Figure 8.9: Maximum values in the vertical of rx_1 for each point in the grid a) $rx_{0M} = 0.05$ case b) $rx_{0M} = 0.2$ case

Once the grid has been built using the specified maximum value of rx_0 (rx_{0M}), we can calculate the value of rx_1 for each point. There is no specific rules regarding rx_1 , but as it was mentioned before, Sikirić et al., 2009 recommends $rx_1 \leq 6$. In figure 8.9 we observe maximum values of

rx_1 in the vertical for each point in the grid for both rx_{0M} . As we can see the counterpart of the degree of masking applied is the value of rx_1 . For a masking set using $rx_{0M} = 0.05$ we have a maximum value of $rx_1 = 10.08$. For the $rx_{0M} = 0.2$ case we have a maximum value of $rx_1 = 38.91$.

Both in figure 8.8a and 8.9b it can be observed that the most sensitive places are very shallow areas near the coast and continental slopes (particularly through the one where the DSO flows in direction to Cape Farewell).

Long term response (75 days)

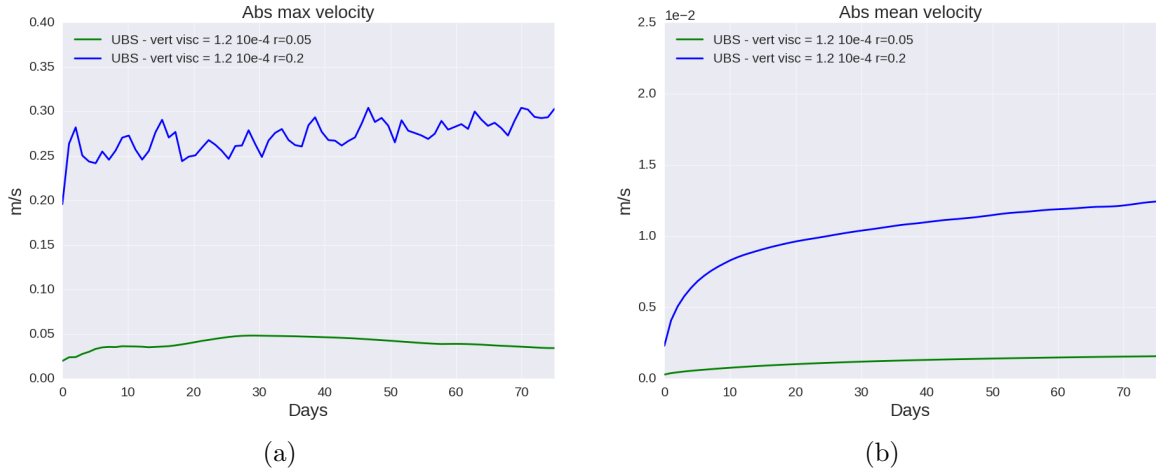


Figure 8.10: Daily mean values for the comparison between enveloping bathymetries built with $rx_{0M} = 0.05$ and $rx_{0M} = 0.2$ a) Maximum of the absolute zonal velocity in the domain b) Mean of the absolute mean zonal velocity in the domain

The increase of rx_1 is also accompanied with an increase of the spurious currents. Regarding the maximum velocities (figure 8.10a) we found values of the order of 25cm/s when the enveloping bathymetry is built with $rx_{0M} = 0.2$ in contrast with the previous one of 3.5cm/s found with $rx_{0M} = 0.05$.

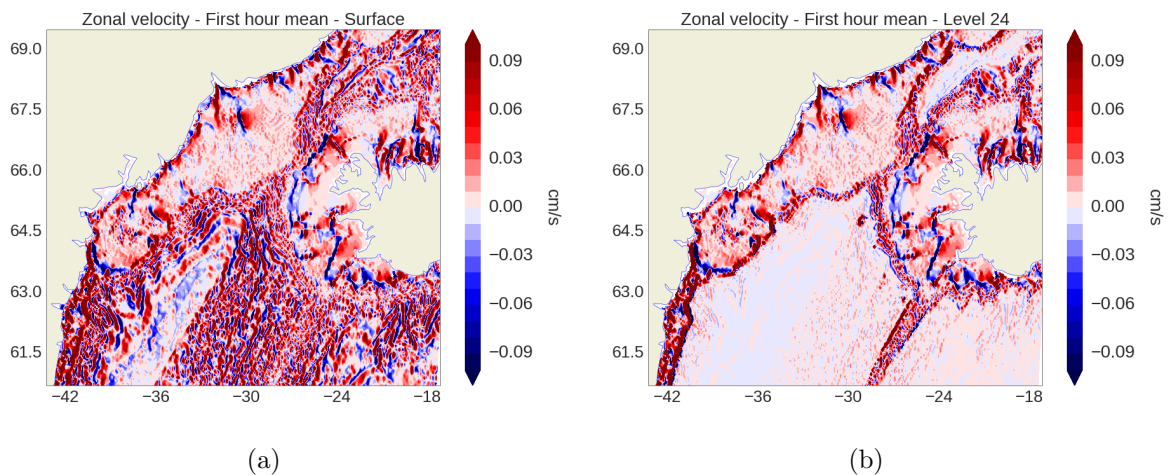


Figure 8.11: First hour mean value of the zonal velocity in cms^{-1} using SH94 stretching and $rx_{0M} = 0.2$ a) At the surface b) At the 24th level

The impact in the mean values (figure 8.10b) is also of the same order. This demonstrated the drastic impact that rx_{0M} has when defining the enveloping bathymetry. To be on the safe side

values close to $rx_{0M} = 0.05$ should be used. On the next chapter we will evaluate the impact of this parameter on a fully realistic setup.

Spatial distribution (1st hour mean)

In order to test the robustness of rx_1 to estimate the spurious currents associated with PGE we show the zonal velocity for the first hour mean at the surface and at level 24th in figure 8.11. The first remarkable aspect is that the velocities at the surface (8.11a) are predominant when compare with a level associated with the mid-depth (8.11b). This is very likely associated to the strong stratification set at the surface to simulate the mixed layer.

The other remarkable aspect is the similarities between the currents at level 24th and the maximum vertical rx_1 values shown in figure 8.9b.

By observing these plots the rx_1 coefficient appears to be very robust to study the locations where the spurious currents are predominant. This can indicate that this coefficient is a more interesting option to set the enveloping bathymetry, instead of rx_0 . The only disadvantage is that it is grid dependent, that means that for each iteration in the smoothing of the real topography we have to set the build the grid to calculate the maximum rx_1 for each grid point.

8.4.4 Stretching effect

We conduct the same test case with $rx_{0M} = 0.2$ and the JC17 stretching. We first observe that this stretching permits more levels of calculation (figure 8.12a), which is equivalent to state that the smoothing needed is less for this stretching. This does not impede to obtain smaller values of rx_1 (figure 8.12b), with a maximum value of $rx_1 = 31.45$, about 20% smaller than with the SH94 stretching.

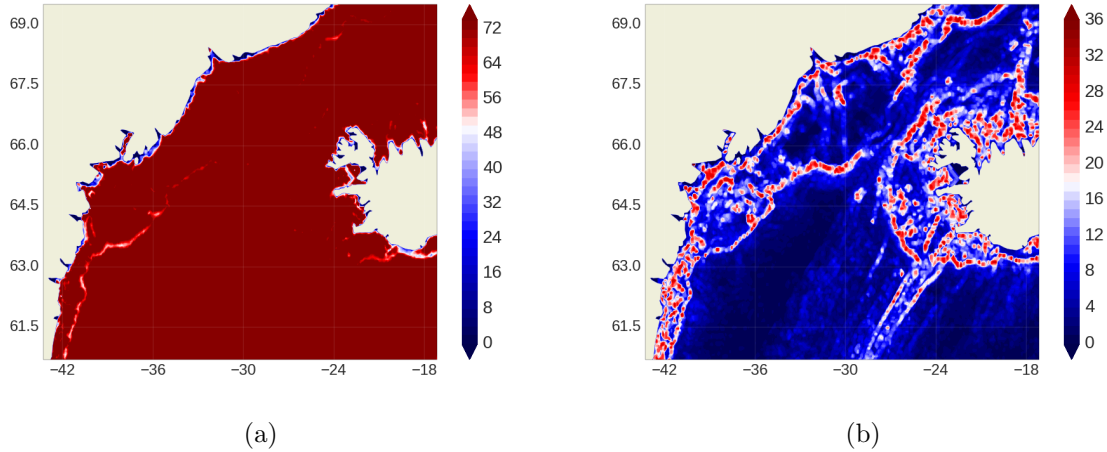


Figure 8.12: *a) Available levels for calculation (mbathy) b) Maximum values in the vertical of rx_1 for each point in the grid. Both for $rx_{0M} = 0.2$ and JC17 stretching*

Long term response (75 days)

In the case of a long-term response analysis the JC17 present higher values of both maximum and mean currents (figure 8.13). At first this would be a contradiction about what was stated before but at the very beginning we can see that the magnitude of the current is smaller for the JC17 case. We therefore study this in a short term period.

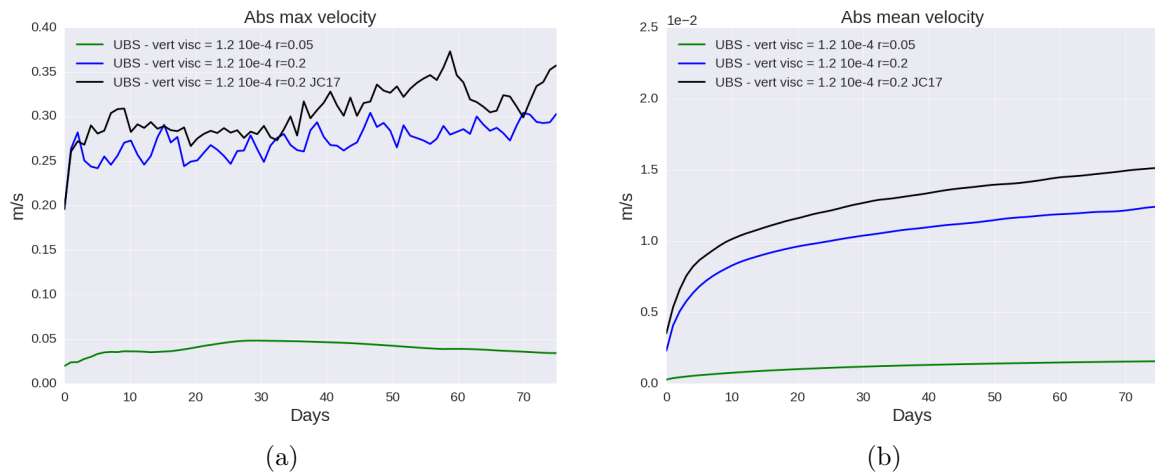


Figure 8.13: *Daily mean values for the comparison between SH94 and JC17 stretchings, enveloping bathymetries built with $rx_{0M} = 0.2$ a) Maximum of the absolute zonal velocity in the domain b) Mean of the absolute zonal velocity in the domain*

Initial response (first 120 hours)

We observe in figure 8.14a that the very first response of the maximum velocities is smaller for the JC17 case. However, the perturbations grows very fast and by the end of this series the magnitude of the currents becomes bigger in the JC17 than in the SH94 case.

Mean values show in figure 8.14b that even at the very beginning the values of the JC17 are bigger and we also observe a higher presence of oscillations. This might mean that there are other processes that gain in importance. Either the way this stretching has shown some benefits when compared with the SH94 stretching and the final convenience on the choice of this stretching will be studied in a fully realistic case.

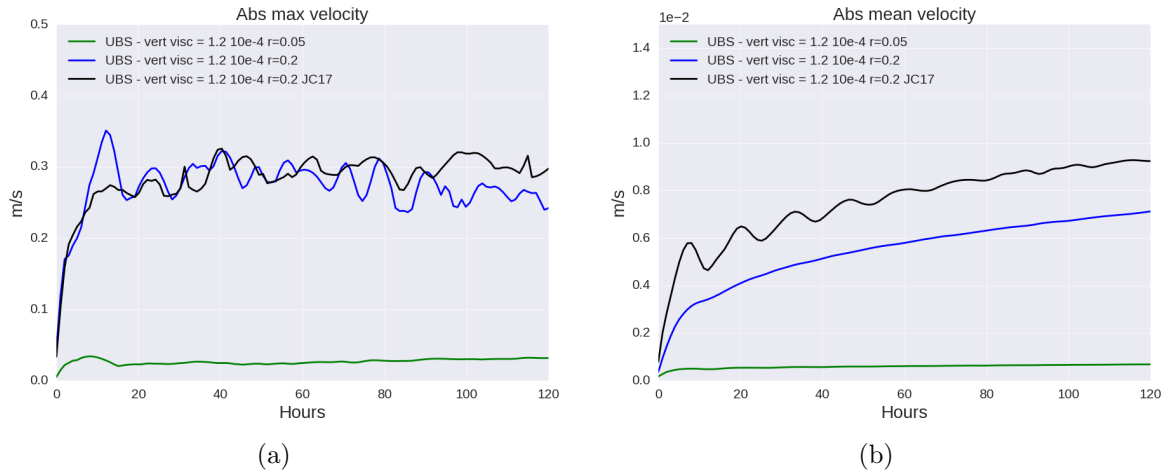


Figure 8.14: Hourly mean values for the comparison between SH94 and JC17 stretchings, enveloping bathymetries built with $rx_{0M} = 0.2$ a) Maximum of the absolute zonal velocity in the domain b) Mean of the zonal velocity in the domain

8.4.5 Horizontal resolution

We would like to mention here some considerations about the use of s-coordinates in a higher horizontal resolution. For this we implemented an AGRIF zoom as it has been done for the z-coordinate case (figure 5.1). For this case we will not present results about the PGE estimation since the increase of horizontal resolution (child grid) is in a coarser resolution context (mother grid) and therefore this estimation would not address directly the question of the impact of resolution in PGE directly. Instead, we compare the values of rx_1 in the zoom region for the mother and child grid in figure 8.15. In this case a $rx_{0M} = 0.2$ was used with the JC17 stretching. We go from the previously observed values of around $rx_1 \approx 38$ to values $5 < rx_1 < 10$. We have to say that bigger values are observed, but these values are due to the presence of the mother grid points at the boundaries.

To make this simulation, the enveloping bathymetries of both mother and child have to match, otherwise the re-interpolation from child to mother grid would not be correct. To do this the different points of the enveloping bathymetry of the child grid, that at the same time correspond to one grid point of the mother grid, have to be at the same depths. This is one reason why the values of rx_1 in figure 8.15b are smaller than in 8.15a. Doing so we can not fully appreciate the benefits of the resolution increase, and in a full $1/60^\circ$ better results should be expected.

PGEs should also be smaller in $1/60^\circ$ apart from the diminution of rx_1 . According to (Beckmann and Haidvogel, 1993), the expression of the error for a flat stratification case (their equation 20b) is an inverse function of the horizontal resolution, among other parameters (rx_0 between them).

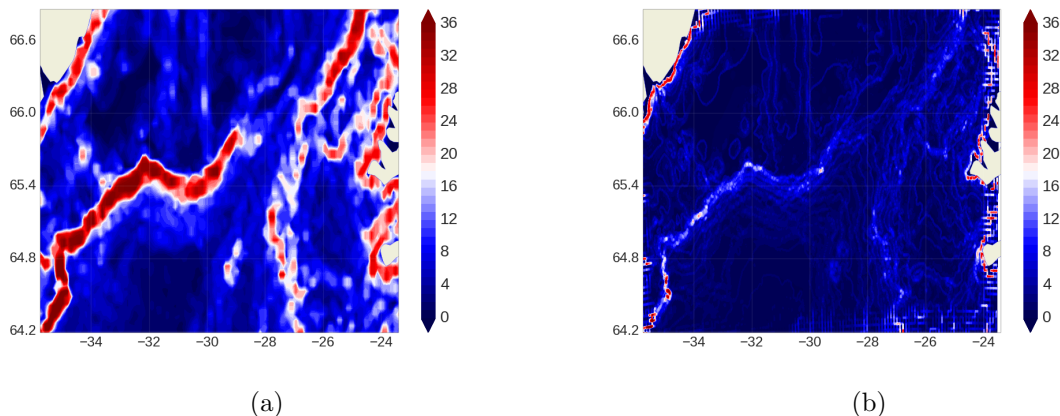


Figure 8.15: *Maximum values in the vertical of rx_1 for each point in the grid in a run with the implementation of AGRIF in s-coordinates. a) Mother grid b) Child grid*

Chapter 9

Realistic configuration results

In the previous sections of this work we explained the different aspects of the implementation of terrain following coordinates in NEMO. We interested ourselves in VQS coordinates type, which is an hybrid z-s coordinate type. We have shown that the different parameters used (the stretching type, the horizontal resolution and the smoothing) had an impact on the spurious currents due to the PGE.

In this section we perform a series of sensitivity tests in the realistic setup to study the impact of these different parameters on the resulting overflow representation. We proceed here in the same way as in z-coordinates. A first set of tests were performed with exactly the same settings as the ones in z-coordinate at $1/12^\circ$ 75L, but using VQS-coordinates for the whole model domain. It is important to keep in mind that the diffusive part of the momentum UBS advection scheme, as it is coded in NEMO v3.6, is of isolevel type. The reference names are shown in table 9.1. In the name of the experiment SE indicates that the horizontal resolution is the standard $1/12^\circ$, SA12 indicates that a local refinement using AGRIF to reach $1/60^\circ$ is used, SH94 or JC17 indicates the stretching type used and Rxx indicates the value of rx_{0M} used to set the enveloping bathymetry.

Table 9.1: *Reference names of the simulations*

Reference name	H. resolution (SE/SA)	Stretching	rx_{0M} (Rxx)
SE12-SH94-R005	$1/12^\circ$	SH94	0.05
SE12-SH94-R01	$1/12^\circ$	SH94	0.10
SE12-SH94-R02	$1/12^\circ$	SH94	0.20
SE12-JC17-R02	$1/12^\circ$	JC17	0.20
SA12-SH94-R02	$1/12^\circ + \text{AGRIF}(1/60^\circ)$	SH94	0.20
SA12-JC17-R02	$1/12^\circ + \text{AGRIF}(1/60^\circ)$	JC17	0.20

By default the filtered version of Cox's original scheme is employed to calculate the slope of the isopycnal diffusion of tracers. The second set of tests use another scheme for this end, the so called "Griffies triads". According to the NEMO book v3.6 "*The solution for s-coordinate passes through the use of different (and better) expression for the constraint on iso-neutral fluxes. Following Griffies, 2003, instead of specifying directly that there is a zero neutral diffusive flux of locally referenced potential density, we stay in the T -S plane and consider the balance between the neutral direction diffusive fluxes of potential temperature and salinity*". The reference names of this second set are shown in table 9.2.

Table 9.2: *Reference names of the simulations with Griffies triads*

Reference name	H. Resolution (SE/SA)	Stretching	rx_{0M} (Rxx)
SE12-SH94-R005-G	1/12°	SH94	0.05
SE12-SH94-R02-G	1/12°	SH94	0.20
SE12-JC17-R02-G	1/12°	JC17	0.20
SA12-SH94-R02-G	1/12°+AGRIF(1/60°)	SH94	0.20

Each of these two sets includes simulations that differ according to the vertical coordinate stretching (SH94 and JC17), the value of the slope parameter rx_{0M} used to build the bathymetry and the horizontal resolution (1/12° and 1/12° plus a local horizontal refinement to reach 1/60°). The detail of the two stretching characteristics is described in section 8.1.

9.1 Enveloping bathymetry

We investigate here the impact on the overflow of the enveloping bathymetry. We compare for that purpose simulations at $1/12^\circ$ 75L, the enveloping bathymetries of which were calculated with different values of rx_{0M} (0.05, 0.10, 0.20). All simulations use the SH94 stretching.

We show the bottom temperature of these 3 simulation in figure 9.1. The simulation that performs the best is the one that uses $rx_{0M} = 0.20$ (figure 9.1c). The temperature along isobaths 1500m and 2000m is colder, as well as in the rest of the basin. The rest of the diagnostics (defined in Chapter 5) support this conclusion and are not shown to avoid redundancy. Even if all these 3 simulations show clear improvements when compared to the reference simulation in z-coordinates ($1/12^\circ$ 46L, figure 6.3d), further considerations need to be done to choose which rx_{0M} value use since this value has an impact on the production of spurious currents associated with PGE. In the following, the reference s-coordinate simulation is the one with $rx_{0M} = 0.2$, corresponding to figure 9.1c.

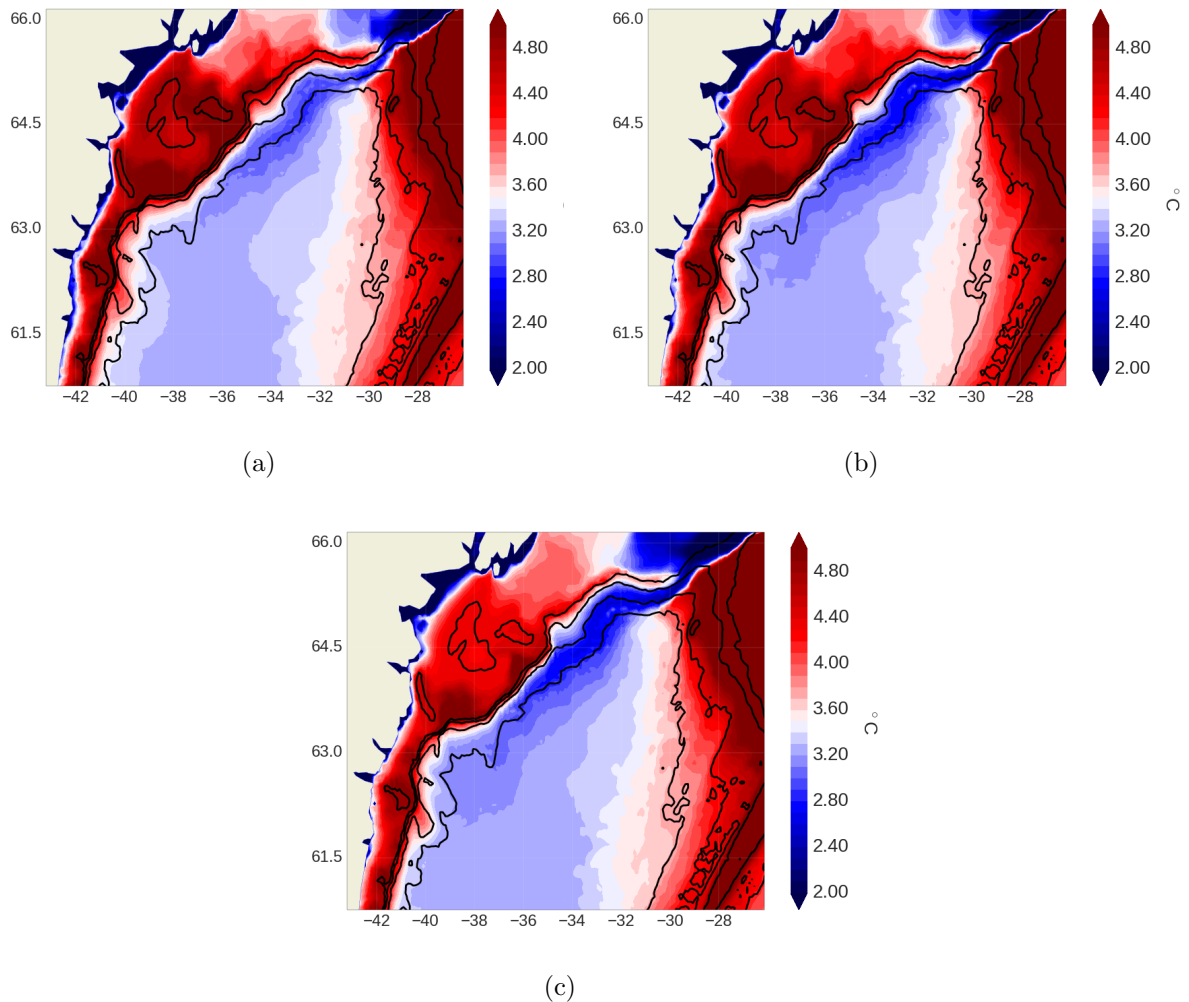


Figure 9.1: Annual mean of the bottom temperature of year 5 at $1/12^\circ$ a) SE12-SH94-R005 b) SE12-SH94-R01 c) SE12-SH94-R02. Isobaths 500m, 1000m, 1500m and 2000m are contoured

Having shown that the use of VQS coordinates produces a significant improvement of the overflow, we investigate in the following the sensitivity of the model solution to different parameters (for example horizontal resolution and stretching).

9.2 Stretching

We investigate here the impact of the stretching used to set the vertical distribution of the s-levels. We compare the model solution for the two types of stretching described in section 8.1: the SH94 and the JC17 stretchings. Both have a refinement of the levels near the surface for a good treatment of the mixed layer, but JC17 also have a refinement of the levels near the bottom. We show here a simulation at $1/12^\circ$ 75L with the enveloping bathymetry obtained with $rx_{0M} = 0.20$.

We show the bottom temperature of the simulation that uses the JC17 stretching in figure 9.2a. When compared to figure 9.1c, it is clear that the JC17 stretching produces colder waters along isobaths 1500m and 2000m, as well as in the rest of the basin. For clarity we show the difference between the JC17 and SH94 solutions in figure 9.2b. The impact near the sill and in the first descent is remarkable, giving around $0.5^\circ C$ colder waters for the JC17 case. The other diagnostics used to describe the overflow also support this conclusion and are not shown.

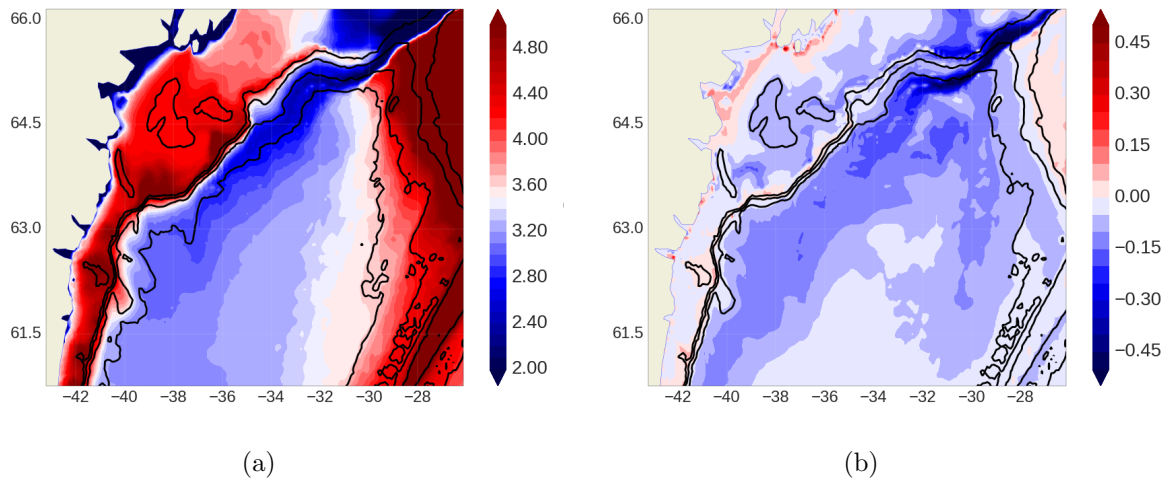


Figure 9.2: Annual mean of the bottom temperature of year 5 at $1/12^\circ$ a) SE12-JC17-R02 b) figure 9.2a minus 9.1c. Isobaths 500m, 1000m, 1500m and 2000m are contoured

9.3 Horizontal resolution

We investigate here the impact of a significant increase of the horizontal resolution in a specific area (from $1/12^\circ$ to $1/60^\circ$). This is investigated for both the SH94 and the JC17 stretchings, using the configuration with the AGRIF local refinement at $1/60^\circ$ (same as in figure 5.1). Enveloping bathymetries are calculated using $rx_{0M} = 0.20$.

The explanation again focus in the mean product of the overflow. We show the annual mean of year 5 of bottom temperature of these 2 simulations in figure 9.3. Bottom waters are considerably colder than the s-coordinate reference for both stretchings.

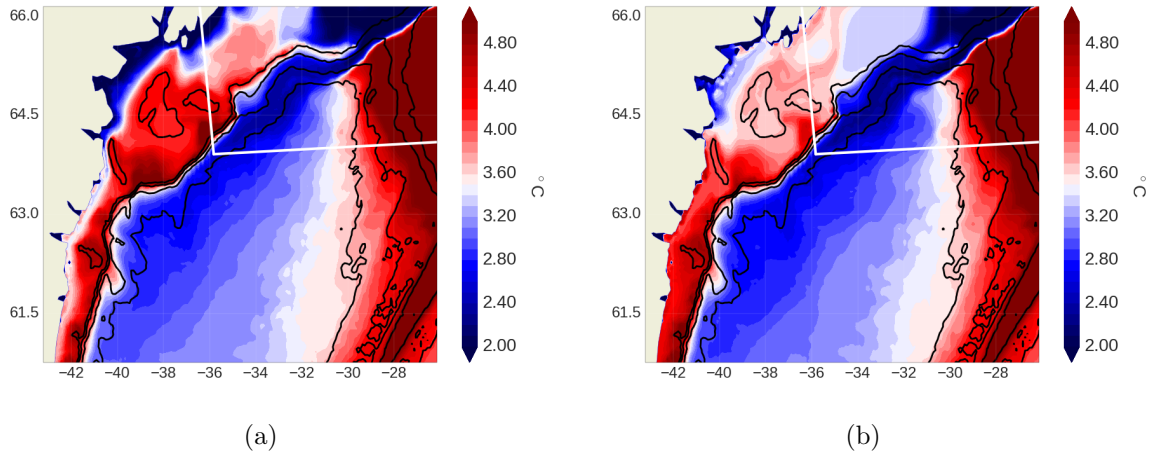


Figure 9.3: Annual mean of the bottom temperature of year 5 at $1/12^\circ$ a) SA12-SH94-R02 b) SA12-JC17-R02. Isobaths 500m, 1000m, 1500m and 2000m are contoured

For clarity we show the difference with the respective solutions at $1/12^\circ$ in figure 9.4. Both cases present some similarities, like the overall $\sim 0.3^\circ C$ colder in the Irminger basin and waters at the sill $\sim 0.5^\circ C$ colder. Warmer waters are found in a few regions in both simulations, like the region to the southeast of the sill on the slope of Iceland, or the very shallow region along the Greenland coast. The other diagnostics (not shown) confirm that the overall response of the overflow is clearly improved with the increase in horizontal resolution.

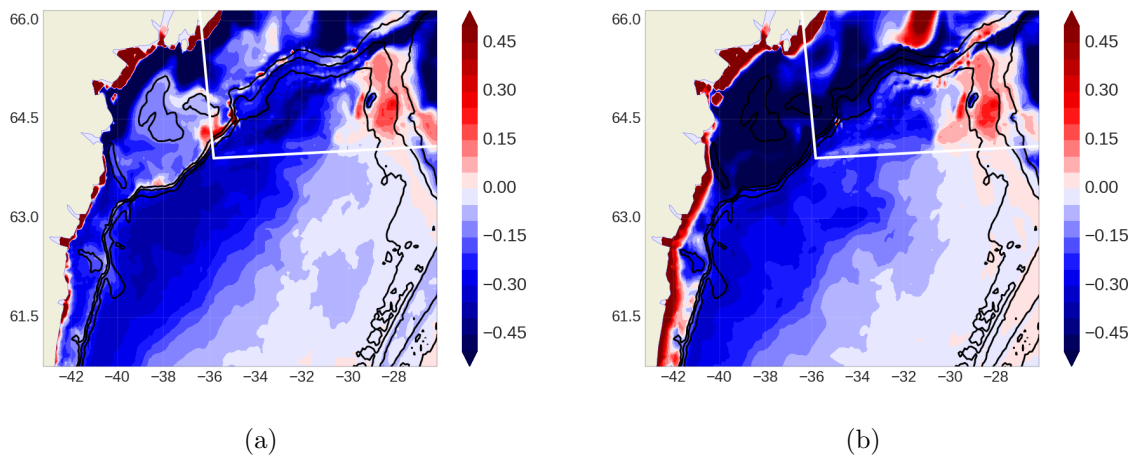


Figure 9.4: Difference of the bottom temperature between solutions a) figure 9.3a minus 9.1c (SH94 stretching) b) figure 9.3b minus 9.2a (JC17 stretching). Isobaths 500m, 1000m, 1500m and 2000m are contoured

9.4 Griffies triads

We investigate here the effect of the parameters explained before (rx_{0M} , stretching, horizontal resolution) but in this case we use the Griffies triads scheme instead of the Cox's original scheme for the isopycnal diffusion of tracers. As explained before, instead of specifying a zero diffusive flux in isoneutral surfaces, the Griffies triads stay in the T-S plane, considering the balances between the isoneutral fluxes of temperature and salinity.

We show the bottom temperature of the simulations presented in Table 9.2 in figure 9.5. All the cases present significant colder bottom temperature than in the s-coordinate reference simulation. The effect of rx_{0M} seems to be less important, with similar bottom temperatures in the cases of $rx_{0M} = 0.05$ and $rx_{0M} = 0.2$ (figures 9.5a and 9.5b). This contrast with the previous result using the Cox's scheme (figures 9.1a and 9.1c), where the impact was much more important.

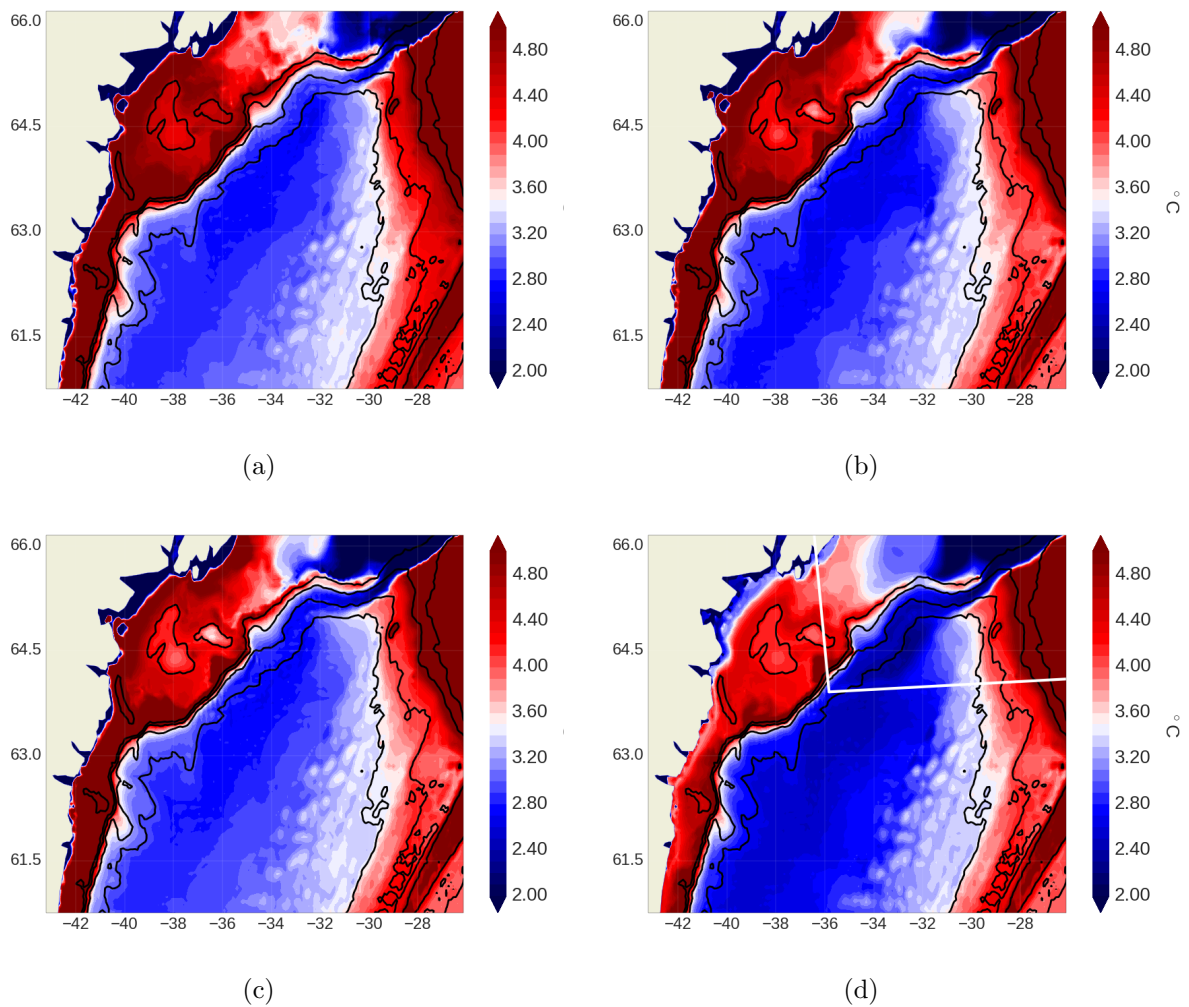


Figure 9.5: Annual mean of the bottom temperature of year 5 at $1/12^\circ$ a) SE12-SH94-R005-G b) SE12-SH94-R02-G c) SE12-JC17-R02-G d) SE12-JC17-R02-G. Isobaths 500m, 1000m, 1500m and 2000m are contoured

Regarding the stretching, the JC17 stretching (figure 9.5c) offers also a very similar solution to the SH94 stretching (figure 9.5a). Regarding the refining of the horizontal resolution, it still offers a considerably colder bottom temperature (9.5d). In this case the difference is not so large, especially because the solution at $1/12^\circ$ (figure 9.5a), already shows a remarkable improvement.

When compared to the solution with the Cox's scheme (figure 9.3a), the difference is not that important as for the cases at $1/12^\circ$, but still the Griffies triads offer a colder bottom temperature when applying the local horizontal refinement.

The small scale features present as white spots in the eastern side of the deep part of the basin are the signature of bathymetric features in the solution. This signature was not present in the previous solutions with the Cox's scheme. We did not find an obvious explanation for this.

9.5 Analysis and understanding

A number of conclusions can be gathered from the results obtained in the simulations analyzed here. The method to calculate the slope for the isopycnal diffusion of tracers exhibits a strong impact on the overall bottom temperature (section 9.4). We found interesting as well to present the results obtained using the default diffusion scheme which is not prepared for this type of vertical coordinate. The effect of the s-coordinates in the representation of the DSO seems to be so important, than even with a non appropriate diffusion of tracers scheme the resulting improvement is drastic. However, the use of this default setting also affects the overall behavior of the simulation and might bring undesirable effects. For example, the Irminger current seems to largely affect the interior of the basin (not shown).

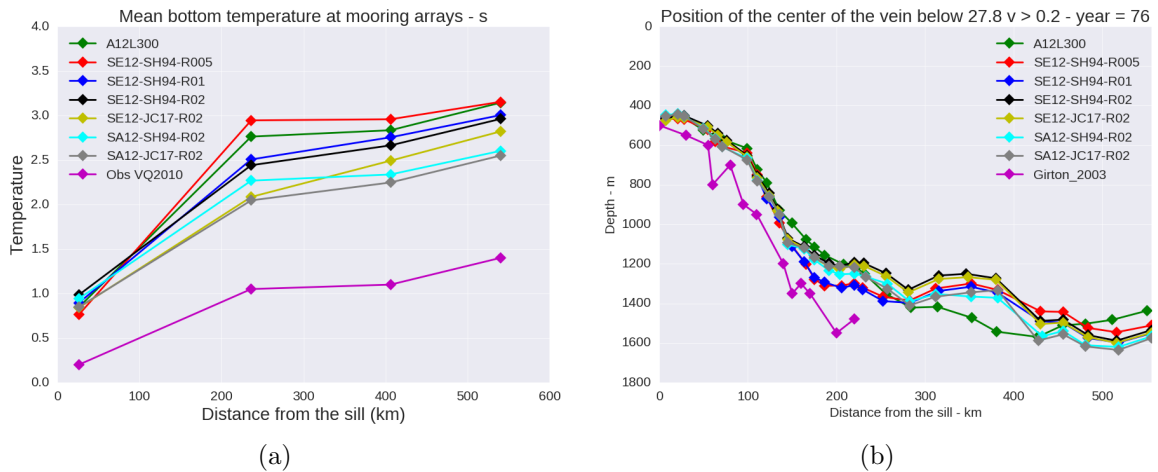


Figure 9.6: *VQS simulations with the default formulation on tracer diffusion a) Minimum mean bottom temperature of the 5th year of calculation of the grid points conforming arrays 1, 15, 22 and 27 (figure 5.3). In pointy magenta line the transport values presented in Voet and Quadfasel, 2010 for the sill, the Dohrn Bank, TTO and Angmassalik arrays. b) Vertical position of the center of the vein. In pointy magenta line the values found by Girton and Sandford, 2003.*

The performance of the s-coordinate simulations presented in this chapter range from similar to considerably better overflow representation than the highest resolution A12L300 simulation in z-coordinates ($1/60^\circ$ 300L). For an easier comparison we included the results of the A12L300 simulation in the mean bottom temperatures calculations in figures 9.6a and 9.7a. From the point of view of this diagnostic the A12L300 performed only better than the SE12-SH94-R005 simulation (without Griffies triads). This is particularly striking if we consider that the added cost of this improved solution was very limited, only of the order of 10%, associated to the change of the pressure gradient formulation, and around 10% for the use of the Griffies triads. This $\sim 20\%$ increase in the cost for the s-coordinates runs contrast to the 7400% (x74 times) of implementing a $1/60^\circ$ 300L in z-coordinates (expected to be proportionally smaller in larger configurations but still extremely high).

Coming back to figures 9.6a (default scheme) and 9.7a (Griffies triads), the effect of larger values of rx_{0M} is the same no matter which formulation for the isopycnal diffusion is used, an overall colder bottom temperature. At the Dohrn Bank array ($\sim 250km$ down the sill) this improvement can be as large as $0.5^\circ C$ when going from $rx_{0M} = 0.05$ to $rx_{0M} = 0.2$ with the default scheme. The impact is smaller for the rest of the arrays, specially when using Griffies triads. The source of the improvement seems to be less mixing due to the reduction of the masking present when using $rx_{0M} = 0.2$ instead of $rx_{0M} = 0.05$. Somehow at the Angmassalik array ($\sim 550km$ down the sill) this difference is hardly noticeable.

The stretching also has shown to play an important role. Changing the SH94 stretching to

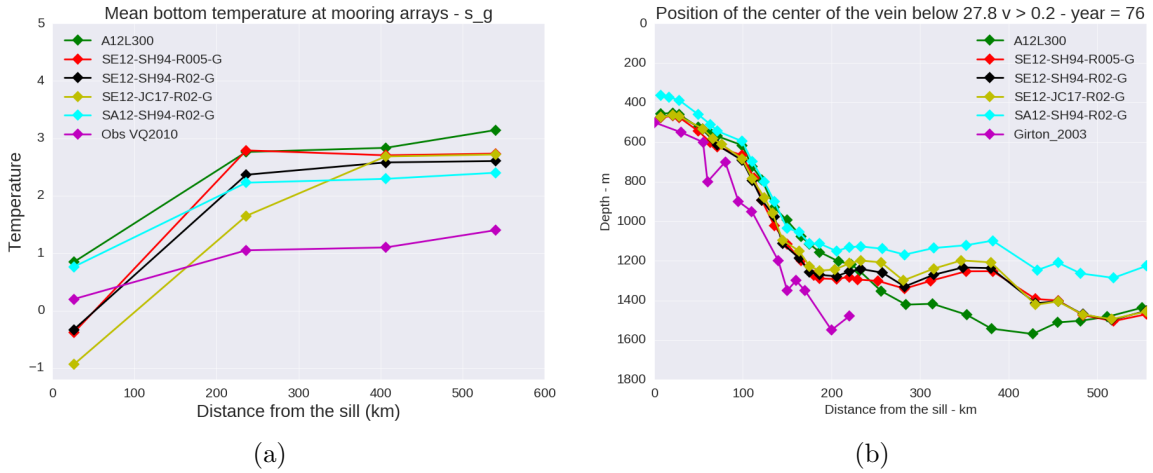


Figure 9.7: VQS simulations with the Griffies triads a) Minimum mean bottom temperature of the 5th year of calculation of the grid points conforming arrays 1, 15, 22 and 27 (figure 5.3). In pointy magenta line the transport values presented in Voet and Quadfasel, 2010 for the sill, the Dohrn Bank, TTO and Angmassalik arrays. b) Vertical position of the center of the vein. In pointy magenta line the values found by Girton and Sandford, 2003.

the JC17 one in the default case (at $1/12^\circ$ with $rx_{0M} = 0.2$) brought a decrease of $0.5^\circ C$ in the minimal mean bottom temperature at the Dohrn Bank array, and performances comparable with the ones obtained at $1/60^\circ$. For the others arrays downstream the difference is a cooling of $\sim 0.2^\circ C$. Using Griffies triads the difference is $\sim 1^\circ C$ at the Dohrn Bank array, but for the following sections the results are comparable. We also have to say that this $\sim 1^\circ C$ improvement is probably related to the fact that the minimum mean bottom temperature at the sill has a value of $\sim -1^\circ C$, which is not realistic and is very different from the rest of the simulations. The stretching effect is smaller at $1/60^\circ$, with an overall decrease of $0.2^\circ C$ when passing from $1/12^\circ$ to $1/60^\circ$, both with and without the Griffies triads formulation.

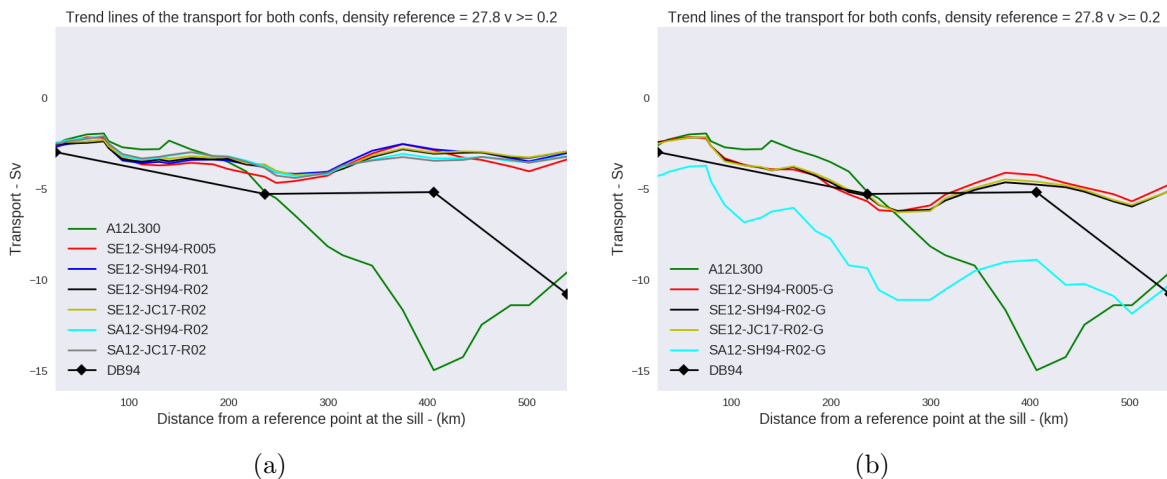


Figure 9.8: Overflow transport calculated along the 27 sections shown in 5.3 and its correspondent tendency lines using a) the default formulation on tracer diffusion b) Griffies triads. In pointy black line the transport values presented in Dickson and Brown, 1994 for the sill, the Dohrn Bank, TTO and Angmassalik arrays. The most performant simulation on z-coordinates (A12L300) was added as a reference.

The evaluation of the path of the overflow might be misleading here and caution must be taken when deriving conclusions from this diagnostic. In figure 9.7b we see that the SA12-SH94-R02-G (in cyan) presents shallower positions of the center of the vein while presenting among the coldest bottom temperatures. The reason for this is that the 27.8 isopycnal reaches shallow depths (see figure 9.13b) at regions where high overflow velocities are present. This combination gives shallower positions of the center of the vein, even though the overall representation of the DSO is improved. This illustrates that a single diagnostic is not enough to characterize the overflow

The transport values of the vein at $1/12^\circ$ resolution are in remarkably good agreement with observations at the Sill, Dohrn Bank and TTO arrays when using Griffies triads (figure 9.8b), but remains weak at the Angmagssalik array. A considerable increase and high transport values are observed in the case of $1/60^\circ$ (both in z-coordinates and in s-coordinates with the SH94 stretching). In the case of the default isopycnal tracer diffusion (figure 9.8a) the transport are slightly smaller than in observations, but still with a reasonable agreement.

The best performance of the overflow was obtained at $1/60^\circ$, with the JC17 stretching, a value of $rx_{0M} = 0.2$ and the Griffies triads (SA12-JC17-R02-G), but reasonably good results were obtained at $1/12^\circ$ (SE12-JC17-R02-G) with the same settings but with a significant decrease of the cost of the simulation. These two simulations are described in detail in the next section.

9.6 Further comments of most performing simulations

In this section we complete the description of simulations SE12-JC17-R02-G ($1/12^\circ$) and SA12-JC17-R02-G ($1/60^\circ$). The way this description is presented follows the objective of evaluating the convenience of increasing the horizontal resolution by a factor of 5, with the associated increase in cost. At the same time we perform a comparison of these two s-coordinates simulations with the highest resolution simulation in z-coordinates (A12L300) and observations.

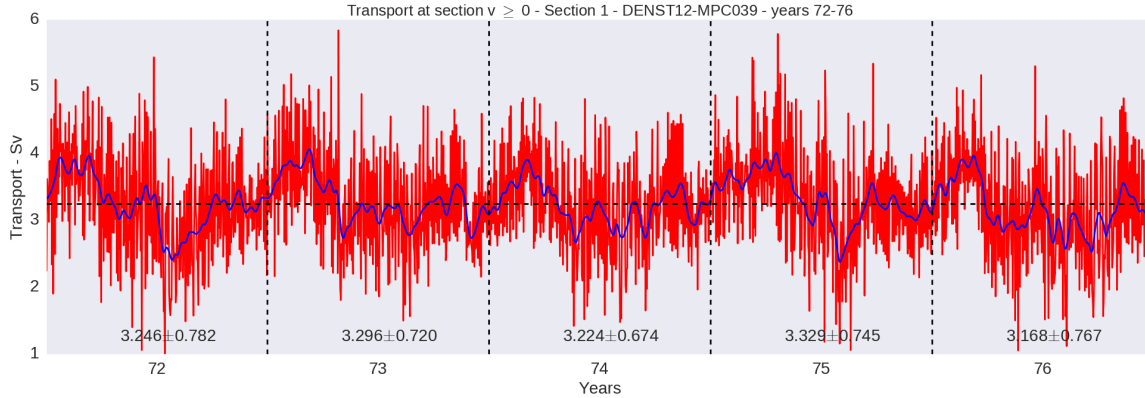


Figure 9.9: *Simulation SE12-JC17-R02-G: Time evolution of the southward volume transport ($v > 0 \text{ m s}^{-1}$) of waters denser than 27.80 at the sill. In red daily values, in blue the smoothed time series (20 day Hanning window). For each year the annual mean with the standard deviation is indicated.*

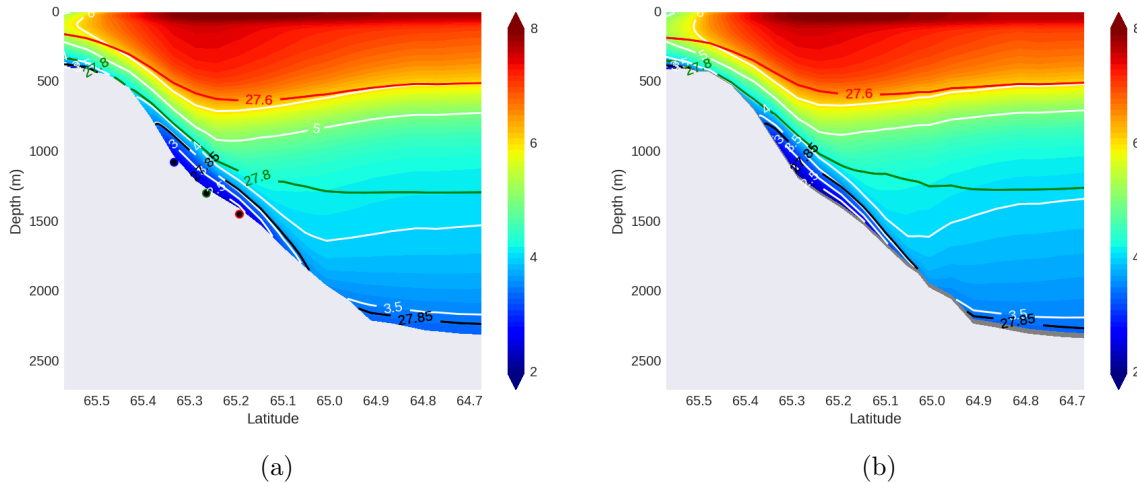


Figure 9.10: *Annual mean temperature of year 5 with temperature and density contours at section 14 (Dohrn Bank array, $\sim 250 \text{ km}$ from the sill) a) SE12-JC17-R02-G. The three color dots indicate the location of the 3 profiles shown in figure 9.16 b) section 14 SA12-JC17-R02-G.*

We first study the transport at the sill in SE12-JC17-R02-G (figure 9.9). Both s-coordinates simulations exhibit a similar transport at the sill and therefore we show this single case. This simulation presents a mean transport $\sim 3.3Sv$, which is slightly greater than in the A12L300 simulation ($\sim 3Sv$), but in agreement with observations ($3.4Sv$ according to Jochumsen et al., 2013). It also evidences a slightly smaller standard deviation of $0.75Sv$ when compared to the $\sim 0.9Sv$ of the A12L300 simulation and the $1.4Sv$ of the observations. With the smoothed version of the time series, we can observe the small interannual variations that were also observed

in both the reference E12L46 (figure 6.2) and A12L300 simulations (figure 7.17). In this case the feeding of overflow waters is also continuous and steady along the whole simulation.

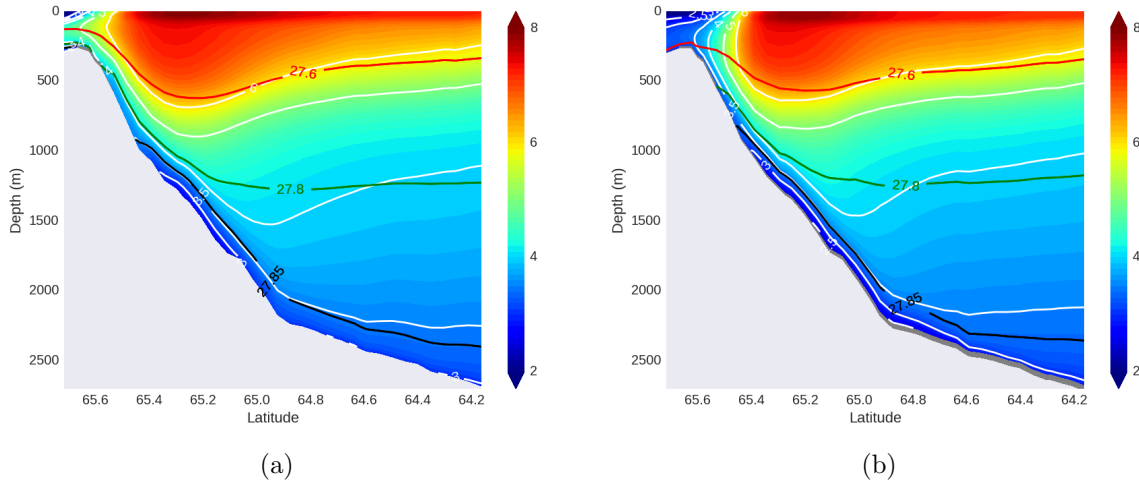


Figure 9.11: Annual mean temperature ($^{\circ}C$) of year 5 with temperature (white) and density (color) contours at section 18 (spill jet section, $\sim 300km$ from the sill) a) SE12-JC17-R02-G b) Section 18 SA12-JC17-R02-G

We now look at the structure of the overflow vein at a number of sections from the sill and downstream, for qualitative comparison ends. The cross section of temperature at section 14 (figure 9.10) shows a very clear presence of a vein at depths down to $\sim 1900m$ and the clear presence of the $2.5^{\circ}C$ contour of the temperature that was not present in A12L300 (figure 7.18a). The 27.85 isopycnal is also very well identified with the vein of fluid. Hardly appreciable differences are found between 9.10a ($1/12^{\circ}$) and 9.10b ($1/60^{\circ}$). These results are close to observations (figure 1.6), where temperatures of $2^{\circ}C$ are found down to $2000m$, but the model simulations are still $0.5^{\circ}C$ warmer (corroborated with daily outputs). Nevertheless this represents a great improvement compared to all z-coordinate simulations.

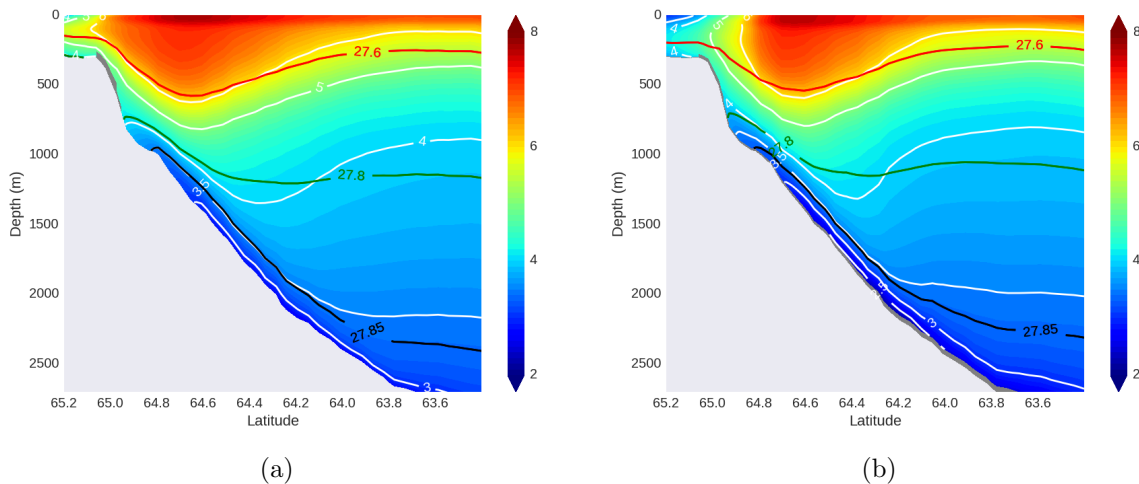


Figure 9.12: Annual mean temperature ($^{\circ}C$) of year 5 with temperature (white) and density (color) contours at section 22 (TTO array, $\sim 400km$ from the sill) a) SE12-JC17-R02-G b) section 22 SA12-JC17-R02-G

At section 18 (figure 9.11) the SA12-JC17-R02-G simulation shows a vein of fluid that spreads

all along the slope with a temperature contour of 3°C and bottom temperatures of 2.5°C for the $1/60^{\circ}$ case (figure 9.11b). The SE12-JC17-R02-G simulation shows no presence of the 2.5°C contour and a thinner vein. Both are in accordance with the results obtained in A12L300. This situation also repeats itself on section 22 (figure 9.12), with the 2.5°C isotherm appearing to be better defined for the $1/60^{\circ}$ than in the previous section. At this section the results of both simulations are also very comparable.

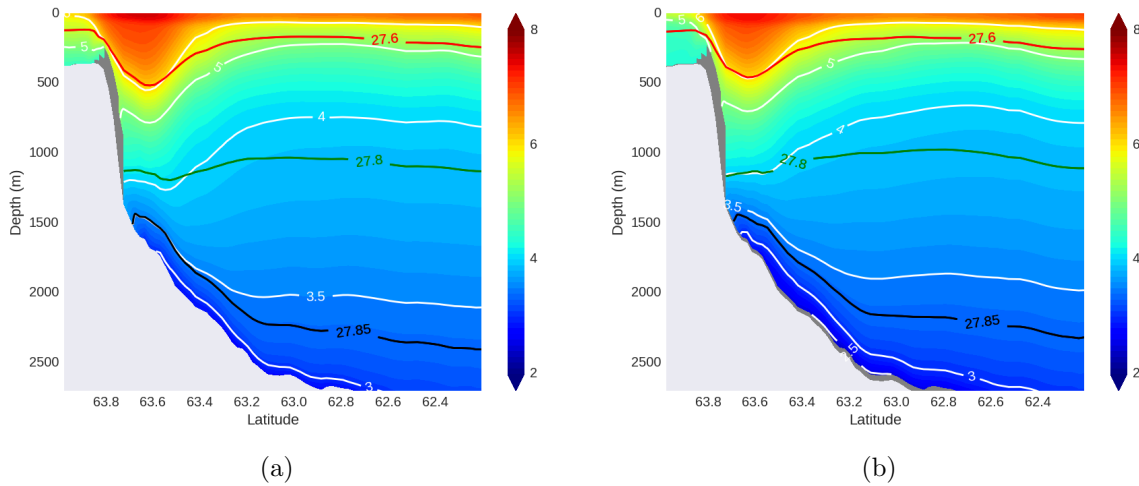


Figure 9.13: Annual mean temperature ($^{\circ}\text{C}$) of year 5 with temperature (white) and density (color) contours at section 27 (Angmagsalik array, $\sim 500\text{km}$ from the sill) a) SE12-JC17-R02-G b) Section 27 SE12-JC17-R02-G

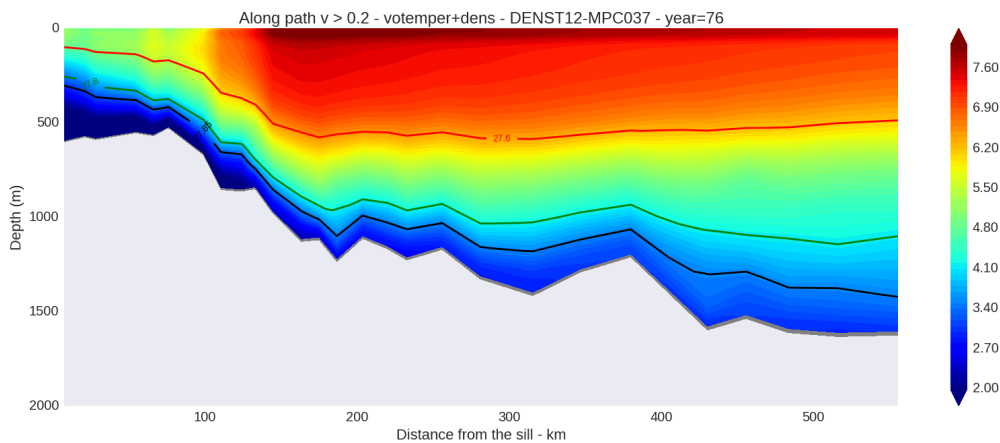


Figure 9.14: SE12-JC17-R02 simulation. Temperature annual mean of year 5 along the path of the overflow (magenta line in figure 5.3a). Density values in contours (27.6 in red, 27.8 in green and 27.85 in black).

At section 27 (figure 9.13) the results in s-coordinates present a remarkable improvement when compared with A12L300 (figure 7.19b). However, in s-coordinates, the benefit of the increase in the horizontal resolution in the AGRIF zoom is well preserved at that section which is not the case in A12L300. The SA12-JC17-R02-G simulation (figure 9.13b) shows a vein of fluid that spreads all along the slope to depths greater than 2500m with a main temperature contour of 3°C , but still with the presence of the 2.5°C contour. The position of the 27.85 agrees very well with observations (figure 1.9), but there is still a warm bias of 0.5°C . This is as well the case

for SE12-JC17-R02-G but to a slightly minor extent (figure 9.13a).

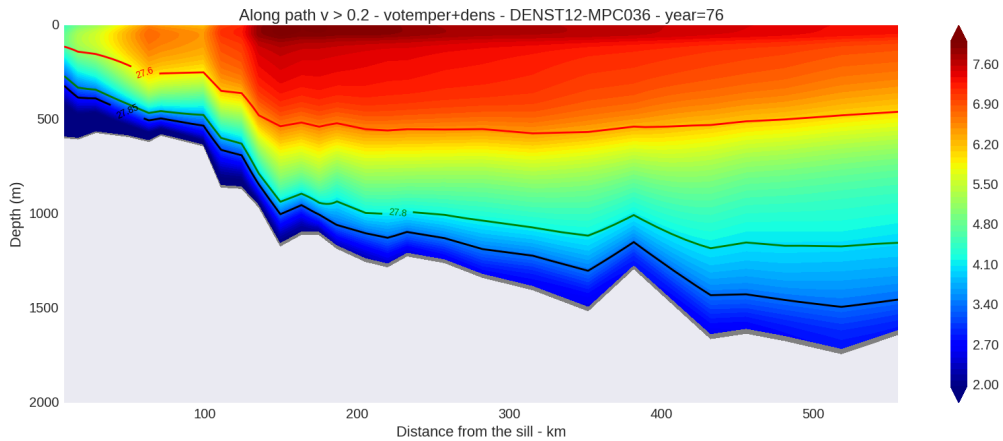


Figure 9.15: SA12-JC17-R02 simulation. Temperature annual mean of year 5 along the path of the overflow (magenta line in figure 5.3a). Density values in contours (27.6 in red, 27.8 in green and 27.85 in black).

The along path temperature is similar in both simulations (figures 9.14 and 9.15). The location of the contoured isopycnals, the cold water coming from the sill and the overall structure of the temperature field are very similar. We could mention just two aspects of the SA12-JC17-R02-G case (figure 9.15). First, warmer water is observed between 50km and 100km from the sill in the Irminger current (0 – 300m depth). Second, the water coming from the sill is somewhat colder.

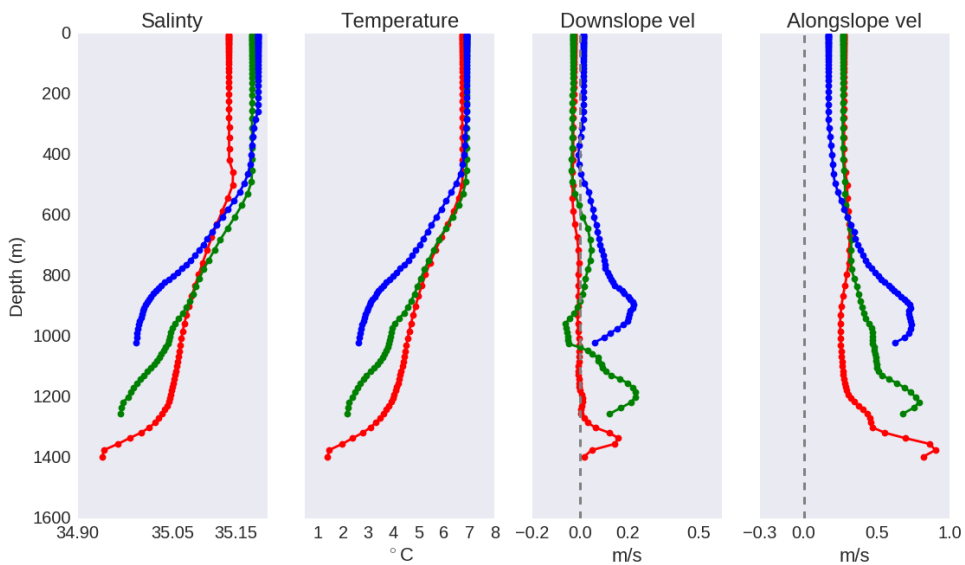


Figure 9.16: Profiles of different quantities for SE12-JC17-R02 for 04/April hour 10 of year 5 at section 14 for the locations indicated in figure 9.10 a) Temperature b) Salinity no c) Cross-slope velocity d) Along-slope velocity

The vertical profiles of different quantities for the simulation SE12-JC17-R02-G are shown in figure 9.16 (in the same way it was done for z-coordinates in figure 7.16). The total depths of the different profiles might be slightly different than in figure 7.16 since in this latter case the bathymetry is the one corresponding to an horizontal resolution of $1/12^\circ$. We have chosen here

the $1/12^\circ$ case in order to show that even at the coarsest of the two resolutions used in these experiments, a well marked vertical shear is seen in the vein of current indicating that the Ekman layer dynamics is better resolved than in a z-coordinate simulation. The shear is greater in the $1/60^\circ$ case, but it is not shown to avoid redundancy. The salinity shows a freshening of ~ 0.12 and the temperature a cooling of 3°C across the overflow plume. Downslope and alongslope velocities identify a bottom intensified current which peaks at values of 0.2ms^{-1} and 0.6ms^{-1} , respectively, at about 100m above the bottom (the likely thickness of the bottom Ekman layer). All these values are quite comparable to those obtained for A12L300 and in good agreement with observations. These results are in accordance with Laanaia et al., 2010, in which it was stated that thanks to the increased resolution at the bottom of terrain following coordinates, it was possible to resolve the Ekman layer, and therefore improve the representation of the gravity current.

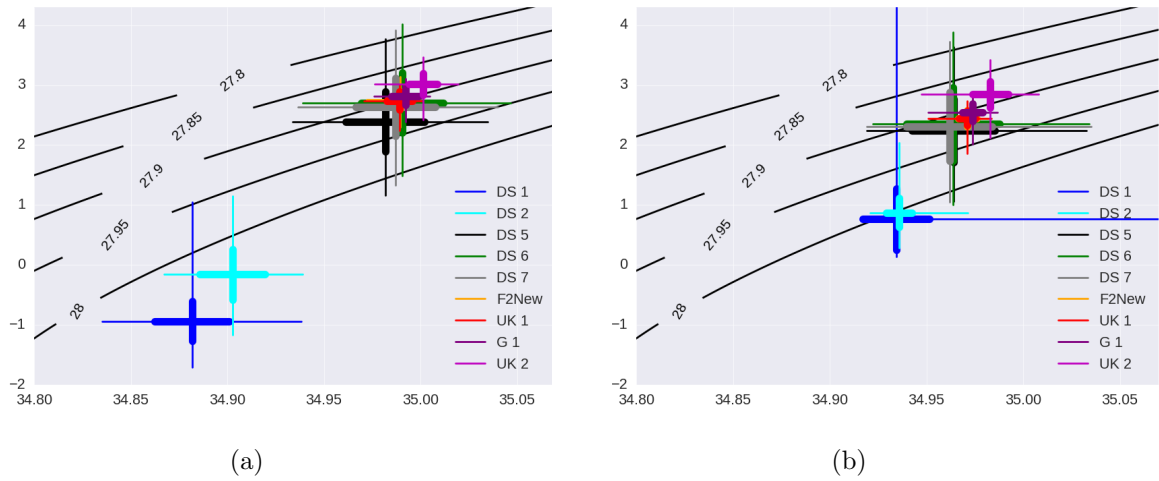


Figure 9.17: Annual mean TS diagram of year 5 of a) SE12-JC17-R02 b) SA12-JC17-R02. Comparable with figure 1.17 from Jochumsen et al., 2015

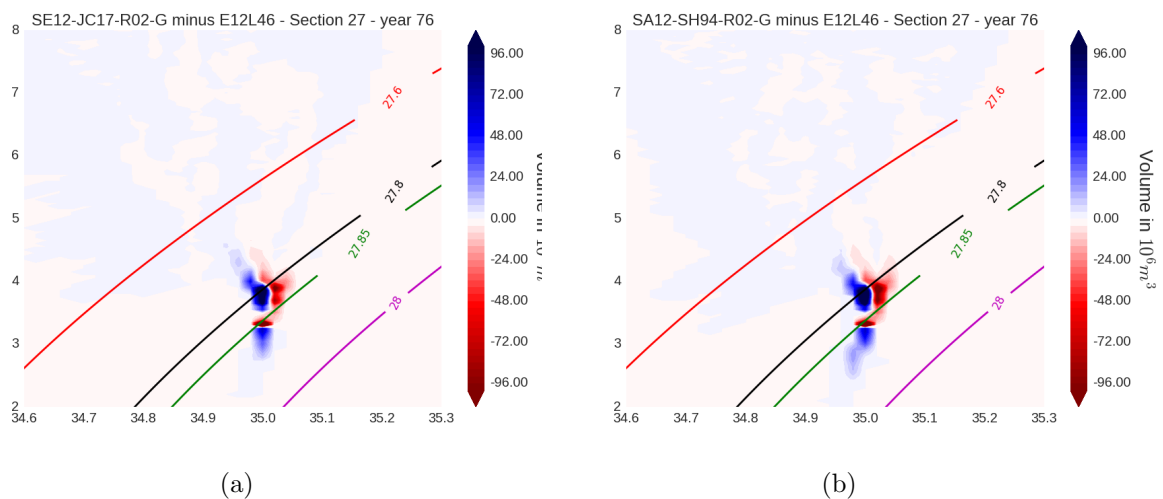


Figure 9.18: Difference of the TS diagrams, annual mean of year 5 at section 27 (Angmagssalik array) a) between SE12-JC17-R02-G and E12L46 b) between SA12-SH94-R02-G and E12L46 .

Some additional information can also be obtained from TS diagrams. In figure 9.17 we observe the TS diagrams for the SE12-JC17-R02-G and SA12-JC17-R02-G simulations. At the sill (DS1

and DS2) the overflow exhibits greater densities (colder and fresher water) at $1/12^\circ$, negative values being observed. This suggest that the circulation north of the sill has been modified (corroborated with plots of bottom temperature). However, at the mooring south of the sill the TS diagrams indicate that the water masses have comparable TS properties. This indicates that the overflow waters are less diluted in the $1/60^\circ$ simulation.

In order to evaluate more directly the improvements obtained with these simulations with the reference simulation in z-coordinate we show the difference of the TS diagrams at section 27 (Angmagssalik array, $\sim 550km$ down the sill) in figure 9.18. Both s-simulations show comparable differences with the z-coordinate reference. First the volume represented by waters of temperature between $2^\circ C$ and $3.2^\circ C$ (waters denser than 27.85) has significantly increased in the s-coordinate simulations, when the volume represented by waters of temperature around $3.2^\circ C$ has significantly reduced. Second, in the temperature range $3.5^\circ C$ to $4^\circ C$, the waters have been freshened. This indicates that the overflow is fresher and colder in the s-coordinate simulations and that the volume of the vein of current has significantly increased.

9.7 Summary and discussion

We studied in part IV the implementation of s-coordinates in a realistic configuration. In particular we used the VQS coordinate type, which consists in a s-coordinate that is defined using an enveloping (smoothed) version of the real bathymetry to set the stretching. This type of coordinate has the particularity that a mask is applied in those places where the enveloping and the real bathymetry are different (becoming a z-coordinate at those places).

We first studied the PGE effect on a neutral stratification with different degrees of masking and different stretching types. We found that the parameter rx_{0M} was a good metric to define the regions where the mask is needed. The spurious currents generated were closely related with this metric, reaching values of $\sim 0.01ms^{-1}$ to $\sim 0.03ms^{-1}$ for $rx_{0M} = 0.05$ and $\sim 0.25ms^{-1}$ for $rx_{0M} = 0.20$. In this way, the parameter rx_1 was found to be a good metric to be used as a comparative indicator in order to compare the amplitude of the spurious currents.

We then studied the implementation of VQS in a realistic setup. Using a series of sensitivity tests we presented here an analysis of the impact on the overflow representation regarding the different possible choices in VQS. At $1/12^\circ$ the most performing solution was obtained with the use of $rx_{0M} = 0.20$ and the JC17 stretching. In general, the solution was dramatically improved by only changing the vertical coordinate type from z to s. We also performed tests at $1/60^\circ$ with a local refinement (AGRIF). In this case very good comparison with long-term observations was found, besides a bias of $\sim 0.5^\circ C$, which is attributed to unrealistic initial and boundary conditions. The comparison between $1/12^\circ$ and $1/60^\circ$ solutions in s-coordinates did not bring significant differences in the overall representation of the overflow, especially if we consider the added computational cost to reach $1/60^\circ$, being the two solutions very similar. The implementation of the Griffies triads for the tracers diffusion (along isopycnal surfaces) showed to improve the solution drastically when compared with the default scheme.

The comparison between the different simulations was done following the same methodology than in z-coordinates, reaffirming the usefulness of the set of diagnostics.

Besides the final representation of the overflow shown to be dramatically improved, this type of coordinate might not be optimal for global or larger configurations. This type of coordinate presents a high constraint for those flows that are not topographically constrained. We noticed that the best improvement was found for $rx_{0M} = 0.20$, a value that may induce large PGE errors elsewhere in the basin, where this type of coordinate is not strictly needed. We therefore investigate in the next part of the work a localized application of the VQS coordinate that leaves the rest of the global z-coordinate untouched and suits for the representation of the overflow.

Part V

Local s-coordinates

Chapter 10

A first try

The VQS is presented as an hybrid option between z and s coordinates. This is, when a given condition is met, an algorithm that generates a change from one coordinate type to the other is used. The condition is managed through the use of a second bathymetry called enveloping bathymetry which is a partially smoothed version of the original bathymetry (it is only smoothed at certain places). Truth is that different logic can be followed to set the different values of the enveloping bathymetry. According to the specific logic taken into consideration, the resulting enveloping bathymetry will be different and therefore the regions and the extent where the z -coordinate is present will be different as well. Based on this one can start to think of an algorithm that sets s -coordinates in specific locations and z -coordinates in the rest of the domain.

A mixed coordinate vertical grid may have the big advantage of using s -coordinates in regions where flows are mostly topographically constrained, with all the advantages that this type of coordinate provides. At the same time it may minimize the generation of the spurious currents to the locations where the s -coordinate is implemented. Finally, a smoothed connection to the z -coordinate should permit the flow to adapt itself to the different coordinate types. In this chapter, we describe how we implemented such an hybrid coordinate system in our regional model of the Denmark Strait.

10.1 Implementation

In order to test this concept we performed a first step with a simplistic implementation. For this, we divided the model domain in four regions. Figure 10.1a shows these four regions delimited by different circles. The region inside the magenta circle is called PuS (for pure s), the region between the magenta and the black circle is called TrS (for transition in s), the region between the dark circle and the blue circle is called TrZ (for transition in z) and the region outside the blue circle is called PuZ (for pure z).

Three enveloping bathymetries over the whole domain are built. The PuS region takes the enveloping bathymetry of a VQS built with $rx_{0M} = 0.2$, guaranteeing a good descent of the vein without introducing excessive spurious currents (as shown in Chapter 9). The enveloping bathymetry for the TrS region is set with a combination between the pure VQS enveloping bathymetry with another enveloping bathymetry built with a smaller value of rx_{0M} ($rx_{0M} = 0.05$ for this case). The enveloping bathymetry for the TrZ region is set with a combination between the enveloping bathymetry built with $rx_{0M} = 0.05$ and the maximum depth of the whole domain. The enveloping bathymetry in the PuZ region is set to be flat, the depth being the maximum depth of the domain. The s -coordinate is then just a z -coordinate. In this case the realistic topography is represented with a full-cell masking.

The distances between the regions is set explicitly by the values of the radius of the different circles (which all have the same center located at the sill of the Denmark Strait). For the case presented here a radius of 20 grid-points is used for the magenta circle, a radius of 40 grid-points

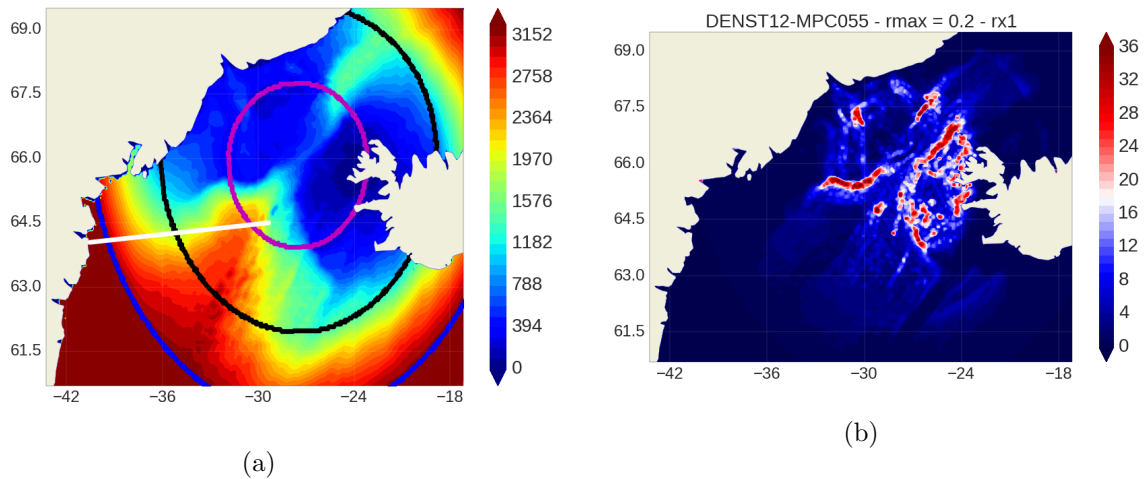


Figure 10.1: *Local sigma implementation in the SL12-SH94-G simulation a) Enveloping bathymetry in meters. The different circles indicate the different regions, having pure VQS coordinates inside the magenta circle and pure z-coordinates outside the blue circle. The white line indicates the section shown in figure 10.2. b) Maximum values in the vertical of the rx_1 parameter (see section 8.1 for explanation).*

for the black circle and a radius of 80 grid-points for the blue circle.

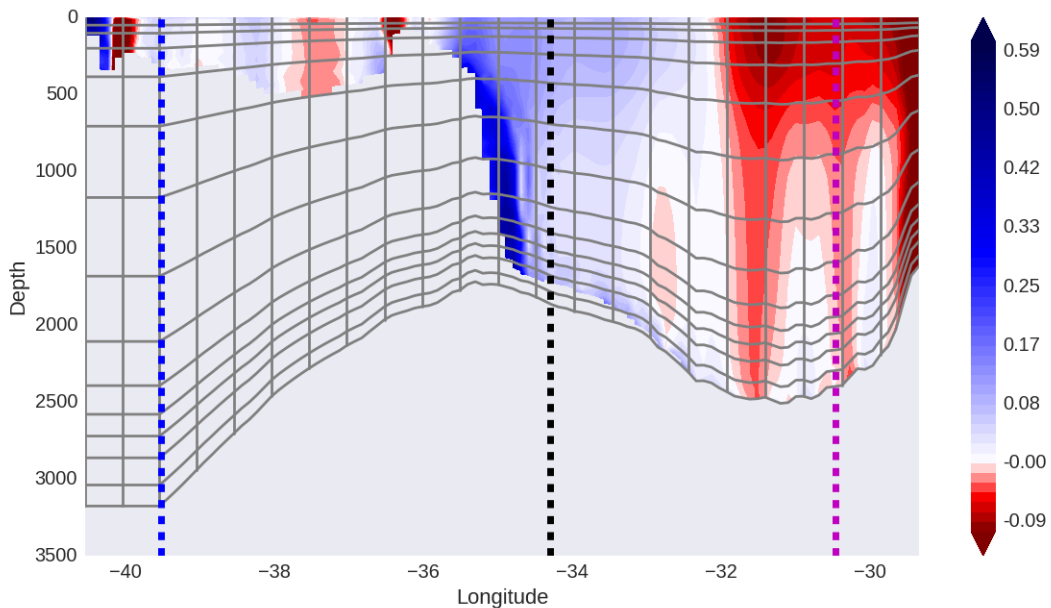


Figure 10.2: *Grid and topography along the section indicated in white in figure 10.1a. Areas in light gray represent the realistic bottom. The vertical colored dashed lines indicate the circles. For clarity only a few horizontal and vertical gridlines are plotted. In red/blue colors and just as a reference, the velocity normal to the section is plotted.*

The combination of enveloping bathymetries (transition between regions) is built using linear weights. For this, for each point we first calculate its distance to the center. With this distance we are able to locate in which particular region this point is located. If this point is in a transition region, the weight is calculated according to the position of this point regarding the inner and

the outer circles. For this end we take as the reference the center, and the weight is calculated in the following way

$$wgt(ji, jj) = (dist((ji, jj), (ji_c, jj_c)) - r_i) / (r_o - r_i) \quad (10.1)$$

where (ji_c, jj_c) are the grid values of the reference point at the sill (center), r_i is the radius of the inner circle and r_o is the radius of outer circle. Once the weight is obtained, the resulting value of the enveloping bathymetry at a given grid-point (ji, jj) is calculated considering the value of the enveloping bathymetry for the inner circle ($hbatt_i(ji, jj)$) at that point with the one of the outer circle ($hbatt_o(ji, jj)$)

$$hbatt(ji, jj) = (1 - wgt)hbatt_i(ji, jj) + (wgt)hbatt_o(ji, jj) \quad (10.2)$$

In this way, we define a particular enveloping bathymetry for each grid-point. The resulting enveloping bathymetry and the vertical coordinate associated can be seen in figure 10.2. The region to the right of the magenta line denotes the PuS region, here the enveloping bathymetry is strictly related with the real one (thanks to the value $rx_{0M} = 0.2$). The region between the magenta and the black circle denotes the TrS region, in which the enveloping bathymetry presents a level of smoothing that increases toward the outer circle (black line). Between the black and blue line we have the TrZ region, where the enveloping bathymetry begins to largely differ from the real one. Here a high level of masking is present. Finally, the region to the left of the blue line is the PuZ region in which the enveloping bathymetry has reached its deepest value and is flat, producing in this particular case a z-coordinate.

An important aspect of defining the transition is to not introduce additional PGE. Comparing figure 10.1b with the full domain case ($rx_{0M} = 0.2$) in figure 8.9b, we can see that this is not the case, the large values of the rx_1 parameter being limited to the magenta circle. Therefore the connection is properly done from this point of view.

10.2 Results

We show here the results of this first implementation of the local s-coordinates. For simplicity we used the standard stretching included in NEMO v3.6 (SH94). The results shown uses the Griffies triads, but a test without it was performed and led to the same conclusions. The reference name assigned to this simulation is SL12-SH94-G (SL for s-local), but we also name it local-s. It is compared to the reference full domain s-coordinate run, in this case SE12-SH94-R02-G (also called the full-s run).

Proceeding in the same way as before, we show in figure 10.3 the annual mean bottom temperature of the last year for those two simulations. The local-s run gives a somewhat warmer solution beyond the blue circle, but both runs remain very similar. We observe that the local-s simulation captures the main imprints of the full-s simulation. The shelf waters all along the Greenland coast, as well as the region where the Irminger current flows, do not seem to be affected by this transition in vertical coordinate.

The comparison of the bottom temperature at the mooring arrays (figure 10.4a) demonstrates that the local-s run produce very similar to those of the full-s run. A small difference of $\sim 0.2^\circ C$ is observed at the sill and at section 14 (the local-s run being colder), practically the same value is reported for section 22 and a marginal difference of $\sim 0.1^\circ C$ (local-s being warmer) at section 27. The vertical position of the center of the vein along the path of the overflow shows as well very small differences between these two simulations (figure 10.4b), the local-s being slightly but systematically shallower outside the PuS region.

The transport calculation also gives extremely similar results (figure 10.5), except for the most downstream value ($> 500km$) where the full-s transport is $\sim 0.3Sv$ greater. In regard to these integrated quantities both simulations perform similarly, confirming that the transition is

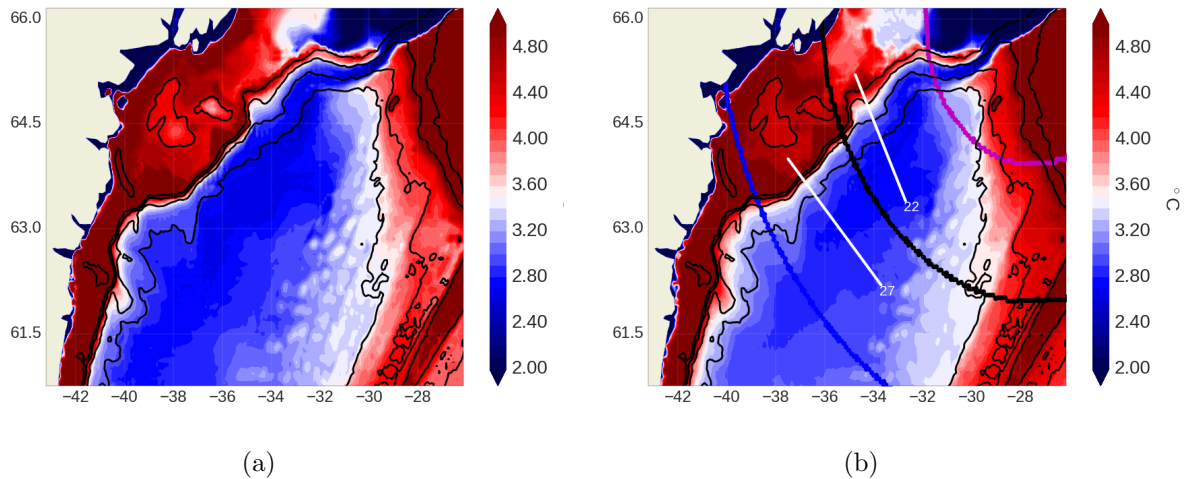


Figure 10.3: Annual mean of the bottom temperature of year 5 at $1/12^\circ$ a) SE12-SH94-R02-G (full domain s) b) SL12-SH94-G (local s-coordinates). Isobaths 500m, 1000m, 1500m and 2000m are contoured, as well as the different circles that denotes the different coordinates regions for the local s-coordinates.

performed correctly. Obviously as we get into the PuZ region, differences between simulations are expected.

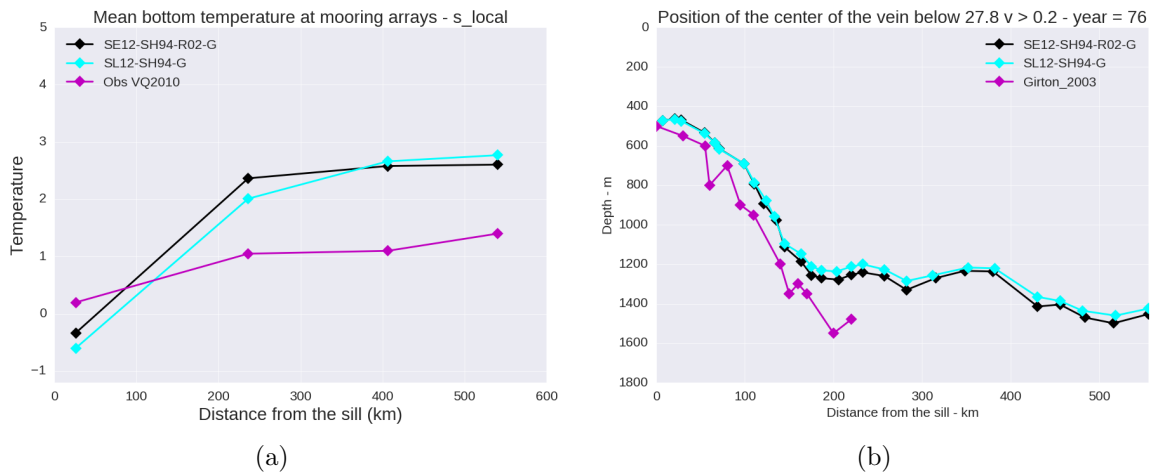


Figure 10.4: Full domain and local s-coordinates simulations using Griffies triads. a) Minimum mean bottom temperature of the 5th year of calculation at the grid points co-located with observational arrays 1, 14, 22 and 27 (figure 5.3). In magenta line the transport values presented in Voet and Quadfasel, 2010 for the sill, the Dohrn Bank, TTO and Angmassalik arrays. b) Vertical position of the center of the vein. In pointy magenta line the values proposed by Girton and Sandford, 2003.

For a qualitative comparison, we show in figure 10.6 two temperature sections and we compare them with the sections shown previously for the full s-coordinate simulation SE12-JC17-R02-G (figures 9.12a and 9.13a). Note that this latter simulation uses the JC17 vertical stretching, different from that used in the full-s run shown in figures 9.12a and 9.13a. Those two sections are in the final part of the overflow path, in the transition regions of coordinates. At these locations the enveloping bathymetry is already very different from the real one, the masking is important and therefore both z and s coordinates are clearly present. Section 22 (TTO) is shown

in figure 9.12a. In a large portion of this section the enveloping bathymetry (in light gray) is very different from the real bathymetry (dark gray); due to the fact that the western portion of this section is in the TrZ region. We observe a clear presence of the 3°C temperature contour, which in conjunction with the 27.85 isopycnal denotes the presence of a bottom intensified vein of current. When comparing with figure 9.12a (full domain s) we found very limited differences, the temperature and density contours are located at very similar places and the warm Irminger current at the top looks extremely similar.

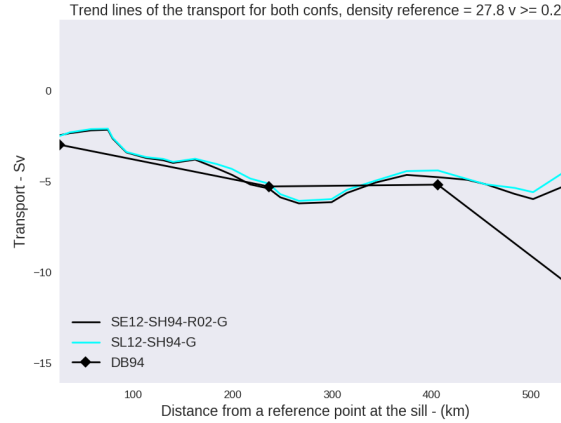


Figure 10.5: *Transport calculated along the 27 sections shown in 5.3 and its correspondent tendency lines using of the full domain s-coordinate and local s-coordinates simulations using Griffies triads. In pointy black line the transport values presented in Dickson and Brown, 1994 for the sill, the Dohrn Bank, TTO and Angmassalik arrays.*

The qualitative comparison of section 27 (figure 10.6b) also agrees very well with the result in full domain s-coordinates (figure 9.13a). Here the difference between the enveloping bathymetry and the real one is huge, with most of the overflow process occurring in z-coordinates. We observe here as well the clear presence of the 3°C temperature contour, and very comparable results with figure 9.13a. Here again the temperature and density contours are located in very similar places. The vein presents some differences in its upper portion, but in a very limited way. Even in this z-coordinate context the main characteristics of the overflow are preserved beyond the VQS region.

10.3 Summary and preliminary conclusions

We have presented here a particular use of the enveloping bathymetry in VQS coordinates in which we explicitly defined different values according to three specific regions. One region keeps the usual definition of the enveloping bathymetry having a pure VQS coordinate; a second region receives the deepest value of the domain (flat enveloping bathymetry), becoming a z-coordinate; and a third region which acts as a transition between the previous two regions. The implementation of such a type of configuration preserves the main imprints of the VQS coordinates in the DSO, while at the same time connects to a z-coordinate region without degrading the overall solution.

The interest of this test was to evaluate the convenience of having z and VQS coordinates on the same region regarding the final representation of the DSO. The idea of tailoring the vertical coordinate is shown here to be very convenient and this opens possibilities for further developments.

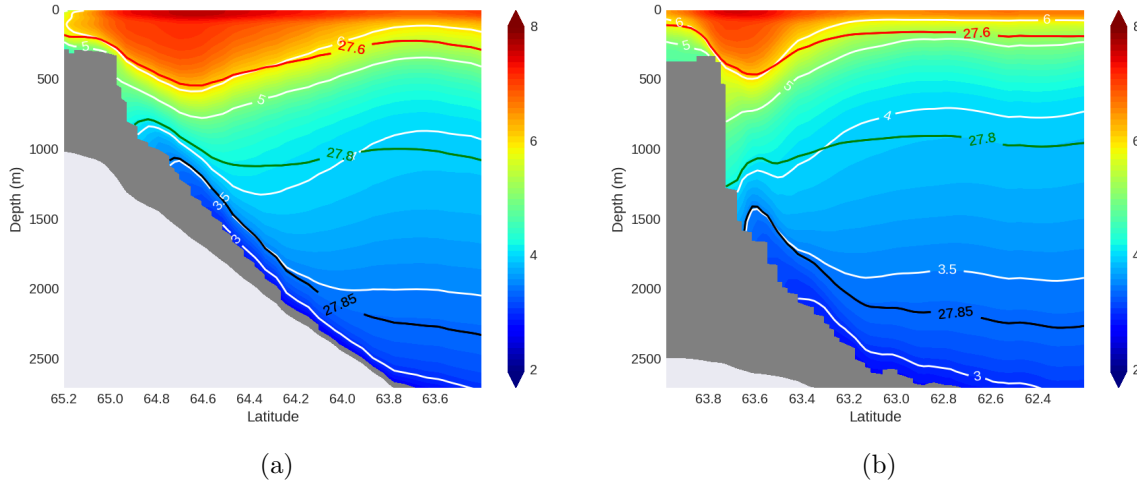


Figure 10.6: *SL12-SH94-G* simulation, annual mean temperature ($^{\circ}\text{C}$) of year 5 in colors, with temperature (white) and density (color) contours a) Section 22 (TTO array, $\sim 400\text{km}$ from the sill, partly in the TrZ region) b) Section 27 (Angmagssalik array, $\sim 500\text{km}$ from the sill, in the TrZ region). In light gray the enveloping bathymetry and in dark gray the real model bathymetry.

10.4 Limitations

Although this very first implementation of having two grids on the same domain showed very interesting results and demonstrated the great potential of the method, one considers that the present implementation in concentric circles is somewhat over-simplistic. In order to set the basis for further development of this type of coordinate we here present what we think are its main limitations:

- It does not consider the value of the enveloping bathymetry (black circle) that connects to the deepest value of the domain. This imposes to use a large number of points all around the local sigma to make this connection.
- The level distribution (stretching) in the z-coordinate region and in the s-coordinates region are the same.
- It is only possible to use one point (center) to set the local sigma
- It does not consider the possibility of overlapping with other local sigma, so it is not possible to treat several regions independently, as the DSO and the Faroe Bank Channel.
- It does not consider the option of using partial cells in the masking

In the following chapter we propose a more sophisticated way of implementation that goes beyond those limits.

Chapter 11

Local VQS Hybrid coordinate

11.1 Implementation

Due to the noticeable improvement of the representation of the overflow with the local sigma presented before and in order to overcome the limitations mentioned in the previous chapter, a more sophisticated implementation of the local s-coordinate was developed.

11.1.1 Connection improvement

In the previous example the connection between the s and the z coordinate regions was done using a fixed number of grid points. This is not optimal since whatever is the value of the local enveloping bathymetry in the limit of the transition TrS region, the same number of points is used to make the value of the enveloping bathymetry equal to the deepest value of the domain.

One of the aspects of a satisfactory connection between coordinates is that it should not introduce spurious currents in the transition regions. We discussed before different ways to estimate the magnitude of these errors through two different metrics, rx_0 and rx_1 . Considering this criteria, one could specify a number of grid points for the transition according to the value of the enveloping bathymetry ($hbatt$) at the limit of the TrS region, set the stretching with the resulting enveloping bathymetry, then calculate rx_0 or rx_1 for the resulting coordinate system. If the resulting field of rx_0 or rx_1 is not satisfactory one could iterate by changing the number of grid points for the connection and so on. The problem with this is that it does not consider a smooth solution in order to let the flow adapt to the change of coordinate, which probably is the most restraining issue.

We choose a different approach here, which is to set the maximum slope between the enveloping bathymetry and the deepest value of the domain as the governing factor to determine the number of grid points used for the connection. Doing so we have an indirect control of the PGE related to the grid in the connection region since both rx_0 and rx_1 depend on the slope of the enveloping bathymetry. We can also control how smooth the progression between the different coordinates is done, having a control on how the grid favors a correct adaptation of the flow.

Since the values of the enveloping bathymetry can be highly changing, which could give place to a variable number of grid points in the connection and in order to avoid abrupt lateral changes in the coordinate system, a final smoothing is added for the TrZ region. For simplicity the smoothing chosen is an average filter, but different filters can be used.

11.1.2 Stretchings

As explained before, we can view the z-coordinate as a particular case of the s-coordinate in which we force the enveloping bathymetry to be flat and the last s level being at the depth of the deepest z-level in the whole domain (at the bottom). In addition to this we can define the level distribution of the z-coordinate as a stretching of the form

$$C_s(k) = -\frac{h_z(k)}{h_{zMax}} \quad (11.1)$$

where $h_z(k)$ is the depth of a given z-level and h_{zMax} is the deepest value of the domain. Therefore a new stretching $C(k)$ can be defined with a weighted linear combination between $C_s(k)$ and the chosen stretching for the s-coordinate $C'(k)$

$$C(k) = f\left(\frac{h_{env}}{h_{zMax}}\right)C_s(k) + \left(1 - f\left(\frac{h_{env}}{h_{zMax}}\right)\right)C'(k) \quad (11.2)$$

The weight is set such that when the enveloping bathymetry approximates to the maximum depth the stretching tends to be equal $C_s(k)$ (the z-coordinate stretching).

We see that this new vertical coordinate can be adapted to any existing s-coordinate stretching. It makes no assumption regarding the existence of masking or not in the s-coordinate, so both pure s-coordinates and VQS are possible.

11.1.3 Region definition

Instead of using one specific point for the center of the PuS region, it might be of interest to have a more generic way to define the PuS region and the associated transition regions. In this way we can think in a succession of points that give origin to the PuS region, for example the points that define a coast or simply the points that are part of a line. In figure 11.1 we show an example of a PuS region defined according to two lines that intersect each other. These two main lines are formed with two extreme points each, denoted with the white dots. By choosing a specific number of grid points for the radius (r_1 hereafter, 10 grid points for the thicker line and 3 points for the thinner one) and knowing the location of the points of these main lines we were able to define the PuS region and the TrS (the radius in this case is two times the one for the PuS region, r_2 hereafter).

One of the main advantages of the method presented is that each point defines independently its corresponding enveloping bathymetry according to its relative position in a given region. In this way, for each main line separately and for each grid point of the domain, we look for the closest point of the main line, if this distance is smaller to r_1 a value of the enveloping bathymetry according to the PuS region is applied. If this distance is between r_1 and r_2 a weighted value was given according to equation 10.2. For the TrZ region, we defined a variable r_3 radius, by using the slope criteria explained in section 11.1.1 (a slope value of 2.5° is used in the case of figure 11.1), in order to connect the closest point of the black region to the maximum domain depth (5800m in this case).

Once the resulting enveloping bathymetries associated to each line are calculated, the final enveloping bathymetries for the local value of the enveloping bathymetry for the TrS and TrZ regions, is set as the deepest one. A final smoothing is applied in the TrZ region which is explained in the following paragraph.

11.1.4 Overlapping between sigma regions

In order to make this implementation even more generic, we included the possibility of having different regions overlapping. After building the $hbatt$ for each line, we define each point of the final $hbatt_F$ as the deepest value of all the $hbatt$ (one for each line of centers) at that particular point. Doing so we guarantee no additional PGE on TrS and TrZ regions (the value for PuS is always the same no matter the line since the enveloping bathymetry here is not built with weights). However, this could introduce problems in the connection with the z-coordinate. And this is why a filter is applied in the TrZ region, giving place to a smoother solution.

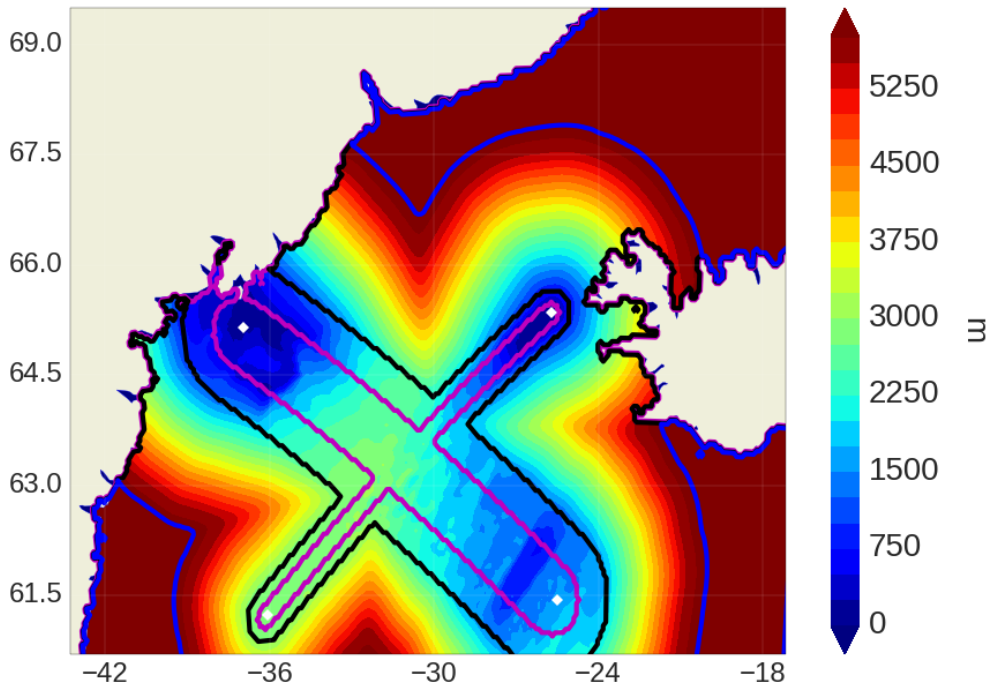


Figure 11.1: *Implementation of local VQS Hybrid coordinate. In this case the PuS and TrS regions are defined using two lines (defined by the white dots). The region inside the magenta contour is the PuS region, the region between the magenta and the black contour is the TrS region, the region between the black and the blue contour is the TrZ region and the region outside the blue contour is the PuZ region. A connection slope of 2.5° was used to connect from the black contour to the blue contour. The maximum domain depth (blue contour) is 5800m. The radius of the thicker line is 10 grid points and the for the thinner line is 3 grid points.*

11.1.5 Inclusion of partial step

In the PuZ regions, which was up to now treated as a full step, we implement the partial step in the same way as it is done in NEMO. For this we introduce the calculation of the variable mbathy (contains the number of levels available for calculation in the domain) for z-coordinate in our routine after setting the stretching. Once this is done we modify the cell thickness of the last wet level in order to match the value of the bathymetry as it is performed in the routine of the code for partial steps (for the PuZ region only).

11.2 A bad connection case

We present here a case where the connection between grids is not properly done. In figure 11.2a we present an enveloping bathymetry built with two radius centered in the same point as in figure 10.1a, but in this case the radius are of 30 grid points instead of 40. The maximum domain depth is in this case 5800m (instead of 3200m of figure 10.1a). The first and second blue lines (from the inside out) denotes the 3200m and 5800m. We see that in this case the connection is rather abrupt, using just a few grid points to change from a relative shallow depth to a depth of $\sim 3000m$ deeper.

The resulting bottom temperature produced by the simulation is shown in figure 11.2b. When compared to figure 10.3b (where a proper connection is made) the results show a warmer bottom, clearly affected by the grid transitions as the changes in bottom temperature are linked with the different colored contours (which depict the different regions).

The conclusion of this very simple example is that if a not sufficient number of points is chosen for the grid connections, the resulting implementation might be far from optimal, as it is the case here.

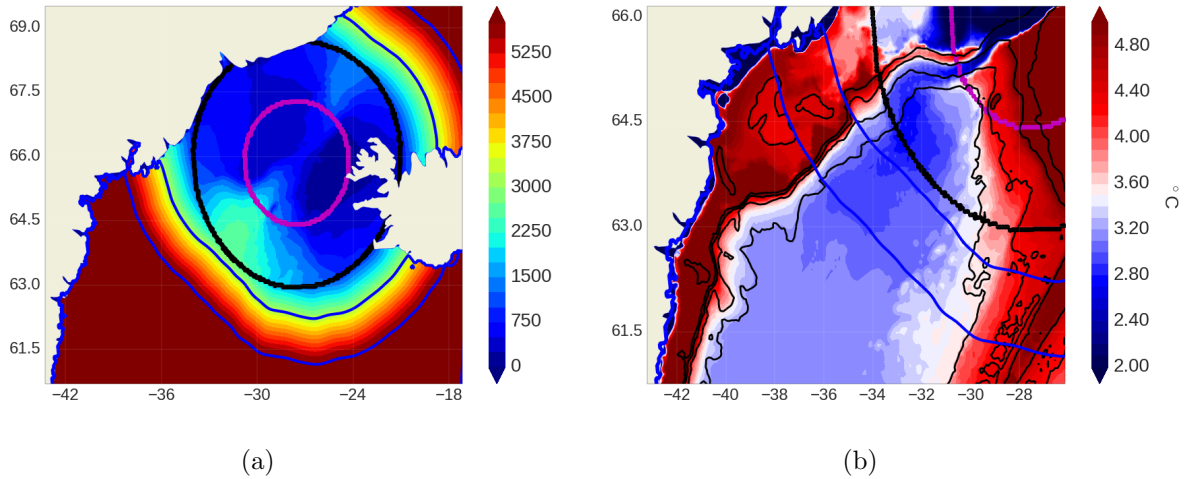


Figure 11.2: *Local sigma implementation in the simulation for a bad connection case a) Enveloping bathymetry in meters. The different circles indicate the different regions, having pure VQS coordinates inside the magenta circle and pure z-coordinates outside the region denoted with blue b) Annual mean of the bottom temperature of year 5 at $1/12^\circ$*

The slope using in this case is the same as in figure 11.1. The reduction in the number of points comes mainly from the fact that the region chosen in this tests is circular, and therefore the smoothing affect less the final solution. In figure 11.1 the smoothing extends the TrZ region due to the presence of the two lines. Therefore, a preliminary test of a given enveloping bathymetry should always be considered.

Part VI

Conclusion and perspectives

Conclusion

We started our study by defining three main objectives: the reach a definition of the Denmark Strait Overflow (DSO) that permits a fair comparison to observations and clear assessments of improvements regarding its representations in models, to quantify the sensitivity of the model representation of the DSO to horizontal and vertical resolution in the z-coordinate context, and to the vertical coordinate type.

We first developed an original realistic model configuration of the Denmark Strait, the domain of which is large enough to follow the evolution of the dense water passing through the sill over a distance of more than $500km$. This model configuration, named DENST12, is based on the NEMO ocean general circulation model. Its nominal resolution is $1/12^\circ$ and 46 vertical levels. The vertical resolution can be increased to 75 and 300 levels. The use of AGRIF mesh refinement software allowed to increase the horizontal resolution to $1/60^\circ$ over a part of the domain that includes the sill and the first hundred kilometres downstream. All model simulations were performed for 5 years, to follow the evolution of the overflow for a period long enough to draw reliable conclusions.

Then, we developed a set of diagnostics that characterized the DSO as a dense, cold and fast vein of fluid confined to the bottom along the continental slope. In this way a complementary definition of the overflow was used, by setting a threshold of velocity ($v \geq 0.2ms^{-1}$) and keeping the density definition $\sigma \geq 27.8$. Due to the high variability that the DSO presents, annual averages were mostly used to evaluate different quantities. One main focus when developing this set of diagnostics was in the comparison with observations. Qualitative comparisons of four specific sections along the path of the overflow were shown to be of significant usefulness. The other main focus was in the comparison between simulations. The diagnostic that summarizes and offers fast conclusions regarding the performance of a specific set of parameters is the domain bottom temperature. The calculation of the position (longitude, latitude, depth) of the core of the overflow was shown to be very powerful to follow the evolution of the overflow properties along its pass downstream from the sill.

The importance of horizontal and vertical resolution was tackled for z-coordinate. The increase of the vertical resolution when the horizontal resolution is kept fixed (at $1/12^\circ$) brought up an unexpected behaviour of the hydrostatic model: the overflow was being more diluted as the number of levels was increased. This was explained by an effect of the parameterization of the convective adjustment which makes the flow to follow the grid-slope rather than the bottom slope. The vertical resolution increase reduces the steepness of the grid slope with regard to the bottom-slope, and then the overflow waters tends to separate from the bottom which results in their greater dilution.

This behaviour, that was still observed at $1/60^\circ$ when the resolution increased from 46 to 75 levels, was no longer observed when high and coherent horizontal resolution were used (i.e. $1/60^\circ$ 300L). It was possible at such high resolution to start to represent small scale motions that enable a considerably better representation of the DSO. With such a high resolution the convective adjustment was limited to a small portion of the vein, and therefore it did not present an impediment for the correct representation of the overflow dynamics. The high resolution also permitted to resolve the vertical shear of the vein of fluid which yield a considerable improvement of the entrainment by the TKE mixing scheme. Of course the cost associated to such a high resolution is prohibitive in nowadays global simulations (the cost is very high even using a local refinement), and we therefore approached the problem of the representation of the DSO with a different vertical coordinate.

The vertical coordinate type chosen was a particular implementation of the generalized terrain following s-coordinates, the so called VQS coordinates which can combine a smooth s-coordinate defined by an enveloping bathymetry with a masking of the s-levels when the enveloping topography is different from the real one. First, it was shown that thanks to varying the level of smoothing of the enveloping bathymetry, a considerable reduction of the spurious currents linked

to numerical inaccuracies in the calculation of the horizontal pressure gradient (the so called Pressure Gradient Errors, PGE) was possible. Second the realistic results showed considerable improvements of the DSO representation with a very limited increase in the computational costs, since the overflow characteristics were still improved at $1/12^\circ$ when compared to the $1/60^\circ$ 300 levels case of the z-coordinate. The implementation of a different scheme to perform the diffusion of tracers along isopycnal surfaces (the Griffies triads) shown to be important for a correct representation of these dynamics.

Finally, we proposed a mixed vertical coordinate to locally treat the overflow problem, the local VQS hybrid coordinate. This vertical coordinate allows to define in a very simple way (a mere selection of points, through lines or any other method) the regions where s-coordinates have to be present. In this way we limited geographically the implementation of s-coordinates where necessary, taking advantage of the good representation of overflows and confining the issue of the spurious currents associated to PGE to that limited region. Its implementation increased the overall computational cost by only $\sim 10\%$ (without considering the cost associated with Griffies triads which also presents advantages in z-coordinates). The results showed that the main positive imprints of s-coordinates regarding the representation of overflows are preserved and that z-coordinates can be used for the rest of the domain. However, more developments are still needed to improve the connection between the regions of transition and this is mentioned in the perspectives.

Perspectives

As already mentioned, the implementation of z-coordinates at $1/60^\circ$ 300L is associated to very high computational costs, even when used locally. It would be interesting to analyze if the representation of overflows remains acceptable at resolutions of $\sim 1/20^\circ$ (which would explain the results of Behrens et al., 2017), and at $1/36^\circ$, which is the horizontal resolution foreseen for operational uses of NEMO. Another direction to carry on this work is the detailed study of the small scale motions observed at $1/60^\circ$ 300L, especially the dynamics of the sheared bottom boundary layer. The future planned NATL60 simulations represent a great opportunity to further investigate these processes.

The implementation of Griffies triads, which were revealed necessary in s-coordinates, also brought considerable improvements to the z-coordinate simulation at $1/12^\circ$ (not shown here). However, studies should be carried out to evaluate the impacts of this scheme on the overall solution. It would also be interesting to know the impact of the horizontal and vertical resolution with its implementation, a study that we did not have time to carry on.

AGRIF demonstrated once more its usefulness to do systematic studies of resolution with very limited modifications in the input data and model set-up. However, our simulations revealed continuity issues between the mother grid (coarser resolution) and the child grid (fine resolution) with increasing vertical resolution (300 levels) that we could not explain. In addition, it would have been of great interest in this study to have the possibility of performing a vertical refinement and/or the possibility to change the vertical grid inside the AGRIF zoom.

Regarding the s-coordinates, our results suggest that a high dissipation of the small spatial scales could seriously reduce the growth of the spurious PGE driven currents. Therefore, it would be interesting to assess the impact of a higher order viscosity (bi-biharmonic for example).

It is likely that the connection of the local s-z hybrid coordinates can be greatly improved, the implementation presented here being a "first attempt". One should try on the one hand to limit the extension of the transition region and on the other hand to reduce the saw-tooth and improve the connection between grids. Some work has already started, in which only a certain number of vertical levels is used on the local implementation, and partial steps added in the transition region. In this way, the saw-tooth still presents a problem in shallow areas, and some effort should be dedicated to improving the masking to reduce again the saw-tooth problem.

The natural continuation of this work is the implementation of the local s-coordinate in a larger

configuration such as the whole north Atlantic to treat other major overflows (Mediterranean outflow, Iceland-Scotland overflow, etc.) or in the global ORCA12 model configuration in other locations where the flow is highly constrained by the topography (around Antarctica, in ice shelves and over the continental shelves of polar oceans). Some work has already started, with the objective to quantify if the improvements of the overflow demonstrated in this work have a significant impact on the large scale circulation and leads to significant correction of the biases found in most global or basin scale simulations.

The main message of this work is that by changing the vertical coordinate type, where it is needed, considerable improvements can be obtained at very reasonable computational costs. The implementation of isopycnal coordinates and its implementation in conjunction with s and z coordinates (ALE coordinates), appears as a very interesting possibility in that matter that should be tackled in the future.

Part VII
Appendix

Chapter 12

Vertical levels distribution

We show here the cell thickness as a function of depth for the different number of vertical levels used in z-coordinates.

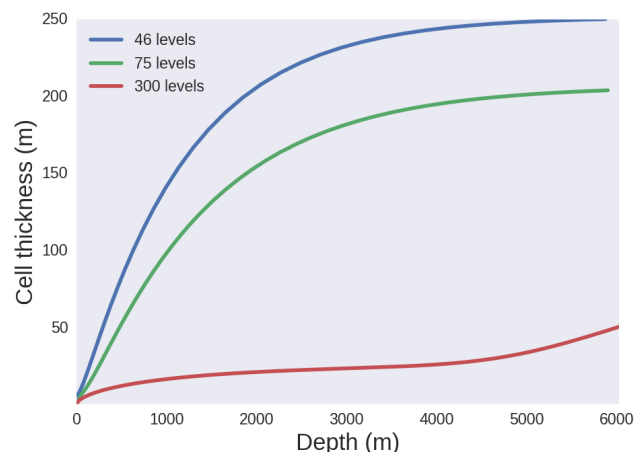


Figure 12.1: Cell thickness distribution as a function of depth for the 46L, 75L and 300L cases in z-coordinates

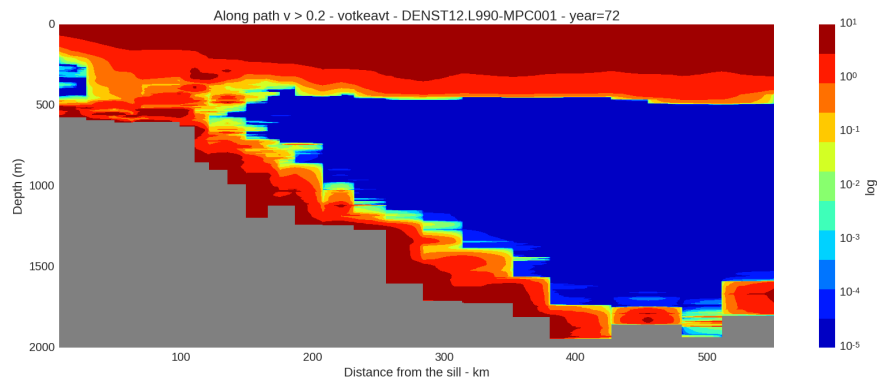
Chapter 13

Additional simulations

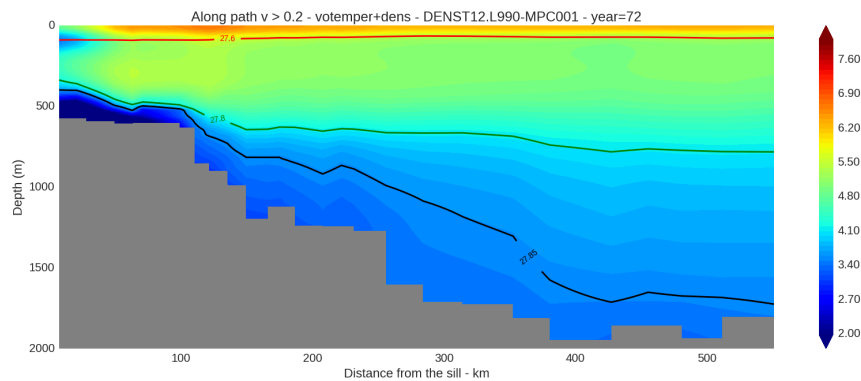
We show here the results of some additional simulations that might be of interest but are not absolutely needed to explain our results.

13.1 The 990L case

In order to try to corroborate what was exposed before we pushed the limit of the present vertical number of levels present in simulations. A test with 990 vertical levels was conducted at $1/12^\circ$. The distribution of levels was set to be constant with a cell thickness of $3.3m$



(a)



(b)

Figure 13.1: For the 990L case, annual mean values along the path of the vein of a) Vertical diffusivity b) Temperature

In figure 13.1a we observe how the behavior observed before for the 300 levels is intensified. In fact, the vertical mixing is increased all along the vein. The mixed layer also presents higher values of vertical diffusivity and a strong discontinuity in the vertical diffusivity value that jumps from a value between $1m^2s^{-1}$ to $10m^2s^{-1}$ to the background value of $10^{-5}m^2s^{-1}$ within a few grid points. In the E12L300 simulation this transition is done in a few hundred meters. A possible explanation is provided. In NEMO v3.6 the formulation of the vertical subgrid scale physics is the same whatever the vertical coordinate is, and given by

$$D_u = \frac{1}{e_{3u}} \partial_k \left(\frac{A^v}{e_{3uw}} \partial_{k+1/2}(u) \right) \quad (13.1)$$

Which in a case of a constant cell thickness (e_3) and a constant vertical diffusivity coefficient (A^v , for example in the mixed layer where we have the EVD always present in winter) the expression becomes (equation 6.28 of NEMO book v3.6)

$$D_u = \frac{A^v}{e_{3u}e_{3uw}} \partial_k (\partial_{k+1/2}(u)) \quad (13.2)$$

The interesting point of this expression is that if we make the cell thickness very small without changing the vertical diffusivity, the preponderance of D_u in the integration might increase considerably, and would become a predominant aspect of our solution.

One additional test was conducted changing the EVD value from $10m^2s^{-1}$ to $0.1m^2s^{-1}$ with no significant changes in the overall solution. The study was interrupted here since the number of issues associated with such a high vertical resolution at this horizontal resolution seemed to demand a large quantity of time. In order to introduce the following results we just mention the fact that the sea ice thickness was rapidly reduced and the cold waters observed in figure 13.1b seemed to come predominantly from this ice dilution.

13.2 Adaptive EVD in 1/12° 300L

In order to test the impact of the previous idea regarding the EVD, a modification on the code was included with the objective of setting the value of the EVD according to the cell thickness. We used a value of $10m^2s^{-1}$ as an upper bound value for those cell thicknesses bigger or equal to $250m$ and a lower bound value of $0.1m^2s^{-1}$ for those cell thicknesses equal or smaller to $10m$. The transition between those two values was set to be quadratic in order to try to keep as constant as possible the relationship $A^v/e_{3u}e_{3uv}$. Both options on tracer only and on tracer and momentum were coded. The test was done using 300 vertical levels in the 1/12° case. The EVD was set to be used on tracers and momentum. The rest of the parameters were kept equal to the reference run.

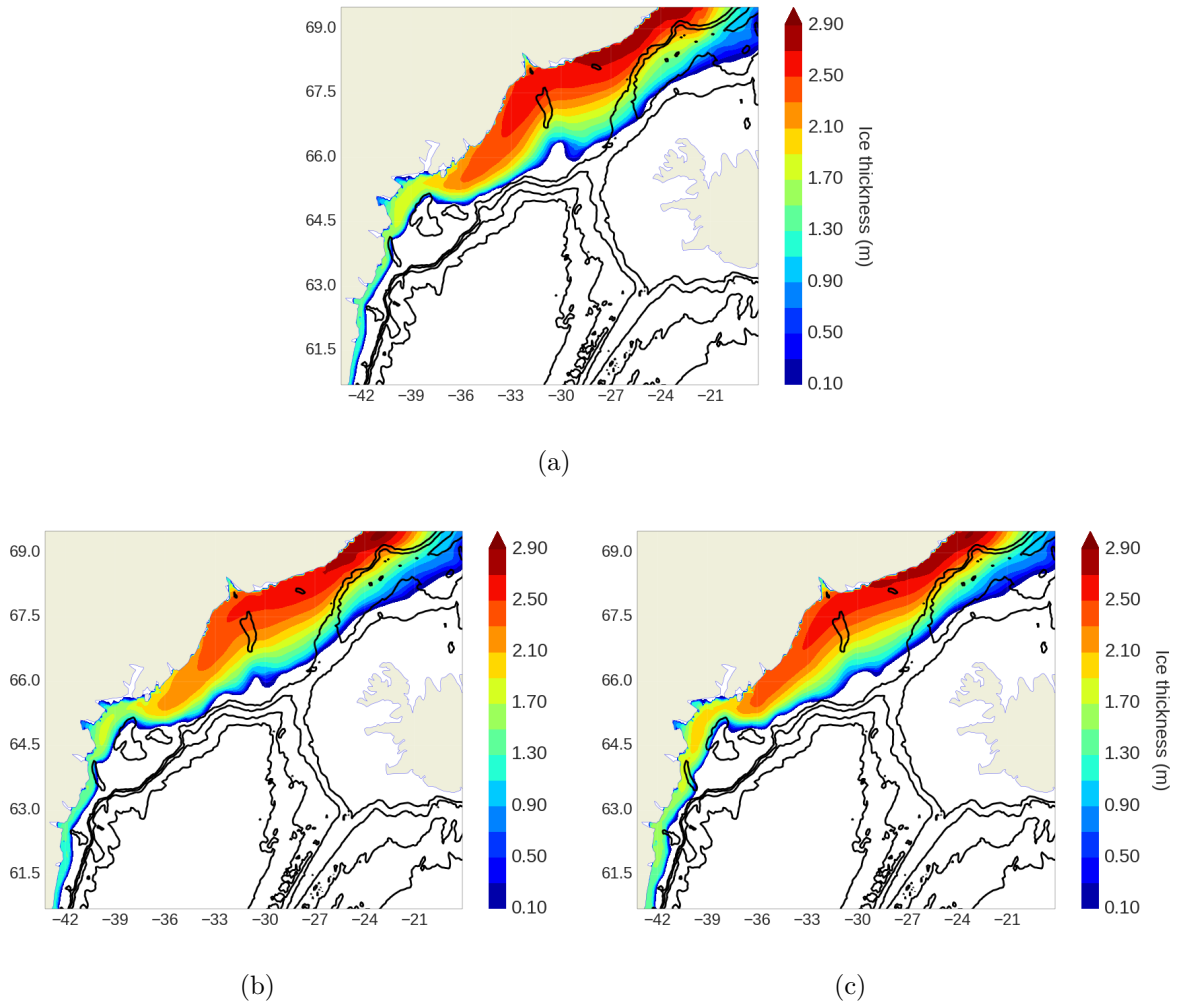


Figure 13.2: Ice thickness for the 24/Apr/72 (114th day of the first year) a) *E12L46* b) *E12L300* c) *E12L300 + adaptive EVD*

One interesting aspect of these simulations is the impact of the sea ice thickness depending the vertical resolution and the value of the EVD coefficient. On figure 13.2a we observe the sea ice thickness for a given daily mean of the reference configuration (46L). When we increased the resolution to 300L we observed a diminution of the sea ice thickness (figure 13.2b) close to the northern boundary and a clear loss of around $20cm$ around $66^\circ N$. We then implemented the adaptive EVD in the 300L case (figure 13.2c) and we observed that the thickness close to the northern boundary was closer to the values observed in the reference simulation. We

also observed higher thickness around 66°N , and the resulting ice thickness that arrived to the southern boundary was bigger. It is important to note that this 20cm change in the sea ice happened on less than four months of the integration. Therefore, care must be taken when defining the value of the EVD coefficient according to the vertical resolution in the mixed layer.

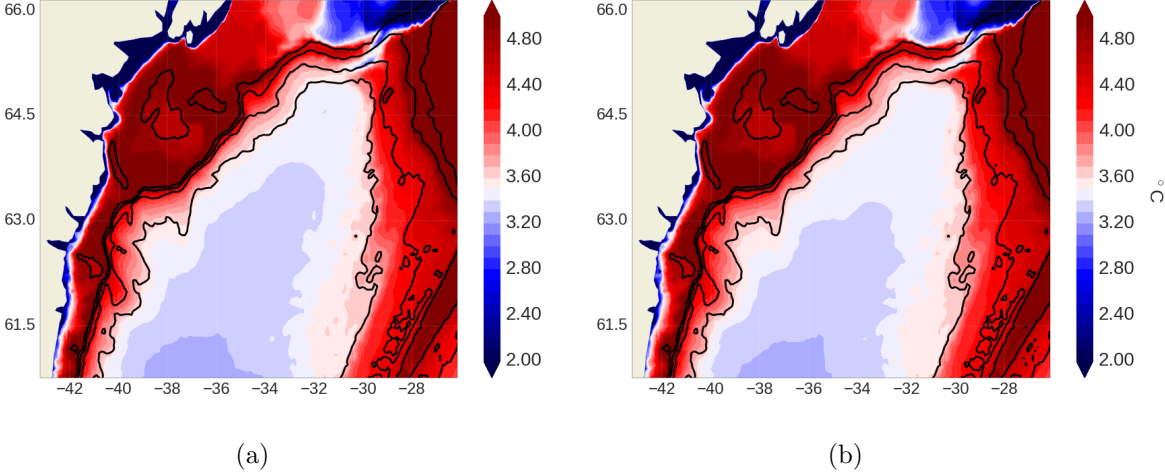


Figure 13.3: Annual mean of the bottom temperature of the 5th year of calculation a) E12L300 b) E12L300 + adaptive EVD

When comparing the results of the bottom temperature (figure 13.3) between the runs with and without the adaptive EVD, we observe that the run with the adaptive EVD presents a warmer bottom. This is not surprising, since a smaller vertical mixing coefficient makes the process of convective adjustment (which is the process that mainly drives the overflow downward at these resolutions) more inefficient. This might lead to a differentiation in the EVD coefficient whether we consider a point in the mixed layer or not.

List of Figures

- 1.1 *Circulation scheme in the region of the Denmark Strait, from Appen et al., 2014* 14
- 1.2 *Planning of the 111 ship campaigns studied in Mastropole et al., 2017. A color was attributed whether there was a non-bolus occupation (light red), a bolus occupation (light blue) or a short occupation (gray)* 15
- 1.3 *Potential temperature profile in colors and isolines of potential density (the magenta line corresponds to a density value of 27.8) showing a) presence and b) absence of a bolus of overflow water. From Mastropole et al., 2017* 16
- 1.4 *Sill of the Denmark Strait, hydrographic sections a) Potential temperature profile in colors and isolines of potential density (the magenta line corresponds to a density value of 27.8) showing the mean of all the available data between 1990 and 2012, from (Mastropole et al., 2017) b) Normal velocity to the section, in blue southward velocities and with a thick blue line the 27.8 density is contoured, from Jochumsen et al., 2013* 16
- 1.5 *Layout of the different sections in the Irminger basin of the ASOF project (Quadfasel, 2004)* 17
- 1.6 *Hydrographic sections number 1 in Quadfasel, 2004, which partially covers the Dohrn Bank array a) Potential temperature b) Potential density* 17
- 1.7 *Spill jet section with normal velocity in colors (in cms^{-1}), from Brearley et al., 2012. Density values are contoured. In white thick lines the geographical and density references to constrain both the spill jet and the DSO a) Section performed in October 2003 b) Section performed in August 2004* 18
- 1.8 *Hydrographic sections obtained in Quadfasel, 2004 at the TTO section (the images have been modified to include latitude values) a) Potential temperature b) Potential density* 19
- 1.9 *Hydrographic sections obtained in Quadfasel, 2004 at the Angmagssalik section (the images have been modified to include latitude values) a) a) Potential temperature b) Potential density* 19
- 1.10 *a) Position of the different hydrographic sections in Girton and Sandford, 2003 b) Depth of the DSO as a function of distance from the sill, from Girton and Sandford, 2003 (calculated using equations 1.1 and 1.2)* 20
- 1.11 *Microstructure measurement of the DSO, from Paka et al., 2013* 21

1.12	Main mooring arrays deployments to study the DSO, being the most important ones (from north to south) the sill array, the Dohrn Bank array, the TTO array and the Angmagssalik array. From Dickson et al., 2008.	22
1.13	Section across the Denmark Strait sill with density in colours, from Macrander et al., 2007. The letters A, B and C indicates the mooring positions, the black thick line denotes the 27.8 isopycnal	23
1.14	a) Transport for the mooring deployments at the sill from Jochumsen et al., 2013. The blue color is assigned when data of the two moorings are available and magenta when only data from the DS1 mooring is available. Light colors are used for the data and solid colors for the filtered version of the data using a hanning filter with a window of 20 days b) Mean transport for each deployment period (horizontal lines), with standard deviation (vertical lines) of the 20-day low pass filtered time series	23
1.15	Bottom Temperature values from Voet and Quadfasel, 2010. The upper panel shows the value obtained from hydrographic sections and the lower panel those obtained by mooring arrays	24
1.16	a) Mooring setup in Jochumsen et al., 2015 b) Mean values of the bottom temperature at the moorings	25
1.17	TS diagram for low-pass filtered mooring records data. The squares depict the average values, the thick horizontal and vertical lines the standard deviation of the mean, and the thin lines the maximum range of properties, from Jochumsen et al., 2017	25
1.18	Scheme of the main physical processes in overflows, from Legg et al., 2009	26
1.19	Ozmidov scale versus Thorpe scale for the Denmark Strait Overflow. Measurements taken from a place next to the Dohrn Bank section (30°W,65°N), from Paka et al., 2013	27
2.1	Schematic of the BBL scheme present in NEMO, from DeMiranda, 2003. The green line denotes the advective part of the scheme, and the red one the diffusive part	28
2.2	Schematic of the DOME configuration, from Reckinger et al., 2015	29
2.3	Different BBL schemes implemented in Snow et al., 2015	30
2.4	Scheme of traditional coordinate types from Griffies, 2003	30
5.1	a) Model domain. In color the ocean depth. The 250, 500m, 1000m, 1500m and 2000m isobaths are contoured. The gray box indicates the region where the grid refinement (to arrive to 1/60°) is applied in some simulations. The point in magenta denotes the reference point chosen for the sill. The white lines denotes the section used for the different calculations in this work (in black the most relevant ones)	41

5.2	<i>Initial condition (January 5 of year 72 of the ORCA12 run, mean over 5 days) a) Bottom temperature. In white the line where the information of figures b and c is obtained. Isobaths 500m, 1000m, 1500m and 2000m are contoured b) Temperature section with temperature contours in white c) Salinity section. Density contours in colors (red for 27.6, green for 27.8 and black for 27.85)</i>	43
5.3	<i>Path of the overflow calculated using different velocity thresholds and different density thresholds. Color indicates the volume transport below 27.80 isopycnal. The magenta lines correspond to a threshold value of 0.2ms^{-1}, black lines 0.1ms^{-1} and white lines 0ms^{-1} a) Using a density threshold of 27.80: annual mean values b) Using a density threshold of 27.85: annual mean values c) Density threshold 27.80: daily snapshot (10/June of year five). Observe the impact of the eddies in the path of the overflow for the velocity thresholds 0ms^{-1} and 0.1ms^{-1} d) Normal velocity to section 18 with density contours, daily snapshot (7/January of year five). $1/60^\circ$ horizontal resolution and 300 vertical levels (child grid). Points calculated with different velocity thresholds according to 5.2 and 5.1. Point-dashed white lines denotes 0ms^{-1} velocity contour, 0.1ms^{-1} velocity contour in solid white lines and 0.2ms^{-1} velocity contour in dashed white lines.</i>	45
6.1	<i>Reference simulation, annual mean of year 5 at the Sill a) Normal velocity in colors with specific velocity values in contours (point-dashed white lines denotes 0ms^{-1} velocity contour, 0.1ms^{-1} velocity contour in solid white lines and 0.2ms^{-1} velocity contour in dashed white lines) b) Temperature in colors and specific temperature values in white contours. Density values in contours (27.6 in red, 27.8 in green and 27.85 in black)</i>	47
6.2	<i>Time evolution of the volume transport of southward ($v > 0\text{ms}^{-1}$) waters denser than 27.80 in the reference simulation. In red daily values and in blue the smoothed time series (20 day hanning window)</i>	48
6.3	<i>Reference simulation, annual mean temperature of year 5 with temperature and density contours (except in d) a) Section 14 (Dohrn Bank array) b) Section 18 (spill jet section) c) Section 27 (Angmassalik array) d) Bottom</i>	49
6.4	<i>Reference simulation, annual mean of year 5 a) Minimum mean temperature value for each array. Observations from (Voet and Quadfasel, 2010) (Obs VQ2010) b) Transport along the path of the overflow for different velocity thresholds (light thin lines) and their associated tendency lines (dark large lines). Observations from (Dickson and Brown, 1994) (DB94). For both figures, the first point corresponds to array 1 (the sill), the second point to array 14 (the Dohrn Bank array), the third point to array 22 (the TTO array) and the fourth to array 27 (the Angmassalik array)</i>	50
6.5	<i>Temperature annual mean of year 5 along the path of the overflow (magenta line in figure 5.3a). Density values in contours (27.6 in red, 27.8 in green and 27.85 in black). Reference simulation.</i>	51
6.6	<i>Vertical diffusivity coefficient annual mean of year 5 along the path of the overflow (magenta line in figure 5.3a). Density values in contours (27.6 in red, 27.8 in green and 27.85 in black). Reference simulation.</i>	51

7.1	<i>E12L46, annual mean of the bottom temperature of year 5, in simulations with a) PS with BBL b) PS without BBL c) FS with BBL d) FS without BBL. Isobaths 500m, 1000m, 1500m and 2000m are contoured</i>	56
7.2	<i>Annual mean of the bottom temperature of year 5 at 1/12° with EVD applied on tracers only a) E12L46 b) E12L75 c) E12L300. Isobaths 500m, 1000m, 1500m and 2000m are contoured</i>	57
7.3	<i>E12L300 annual mean of the bottom temperature of year 5, using a) TKE scheme with no EVD b) Constant background diffusivity of $1.2 \times 10^{-5} \text{m}^2 \text{s}^{-1}$ and EVD c) GLS scheme with EVD d) GLS scheme with no EVD. Isobaths 500m, 1000m, 1500m and 2000m are contoured</i>	58
7.4	<i>Annual mean of the bottom temperature of year 5 at 1/12° with EVD applied on tracers only a) A12L46 b) A12L75 c) A12L300. Isobaths 500m, 1000m, 1500m and 2000m are contoured. In white lines the region where the local refinement is applied</i>	59
7.5	<i>Annual mean of the bottom temperature of year 5 at 1/12° with EVD applied on tracers and momentum (EVD=1) a) E12L46 b) E12L75 c) E12L300. Isobaths 500m, 1000m, 1500m and 2000m are contoured</i>	60
7.6	<i>Annual mean of the bottom temperature of year 5 at 1/12° with EVD applied on tracers and momentum (EVD=1) a) A12L46 b) A12L75 c) A12L300. Isobaths 500m, 1000m, 1500m and 2000m are contoured. In white lines the region where the local refinement is applied</i>	61
7.7	<i>Annual mean of the bottom temperature of year 5 at 1/12° with no slip lateral boundary condition a) E12L46 b) E12L75 c) E12L300. Isobaths 500m, 1000m, 1500m and 2000m are contoured</i>	62
7.8	<i>Annual mean of the bottom temperature of year 5 at 1/12° with no slip lateral boundary condition a) A12L46 b) A12L75 c) A12L300. Isobaths 500m, 1000m, 1500m and 2000m are contoured. In white lines the region where the local refinement is applied</i>	63
7.9	<i>Annual mean of the bottom temperature of year 5 at 1/12° using the EEN vector formulation for the momentum advection (EVD=1) a) E12L46 free-slip b) A12L300 free-slip c) A12L300 no-slip. Isobaths 500m, 1000m, 1500m and 2000m are contoured. In white lines the region where the local refinement is applied . . .</i>	64
7.10	<i>Transport calculated along the 27 sections shown in 5.3 and its correspondent tendency lines for a) 1/12° simulations b) 1/12°+agrif simulations. In pointy black line the transport values presented in Dickson and Brown, 1994 for the sill, the Dohrn Bank, TTO and Angmassalik arrays.</i>	66
7.11	<i>a) Minimum mean bottom temperature of the 5th year of calculation of the grid points conforming arrays 1, 15, 22 and 27 (figure 5.3). In pointy magenta line the transport values presented in Voet and Quadfasel, 2010 for the sill, the Dohrn Bank, TTO and Angmassalik arrays. b) Vertical position of the center of the vein. In pointy magenta line the values found by Girton and Sandford, 2003. . .</i>	67

7.12	<i>Scheme representing the successive operations for a particle at the top of a seamount in z-coordinates which is advected in the horizontal and the vertical a) For a vertical resolution equal to the horizontal one b) For an increased vertical resolution of two times</i>	69
7.13	<i>Annual mean of year 5 of the vertical diffusivity along the path of the vein calculated for each simulation a) E12L46 b) A12L46 c) E12L300 d) A12L300. The values of the depth of the vein can be found in figure 7.11b. For figures b and d the vertical white lines denotes the end of the AGRIF zoom.</i>	71
7.14	<i>Annual mean of year 5 of the vertical diffusivity at section 18 a) E12L300 b) A12L300. In white contours isopycnals 27.80 and 27.85. The three points in colors are the locations were the vertical profiles are plotted in figures 7.16 and 7.15</i>	72
7.15	<i>Vertical profiles of downslope velocity for 12/March of year 5 at section 18 at the locations indicated in figure 7.14b a) A12L46 b) A12L75 c) A12L300 d) E12L300</i>	73
7.16	<i>Vertical profiles of different quantities for A12L300 for 02/January hour 3 of year 5 at section 14 for the location indicated with a red dot in figure 7.18a a) Temperature b) Salinity no c) Cross-slope velocity d) Along-slope velocity</i>	73
7.17	<i>Time evolution of the volume transport of southward ($v > 0\text{ms}^{-1}$) waters denser than 27.80 in A12L300. In red daily values and in blue the smoothed time series (20 day hanning window)</i>	75
7.18	<i>A12L300 simulation, annual mean temperature of year 5 with temperature and density contours a) Section 14 (Dohrn Bank array). The red dot indicates the location of the profile shown in figure 7.16 b) Section 18 (spill jet section)</i>	75
7.19	<i>A12L300 simulation, annual mean temperature of year 5 with temperature and density contours a) Section 22 (TTO array) b) Section 27 (Angmassalik array) .</i>	76
7.20	<i>Temperature annual mean of year 5 along the path of the overflow (magenta line in figure 5.3a). Density values in contours (27.6 in red, 27.8 in green and 27.85 in black). Reference simulation.</i>	76
7.21	<i>Annual mean TS diagram of year 5 of a) E12L300 (reference simulation) b) A12L300. Comparable with figure 1.17 from Jochumsen et al., 2015 c) Configuration domain with the location of the points. The thick horizontal and vertical lines are the mean values plus/minus one standard deviation, and the thin lines are the maximum range of properties.</i>	77
7.22	<i>Difference of the TS diagrams between A12L300 and E12L46 annual mean of year 5 at section 27 (Angmagssalik array). Density values in contours.</i>	78
7.23	<i>A12L300 simulation, hourly snapshots of bottom temperature a) 23/April year 3 - 9h b) 15h after c) 26h after d) 39h after. The 500m, 1000m, 1500m and 2000m isobaths are contoured.</i>	79
7.24	<i>Hourly snapshot of the relative vorticity at 540m a) E12L300 b) A12L300</i>	80
8.1	<i>Scheme of the terrain following coordinate for a given depth (h). The depth of a given vertical point is $H(k)$ and the cell thickness associated to this point is $\Delta z(k)$. The superior line represents the surface.</i>	84

8.2	<i>SH94 Stretching as a function of 75 vertical levels and 3350m maximum depth (approximate maximum depth in the DENST12 configuration), $\theta = 6.0$ and different values of b (ranging from 0.1 to 0.9) a) Cell thickness b) Level depth . . .</i>	86
8.3	<i>Cell thickness as a function of levels with 75 vertical levels and 3350m maximum depth (approximate maximum depth in the DENST12 configuration) JC17 stretching</i>	87
8.4	<i>Detail of the resulting masking in an example section. In colors the normal velocity. The red thick line represents the real bathymetry and the black thick line represents the enveloping bathymetry. In order to improve the visibility of the plot not all the vertical and horizontal grid points are plotted a) $rx_{0M} = 0.05$ case b) $rx_{0M} = 0.2$ case</i>	90
8.5	<i>Stratification used for the PGE test case, from Siddorn and Furner, 2013</i>	91
8.6	<i>Initial response of the series of sensitivity tests using the DENST12 configuration and $rx_{0M} = 0.05$. Hourly mean values of the first 5 days a) Maximum of the absolute zonal velocity in the domain b) Mean of the absolute zonal velocity in the domain</i>	92
8.7	<i>Long-term response of the series of sensitivity tests using the DENST12 configuration and $rx_{0M} = 0.05$. Daily mean values a) Absolute maximum zonal velocity in the domain b) Absolute mean zonal velocity in the domain</i>	93
8.8	<i>Available levels for calculation (mbathy) for our 75 vertical level tests a) $rx_{0M} = 0.05$ case b) $rx_{0M} = 0.2$ case</i>	95
8.9	<i>Maximum values in the vertical of rx_1 for each point in the grid a) $rx_{0M} = 0.05$ case b) $rx_{0M} = 0.2$ case</i>	95
8.10	<i>Daily mean values for the comparison between enveloping bathymetries built with $rx_{0M} = 0.05$ and $rx_{0M} = 0.2$ a) Maximum of the absolute zonal velocity in the domain b) Mean of the absolute mean zonal velocity in the domain</i>	96
8.11	<i>First hour mean value of the zonal velocity in cms^{-1} using SH94 stretching and $rx_{0M} = 0.2$ a) At the surface b) At the 24th level</i>	96
8.12	<i>a) Available levels for calculation (mbathy) b) Maximum values in the vertical of rx_1 for each point in the grid. Both for $rx_{0M} = 0.2$ and JC17 stretching</i>	98
8.13	<i>Daily mean values for the comparison between SH94 and JC17 stretchings, enveloping bathymetries built with $rx_{0M} = 0.2$ a) Maximum of the absolute zonal velocity in the domain b) Mean of the absolute zonal velocity in the domain . . .</i>	98
8.14	<i>Hourly mean values for the comparison between SH94 and JC17 stretchings, enveloping bathymetries built with $rx_{0M} = 0.2$ a) Maximum of the absolute zonal velocity in the domain b) Mean of the zonal velocity in the domain</i>	99
8.15	<i>Maximum values in the vertical of rx_1 for each point in the grid in a run with the implementation of AGRIF in s-coordinates. a) Mother grid b) Child grid</i>	100
9.1	<i>Annual mean of the bottom temperature of year 5 at $1/12^\circ$ a) SE12-SH94-R005 b) SE12-SH94-R01 c) SE12-SH94-R02. Isobaths 500m, 1000m, 1500m and 2000m are contoured</i>	103

9.2	<i>Annual mean of the bottom temperature of year 5 at 1/12° a) SE12-JC17-R02 b) figure 9.2a minus 9.1c. Isobaths 500m, 1000m, 1500m and 2000m are contoured</i>	104
9.3	<i>Annual mean of the bottom temperature of year 5 at 1/12° a) SA12-SH94-R02 b) SA12-JC17-R02. Isobaths 500m, 1000m, 1500m and 2000m are contoured</i>	105
9.4	<i>Difference of the bottom temperature between solutions a) figure 9.3a minus 9.1c (SH94 stretching) b) figure 9.3b minus 9.2a (JC17 stretching). Isobaths 500m, 1000m, 1500m and 2000m are contoured</i>	105
9.5	<i>Annual mean of the bottom temperature of year 5 at 1/12° a) SE12-SH94-R005-G b) SE12-SH94-R02-G c) SE12-JC17-R02-G d) SE12-JC17-R02-G. Isobaths 500m, 1000m, 1500m and 2000m are contoured</i>	106
9.6	<i>VQS simulations with the default formulation on tracer diffusion a) Minimum mean bottom temperature of the 5th year of calculation of the grid points conforming arrays 1, 15, 22 and 27 (figure 5.3). In pointy magenta line the transport values presented in Voet and Quadfasel, 2010 for the sill, the Dohrn Bank, TTO and Angmassalik arrays. b) Vertical position of the center of the vein. In pointy magenta line the values found by Girton and Sandford, 2003.</i>	108
9.7	<i>VQS simulations with the Griffies triads a) Minimum mean bottom temperature of the 5th year of calculation of the grid points conforming arrays 1, 15, 22 and 27 (figure 5.3). In pointy magenta line the transport values presented in Voet and Quadfasel, 2010 for the sill, the Dohrn Bank, TTO and Angmassalik arrays. b) Vertical position of the center of the vein. In pointy magenta line the values found by Girton and Sandford, 2003.</i>	109
9.8	<i>Overflow transport calculated along the 27 sections shown in 5.3 and its correspondent tendency lines using a) the default formulation on tracer diffusion b) Griffies triads. In pointy black line the transport values presented in Dickson and Brown, 1994 for the sill, the Dohrn Bank, TTO and Angmassalik arrays. The most performant simulation on z-coordinates (A12L300) was added as a reference.</i>	109
9.9	<i>Simulation SE12-JC17-R02-G: Time evolution of the southward volume transport ($v > 0\text{ms}^{-1}$) of waters denser than 27.80 at the sill. In red daily values, in blue the smoothed time series (20 day Hanning window). For each year the annual mean with the standard deviation is indicated.</i>	111
9.10	<i>Annual mean temperature of year 5 with temperature and density contours at section 14 (Dohrn Bank array, $\sim 250\text{km}$ from the sill) a) SE12-JC17-R02-G. The three color dots indicate the location of the 3 profiles shown in figure 9.16 b) section 14 SA12-JC17-R02-G.</i>	111
9.11	<i>Annual mean temperature ($^{\circ}\text{C}$) of year 5 with temperature (white) and density (color) contours at section 18 (spill jet section, $\sim 300\text{km}$ from the sill) a) SE12-JC17-R02-G b) Section 18 SA12-JC17-R02-G</i>	112
9.12	<i>Annual mean temperature ($^{\circ}\text{C}$) of year 5 with temperature (white) and density (color) contours at section 22 (TTO array, $\sim 400\text{km}$ from the sill) a) SE12-JC17-R02-G b) section 22 SA12-JC17-R02-G</i>	112

9.13	<i>Annual mean temperature (°C) of year 5 with temperature (white) and density (color) contours at section 27 (Angmagsalik array, ~ 500km from the sill) a) SE12-JC17-R02-G b) Section 27 SE12-JC17-R02-G</i>	113
9.14	<i>SE12-JC17-R02 simulation. Temperature annual mean of year 5 along the path of the overflow (magenta line in figure 5.3a). Density values in contours (27.6 in red, 27.8 in green and 27.85 in black).</i>	113
9.15	<i>SA12-JC17-R02 simulation. Temperature annual mean of year 5 along the path of the overflow (magenta line in figure 5.3a). Density values in contours (27.6 in red, 27.8 in green and 27.85 in black).</i>	114
9.16	<i>Profiles of different quantities for SE12-JC17-R02 for 04/April hour 10 of year 5 at section 14 for the locations indicated in figure 9.10a a) Temperature b) Salinity no c) Cross-slope velocity d) Along-slope velocity</i>	114
9.17	<i>Annual mean TS diagram of year 5 of a) SE12-JC17-R02 b) SA12-JC17-R02. Comparable with figure 1.17 from Jochumsen et al., 2015</i>	115
9.18	<i>Difference of the TS diagrams, annual mean of year 5 at section 27 (Angmagssalik array) a) between SE12-JC17-R02-G and E12L46 b) between SA12-SH94-R02-G and E12L46</i>	115
10.1	<i>Local sigma implementation in the SL12-SH94-G simulation a) Enveloping bathymetry in meters. The different circles indicate the different regions, having pure VQS coordinates inside the magenta circle and pure z-coordinates outside the blue circle. The white line indicates the section shown in figure 10.2. b) Maximum values in the vertical of the rx_1 parameter (see section 8.1 for explanation).</i>	121
10.2	<i>Grid and topography along the section indicated in white in figure 10.1a. Areas in light gray represent the realistic bottom. The vertical colored dashed lines indicate the circles. For clarity only a few horizontal and vertical gridlines are plotted. In red/blue colors and just as a reference, the velocity normal to the section is plotted.121</i>	
10.3	<i>Annual mean of the bottom temperature of year 5 at 1/12° a) SE12-SH94-R02-G (full domain s) b) SL12-SH94-G (local s-coordinates). Isobaths 500m, 1000m, 1500m and 2000m are contoured, as well as the different circles that denotes the different coordinates regions for the local s-coordinates.</i>	123
10.4	<i>Full domain and local s-coordinates simulations using Griffies triads. a) Minimum mean bottom temperature of the 5th year of calculation at the grid points co-located with observational arrays 1, 14, 22 and 27 (figure 5.3). In magenta line the transport values presented in Voet and Quadfasel, 2010 for the sill, the Dohrn Bank, TTO and Angmassalik arrays. b) Vertical position of the center of the vein. In pointy magenta line the values proposed by Girton and Sandford, 2003.</i>	123
10.5	<i>Transport calculated along the 27 sections shown in 5.3 and its correspondent tendency lines using of the full domain s-coordinate and local s-coordinates simulations using Griffies triads. In pointy black line the transport values presented in Dickson and Brown, 1994 for the sill, the Dohrn Bank, TTO and Angmassalik arrays.</i>	124

10.6	<i>SL12-SH94-G simulation, annual mean temperature ($^{\circ}\text{C}$) of year 5 in colors, with temperature (white) and density (color) contours a) Section 22 (TTO array, $\sim 400\text{km}$ from the sill, partly in the TrZ region) b) Section 27 (Angmagssalik array, $\sim 500\text{km}$ from the sill, in the TrZ region). In light gray the enveloping bathymetry and in dark gray the real model bathymetry.</i>	125
11.1	<i>Implementation of local VQS Hybrid coordinate. In this case the PuS and TrS regions are defined using two lines (defined by the white dots). The region inside the magenta contour is the PuS region, the region between the magenta and the black contour is the TrS region, the region between the black and the blue contour is the TrZ region and the region outside the blue contour is the PuZ region. A connection slope of 2.5° was used to connect from the black contour to the blue contour. The maximum domain depth (blue contour) is 5800m. The radius of the thicker line is 10 grid points and the for the thinner line is 3 grid points.</i>	128
11.2	<i>Local sigma implementation in the simulation for a bad connection case a) Enveloping bathymetry in meters. The different circles indicate the different regions, having pure VQS coordinates inside the magenta circle and pure z-coordinates outside the region denoted with blue b) Annual mean of the bottom temperature of year 5 at $1/12^{\circ}$</i>	129
12.1	<i>Cell thickness distribution as a function of depth for the 46L, 75L and 300L cases in z-coordinates</i>	136
13.1	<i>For the 990L case, annual mean values along the path of the vein of a) Vertical diffusivity b) Temperature</i>	137
13.2	<i>Ice thickness for the 24/Apr/72 (114th day of the first year) a) E12L46 b) E12L300 c) E12L300 + adaptive EVD</i>	139
13.3	<i>Annual mean of the bottom temperature of the 5th year of calculation a) E12L300 b) E12L300 + adaptive EVD</i>	140

List of Tables

7.1	<i>Reference names of the configurations</i>	55
9.1	<i>Reference names of the simulations</i>	101
9.2	<i>Reference names of the simulations with Griffies triads</i>	101

References

- Appen, Wilken-Jon von, Inga M. Koszalka, Robert S. Pickart, Thomas W.N. Haine, Dana Mastropole, Marcello G. Magaldi, Hédinn Valdimarsson, James Girtton, Kerstin Jochumsen, and Gerd Krahnemann (2014). “The East Greenland Spill Jet as an important component of the Atlantic Meridional Overturning Circulation.” In: *Deep-Sea Research I* 92 75–84.
- Barnier, Bernard, Gurvan Madec, Thierry Penduff, Jean-Marc Molines, Anne-Marie Treguier, Julien Le Sommer, Aike Beckmann, Arne Biastoch, Claus Böning, Joachim Dengg, Corine Derval, Edmée Durand, Sergei Gulev, Elizabeth Remy, Claude Talandier, Sébastien Theetten, Mathew Maltrud, Julie McClean, and Beverly De Cuevas (2006). “Impact of partial steps and momentum advection schemes in a global ocean circulation model at eddy-permitting resolution.” In: *Ocean Dynamics* 56: 543–567. DOI: 10.1007/s10236-006-0082-1.
- Bates, M. L., S. M. Griffies, and M. H. England (2012). “A dynamic, embedded Lagrangian model for ocean climate models. Part I: Theory and implementation.” In: *Ocean Model*.
- Beckmann, A. and R. Doscher (1997). “A Method for Improved Representation of Dense Water Spreading over Topography in Geopotential-Coordinate Models.” In:
- Beckmann, Aike and Dale B. Haidvogel (1993). “Numerical Simulation of Flow around a Tall Isolated Seamount. Part I: Problem Formulation and Methodology.” In: *Journal of Physical Oceanography*.
- Behrens, E., K. Våge, B. Harden, A. Biastoch, and C. W. Böning (2017). “Composition and variability of the Denmark Strait Overflow Water in a high-resolution numerical model hindcast simulation.” In: *J. Geophys. Res. Oceans*, 122. DOI: 10.1002/2016JC012158.
- Brearley, Alexander, Robert S. Pickart, Hédinn Valdimarsson, Steingrímur Jonsson, Raymond W. Schmitt, and Thomas W.N. Haine (2012). “The East Greenland boundary current system south of Denmark Strait.” In: *Deep-Sea Research I* 63 (2012) 1–19.
- Brodeau, L., B. Barnier, A.M. Treguier, T. Penduff, and S. Gulev (2009). “An ERA40-based atmospheric forcing for global ocean circulation models.” In: *Ocean Modelling*, 31, 88–104. DOI: 10.1016/j.ocemod.2009.10.005.
- Cenedese, C., J. A. Whitehead, T. Ascarelli, and M. Ohiwa (2004). “A dense current flowing down a sloping bottom in a rotating fluid.” In: *Journal of Physical Oceanography* 34.
- Danabasoglu, Gokhan, William G. Large, and Bruce P. Briegleb (2010). “Climate impacts of parameterized Nordic Sea overflows.” In: *Journal of Geophysical Research*, Vol. 115, C11005. DOI: 10.1029/2010JC006243.

- Debreu, Laurent, Eric Blayo, and Bernard Barnier (2005). “A general adaptive multi-resolution approach to ocean modelling: experiments in a primitive equation model of the north Atlantic.” In:
- DeMiranda, A. (2003). “Implémentation et validation d’un modèle de couche de fond (bbl) dans opa.” In: *Rapport d’activité Mercator-Ocean-BBL-I-2003*.
- Dickson, R. R., J. Meincke, and P. Rhines (2008). “Arctic–Subarctic Ocean Fluxes. Defining the Role of the Northern Seas in Climate.” In: *Springer Science and Business Media*, 443–474.
- Dickson, Robert R. and Juan Brown (1994). “The production of North Atlantic Deep Water: Sources, rates, and pathways.” In: *Journal of Geophysical Research*, Vol. 99, No. C6, pages 12,319–12,341.
- Doscher, R. and A. Beckmann (2000). “Effects of a bottom boundary layer parameterisation in a coarse-resolution model of the North Atlantic Ocean.” In: *Journal of Atmospheric and Oceanic Technology*, Vol. 17.
- Dukhovskoy, Dmitry S., Steven L. Morey, Paul J. Martin, James J. O’Brien, and Cortis Cooper (2009). “Application of a vanishing, quasi-sigma, vertical coordinate for simulation of high-speed, deep currents over the Sigsbee Escarpment in the Gulf of Mexico.” In: *Ocean Modelling* 28 250–265. DOI: 10.1016/j.ocemod.2009.02.009.
- DYNAMO (2001). “Dynamics of the North Atlantic Circulation (DYNAMO).” In: *Progress in Oceanography - Special issue*.
- Ezer, Tal and George L. Mellor (2004). “A generalized coordinate ocean model and a comparison of the bottom boundary layer dynamics in terrain-following and in z-level grids.” In: *Ocean Modelling* 6 379–403. DOI: 10.1016/S1463-5003(03)00026-X.
- Fan, Xue, Uwe Send, Pierre Testor, Johannes Karstensen, and Pascale Lherminier (2013). “Observations of Irminger Sea Anticyclonic Eddies.” In: *Journal of Physical Oceanography*. DOI: 10.1175/JPO-D-11-0155.1.
- Gaspar, Philippe, Yves Grégoris, and Jean-Michel Lefevre (1990). “A Simple Eddy Kinetic Energy Model for Simulations of the Oceanic Vertical Mixing’ Tests at Station Papa and Long-Term.” In: *American Meteorological Society Ocean Modelling* 45-46 27-36.
- Girton, James B., L. J. Pratt, D. Sutherland, and J. Price (2006). “Is the Faroe Bank Channel overflow hydraulically controlled?” In: *Journal of Physical Oceanography* 36.
- Girton, James B. and Thomas B. Sandford (2003). “Descent and Modification of the Overflow Plume in the Denmark Strait.” In: *Journal of Physical Oceanography* 33.
- Gregorio, S., T. Penduff, G. Serazin, J.-M. Molines, B. Barnier, and J. Hirschi (2015). “Intrinsic variability of the Atlantic Meridional Overturning Circulation at interannual-to-multidecadal timescales.” In: *J. Phys. Oceanogr.*, 45, 7, pp. 1929–1946. DOI: 10.1175/JPO-D-14-0163.1.
- Griffies, Stephen M. (2003). “Fundamentals of Ocean Climate Models.” In: *Princeton University Press*.

- Griffies, Stephen M. (2012). “Elements of the Modular Ocean Model (MOM).” In: *GFDL Ocean Group Technical Report No. 7. NOAA/Geophysical Fluid Dynamics Laboratory*. DOI: <http://www.mom-ocean.org/web/docs>.
- Griffies, Stephen M., Ronald C. Pakanowski, and Robert W. Hallberg (2000). “Spurious Diapycnal Mixing Associated with Advection in a z-Coordinate Ocean Model.” In: *Monthly Weather Review* Volume 128.
- Haney, Robert L. (1991). “On the pressure gradient force over steep topography in sigma coordinate ocean models.” In:
- Hervieux, Gaelle (2007). “Numerical study of current-topography interactions: subpolar gyre, Gibraltar and Nordic Sea straits.” In: *Université Joseph-Fourier - Grenoble I jtel-00730205*.
- Hoyer, Jacob L. and Detlef Quadfasel (2001). “Detection of deep overflows with satellite altimetry.” In: *Geophysical Research Letters* 28.8.
- Ilıcak, Mehmet, Alistair J. Adcroft, Stephen M. Griffies, and Robert W. Hallberg (2011). “Spurious dianeutral mixing and the role of momentum closure.” In: *Ocean Modelling* 45–46 37–58. DOI: 10.1016/j.ocemod.2011.10.003.
- Jochumsen, K., M. Kollner, D. Quadfasel, S. Dye, B. Rudels, and H. Valdimarsson (2015). “On the origin and propagation of the Denmark Strait overflow water anomalies in the Irminger Basin.” In: *J. Geophys. Res. Oceans*, 120. DOI: 10.1002/2014JC010397.
- Jochumsen, K., D. Quadfasel, H. Valdimarsson, and S. Jónsson (2013). “Variability of the Denmark Strait overflow: Moored time series from 1996–2011.” In: *J. Geophys. Res.*, 117, C12003. DOI: 10.1029/2012JC008244.
- Jochumsen, Kerstin, Martin Moritz, Nuno Nunes, Detlef Quadfasel, Karin M. H. Larsen, Bogi Hansen, Hedinn Valdimarsson, and Steingrímur Jonsson (2017). “Revised transport estimates of the Denmark Strait overflow.” In: *Journal of Geophysical Research*. DOI: 10.1002/2017JC012803.
- Käse, R. H. and Andreas Oschlies (2000). “Flow thorough the Denmark Strait.” In: *Journal of Geophysical Research*, Vol. 105, No. C12.
- Koszalka, Inga M. K., Thomas W. N. Haine, and Marcello G. Magaldi (2013). “Fates and Travel Times of Denmark Strait Overflow Water in the Irminger Basin.” In: *American Meteorological Society*. DOI: 10.1175/JPO-D-13-023.1.
- Laanaia, N., A. Wirth, J. M. Molines, B. Barnier, and J. Verron (2010). “On the numerical resolution of the bottom layer in simulations of oceanic gravity currents.” In: *Ocean Sci.*, 6, 563–572.
- Legg, Sonya, Bruce Briegleb, Yeon Chang, Eric P. Chassignet, Gokhan Danabasoglu, Tal Ezer, Arnold L. Gordon, Stephen Griffies, Robert Hallberg, Laura Jackson, William Large, Tamay M. Özgökmen, Hartmut Peters, Jim Price, Ulrike Riemenschneider, Wanli Wu, Xiaobiao Xu, and Jiayan Yang (2009). “Improving oceanic overflow representation in climate models.” In: *American Meteorological Society*.

- Legg, Sonya, Robert W. Hallberg, and James B. Girton (2006). “Comparison of entrainment in overflows simulated by z-coordinate, isopycnal and non-hydrostatic models.” In: *Ocean Modelling* 11 69–97.
- Macrander, A., U. Send, H. Valdimarsson, S. Jónsson, and R. H. Käse (2005). “Interannual changes in the overflow from the Nordic Seas into the Atlantic Ocean through Denmark Strait.” In: *Geophysical Research Letters*, Vol. 32, L06606. DOI: 10.1029/2004GL021463.
- Macrander, Andreas, Rolf H. Kase, Uwe Send Hédinn Valdimarsson, and Steingrímur Jónsson (2007). “Spatial and temporal structure of the Denmark Strait Overflow revealed by acoustic observations.” In: *Ocean Dynamics* 57: 75–89. DOI: 10.1007/s10236-007-0101-x.
- Madec, Gurvan (2008). “NEMO ocean engine.” In: *Note du Pôle de modélisation, Institut Pierre-Simon Laplace (IPSL). France, No. 27.*
- Madec, Gurvan, Francois Lott, Pascale Delecluse, and Michel Crépon (1996). “Large-Scale preconditioning of deep-water formation in the Northwestern Mediterranean Sea.” In: *Journal of Physical Oceanography* 26.
- Mastropole, Dana, James Girton, Hédinn Valdimarsson, Kjetil Våge, Robert S. Pickart, and Kerstin Jochumsen (2017). “On the hydrography of Denmark Strait.” In: *J. Geophys. Res. Oceans* 122. DOI: 10.1002/2016JC012007.
- Mellor, G. L., T. Ezer, and L.-Y. Oey (1994). “The pressure gradient conundrum of sigma coordinate ocean models.” In: *Journal of atmospheric and oceanic technology*.
- Mellor, G. L., L.-Y. Oey, and T. Ezer (1998). “Sigma Coordinate Pressure Gradient Errors and the Seamount Problem.” In: *Journal of atmospheric and oceanic technology*.
- Paka, V., B. Rudels, D. Quadfasel, and V. Zhurbas (2010). “Measurements of turbulence in the zone of strong bottom currents in the Strait of Denmark.” In: *Doklady Earth Sciences* 432.
- Paka, V., V. Zhurbas, B. Rudels, D. Quadfasel, A. Korzh, and D. Delisi (2013). “Microstructure measurements and estimates of entrainment in the Denmark Strait overflow plume.” In: *Ocean Sci.*, 9, 1003–1014. DOI: 10.5194/os-9-1003-2013.
- Penduff, T., M. Juza, B. Barnier, J. Zika, W.K. Dewar, A.-M. Treguier, J. M. Molines, and N. Audiffren (2011). “Sea-level expression of intrinsic and forced ocean variabilities at interannual time scales.” In: *J. Climate*, 24, 5652–5670. DOI: 10.1175/JCLI-D-11-00077.1.
- Penduff, T., J. LeSommer, B. Barnier, J. M. Molines, and G. Madec (2007). “Depth dependent effects of momentum advection, sidewall boundary conditions and partial step topography in 1/4° global ocean simulations.” In: *Ocean Sci.*, 9, 1003–1014. DOI: 10.5194/os-9-1003-2013.
- Petersen, Mark R., Douglas W. Jacobsen, Todd D. Ringler, Matthew W. Hecht, and Mathew E. Maltrud (2015). “Evaluation of the arbitrary Lagrangian–Eulerian vertical coordinate method in the MPAS-Ocean model.” In: *Ocean Modelling* 86 93–113. DOI: 10.1016/j.ocemod.2014.12.004.
- Phillips, N. A. (1957). “A coordinate system having some special advantages for numerical forecasting.” In: *Journal of Meteorology* 14 184–185.

- Pickart, Robert S., Daniel J. Torres, and Paula S. Fratantoni (2005). “The East Greenland Spill Jet.” In: *American Meteorological Society*.
- Quadfasel, Detlef (2004). “Unpublished manuscript - Cruise Report FS Alexander von Humboldt 44-04-12.” In:
- Reckinger, Shanon M., Mark R. Petersen, and Scott J. Reckinger (2015). “A study of overflow simulations using MPAS-Ocean: Vertical grids, resolution, and viscosity.” In: *Ocean Modelling* 96 291–313. DOI: 10.1016/j.ocemod.2015.09.006.
- Riemenschneider, Ulrike and Sonya Legg (2007). “Regional simulations of the Faroe Bank Channel overflow in a level model.” In: *Ocean Modelling* 17 93–122. DOI: 10.1016/j.ocemod.2007.01.003.
- Ross, CK (1975). “Overflow 73, current measurements in Denmark Strait.” In: *ICES 1975, CM 1975/C: 6, 7pp +6 Figs (mimeo)*.
- Rudels, Bert, Patrick Eriksson, Hannu Grönvalland Riikka Hietala, and Jouko Launiainen (1999). “Hydrographic Observations in Denmark Strait in Fall 1997, and their Implications for the Entrainment into the Overflow Plume.” In: *Geophysical Research Letters*.
- Serazin, G., T. Penduff, S. Gregorio, B. Barnier, J.-M. Molines, and L. Terray (2015). “Intrinsic variability of sea-level from global 1/12° ocean simulations: spatio-temporal scales.” In: *J. Climate*, 28, 4279–4292. DOI: 10.1175/JCLI-D-14-00554.1.
- Shapiro, G., M. Luneva, J. Pickering, and D. Storkey (2013). “The effect of various vertical discretization schemes and horizontal diffusion parameterization on the performance of a 3-D ocean model: the Black Sea case study.” In: *Ocean Science*, 9, 377–390. DOI: 10.5194/os-9-377-2013.
- Siddorn, J.R. and R. Furner (2013). “An analytical stretching function that combines the best attributes of geopotential and terrain-following vertical coordinates.” In: *Ocean Modelling* 66 1–13. DOI: 10.1016/j.ocemod.2013.02.001.
- Sikirić, Mathieu Dutour, Ivica Janeković, and Milivoj Kuzmić (2009). “A new approach to bathymetry smoothing in sigma-coordinate ocean models.” In: *Ocean Modelling* 29 128–136. DOI: 10.1016/j.ocemod.2009.03.009.
- Snow, Kate, Andrew McC. Hogg, Stephanie M. Downes, Bernadette M. Sloyan, and Stephen M. Griffies Michael L. Bates (2015). “Sensitivity of abyssal water masses to overflow parameterisations.” In: *Ocean Modelling* 89 84–103.
- Song, Yuhe and Dale Haidvogel (1994). “A semi-implicit ocean circulation model using a generalized topography-following coordinate system.” In: *Journal of Computational Physics* 115 228–244.
- Spall, Michael A. and James F. Price (1997). “Mesoscale variability in the Denmark Strait: The PV outflow hypothesis.” In: *Journal of Physical Oceanography* 28.

- Våge, Kjetil, Robert S. Pickart, Michael A. Spall, G.W.K. Moore, Hédinn Valdimarsson, Daniel J. Torres, Svetlana Y. Erofeeva, and Jan Even Ø. Nilsen (2013). “Revised circulation scheme north of the Denmark Strait.” In: *Deep-Sea Research I* 79 (2013) 20–39.
- Voet, G. and D. Quadfasel (2010). “Entrainment in the Denmark Strait overflow plume by meso-scale eddies.” In: *Ocean Sci.*, 6, 301–310.
- Willebrand, Jürgen, Bernard Barnier, Claus Böning, Christian Dieterich, Peter D. Killworth, Christian Le Provost, Yanli Jia, Jean-Marc Molines, and Adrian L. New (2001). “Circulation characteristics in three eddy-permitting models of the North Atlantic.” In: *Progress in Oceanography* 48.
- Winton, Michael, Robert Hallberg, and Anand GNAnadesikan (1998). “Simulation of Density-Driven Frictional Downslope Flow in Z-Coordinate Ocean Models.” In: *American Meteorological Society*.